

POLITECNICO DI TORINO

Corso di Laurea Magistrale in
Ingegneria Biomedica

Tesi di Laurea Magistrale

Holmium-doped bioactive glass scaffolds for bone cancer treatment



Relatori

Prof. Francesco Baino
Prof. ssa Enrica Vernè

.....
.....

Candidato

Sara Ciavattini
.....

Ottobre 2020

INDEX

Abstract	I
Chapter 1.....	1
Bone Cancer: Current Trends in the Treatment of Malignant Tumoral Diseases.....	1
1.1 The Bone Tissue	1
1.1.1 The Bone Matrix	2
1.1.2 The Cells of Mature Bone	3
1.1.3 Lamellar Bone Tissue	4
1.1.4 The Periosteum and Endosteum.....	7
1.1.5 Bone Development and Growth.....	8
1.1.5.1 Intramembranous Ossification	9
1.1.5.2 Endochondral Ossification	10
1.1.6 Blood and Nerve Supply to Bones.....	11
1.1.7 Bone Remodelling.....	12
1.1.8 Factors Regulating Bone Formation and Bone Remodelling	14
1.2 Bone Cancer.....	15
1.2.1 Definition of Tumour and General Features of Neoplastic Development	15
1.2.2 Characteristics of Bone Tumours.....	17
1.2.2.1 Primary Bone Tumours.....	17
1.2.2.2 Secondary Bone Tumours.....	20
1.3 Bone Cancer Treatments.....	20
1.3.1 Surgical Therapy	20
1.3.2 Chemotherapy	22
1.3.3 Radiation Therapy.....	23
1.3.4 Thermoablative Techniques.....	25
1.3.5 Other Possible Methods	27
1.3.6 Summary of Bone Cancer Treatments	28
1.4 Materials for Bone Tumour Treatment.....	29
1.4.1 Materials for Surgery	29
1.4.1.1 Transplant Materials (Bone Grafts)	30
1.4.1.2 Biological Materials	31
1.4.1.3 Synthetic Bone Substitutes.....	32
1.4.2 Drug Delivery Materials	34
1.4.3 Materials for Brachytherapy	37
1.5 Conclusions	37

Chapter 2.....	44
Bioactive Glasses	44
2.1 Glass and its Components	44
2.2 Bioactive Materials	46
2.3 The Invention of Bioactive Glass	47
2.3.1 Bioactivity Mechanism	49
2.3.1.1 Formation of the HCA Layer	50
2.3.1.2 Ionic Dissolution Products and Osteogenesis	51
2.3.1.3 Influence of the Ionic Dissolution Products.....	52
2.4 Categories of Bioactive Glasses.....	52
2.4.1 Silicate Bioactive Glasses	53
2.4.2 Borate Bioactive Glasses	53
2.4.3 Phosphate Bioactive Glasses.....	54
2.4.4 Black Glasses	54
2.4.5 Doped Bioactive Glasses	55
2.5 Manufacturing Techniques for the Production of BGs.....	55
2.5.1 Melt-Derived Technique	55
2.5.2 Sol-Gel Technique	57
2.5.2.1 Hydrolysis and Polycondensation.....	59
2.5.2.2 Physical, Chemical and Biological Properties of Sol-Gel Derived Materials	61
2.6 Clinical Applications of Bioactive Glasses	63
2.6.1 Bone Repair and Orthopaedic Surgery	64
2.6.2 Chondrogenesis and Osteochondral Tissue Engineering.....	65
2.6.3 Soft Tissue Repair	65
2.6.4 Cancer Therapy	66
2.6.4.1 Mesoporous Bioactive Glasses for Targeted Tumour Therapy	67
2.6.4.2 Magnetic Bioactive Glasses for Hyperthermia Treatment.....	69
2.6.4.3 Bioactive Glasses Applied in Brachytherapy.....	71
2.6.5 Clinical Products based on Bioactive Glasses: a Historical Overview	78
2.7 Bioactive Glass Scaffolds for Bone Tissue Engineering	80
2.7.1 Fabrication Techniques	84
2.7.1.1 Foaming Methods	84
2.7.1.2 Thermal Consolidation of Particles.....	85
2.7.1.3 Freeze-Drying	86
2.7.1.4 Foam Replica Method.....	87
2.7.1.5 Solid Freeform Fabrication	88
2.8 Conclusions	97

Chapter 3.....	110
Production of Bioactive Glass Scaffolds by Foam Replica Method.....	110
3.1 The Foam Replica Method.....	110
3.2 Variants of the Process and Impact on the Morphological Properties.....	111
3.2.1 Replica of Synthetic Templates	112
3.2.2 Replica of Natural Templates	121
3.2.2.1 Replica of Marine Sponges	121
3.2.2.2 Replica of Bread.....	124
3.2.2.3 Replica of Vegetal and Fungal Templates	125
3.2.2.4 Replica of Demineralized Bone Matrix	128
3.3 Mechanical Properties	130
3.4 Mass Transport Properties	137
3.5 In Vivo Studies	139
3.6 Conclusions	148
Chapter 4.....	156
Materials and Methods	156
4.1 Introduction to the Experimental Activity and Scope of the Work	156
4.2 Synthesis of Ho-doped Sol-Gel Glass	158
4.3 Glass Processing at Politecnico di Torino (Turin, Italy)	159
4.3.1 Scaffold Manufacturing	160
4.3.1.1 Materials.....	160
4.3.1.2 Scaffold Fabrication Stages	160
4.4 Glass Characterization - Federal University of ABC (São Paulo, Brazil).....	164
4.4.1 Thermal Analysis	164
4.4.1.1 Differential Scanning Calorimetry	164
4.4.1.2 Thermogravimetric Analysis.....	166
4.4.1.3 Derivative Thermogravimetry.....	167
4.4.2 Neutron Activation Analysis.....	167
4.4.3 Fourier-Transform Infrared Spectroscopy	169

4.5 Glass Characterization - Politecnico di Torino (Turin, Italy) ..	170
4.5.1 Particle Size Analysis.....	170
4.5.2 Thermal Analysis	171
4.5.2.1 Differential Thermal Analysis	172
4.5.2.2 Hot Stage Microscopy.....	173
4.5.3 X-Ray Diffraction	175
4.5.4 Scanning Electron Microscopy and Energy Dispersive Spectroscopy	177
4.5.5 Brunauer, Emmett and Teller Theory (BET).....	181
Chapter 5.....	188
Results and Discussion	188
5.1 Characterization of Ho-doped Dried Gel and Ho-doped Bioactive Glass at Federal University of ABC (São Paulo, Brazil)	188
5.1.1 Thermal Analysis	188
5.1.2 Neutron Activation Analysis.....	191
5.1.3 Fourier Transform-Infrared Spectroscopy	191
5.2 Ho-doped Bioactive Glass Characterization at Politecnico di Torino (Turin, Italy)	193
5.2.1 Particle Size Analysis.....	193
5.2.2 Thermal Analysis	195
5.2.3 X-Ray Diffraction	203
5.2.4 Scanning Electron Microscopy and Energy Dispersive Spectroscopy	205
5.2.5 Textural Analysis	211
5.3 Ho-doped Scaffold Preparation and Characterization - Politecnico di Torino (Turin, Italy)	216
5.3.1 Morphological and Compositional Analysis of the 3D Structures	220
5.4 Ho-doped Bioactive Glass Scaffold Limitations.....	227
5.5 Conclusions	228
Chapter 6.....	233
Conclusions and Future Developments	233
6.1 Contextualization of the Research Activity	233
6.2 Main Experimental Results.....	234
6.3 Improvements and Future Developments.....	238

Abstract

Bone can be affected by tumours, thus being subjected to alteration of its physiological structure with possible negative impact on its mechanical resistance.

Brachytherapy has proven to be a very advantageous technique to destroy cancer because it allows a high dose of radiation to be safely delivered into the tumour, minimizing the damage to adjacent healthy tissue.

Bioactive glass (BG) scaffolds are particularly interesting devices for brachytherapy due to their ability to carry out the therapeutic action *in situ* and support bone tissue ingrowth after the treatment. One of the most popular techniques for producing BG scaffolds is the foam replica method, which allows obtaining highly porous and interconnected 3D bone-like scaffolds.

After providing a comprehensive review of the state of the art in such fields, this experimental work aimed at developing BG scaffolds containing holmium (Ho) for the treatment of bone cancer by brachytherapy. Holmium-166 (^{166}Ho), obtained from holmium-165 (^{165}Ho) by neutron activation, has suitable physical properties for brachytherapy. A few compositions of BGs containing holmium have been already produced by some research teams but no example of BG scaffold containing holmium has been reported to date.

Ho-doped BG (Ho-BG) was produced by sol-gel process at Federal University of ABC (São Paulo, Brazil). Thermal analysis, such as Differential Scanning Calorimetry (DSC), Thermogravimetric Analysis (TGA) and Derivative Thermogravimetry (DTG) were performed on the dry gel powders in order to investigate the gel behaviour under heat treatment. In addition, Neutron Activation Analysis (NAA) and Fourier-Transform Infrared Spectroscopy (FTIR) were performed on the Ho-BG powders in order to evaluate the composition and structure of the glass, respectively.

Since the particle size analysis showed the heterogeneity of the particle size, the glass powders were ground and sieved by using a sieve with mesh of 32 μm in diameter. The resulting powders, named Ho-BG32 powders, exhibited diameters below 32 μm , as expected. Differential Thermal Analysis (DTA) and Hot Stage Microscopy (HSM) were performed both on Ho-BG powders and Ho-BG32 powders in order to determine glass transition, crystallization onset, melting temperature, as well as first shrinkage and maximum shrinkage temperatures. X-Ray Diffraction (XRD), performed both on Ho-BG powders and Ho-BG32 powders, confirmed the amorphous nature of the material. Ho-BG powders were analysed by Scanning Electron Microscopy (SEM) and Energy Dispersive Spectrometry (EDS) in order to investigate powders morphology and their composition, respectively. The nanoporous texture and the surface area both of Ho-BG powders and Ho-BG32 powders were investigated by N_2 sorption measurements and BET analysis.

Once the powder characterization was completed, scaffolds were fabricated by foam replica method. Morphological and compositional analyses were performed in order to evaluate the potential suitability of these devices for bone replacement and regeneration. The scaffolds exhibited a total porosity of 86%. The pores were well interconnected and showed a bimodal size distribution. However, the scaffolds exhibited high brittleness. Therefore, the fabrication process should be optimized in order to obtain more resistant scaffolds. Moreover, additional *in vitro/in vivo* studies deserve to be carried out in order to verify the suitability of these scaffolds for the intended purpose.

Chapter 1

Bone Cancer: Current Trends in the Treatment of Malignant Tumoral Diseases

The aim of this chapter is to provide an overview of current methods and materials used in clinical practice for the treatment of malignant bone tumours.

In the first part of the chapter, the bone tissue will be introduced, by focusing on the cells that are found in this tissue and on the mechanism of bone development and growth.

Then, the attention will be shifted to bone tumours. Cancer features will be defined, and the most common bone cancer types will be presented.

In the second part of the chapter, the most common bone cancer treatments will be displayed in their general aspects.

Finally, the materials currently used for bone cancer treatment, such as materials for surgery, for drug delivery, and for brachytherapy will be discussed.

1.1 The Bone Tissue

The bones are part of the skeletal system, which is also composed of cartilages, ligaments and other connective tissues [1]. The skeletal system exerts numerous functions. It provides structural support for the entire body, permits movement and locomotion by providing levers for the muscles, and protects tissues and organs. In addition, it produces blood cells, and acts as a mineral storage since the calcium salts of bone are an important reserve that maintains normal concentrations of calcium and phosphate ions in body fluids [1].

In human skeleton there are 206 major bones [1], which can be classified according to their shape, as follow:

- Long bones: they have two epiphyses, a diaphysis, and two metaphysis (Figure 1) [1].
The epiphyses are the proximal and distal ends of the bone. The diaphysis is the tubular shaft that is connected to the epiphysis at a narrow zone known as metaphysis [1]. The hollow region in the diaphysis is called medullary cavity, which is filled with yellow marrow [2]. The diaphysis is mainly composed of dense cortical bone, whereas the metaphysis and epiphysis are composed of trabecular meshwork bone surrounded by a relatively thin shell of dense cortical bone [3].
- Short bones: they are composed of spongy bone covered by compact bone [1].
- Flat bones: they are composed of spongy bone covered by two thin, parallel surfaces of compact bone [1].
- Irregular bones: they have complex shapes, and their interior structure is equally varied [1].
- Sesamoid bones: they develop inside tendons, and they are usually small, round, and flat [1].
- Sutural bones: they are small and flat [1].
- Pneumatized bones: they may either be hollow bones or may contain numerous air pockets [1].

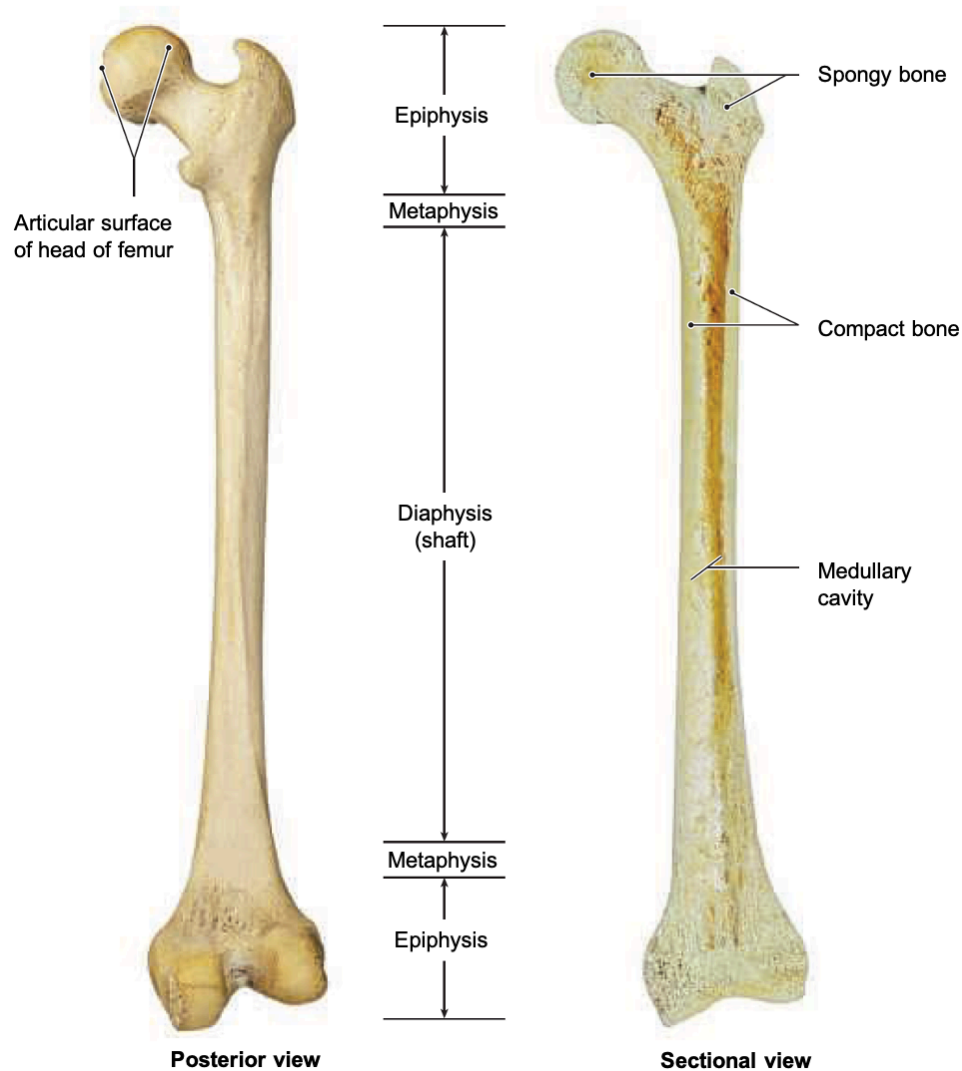


Figure 1: Anatomy of a representative bone [1].

1.1.1 The Bone Matrix

Bone tissue is a connective tissue that owes its typical physical characteristics to the combination of organic and inorganic substances, resulting in the bone extracellular matrix [4].

Organic substance is basically composed of ossein (collagen fibres) and a glycoprotein called osteomucoid [4].

Inorganic substance, which represents about 60-70 wt% of bone tissue in adults, is composed of calcium phosphate (86%), calcium carbonate (12%), magnesium phosphate (1.5%), calcium fluoride (0.5%), and iron oxide (traces) [4].

Bone matrix is solid because of the deposition of calcium salts around the protein fibres [1].

Calcium phosphate, $\text{Ca}_3(\text{PO}_4)_2$ interacts with calcium hydroxide $\text{Ca}(\text{OH})_2$ to form crystals of hydroxyapatite $\text{Ca}_{10}(\text{PO}_4)_6(\text{OH})_2$ (HA). Upon crystals growth and development, different ions are incorporated, including sodium, magnesium and fluoride, and other calcium salts, such as calcium carbonate [1]. Due to the dominant presence of inorganic components, bone is characterized by a good resistance to compression stresses. In fact, calcium phosphate crystals tolerate compression, but

they break into small pieces when exposed to bending or twisting stresses, because they are inflexible [1].

Organic components provide a framework for the formation of hydroxyapatite crystals, thus conferring to the tissue mechanical properties complementary to that determined by the inorganic part. Indeed, it is known that collagen fibres are flexible, and show good behaviour under stretching, twisting, and bending. However, they do not bear compression [1].

The result of the interaction between organic and inorganic substance is a protein–crystal combination, with intermediate properties between those of collagen and those of pure mineral crystals [1].

1.1.2 The Cells of Mature Bone

Bone tissue is composed of four types of specialized cells: osteoblasts, osteocytes, osteoclasts, and osteoprogenitor cells (Figure 2).

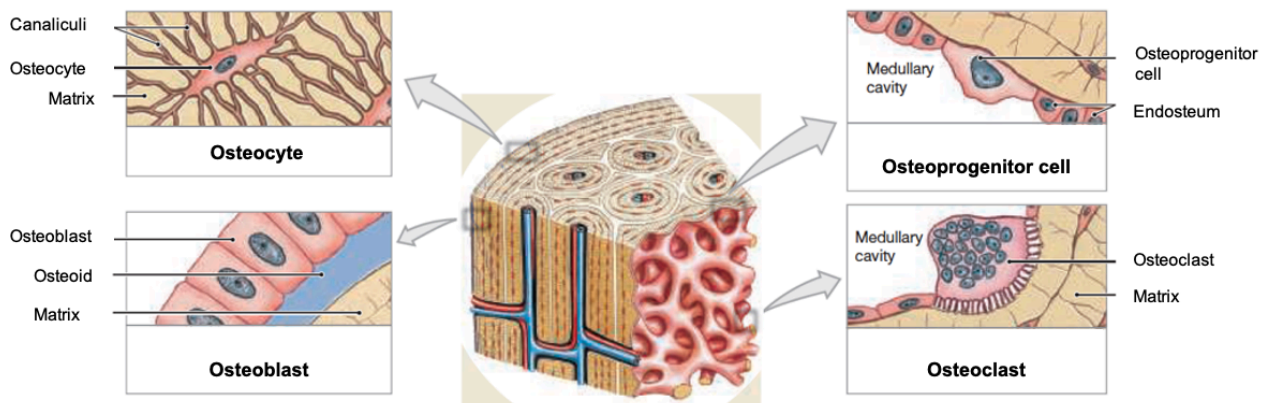


Figure 2: Cells of bone tissue [1].

- **Osteoblasts** are cuboidal cells of 15-30 μm thickness, structured as a layer [5]. They are bone-forming cells that synthesize and secrete osteoid, which is the organic component of the bone matrix. Osteoid is composed of type I collagen, glycosaminoglycans and proteoglycans [6]. Additionally, osteoblasts participate in the calcification and resorption processes of bone, and regulate the flux of calcium and phosphate in and out of bone [5]. Osteoblasts derives from mesenchymal progenitors [5], and when they are surrounded by matrix, they differentiate into osteocytes [1].
- **Osteocytes** represent the most abundant cell type in mature bone [7]. They are the mechanosensory cells of bone, and play an important role in functional adaptation of bone [7]. They are involved in bone turnover, they direct the release of calcium from bone into blood, and the deposition of calcium salts into the surrounding matrix [4]. Osteocytes are located in small areas called *lacunae*, which are connected to each other by channels called *canaliculi* [1]. Canaliculi are occupied by a dendritic process that connects osteocytes to each other, with cells on bone surface, and bone marrow [8].

Osteocytes derive from the incorporation of osteoblasts into the bone matrix [7].

- **Osteoclasts** are multinucleated giant cells, that can exceed 100 μm , responsible for bone resorption and removal [1].

Osteoclasts secrete acids by the exocytosis of lysosomes. These acids initiate an erosion process called osteolysis, which consists in the dissolution of the bony matrix and the release of both amino acids and the stored calcium and phosphate. This process increases calcium and phosphate concentrations in body fluids [1].

Furthermore, osteoclasts may also be involved in osteoblast differentiation, immune system activation, and the proliferation of tumour cells in bone [1].

Osteoclasts derive from stem cells [1].

Osteoclasts and osteoblasts cooperate, and the balance between their activities is very important. While osteoclasts are always involved in matrix removal and minerals release, osteoblasts activity guarantees the production of new matrix, which quickly binds minerals. When osteoblasts are more active than osteoclasts, bones become stronger and more massive [1].

- **Osteoprogenitor cells** are the stem cells of bone [1].

They differentiate from mesenchyme, and divide to produce daughter cells that differentiate into osteoblasts [1], [6]. In mature bone, where there is no active new bone formation or remodelling, the osteoprogenitor cells become flattened spindle cells, closely attached to the bone surface and are called inactive osteoblasts. During bone growth, instead, these cells increase both in number and size, and differentiate into active osteoblast [6].

1.1.3 Lamellar Bone Tissue

Bone tissue can be composed of either non-lamellar tissue or lamellar tissue [4].

Differently from non-lamellar bone, the lamellar tissue is characterized by a precise orientation of the bone cells and the fundamental substance [4]. It is composed of bony lamellas consisting of both organized and amorphous components of fundamental substance. The organized part is composed of collagen fibrils, which run parallel to each other in one or more concentrically superimposed layers. The amorphous part fills the spaces left free by the organized part and by the extensions of the bone cells [4].

Lamellar bone tissue constitutes most of the bones of human body, and includes compact and spongy bone [4].

Compact bone represents 80% of the skeletal mass. It is relatively solid and dense [5], and has a porosity of 5% to 15% [9]. It forms the surface of all bones with different thicknesses [2].

The functional unit of mature compact bone is the cylindrical osteon or Haversian system, in which interstitial lamellae fill in the spaces between the osteons, while circumferential lamellae occur at the external and internal surfaces of bone [1].

A diagram of compact bone is shown in Figure 3.

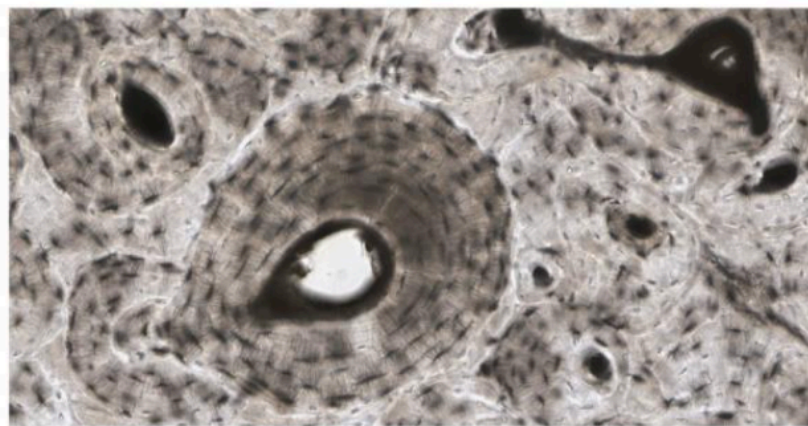
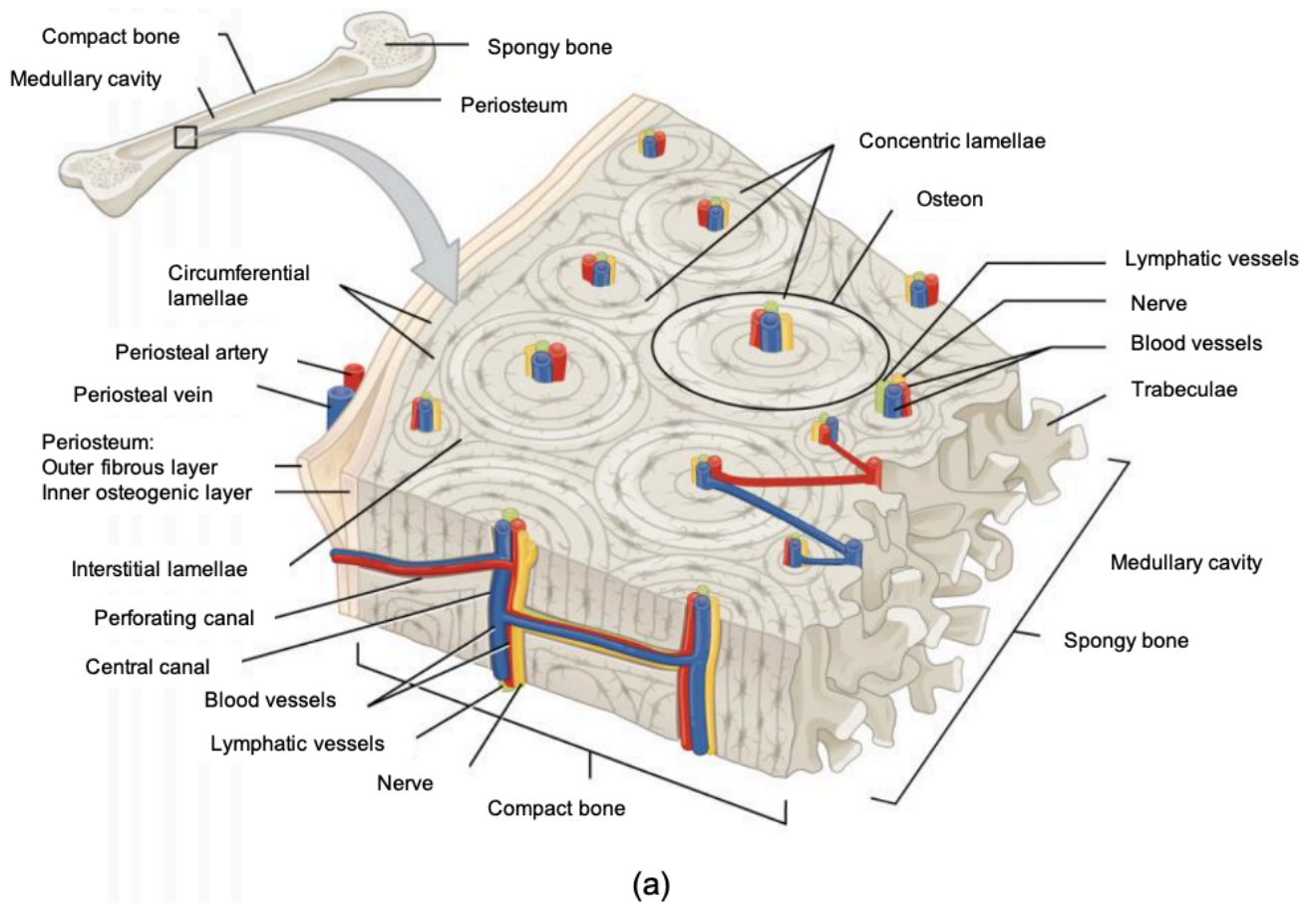
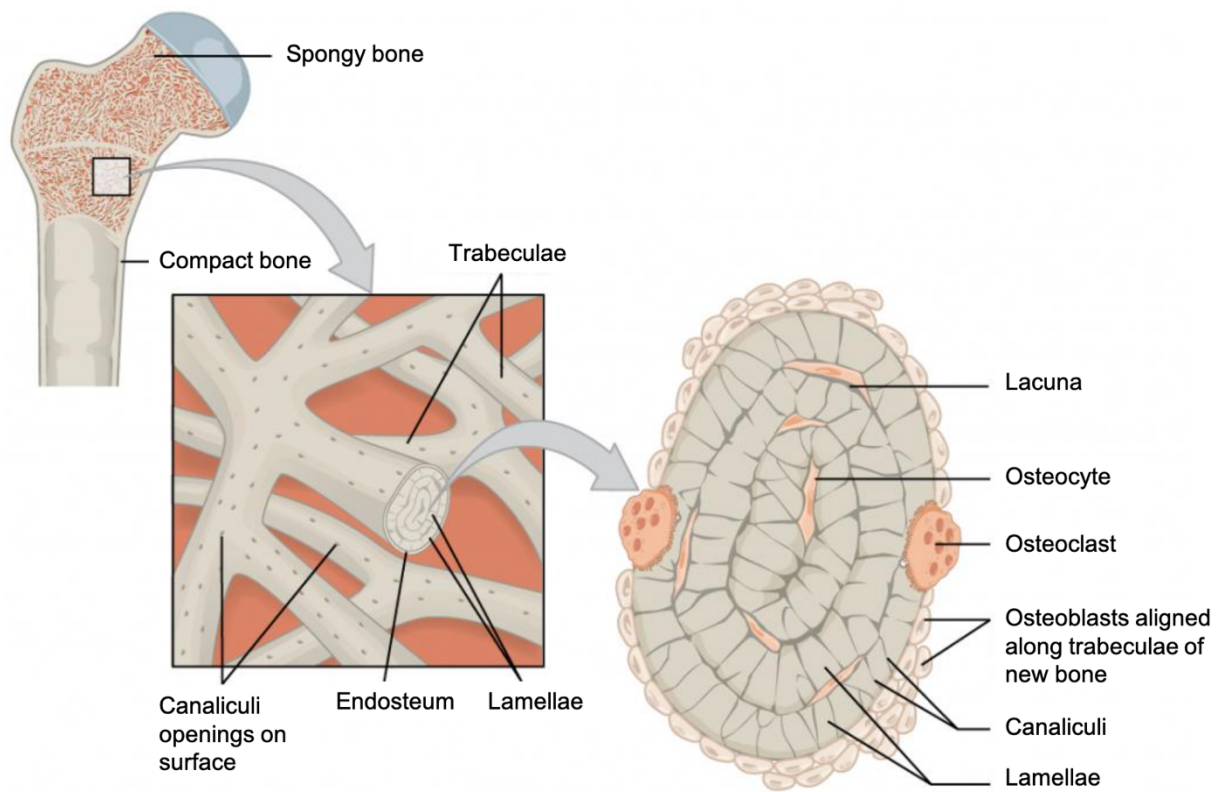


Figure 3: Compact bone: (a) schematic representation, and (b) micrograph of the compact bone [2].

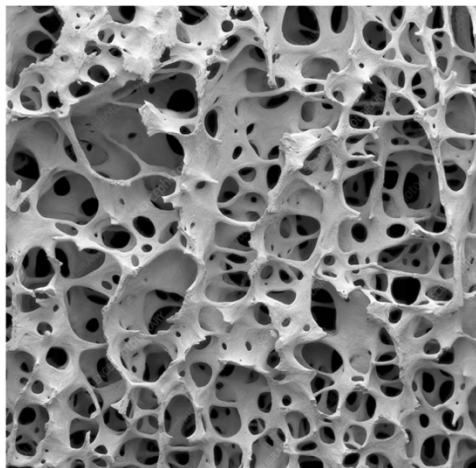
Spongy bone, also called trabecular bone or cancellous bone, represents the remaining 20% of the skeletal mass [5]. It forms an open network of struts and plates [2]. Its porosity ranges from 50% to 95% [9]. It is lighter than compact bone, but trabeculae give spongy bone considerable strength despite its low weight. Thus, the presence of spongy bone reduces the weight of the skeleton and makes it easier for muscles to move the bones [1].

Spongy bone surrounds the medullary cavity which contains bone marrow, connective tissue and stem cells [2]. In addition, spongy bone is found wherever bones are not stressed heavily or where stresses arrive from many directions [1].

A diagram of spongy bone is shown in Figure 4.



(a)



(b)

Figure 4: Spongy bone: (a) schematic representation, and (b) micrograph of the spongy bone [2].

The different structure gives the cortical and the spongy bone different mechanical properties, as shown in Table 1.

Table 1: Mechanical properties of cortical and spongy bone. Table adapted from Boccaccini et al. [10]

Mechanical Property	Cortical Bone	Spongy Bone
Compressive strength (MPa)	130-200	0.1-16
Tensile strength (MPa)	50-151	n.a.
Compressive elastic modulus (GPa)	11.5-17	0.12-1.1
Young's modulus (GPa)	7-30	0.05-0.5
Fracture toughness ($\text{MPa} \cdot \text{m}^{1/2}$)	2-12	n.a.

Since cortical and trabecular bone have different structure, and as result different mechanical properties, they act differently.

For example, as concern femur, when you are standing, the diaphysis composed of compact bone, transfers your body weight from your hip to your knee. The osteons within the shaft are parallel to its long axis, and consequently, the femur is very strong when stressed along that axis. Differently, a collision to the side of the shaft may elicit a break, or fracture [1].

The epiphyses of the femur are composed of spongy bone. The trabeculae are oriented along the stress lines, but with extensive cross-bracing. At the proximal epiphysis, the trabeculae transmit forces from the hip across the metaphysis to the femoral diaphysis; at the distal epiphysis, the trabeculae transmit the forces across the knee joint to the leg [1].

1.1.4 The Periosteum and Endosteum

Bone is externally covered by periosteum and internally by endosteum, as shown in Figure 5.

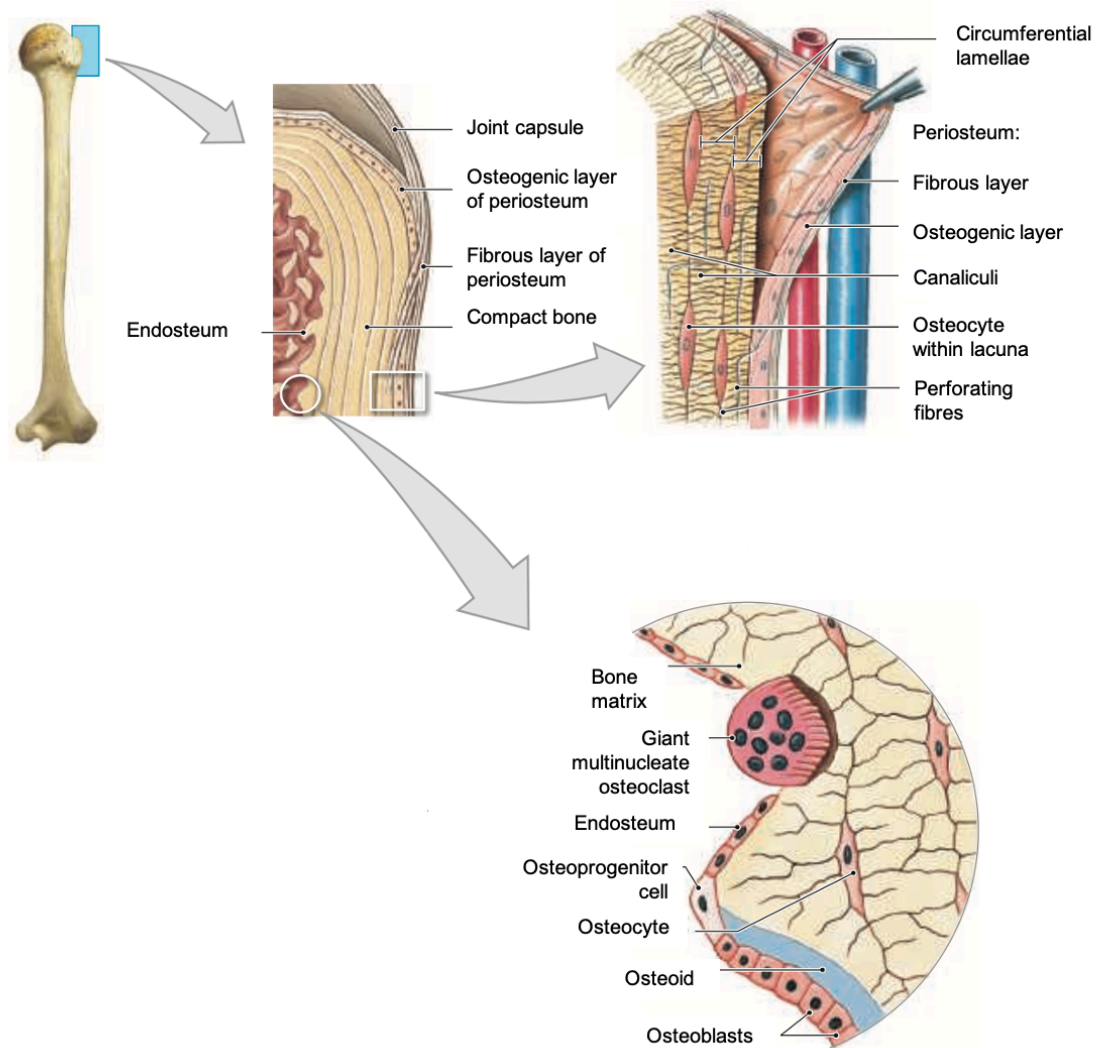


Figure 5: Anatomy and histology of the periosteum and endosteum [1].

Periosteum isolates and protects the bone from surrounding tissue, permits blood circulation, participates in bone growth and repair and attaches the bone to the connective tissue network [1]. Furthermore, it contains osteogenic cells that regulate the outer shape of bone [11].

Periosteum acts in synergy with endosteum, which regulates the cortical thickness, the size and the position of bone in the space [11]. Endosteum contains osteoprogenitor cells [1]. Endosteum covers the medullary (marrow) cavity, the inner surface of the central and perforating canals, and the spongy bone [1].

1.1.5 Bone Development and Growth

From fecundation to about eight weeks of age, embryo's skeletal components are composed either of mesenchyme or hyaline cartilage. Afterwards both mesenchyme and cartilage are replaced by bone. This process is called ossification [1].

There are two forms of ossification: intramembranous ossification and endochondral ossification [1].

1.1.5.1 Intramembranous Ossification

Intramembranous ossification begins during fetal development and, leads to the formation of both compact and spongy bone belonging to the skull, clavicles, shoulders and face's flat bones [2].

Figure 6 shows the main phases of intramembranous ossification.

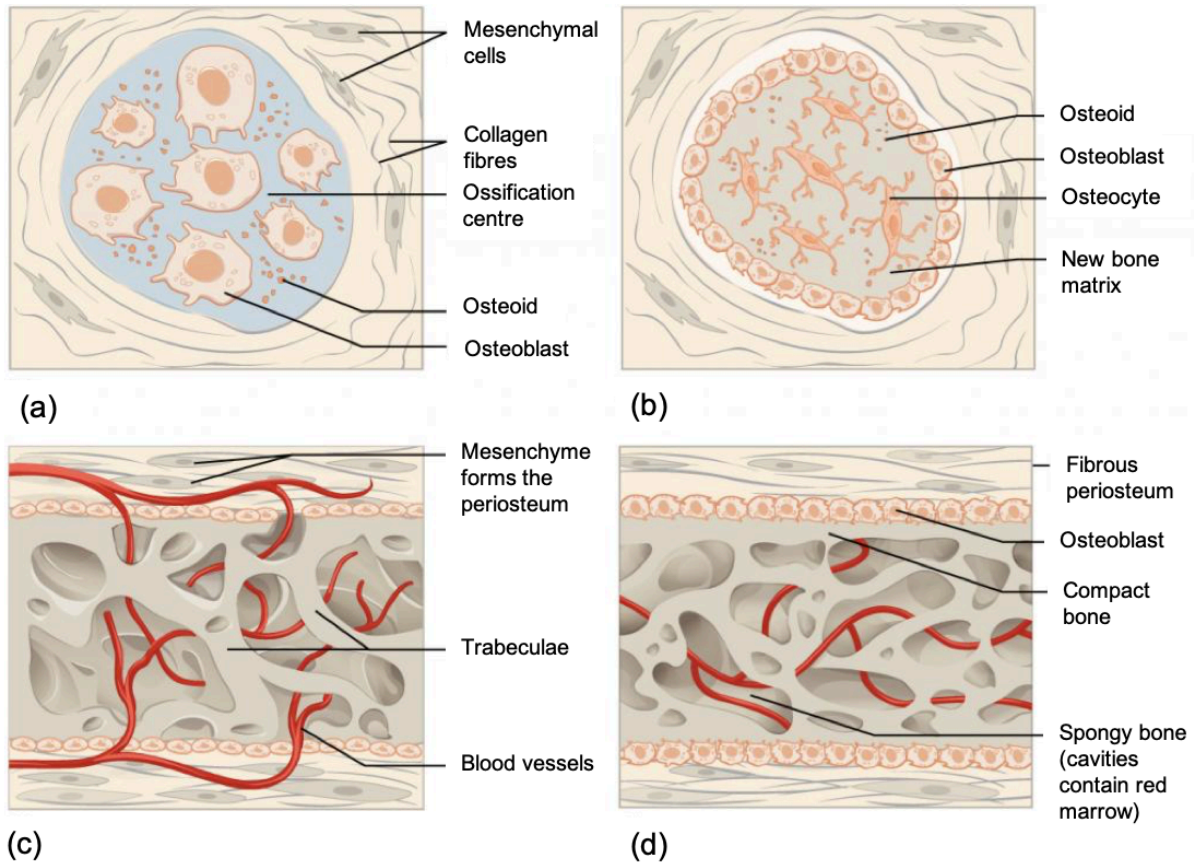


Figure 6: Intramembranous ossification [2].

Starting from the ossification centre, osteoblasts cluster together to secrete the osteoid, which, after few days, envelopes them (Figure 6a) [1].

Afterwards, osteoblasts start to differentiate into osteocytes, then trapped into small areas called lacunae (Figure 6b) [1].

Bone growth continues to progress outward from the ossification centre in small struts called spicules, while mesenchymal stem cells differentiation produces additional osteoblasts [1].

As bone growth is an active process, continue oxygen and nutrient supply is required, and the rate of new bone formation is directly linked to the formation of an interconnected blood vessel network between the spicules. In fact, as spicules interconnect, they trap blood vessels, thus creating bony slabs constituting the trabecular matrix [1].

At the same time, osteoblasts take part in the formation of the periosteum in the surface of the trabecular bone (Figure 6c) [2].

Finally, adjacent slabs fuse together, and nearby blood vessels condense into red marrow (Figure 6d) [1].

1.1.5.2 Endochondral Ossification

Bones at the base of the skull and long bones form via endochondral ossification [2].

Figure 7 shows the phases of endochondral ossification.

After 6-8 weeks from the conception, some mesenchymal cells differentiate into cartilage cells, called chondrocytes (Figure 7a) [2].

Chondrocytes proliferate and deposit matrix to form a cartilage model of the future bone [5]. Subsequently, a membrane called perichondrium forms on the cartilage (Figure 7b) [2]. Chondrocytes mature and grow in size and the matrix calcifies. Calcification of the matrix does not allow nutrients to reach the chondrocytes in the core, determining their death and the consequent breakdown of the surrounding cartilage. The blood vessels invade the resulting spaces, slowly creating the medullary cavity. As the cartilage grows, the capillaries penetrate it. This causes the transformation of the perichondrium into periosteum. Ossification begins at the primary ossification centre, located in the periosteum (Figure 7c) [2].

Chondrocytes and cartilage continue to grow at the bone epiphysis, thus increasing its length (Figure 7d), while in the diaphysis, cartilage is replaced by bone. Secondary ossification centers develop (Figure 7e) [2].

When the fetal skeleton is fully formed, the only two areas in which the cartilage keeps are in the articular surface as articular cartilage, and between the diaphysis and the epiphysis as the epiphyseal plate (Figure 7f) [2].

After birth, this same series of events occurs in the epiphysis in areas, called secondary ossification centres (Figure 7g) [2].

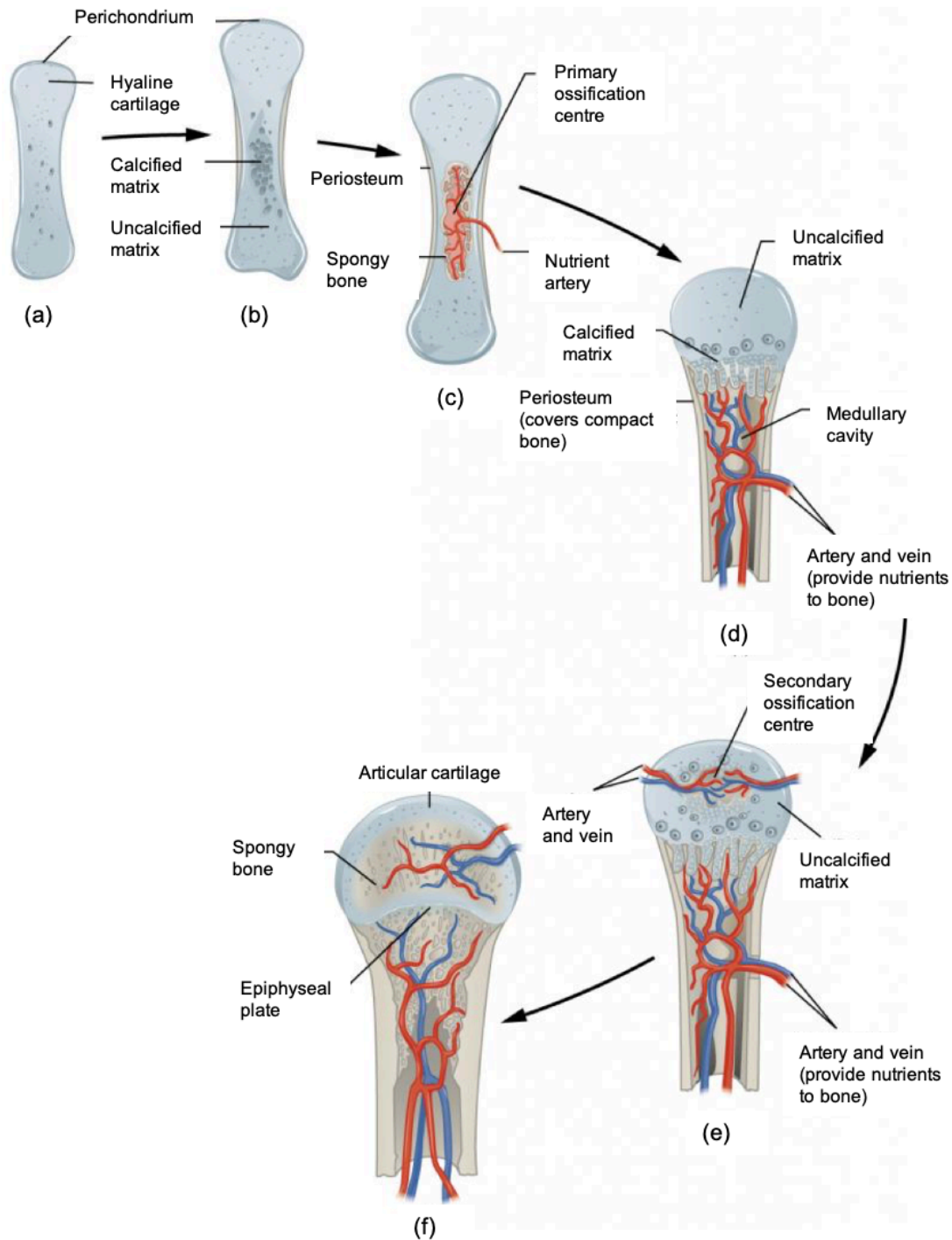


Figure 7: Endochondral ossification [2].

1.1.6 Blood and Nerve Supply to Bones

Bone tissue is highly vascularized. There are four major sets of vessels involved (Figure 8):

- **Nutrient artery** and **nutrient vein** form at the beginning of endochondral ossification, when blood vessels invade the cartilage model. They cross diaphysis, through an opening called *foramen*, to reach the medullary cavity. Ascending and descending branches of nutrient artery get near epiphyses [1].

- **Metaphyseal vessels** provide blood to the inner surface of each epiphyseal cartilage, where cartilage is replaced by bone [1].
- **Epiphyseal vessels** provide the bone tissue and medullary cavities of epiphyses crossing the bone through foramina contained in the epiphyseal ends of long bones [1].
- **Periosteal vessels** are incorporated into the developing bone surface. They supply blood to the superficial osteons of the trunk. During endochondral ossification, branches of these vessels crossing epiphyses carry the blood to the secondary ossification centres [1].

Furthermore, the periosteum is crossed by lymphatic vessels and sensory nerves. Lymphatic vessels collect a fluid derived from the interstitial fluid, called lymph, from vessels that through perforating canals reach osteons. Sensory nerves innervate the endosteum, epiphyses, and the medullary cavity [1].

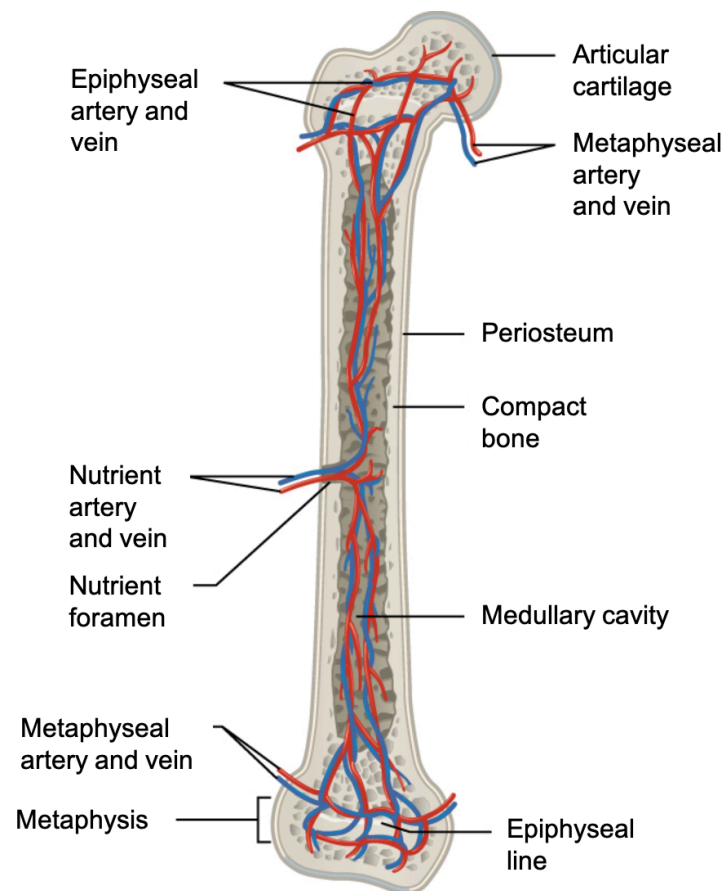


Figure 8: Vessels involved in the vascularization of bone tissue [2].

1.1.7 Bone Remodelling

Bone remodelling is the dynamic process that permits the maintenance of bone tissue, the repair of damaged tissue and the homeostasis of the P-Ca metabolism [12], [13].

It consists of bone resorption by osteoclasts and bone formation by osteoblasts [12], [13]. Bone resorption always takes place before bone formation, and the quantity of bone resorbed is similar to the amount of bone formed [13].

Through this process about 5% of cortical bone and 20% of trabecular bone is renewed per year. Skeleton is completely renewed every ten years [13].

Bone remodelling occurs throughout life. Bone mass reaches the maximum value at the age of thirty and is maintained until the age of fifty [13].

Bone remodelling occurs in basic multicellular units (BMU) that are small areas of the cortical and trabecular surface [13].

Bone remodelling takes place in five steps, as shown in Figure 9:

1. **Quiescent phase** is when the bone is at rest [13].
2. In the **activation phase** the bone surface activates, the elongated mature osteoblasts placed on the endosteal surface retract, and the endosteal membrane is digested by collagenase action. The mineralized surface is exposed, and attracts the circulating osteoclasts [13].
3. In the **resorption phase** osteoclasts begin to decompose both the mineral matrix and the osteoid matrix, and the macrophages complete the process. Growth factors are released [13].
4. During the **formation phase**, the released growth factors attract preosteoblasts in the resorbed areas. Preosteoblasts synthesize a cementing material upon which the new tissue sticks. Furthermore, preosteoblasts express bone morphogenetic protein (BMP) responsible for differentiation. Some days later, the osteoid material is synthesized by differentiated osteoblasts [13].
5. Thirty days later the last phase, called the **mineralization phase**, begins, and then it ends at 90 days in the trabecular and at 130 in the cortical bone [13].

Finally, the quiescent phase begins again and the process repeats [13].

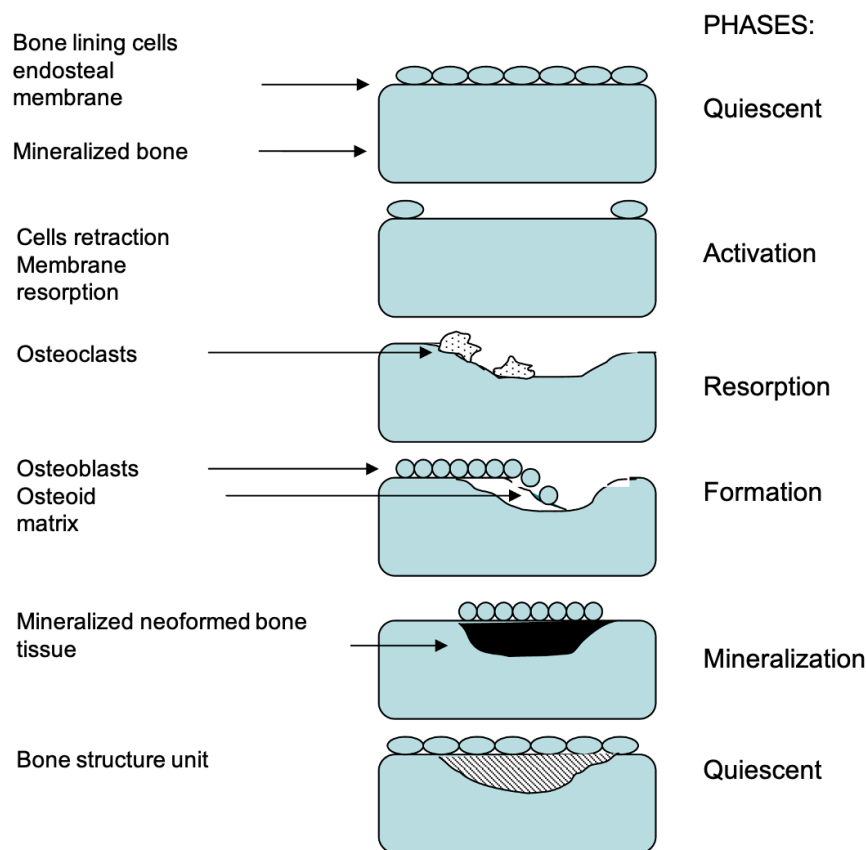


Figure 9: Bone remodelling. Figure adapted from Fernández-Tresguerres Hernández-Gil [13].

1.1.8 Factors Regulating Bone Formation and Bone Remodelling

Bone formation and bone remodelling are influenced by many factors, as shown in Table 2.

Table 2: Factors regulating bone formation and remodelling.

Type of Factor		Mechanism of Action	Ref.
Genetic		It determines bone mass.	[13]
Mechanical		Muscular action increases bone formation, while physical inactivity stimulates bone resorption.	[13]
Vascular		It supplies blood cells, oxygen, minerals, ions, glucose, hormones and growth factors.	[1]
Nerve		It supplies blood cells, oxygen, minerals, ions, glucose, hormones and growth factors.	[1]
Nutritional	Vitamin A	It incites osteoblasts activity.	[1]
	Vitamin C	It is necessary in collagen synthesis and osteoblast differentiation for enzymatic reactions.	[1]
	Vitamin D3	It synthesizes calcitriol, that is an essential hormone for calcium and phosphate ion absorption into the blood.	[1]
	Calcium	It is necessary for mineralization.	[1]
Hormone	Thyroid hormone	It activates osteoblasts to synthesize osteoid matrix, and at the same time it promotes osteoclasts proliferation to stimulate resorption.	[13]
	Parathyroid hormone	It stimulates osteoclasts and osteoblasts, increases the rate of calcium absorption along the small intestine, and decreases the rate of calcium loss in urine.	[1]
	Calcitonin	It inhibits osteoclasts.	[1]
	Growth hormone	It stimulates bone growth.	[1]
	Thyroxine	It stimulates bone growth.	[1]
	Testosterone	It makes bone produce faster than epiphyseal cartilage expansion by acting on osteoblasts.	[1]
	Sex hormone	It makes bone produce faster than epiphyseal cartilage expansion by acting on osteoblasts. It is indispensable in order to maintain bone mass in adults.	[1]
	Insulin	It stimulates matrix synthesis.	[13]

1.2 Bone Cancer

Millions cancer cases are reported every year, as well as millions of cancer-related deaths are also registered. However, bone cancer is rare, representing less than 1% of all cancers.

In recent years, the relationship between bone and cancer changed significantly, with a remarkable increase in bone metastases incidence due to an improvement of patients' survival.

1.2.1 Definition of Tumour and General Features of Neoplastic Development

Tumours, also called **neoplasms**, are pathological conditions generally characterized by the appearance of a cellular mass in a tissue or organ [14].

Cancer cells derive from a somatic cell, which underwent a progressive series of damages in its genome. Most of the tumours have a monoclonal origin, as their cell population derives from a single mutated cell [14].

The carcinogenesis process consists of three main stages:

1. The **initiation**, during which one or more mutations, or epigenetic alterations, transform a normal cell into a latent neoplastic cell [14].
2. The **promotion**, in which the tumour becomes clinically evident, as a consequence of the accumulation of further genomic damage. Under the action of proliferative stimuli, mutated cells multiply, thus increasing the tumour mass dimension [14].
3. The **progression** consists in further appearance of mutations in the genome of some cells of the tumour population, such as those responsible for the appearance of the metastatic phenotype, which can take the reproductive upper hand for selective phenomena [14].

Cancer cells are independent of the control mechanisms of cell multiplication, which becomes continuous and unlimited in time and space. The multiplicative autonomy of cancer cells derives from the reduction or loss of the regulatory mechanisms of cell proliferation and from the reduction or loss of the possibility of experiencing programmed death [14].

However, not all cells that undergo genomic damage give rise to a neoplasm. This is due to three conditions: first, some transformed cells do not survive; second, many of them are able to repair the genome damage before cell multiplication; finally, they can be neutralized by the immune system. Among these three defence mechanisms, the first two are currently considered the most effective. In fact, human tumours express numerous but weak antigens, not very immunogenic, which too often fail to evoke a host immune response [14].

Nevertheless, there are many other mechanisms through which tumours can evade the destructive activity of the immune system [14]. First, the tumour may not express, or may have lost the expression of tumour antigens and therefore it is not recognized as foreign by the immune system. Furthermore, it may happen that the tumour antigens are masked by mucopolysaccharide molecules and therefore they are invisible from the outside; in some cases the cancer cells can coat themselves with a fibrin layer by activating the coagulation system [14].

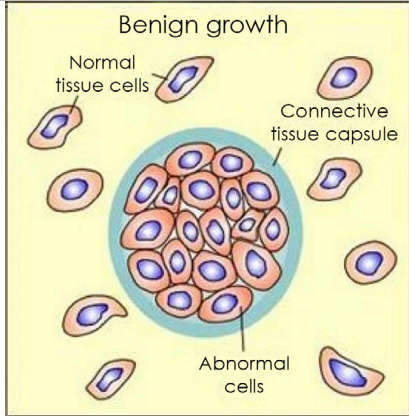
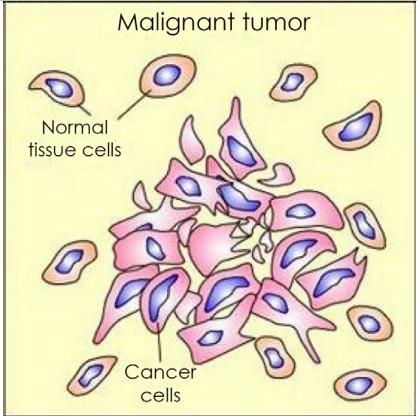
Tumours can be grouped into four classes according to location where they occur.

- **Carcinomas:** Carcinomas form solid tumours. A carcinoma generally begins within the skin or the tissue that covers the surface of internal organs and glands. Prostate cancer, breast cancer, lung cancer, and colorectal cancer are common carcinomas [15].
- **Sarcomas:** Sarcomas start in the tissues which support and connect the body such as bone, adipose, muscles, nerves, tendons, joints, blood or lymph vessels, cartilage [15].
- **Leukaemia:** Leukaemia is the cancer of the blood. There are four main types of leukaemia: acute lymphocytic leukaemia, chronic lymphocytic leukaemia, acute myeloid leukaemia, and chronic myeloid leukaemia [15].
- **Lymphomas:** Lymphoma is a cancer that affects the lymphatic system. The main types of lymphomas are Hodgkin lymphoma and non-Hodgkin lymphoma [15].

Tumours are classified into benign or malignant, with a substantial difference in terms of prognosis for the patient; however, they share some aspects, such as the development process [16].

The main differences between benign and malignant tumours are shown in Table 3.

Table 3: The main differences between benign and malignant tumours. Table adapted from Yinan et al. [15].

Mass Characteristics	Benign Tumours	Malignant Tumours
Morphology demonstration	 <p>Benign growth</p> <p>Normal tissue cells</p> <p>Connective tissue capsule</p> <p>Abnormal cells</p>	 <p>Malignant tumor</p> <p>Normal tissue cells</p> <p>Cancer cells</p>
Rate of growth	Grow slowly	Grow rapidly
Spread	Localized	Metastasize
Margin	Smooth and round capsulated	Spiculated noncapsulated
Invasion	Non invasive	Invasive and infiltrate
Differentiation	Well differentiated	Poorly differentiated
Mitosis	Low mitotic index	High mitotic index
Attenuation effects	Posterior enhancement	Posterior shadowing
Compressibility	Compressible and limited mobility	Non compressible and not mobile
Vascularity	No increased vascularity	Increased vascularity in the lesion or presence of feeding vessels
Treatment	Removal will alleviate	Removal will not restore the function

Benign tumours are neoplasms with finite form, and they share the same characteristics as the tissue from which they originated. They do not tend to invade the surrounding organs and they do not cause metastasis. In general, benign tumours respond positively to treatment and the prognosis is usually favourable.

Malignant tumours are neoplasms characterized by the presence of a cell mass in progressive replication, capable of spreading and invading various parts of the body by originating metastasis. These abnormal cells travel through the bloodstream, the circulatory system and the lymphatic system [16].

A primary tumour is a tumour that grows and develops in the anatomical site, that is where the first tumour cells are found. While a benign tumour is destined to remain a primary tumour, a malignant tumour originates metastasis that are secondary tumours in other anatomical sites [17].

1.2.2 Characteristics of Bone Tumours

Just like many other tissues and organs in the human body, bone can be affected by tumours too, thus being subjected to alteration of the physiological structure with possible negative impact on its mechanical resistance [18].

Bone tumour includes both benign and malignant lesions. Benign tumours are much more common than malignant ones. However, the exact incidence of bone tumours is unknown, because many benign lesions are not biopsied [18]. Primary malignant bone tumour are relatively rare, occurring at a rate of about one to 100000 [19]. Benign tumours usually occur in young people while malignant ones develop elderly [18].

Although the cause of most bone cancers is unknown, genetic alterations play an important role [18]. Bone tumours manifest themselves in various ways. Benign lesions are often asymptomatic and are diagnosed as occasional findings. However, many tumours cause pain or manifest themselves as a slowly growing mass [18]. Sometimes the first indication of the presence of a bone tumour is a sudden pathological fracture [18]. Clinical imaging techniques as computed tomography (CT), magnetic resonance imaging (MRI) and bone scintigraphy play an important role in the diagnosis of these lesions. In most cases biopsy and histological examination are necessary [17].

1.2.2.1 Primary Bone Tumours

In 1972, the World Health Organization (WHO) classified primary skeletal tumours according to specific histogenetic criteria, which make it possible to identify the neoplasm basing on both the cells origin and the composition of the intracellular substance produced by the neoplastic cells [17].

In according to WHO, primary skeletal tumours can be divided into four main categories:

- **Bone-forming tumours** produce bone, that is deposited in the form of interlaced trabeculae [18]. This class of tumours includes osteoma, osteoid osteoma, osteoblastoma, osteosarcoma, and fibrous dysplasia [18].
- **Cartilage-forming tumours** are characterized by the formation of hyaline or myxoid cartilage; fibrous cartilage and elastic cartilage are rare components [18]. This group of tumours includes osteochondroma, chondroma, chondroblastoma, chondromyxoid fibroma, chondrosarcoma [18].
- **Fibrous tumours** are composed predominantly of fibrous tissue [18]. They include fibrous defect of the cortical, non-ossifying fibroma, and variant of fibrosarcoma [18].

- **Others common tumours** are Multiple myeloma, Ewing's sarcoma, giant cell tumour, aneurysmal bone cysts, etc [18].

Usually benign tumours do not required treatment. If they cause problems, such as pain, interference with joint movement, or destruction of healthy surrounding tissue, they are removed surgically or treated by thermoablative techniques.

Malignant tumours, on the other hand, need always to be treated.

Multiple myeloma is the most frequent primitive malignant bone cancer, but it is often considered a bone marrow cell tumour rather than a bone tumour because it is hematopoietic in origin (Figure 10) [20]. It is a neoplasm of plasmacells which produce monoclonal immunoglobulin and invade and destroy adjacent bone tissue [21].

The incidence of multiple myeloma is 2-4 cases per 100000 [21]. The ratio of men to women is 1.6:1, and the average age at diagnosis is about 65 years [21].

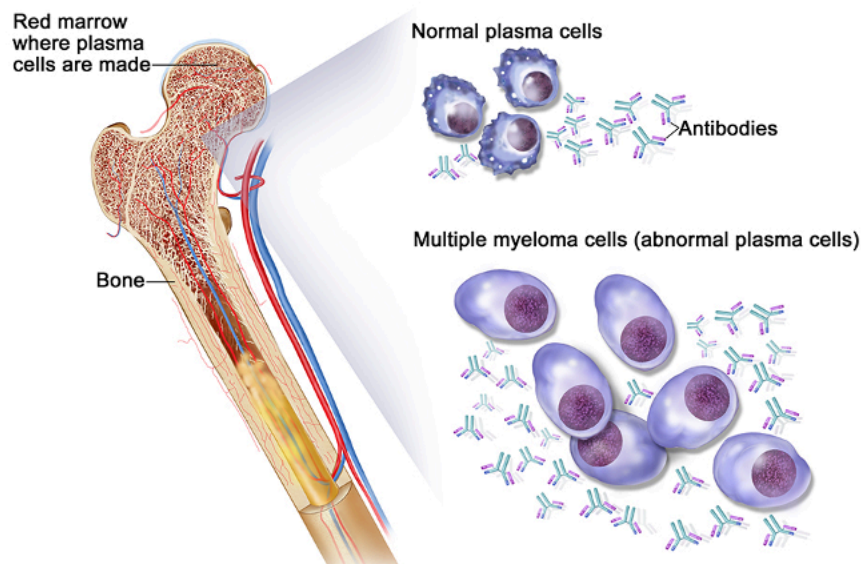


Figure 10: Representation of multiple myeloma [22].

Other common bone malignant tumours include Ewing's sarcoma, chondrosarcoma and osteosarcoma (Figure 11).

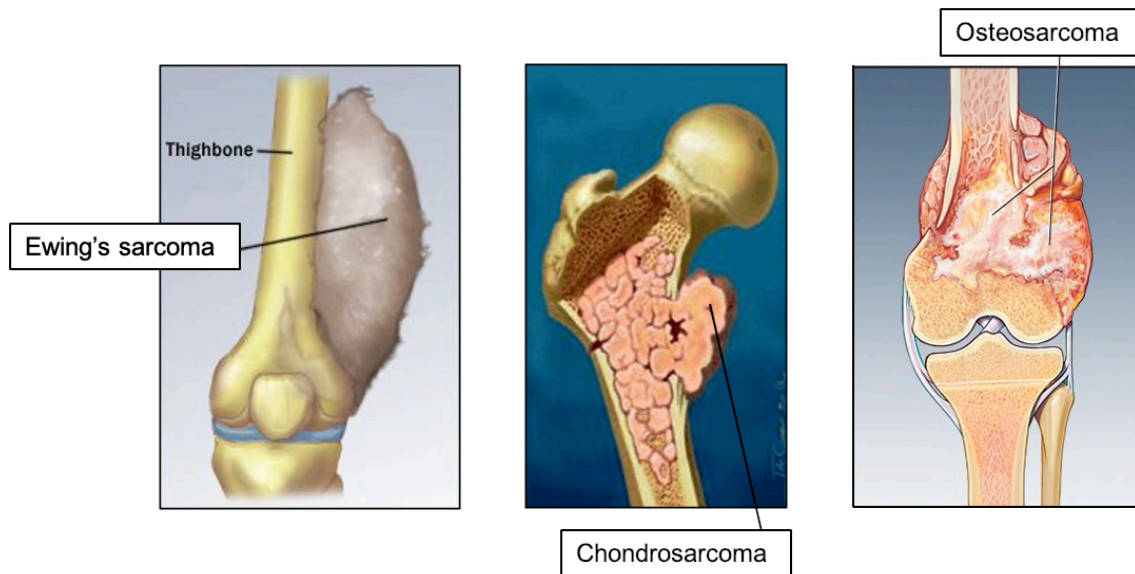


Figure 11: Representation of Ewing's sarcoma [23], chondrosarcoma [23], and osteosarcoma [24].

Ewing's sarcoma is classified as a primitive neuroectodermal tumour (PNET), deriving from cellular elements of the neural crest [17].

Histologically, the tumour is made up of a carpet uniform of small round cells, tightly packed, without any intercellular matrix [17].

This lesion originates in the medullary cavity and generally invades the cortex, the periosteum and soft tissues [18].

The incidence of Ewing's sarcoma is 1 case per 312500 per years. Men are more affected than women and 90% of the cases occur in subjects between 5 and 25 years of age [17].

Chondrosarcoma is a malignant tumour in which neoplastic cells produce only cartilage and not bone tissue [17].

Depending on the location in the bone, chondrosarcoma can be distinguished in central, peripheral and periosteum. Central chondrosarcoma occurs in the form of nodules, which invade the medullary canal and erode the cortex until it overcomes it. The peripheral one develops on the surface of the bone and expands directly into the soft parts. Periosteum (or juxtacortical) chondrosarcoma is composed of a mass of periosteal origin that can cause "bowl" erosion of the cortex with which it is in contact [17].

The estimated overall incidence of chondrosarcoma is 1 in 200000 per year [25]. It is more common in males, and in adults (30-60 years) [17].

Osteosarcoma is a mesenchymal tumour in which neoplastic cells produce bone matrices [18]. There are different varieties of this tumour. Classic osteosarcoma accounted for approximately 80% of all cases and it usually occurs in bones not affected by previous lesions [18]. This tumour generally arises in the metaphyseal region of the long bones of the limbs and almost 50% arises in the region near the knee [18].

The incidence of osteosarcoma is two cases per million inhabitants per year [17]. Men are more affected than women (1.6:1). It occurs in patients of all ages, but it predominantly affects people

between 10 and 30 years of age and elderly people suffering Paget's bone disease, bone infarcts and prior radiation therapy [18].

1.2.2.2 Secondary Bone Tumours

Secondary bone tumours are mainly represented by metastases from carcinomas, while those represented by sarcomas are extremely rare. Metastatic lesions mostly occur in the trunk skeleton and limb roots; however, other anatomical sites are possible [17].

In order of frequency, the primitive sites of origin of bone metastases are the breast, the prostate, the lung and the kidney, while more rarely secondary bone tumours originate from thyroid, gastric, intestinal and pancreatic neoplasms. The distribution by gender and age is obviously referable to the one of the primary tumours [17].

Metastases may cause resorption or neoformation bone [17].

The macroscopic aspect of a metastasis is highly variable. The consistency can be encephaloid, fibrous or ivory; the colour varies from whitish to grey, up to black, as in melanoma metastases. The appearance can be modified by the presence of necrotic and haemorrhagic areas [17].

Bone metastases occur by blood, being the presence of lymphatic vessels in the bone doubtful and in any case scarce. Lung cancer metastasizes directly (through the pulmonary veins and the left heart), while others can skip the lung and liver filter thanks to anastomoses existing between the caval network and the paravertebral venous plexuses. This "direct" venous path explains the predilection secondary locations to the skeleton of the trunk [17].

1.3 Bone Cancer Treatments

Cancer therapy was born at first as surgical therapy aimed at eradicating the tumour by invasive approaches. With the discovery of radiation, and with the pharmacology and radiation progress, radiotherapy and chemotherapy were born [14]. Currently, also thermoablatative techniques, cell-based gene therapy, photodynamic therapy, immunotherapy and immunomodulation are used to treat bone cancers.

1.3.1 Surgical Therapy

Surgical therapy aims at removing the tumour without damaging the surrounding structures. It is also used to collect cancer tissue necessary for molecular characterization of the individual patient's tumour, in order to make a precise diagnosis [14].

Wherever possible, surgical therapy tries limb salvage, since amputations cause many problems, including pain in the phantom limbs and in the stump [26].

Before surgical treatment, it is preferable to treat bone tumours in order to reduce the soft tissue mass, thus allowing an easier resection [26].

To evaluate the radicality of the resection two aspects must be considered: on the one hand, the tumour mass must be completely removed, and on the other hand, the functionality of the organ concerned the blood circulation and lymphatic vessels must be preserved [14].

Surgical margins are graded according to the system of the Musculoskeletal Tumour Society [27] (Figure 12).

- **Intralesional margin:** Intralesional margin is obtained by violating the margin of the tumour and scrape it out carefully [27].

For high-grade bone tumour, intralesional surgery should be avoided even if surgical treatment is combined with radiation therapy and chemotherapy [26], because it results in 100% local recurrence [27].

Intralesional curettage with the use of an adjuvant proved to be adequate for low-grade chondrosarcoma, since it leads to a low risk of recurrence [26].

- **Marginal margin:** A marginal line of resection goes through the reactive zone of the tumour, which contains inflammatory cells, fibrous tissue, and cancer cells [27].

The local recurrence of malignant tumour resected through the reactive zone is 25-50% [27].

- **Wide margin:** A wide line of surgical resection is accomplished when the entire tumour is removed with a cuff of healthy tissue [27]. Usually the goal is to achieve a margin of at least 1 cm [26].

Generally, the larger is the margin, the lower is the probability of recurrence [26]. The local recurrence is about 10% when a wide margin is achieved [27].

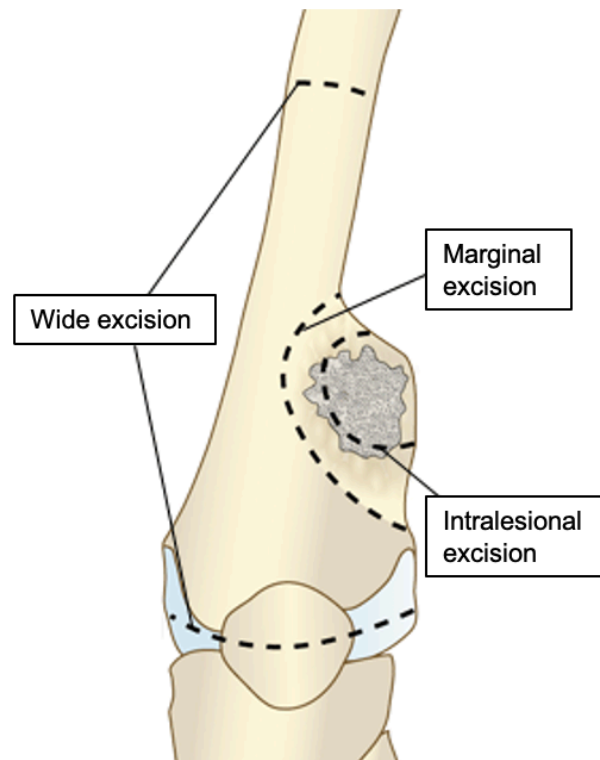


Figure 12: Surgical margins for bone sarcomas [28].

After the surgical removal of bone cancer, it is common to use transplant materials (bone grafts), biological materials, and synthetic bone substitutes to fill bone defects deriving from this operation. Surgical therapy limit is due to the tumour size, the inaccessibility of the lesion, the extension of the invasion, the presence of metastases and, above all, to the involvement of important structures of the organism as vessels and nerves [14].

Other purposes of surgery, as mentioned above, concern diagnosis and biomolecular staging. By means of targeted biopsies, the surgeon supplies the necessary tissue for a preventive histological

examination (grading) and, above all, for obtaining a gene profile that allows the use of certain therapies on specific molecular targets [14].

Currently, surgical therapy is used to remove benign tumours that cause problems, and it is the treatment of choice for most primary malignant tumours [29].

1.3.2 Chemotherapy

Chemotherapy is a type of anti-cancer drug treatment [30]. Traditional chemotherapeutic agents act by killing cells that divide rapidly, such as cancerous cells [31]. Some drugs kill dividing cells by damaging the area of the cell's control centre that control the division. Other drugs interrupt the chemical processes involved in cell division [32].

Chemotherapy can be administered through the following routes:

- Injections into the bloodstream (usually through a vein) [32].
- Drips (intravenous infusion) into the bloodstream through a vein [32].
- Tablets [32].
- Capsules [32].

Since chemotherapy drugs circulate in the bloodstream, they can reach cancer cells almost anywhere in the body. This is known as systemic treatment [32].

Chemotherapy alone can cure less than 10% of all cancer patients who have an advanced tumour [33]. In fact, chemotherapy is usually combined with radiation therapy and surgical therapy in order to obtain better clinical results [33].

Chemotherapy is currently used in three different types of treatment:

- **Primary induction treatment** consists in administering chemotherapy as primary therapy in patients who have advanced cancer, for whom there is no alternative therapy. This approach is mainly used in patients with advanced metastatic cancer, and the main purpose of treatment is to relieve tumour symptoms, improve quality of life and slow down tumour progression. This therapy is curative only for a small percentage of patients with advanced disease [33].
- **Neoadjuvant treatment** consists in administering chemotherapy in patients with localized cancer, for whom local therapy such as surgery or radiation are insufficient. The aim of this approach is to reduce the dimension of the primary tumour, so that surgical resection can be executed easier and more efficacious [33].
- **Adjuvant treatment** refers to the use of chemotherapy as an adjuvant to local therapy, such as surgery. Chemotherapy is administered after surgical treatment, and the aim is to decrease the incidence of both local and systemic recurrence, improve the quality of life of patients and increase survival. If an appropriate dose and schedule are administered, adjuvant therapy may have curative potential following surgical resection of the primary tumour [33].

Chemotherapy drugs cause side effects because they affect also healthy body tissues where the cells are constantly growing and dividing, such as the hair, which is always growing, the bone marrow, which is constantly producing blood cells, the skin and the lining of the digestive system, which are constantly renewing themselves. However, normal cells can replace or repair the healthy cells that are damaged by chemotherapy. So, most side effects disappear once your treatment is over [32].

Chemotherapy plays a pivotal role in the treatment of multiple myeloma, osteosarcoma and Ewing's sarcoma, and at present new chemotherapy agents are studied to treat chondrosarcoma and giant cell tumour [34].

For the treatment of multiple myeloma, many chemotherapy drugs are used alone or in combination, such as melphalan, cyclophosphamide, vincristine, doxorubicin [35].

Chemotherapy for the treatment of osteosarcoma is based on the combination of four active drugs: doxorubicin, cisplatin, high-dose methotrexate (HDMTX) and ifosfamide [34].

In addition to the drugs used to treat osteosarcoma, chemotherapy for the treatment of Ewing's sarcoma also includes vincristine, etoposide and cyclophosphamide [34].

The drugs that are commonly used in clinical practice for chemotherapy treatment of bone cancer are given in Table 4.

Table 4: Summary of the most common chemotherapy drugs for bone tumours treatment.

Drug	Molecular Formula	Mechanism of Action	Ref.
Melphalan	$C_{13}H_{18}Cl_2N_2O_2$	Forms DNA crosslinks, resulting in inhibition of DNA synthesis and function.	[33]
Doxorubicin	$C_{27}H_{29}NO_{11}$	Oxygen free radicals bind to DNA causing single- and double-strand DNA breaks; inhibits topoisomerase II, an enzyme that deals with cutting and relegating double stranded DNA; intercalates into DNA.	[33]
Cisplatin	$Cl_2H_6N_2Pt$	Forms intrastrand and interstrand DNA cross-links; binding to nuclear and cytoplasmic proteins.	[33]
Methotrexate	$C_{20}H_{22}N_8O_5$	Binds to the active catalytic site of dihydrofolate reductase, leading to the inhibition of tetrahydrofolate synthesis. This inhibition intervenes with the formation of DNA, RNA, and cellular proteins.	[33]
Vincristine	$C_{46}H_{56}N_4O_{10}$	Inhibits mitosis.	[33]
Etoposide	$C_{29}H_{32}O_{13}$	Inhibits topoisomerase II.	[33]
Cyclophosphamide	$C_7H_{15}Cl_2O_2N_2P$	Forms DNA crosslinks, resulting in inhibition of DNA synthesis and function.	[33]
Ifosfamide	$C_7H_{15}Cl_2N_2O_2P$	Capable of intercalating alkyl groups within the DNA double strand. In this way, DNA undergoes modifications that prevent the cell from replicating correctly, thus leading to apoptosis.	[33]

1.3.3 Radiation Therapy

Radiation therapy consists in hitting the tumour with ionizing radiation in order to destroy or reduce the tumour mass [14].

Particularly, radiation therapy aims to damage the cancer cells DNA, so that cells lose the capability to divide and proliferate, and finally die [36].

Radiation is a physical agent that forms ions and stores energy in the cells of the tissue that crosses [37]. It can have a direct or indirect effect on DNA: it can directly interact with DNA and cause damage to the cell, or it can damage all the cellular components through the production of free radicals. The latter damage comes from the ionization or excitation of the water component of the cells [36].

The types of cell death induced by radiation are the following:

- **Apoptosis:** It is also known as programmed cell death, and it is the main cell death mechanism involved in radiation therapy [38]. The cell shrinks, apoptotic bodies are formed, but the cell membrane remains intact. Mitochondria play an important role in this process [36].
- **Mitotic cell death:** It happens during or after aberrant mitosis and it is caused by mis-segregation of chromosomes that leads to the giant cells' composition with aberrant nuclear morphology, multiple nuclei [39].
- **Necrosis:** It consists in the swelling of the cells, with subsequent breakdown of the cell membrane, and loss of intracellular content [40].
- **Senescence:** It consists in the permanent loss of the proliferative capacity [40]. Senescence cells are alive, but do not divide, synthesize DNA, spread and flatten [36].
- **Autophagy:** It is a genetically regulated form of programmed cell death, in which the cell digests itself and involves the autophagic/lysosomal compartment [36].

However, radiation therapy does not kill cancer cells immediately, but hours, days and weeks can pass before tumour cells start to die. Whereupon tumour cells continue to die for weeks to months after radiation therapy ends [36].

Radiation damages both normal cells and cancer cells, but healthy cells repair faster than cancer ones and manage to maintain their function [41].

Radiation can be delivered in two different ways (Figure 13):

- **External beam radiation** is delivered from outside the body to the location of the tumour. The most used type of radiation are x-rays. This is the most common route in the clinical practice (Figure 13a) [36].
- **Internal radiation** or **brachytherapy** is delivered from inside the body by radioactive sources, sealed in catheters or seeds directly into the tumour site (Figure 13b) [36].

Radioactive sources can be left in site permanently or removed and replaced at regular intervals. In the first case, it is referred to permanent brachytherapy, and in the second to temporary brachytherapy [42].

It is a very powerful technique because *in situ* irradiation includes many advantages, such as the possibility to use a weaker, shorter range radiation that minimizes the damage to adjacent, healthy tissue. Therefore, larger doses of radiation can be safely used, and this increases the probability of destroying the tumour [43].

This approach is commonly used in the treatment of gynaecological and prostate malignant tumours as well as in situations where retreatment is indicated [36]. In addition, some studies have shown the effectiveness of brachytherapy to relieve patients from symptoms (palliative treatment) caused by bone metastases [44].

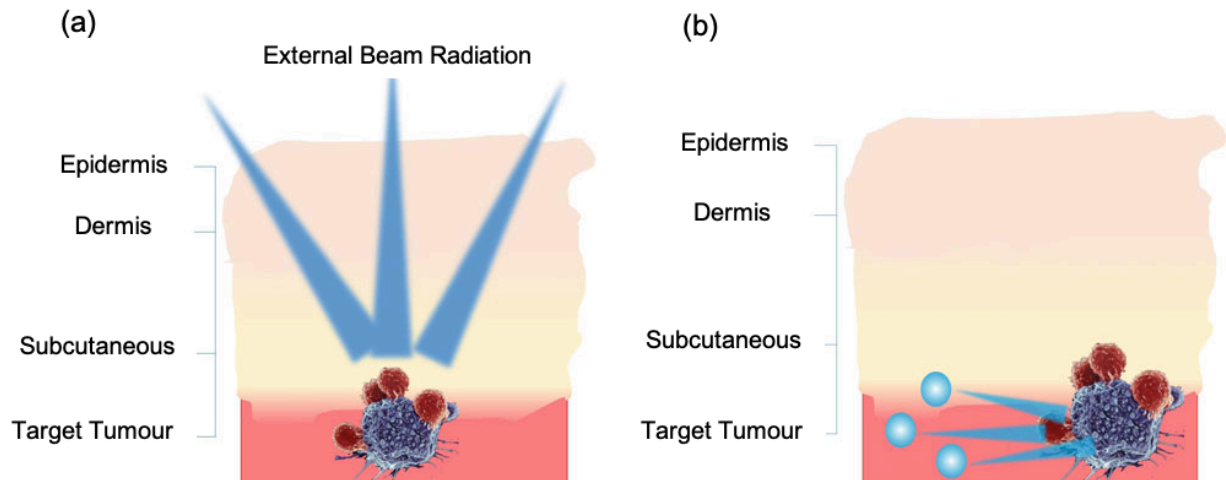


Figure 13: (a) Scheme demonstrating tissue absorption of external beam radiation. It is observed the radiation emitted damages both tumour and healthy cells through electron excitation and release of energy. (b) Schematic figure illustrating the principle of brachytherapy: radioactive seeds (blue spheres) emitting beta and/or gamma rays into the target tumor [45].

Generally, radiation therapy can be used for two different purposes: the first is to destroy cancer, the other one is for palliative treatment [36].

Radiation therapy can be used in combination with surgery therapy, chemotherapy or immunotherapy [36].

Radiation therapy administered before surgery is called neoadjuvant therapy and has the purpose of reducing the tumour. Radiotherapy administered after surgery, instead, is called adjuvant therapy, and its goal is to destroy the residual microscopic cancer cells [36].

The most common side effects of radiation therapy are fatigue, alopecia, skin burns, nausea, diarrhoea, and risk of secondary cancers [15].

At present, radiation therapy is often used to treat Ewing's sarcoma [46].

1.3.4 Thermoablative Techniques

The purpose of thermoablative techniques is to induce coagulation necrosis in the target organ or tissue by use of special applicators, such as electrodes, antennas, and probes, positioned in the tumour by means of image guidance [29].

Depending on the procedure, the tissue can be cooled or heated. In cryoablation the tissue is cooled below -20°C , while in hyperthermal ablation the tissue is heated above 80°C . The techniques that exploit hyperthermal ablation are radiofrequency ablation (RFA), microwave ablation (MWA), laser ablation, and high-intensity focused ultrasound (HIFU) [29].

The extension of coagulation necrosis depends on the amount of energy applied, the interactions with the target tissue, and the heat dissipation [47].

The imaging method used to position the applicators depends on the treatment, the operator and the available equipment. However CT or MRI are the most used methods [29].

Nowadays, thermal ablation is mainly used to treat benign bone tumours. It represents the method of choice for the treatment of osteoid osteoma [29]. However, thermoablative techniques are also used to reduce the pain due to painful bone metastases [29].

Cryoablation consists in cooling the tumour tissue at temperature below -20°C . Energy is transferred from the probe to the surrounding tissue through the conduction and convection mechanisms [48]. The cryoablation probes are formed of two chambers which are full of compressed gases. Cryoablation is based on the Joule-Thomson effect, which, depending on the inversion temperature of the gases used, causes a temperature change as soon as the gases expand around the tip of the probe. Argon, nitrogen, or oxygen inversion temperature is above room temperature; accordingly, the temperature decreases as these gases extend [29]. While hydrogen and helium inversion temperatures are below room temperature, accordingly when these gases extend, the temperature rises. Therefore, cryoablation systems use compressed argon and helium for cooling and unfreezing, respectively [29]. During cryoablation, an ice ball forms on the tip of the probe. To ensure a total ablation of the target lesion, the boundary of the ice ball should broaden at least 5 mm beyond the lesion itself [29]. A cryoablation benefit is the intrinsic analgesic effect, that makes the patient feel less pain during and after the treatment [49]. Cryoablation is commonly used for the treatment of osteoid osteoma [29].

RFA is the most used thermoablative procedure. A 150-250 W generator is used to generate an alternating current. When using a unipolar system, a neutral electrode is applied to the surface of the body, and the alternating current oscillates between the neutral electrode and the radio frequency (RF) electrode inserted in the tumour. When using the bipolar system, the neutral electrode is not used, and the RF electrode functions both as an anode and as a cathode [29]. High frequency alternating current (460-500 kHz) induces agitation of the tissue ionic molecules, which produces frictional heat. The latter in turns destroys adjacent tumour tissue [50]. Depending on the electrical-conductive properties of the treated tissue, a different thermal effect is obtained. Tissue temperatures between 60°C and 100°C leads to protein denaturation, instantaneous cell death, and coagulative necrosis of the tumour [50]. Temperatures above 100°C cause water vaporization and the carbonization of the tissue near to the electrode. This leads to a decrease in electrical conductance and a not optimal result [51]. The effectiveness of this technique is reduced by the presence of vascular structures near the treated area, which dissipate heat, acting as cooling circuits [51]. A curative tumour ablation procedure should include a 0.5-1-cm margin of healthy tissue around the target tumour to remove any microscopic foci and prevent a local recurrence [51]. Conversely, RFA used for palliative purposes is directed to the bone-tumour interface, where the main form of pain is found [52]. RFA is currently regarded as the method of choice for osteoblastoma [29].

MWA consists in applying an electromagnetic field (915 MHz or 2.45 GHz) to the tumour through an electrode-antenna [29], [52]. The electromagnetic field interacts with the tissues causing the agitation of the water molecules, which in turns generates kinetic energy, and as result frictional heat [29]. The heat produced causes the coagulate necrosis of the tumour [52]. This technique offers numerous advantages compared to RFA: first of all, since it is based on an electromagnetic field, rather than a current flow, it is independent from changes in the resistance of the tissues, consequently higher temperatures are reached which involve a shortening of the ablation time. In addition, the dissipating effect exerted by the blood vessels close to the target area is less than the one of RFA, because MWA heats a greater volume of tissue [53]. Finally, this technique does not require the use of a neutral electrode [54].

On the other hand, MWA requires the use of more expensive materials than RFA, and the antennas, being very flexible, are difficult to position [29].

MWA is suitable for the treatment of osteoid osteoma [29].

Laser ablation uses infrared light to generate heat and ablate the tumour [52].

The light energy is transmitted through a bare-tip optical fibre and spreading through the target tissue produces photocoagulation, or rather the denaturation of proteins and instantaneous cell necrosis [50].

Photocoagulation is induced by a neodymium: yttrium aluminium garnet generator or diode [50].

Commonly, the extent of the necrosis is proportional to the stored energy. Therefore, multiple fibre applicators are needed for the treatment of larger lesions [50].

Laser ablation is usually used for the treatment of osteoid osteomas [52].

HIFU is a new, non-invasive technique that consists in focusing ultrasound waves with frequencies in the low megahertz range only in the tumour volume, sparing the adjacent tissues. The mechanical energy of the sound wave is transformed into thermal energy, reaching a temperature of 90 °C [55].

The effectiveness of the technique lies in hitting the tissue in depth, and depends on the intensity and frequency of the sound wave and on the characteristics of the tissue [55].

Sonication also causes gas formation which deform the ultrasound beam, therefore short breaks between individual sonication are necessary to avoid this [29].

MR-guided HIFU was approved by the FDA for palliative treatment of bone lesions, and it is commonly used for the treatment of painful bone metastases [29].

1.3.5 Other Possible Methods

In selected cases, bone cancer can be treated by using cell/gene therapy, photodynamic therapy, monoclonal antibodies or stem cell transplants.

Cell-based gene therapy is an experimental procedure in which cells act as bioactive carriers releasing osteoinductive genes locally, to obtain bone regeneration [56]. In addition, genetically modified cells keep the genes in the site of interest for a long period of time, facilitating bone healing [57].

The most used genes belong to the family of Bone Morphogenic Protein (BPM) [58].

The use of gene therapy is however limited by a number of safety issues based on viral and nonviral vectors, in the clinical setting [58].

Cell-based techniques are principally based on mesenchymal stem cells (MSCs), that have been extensively engaged in combination with opportune osteoinductive scaffolds, and considered the most valid *in vivo* bioactive bone substitutes [58]. MSCs have a great potential for self-renewal, high plasticity and multilineage [59]. These cells are also called “stromal stem cells” because they are located in the stroma of bone marrow and other tissues and organs [60]. MSCs are easily isolated and expand ex-vivo, preserving plasticity and self-renewal potential [61].

However, to produce clinical-grade MSCs cell factories are necessary that have to conform with the same rules required for the drug manufacturing industries, because MSCs, in agreement to European tissue banking regulations, are accounting as medical products [62].

Nowadays rare clinical trials are ongoing that exploit MSC-based method as bone regenerative technique [63].

Photodynamic therapy is based on the fact that cancer cells internalize some chemical compounds, such as porphyrins and photocyanins, which, when excited by a laser, generate radicals killing the cell that contains them [14].

Immunotherapy and **immunomodulation** are specific strategies for identifying and affecting cancer cells with specific mechanisms of immunopathological damage, either by enhancing endogenous reactions (immunomodulation), or by activating from the outside the immune response against tumours, or by providing effectors (dendritic and natural cells killer) specific to the tumour of the individual patient [14].

Stem Cell Transplants, including peripheral blood, bone marrow, and cord blood transplants, are strategies that provide blood-forming stem cells [15].

Cancer treatments such as chemotherapy and radiation therapy kill all the stem cells and arrest the bone marrow from producing blood cells. The killed stem cells of the body are replaced by the transplanted stem cells [15]. This method is used to treat multiple myeloma [15].

However, some types of transplants are used to fight the cancer cells, rather than simply restore normal blood cells. In fact, donated cells (white blood cells) can sometimes find and kill cancer cells better than the immune cells of the person with the tumour ever could. This is called the graft-versus-host disease (GvHD) effect [15].

1.3.6 Summary of Bone Cancer Treatments

Table 5 summarizes the recommended treatment(s) for the most common malignant bone tumours.

Table 5: Summary of recommended treatment(s) for the most common malignant bone tumours.

Tumour	Recommended treatment	Notes	Ref.
Multiple myeloma	Chemotherapy associated with stem cell transplant. An alternative is represented by radiotherapy.	Stem cells are taken either from the patient's own blood or from the bone marrow of an external donor and are infused into the sick person 24 h after chemotherapy treatment.	[35]
Osteosarcoma	The combination of surgical therapy with pre and post-operative chemotherapy.	The high dose antitumour therapy before the surgery aims at the necrosis of the tumour cells, reduction of the volume of the neoplastic mass and a better definition of the margins. In this way a less demolitive surgery can be performed, which preserves the bone and avoids amputations.	[17]
Chondrosarcoma	Surgical therapy.	The treatment involves extensive resection of the lesion.	[17]
Ewing's sarcoma	The combination of three therapeutic modalities: chemotherapy that is always practiced, surgery when possible, and radiotherapy as an alternative to surgery or associated with it in case of non-radical resection of the tumour.	Chemotherapy is performed both before and after surgery. Surgical treatment suggests wide resection of lesions in the appendicular skeleton and precise resection for lesions in the axial skeleton. Radiation therapy can be used alone to locally control the tumour, or in combination with surgery, or in combination with surgery and chemotherapy in a neoadjuvant way.	[17], [64].

1.4 Materials for Bone Tumour Treatment

Materials for bone cancer treatment refer to materials for surgery and for chemotherapy drug delivery as well as materials for brachytherapy, since the other techniques currently used to treat bone tumours do not require the support of any specific material.

1.4.1 Materials for Surgery

A material for surgery is a material used to fill bone defects resulting from the surgical removal of bone cancer.

Materials for surgery includes transplant materials (bone grafts), biological materials, and synthetic bone substitutes.

1.4.1.1 Transplant Materials (Bone Grafts)

Bone grafting is a surgical procedure that uses transplanted bone to repair and rebuild diseased or damaged bones [65].

Osteogenesis, osteoinduction, osteoconduction and osteointegration are the four most important characteristics that a bone graft should have [66].

Osteogenesis is the formation of new bone beginning with osteoprogenitor cells that are in the graft, which survive the transplant, proliferate and differentiate into osteoblasts and eventually to osteocytes [67].

Osteoinduction is the stimulation and the recruitment of nearby undifferentiated mesenchymal stem cells to the graft site, which differentiate into chondrocytes and osteoblasts [68]. This process is mediated by a signaling cascade and the activations of some intra and extracellular receptors, the most important of which are part of the TGF-beta superfamily [68].

Osteoconduction is the ability to allow the growth of vascular tissue and the creation of a new Haversian systems into the architecture of the graft material [66].

Osteointegration is the connection between the host bone and the graft material without an intervening layer of fibrous tissue [69].

The three kinds of bone graft are autograft, allograft and xenograft (Figure 14).



Figure 14: Bone grafts: (a) Cortical strut autograft from fibula in a proximal humeral non-union treated by ORIF [63]. (b) Allograft got from a banked femoral head [63]. (c) Acetabular bone defect filled with bovine bone xenograft in chips [63].

Autograft is considered the gold standard of bone grafting because it exhibits all of the four desired characteristics mentioned above (osteogenesis, osteoinduction, osteoconduction and osteointegration [67], [66]), and elicits no immune response in the patient (Figure 14a).

It consists in using the bone obtained from the same patient receiving the graft. The bone is usually taken from non-essential bones such as the iliac crest, the fibula, the ribs [63].

However, autograft bone has also some disadvantages related to the morbidity at the donor site and the availability of the tissue. The operation could lead post-operative pain and complications including creation of hematoma, blood loss, nerve damage, infection, arterial damage, fracture, aesthetic deformity [67].

Allograft is the most used bone substitute (Figure 14b). It is a graft picked up from a member of the same species as the host but genetically different [66].

It is taken from either living donors or nonliving donors and it is handled in a bone bank [63].

It can be used fresh, frozen, freeze-dried, mineralized and demineralized [66].

The cortical bone is prepared in the form of chips, granules and wedges, while the cancellous bone is in the form of powder [66].

Allograft poses the risk of transmitting viral diseases, but it is almost eliminated through tissue processing and sterilization. However, with these treatments, graft's mechanical and biological properties are weakened [67].

Allograft is osteoconductive and slightly osteoinductive, but it has not osteogenic characteristics because tissue processing reduces the host's immune response and consequently there are not viable cells to donate osteogenic qualities [63], [67].

Xenograft is collected from a genetically different species than the host (Figure 14c) [66].

Bovine bone is the most used xenograft [66]. The bone is lyophilized, or demineralized and deproteinized, and then distributed as a calcified matrix [63].

Another common xenograft is coralline hydroxyapatite, which is generated from ocean coral [66]. Initially it is mainly composed of calcium carbonate, then it is processed to remove most of the organic content, and finally a calcium phosphate skeleton is achieved [66].

Others xenografts used are chitosan, gusuibu and red algae [66].

1.4.1.2 Biological Materials

Biological graft materials include demineralized bone matrix and collagen (Figure 15).

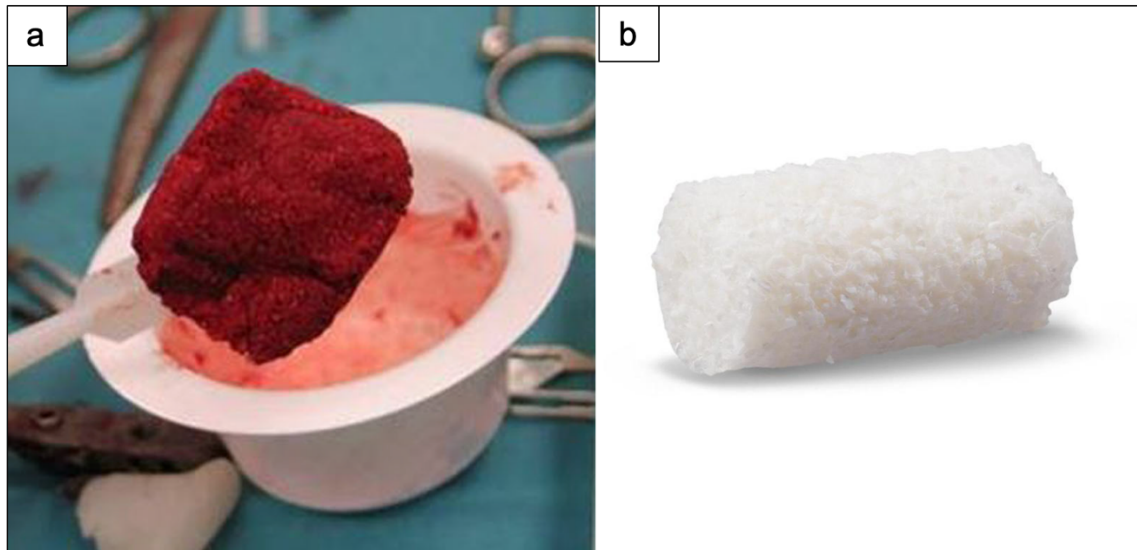


Figure 15: (a) Demineralized bone matrix [63]. (b) Collagen [70].

Demineralized bone matrix (DBM) is obtained by decalcification of the cortical bone, which is processed to reduce the infection potential and immunogenic response of the host (Figure 15a) [67]. The DBM retains the trabecular structure of the original tissue, and acts as an osteoconductive scaffold despite the removal of the mineral phase caused a decrease in structural strength [67].

DBM is more osteoinductive than allograft because growth factors are more available. However, DBM is more used as a bone graft extender than as a bone graft substitute [67].

Collagen promotes mineral deposition, vascular ingrowth, and growth factor binding, offering a favourable environment to bone regeneration (Figure 15b) [67]. However, collagen may lead to potential immunogenicity and offers minimal structural support [67].

Collagen is not a valid graft material but, when coupled with bone morphogenetic proteins, osteoprogenitor precursors, or hydroxyapatite, it improves notably graft properties [67].

1.4.1.3 Synthetic Bone Substitutes

Synthetic bone substitutes are biocompatible and induce minimal fibrotic changes. They support new bone formation and undergo remodelling. In addition, they have similar toughness, modulus of elasticity, and compressive strength to that of the bone being replaced [66].

Synthetic bone substitutes are less painful, require less operating time, and lead to less blood loss than bone grafts [63].

They also have some disadvantages such as low resorption, difficulty in handling, and the possible development of an inflammatory reaction from a foreign body [67].

The most common synthetic bone substitutes are ceramics bone substitutes, calcium phosphate cements (CPCs), calcium sulphate (CS), synthetic polymers, bioactive glasses (BGs), and glass ionomer cements (Figure 16).

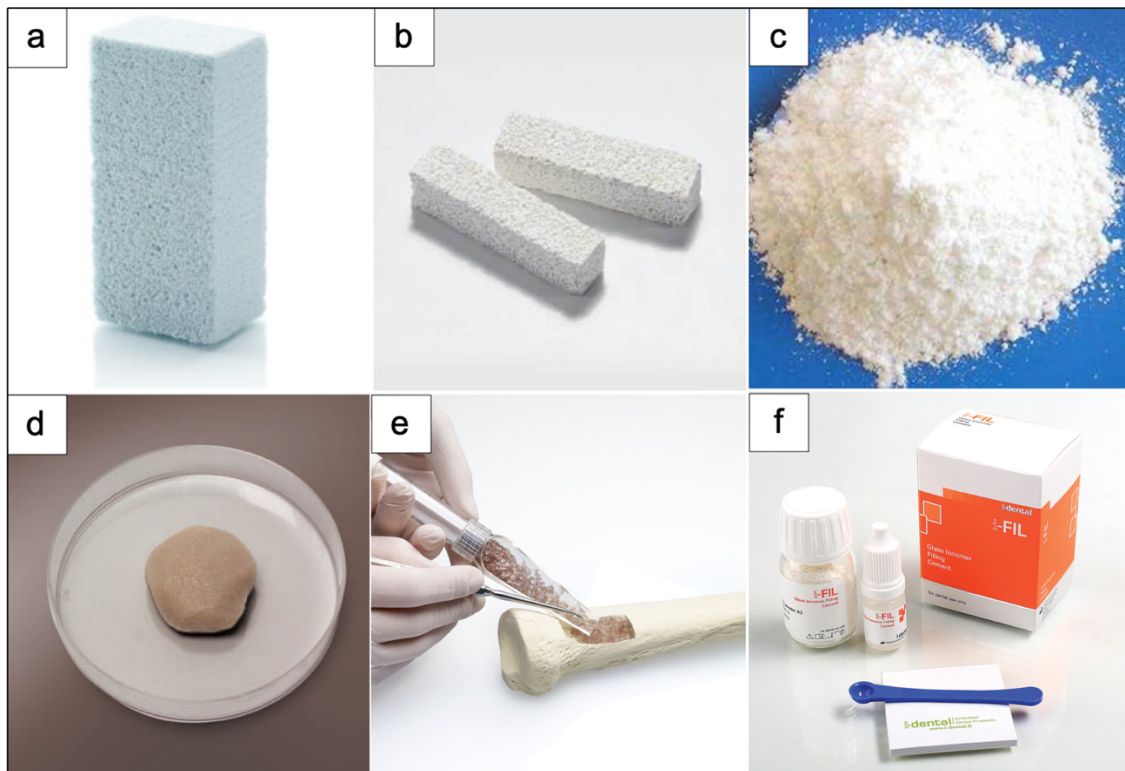


Figure 16: (a) Bone substitute of hydroxyapatite and tricalcium phosphate [71]. (b) CPCs [72]. (c) Calcium sulphate [73]. (d) Bone substitute containing PEG [74]. (e) Bioactive glass granules (BonAlive®) [75]. (f) Glass ionomer cement [76].

Ceramics bone substitutes are calcium-based replacements, a blend of HA and tricalcium phosphate (TCP) (Figure 16a). HA is a mineral approximately inert that is maintained *in vivo* for long periods of time, while TCP, that is the HA amorphous phase, is biodegraded within 6 weeks of its implant [63]. HA has high mechanical strength, while TCP possesses poor mechanical qualities [63].

The most used ceramic bone substitute is a biphasic calcium phosphate that combines 60–40% HA with 40–60% TCP in order to achieve a balance regarding bone resorption and mechanical support [63]. For bone ingrowth, macroporosity of about 100–400 μm and interconnected porosity are required [63]. HA-TCP are obtainable in form of blocks, granules, and injectable kits [63].

The main limit of ceramic bone substitutes is the strength, which varies between 10 and 60 MPa, and is much lower than the compression strength of the cortical bone, which, as already mentioned, is between 130 and 200 MPa [63].

Calcium phosphate cements are white powders, consisting of calcium phosphate, that when blended with a liquid, create a cement which can be modelled during surgery to adjust the silhouette of bone loss (Figure 16b). In 20 minutes, the cement hardens and forms nanocrystalline hydroxyapatite [63]. The cement is biocompatible, osteoconductive, and with time it is reabsorbed and replaced with new bone [63]. However, it is very fragile, so it is not used for load-bearing applications [63].

Calcium sulphate deserves to be mentioned, since it allows an adequate gap filler, provides for vascular ingrowth, and resorbs fast and totally (Figure 16c) [63].

Synthetic polymers are divided into degradable and non-degradable types. Degradable polymers have the double advantage of improving healing and being completely absorbed by the body [63]. The most used synthetic polymers are polylactic-co-glycolic acid (PLGA), polycaprolactone (PCL), and polyethylene glycol (PEG) (Figure 16d) [63].

Bioactive glasses are very beneficial materials since they generate both osteo-conductive and osteo-productive events [77]. Bioactive glasses are able to promote the growth of bone cells [78], and to bond strongly with hard and soft tissues [79], [80].

BGs, after being implanted, undergo specific reactions, leading to the formation of an amorphous calcium phosphate (ACP) or HA phase on the glass surface, which is responsible for their strong bonding with the surrounding tissue [80]. In addition, BGs release ions that activate expression of osteogenic genes [81], and foster angiogenesis [82].

The degradation rate of bioactive glass can be adjusted, by controlling the chemical composition of the glass, to match that of bone ingrowth and remodelling [83].

The structure and chemistry of BGs can be customized by changing either composition, or manufacturing technique [83].

For all these reasons, bioactive glasses are considered very promising materials as bone substitutes (Figure 16e). They will be discussed in more detail in Chapter 2.

Glass ionomer cements are composed of calcium/aluminium/fluorosilicate glass powders, blended with polycarboxylic acid to obtain a porous cement paste (Figure 16f). The paste takes 5 minutes to harden, after which it is insoluble in water [67].

They have a compressive strength and modulus of elasticity similar to that of the cortical bone. They are biocompatible, and their porous structure promotes osteoconduction, and subsequently bone ingrowth. These cements aren't resorbable, and therefore they aren't replaced by bone [67].

1.4.2 Drug Delivery Materials

In recent years, chemotherapy drug delivery materials have gained interest, since they allow to overcome the limits of conventional therapy [84].

In fact, conventional chemotherapy provides that the drug reaches not only the target sites where it must exert a therapeutic effect but also other organs, where it may cause unfavourable effect. Accordingly, the drug concentration reaching the tumour area, can be lower than the therapeutic level. The prescription of higher doses of the chemotherapy drug, in order to obtain a better therapeutic effect, increases the risk of unwanted and side effects [84].

Drug encapsulation in a carrier has many advantages, such as targeted drug delivery, protection from degradation in the bloodstream, better drug solubility, enhanced drug stability, decreased toxic side effects, and enhanced pharmacokinetic and pharmacodynamic drug properties [85].

Nanoscale drug carriers have properties of self-assembly, stability, specificity, drug encapsulation, and biocompatibility as a result of their material composition [84].

Recently, various drug delivery compounds based on synthetic polymers, proteins, lipids, and organic and inorganic particles have been developed [85]. They are shown in Figure 17.

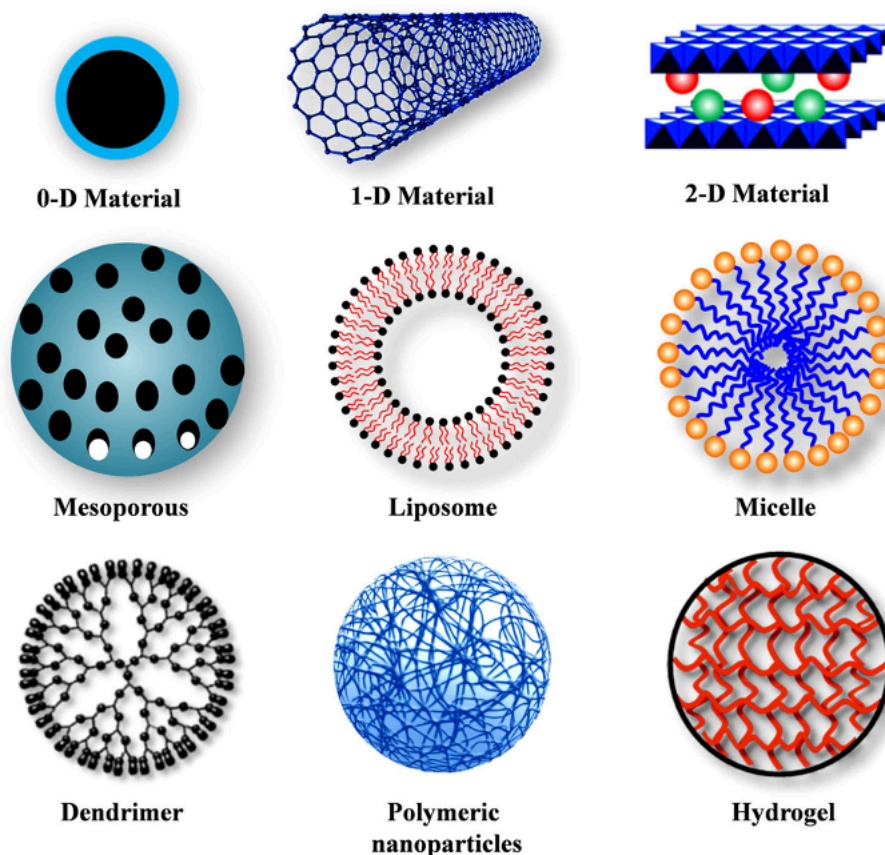


Figure 17: Various types of nanocarriers used as controlled delivery vehicles for cancer treatment [85].

Nanocarriers commonly used in chemotherapy can be divided into two groups designed for targeted or non-targeted drug delivery:

- Organic nanocarriers: vehicles that use organic molecules as a major building block material. They include liposomes, lipids, dendrimers, carbon nanotubes, emulsions, and synthetic polymers [85].
- Inorganic nanocarriers: vehicles that use inorganic elements (commonly metals) as a core. They are quantum dots, carbon nanotubes, layered double hydroxides, mesoporous silica and magnetic nanoparticles [85].

Table 6 summarizes some examples of drug delivery systems, suitable for solid tumours or multiple myeloma, that have either been approved or are in clinical or preclinical development stages [85].

Table 6: Various drug delivery carriers used in cancer therapy. Table adapted from Senapati et al. [85].

Material	General Description of Material	Description of Specific Carrier	Carrier Commercial Name	Specificity	Ref.
Layered double hydroxide (LDH)	Layers of a divalent metal ion, such as Mg^{2+} , Ca^{2+} , Ni^{2+} , and Zn^{2+} , with a trivalent metal ion isomorphically substituted to give the layers a net positive charge.	Raloxifene intercalated into the interlayer gallery of LDH host.	-	Solid tumour.	[85], [86]
Iron oxide nanoparticles	They are composed of an inner magnetic particle core and a hydrophilic coating of polymers.	Phospholipid-PEG coated superparamagnetic iron oxide nanoparticles.	Nano Therm	Solid cancer.	[85], [86]
Mesoporous silica nanoparticles (MSN)	They are characterized by large specific surface area, large pore volume, controllable particle size, good biocompatibility and grate ability to protect drugs from degeneration or denaturation.	Azobenzene-modified mesoporous silica for NIR-triggered anticancer drug delivery.	-	Solid tumour.	[85], [86]
		Endosomal pH-sensitive MSN for doxorubicin delivery.	-	Solid tumour.	[85], [86]
Polymeric nanoparticles	Solid, biocompatible, colloidal and often biodegradable nanoparticles. They can be made from synthetic polymers, copolymer, or from natural polymers.	PEG-PLGA nanoparticle formulation of docetaxel.	BIND-014	Solid malignancies.	[85], [86]
Liposomes	Spherical vesicles with a hydrophilic cavity surrounded by one or several lipid bilayers that allows the encapsulation of drugs with different solubility.	Liposomal doxorubicin.	Doxil	Multiple myeloma.	[85], [86]
Dendrimer	Globular, radially symmetric, water-soluble macromolecules with well-defined sizes, and branched structures.	Complexation of doxorubicin with cationic poly-L-lysine dendrimer.	-	Solid tumour.	[85], [86]

1.4.3 Materials for Brachytherapy

Feng et al. [44] have found that seeds containing Iodine-125 (^{125}I) as radioactive element are useful for palliative treatment of bone metastases by brachytherapy. After ^{125}I seeds implantation, patients have reported significant reduction in metastasis pain and improvement in quality of life [44].

Most commercialized seeds for brachytherapy are composed of a titanium capsule [87] which is usually less than 0.5 cm in length and 0.8 mm in diameter [88]. Titanium, it is a suitable material for this purpose, since it has the characteristics of no toxicity, it is undegradable, and it shows good biocompatibility [87]. This capsule contains the source, and it is used to avoid direct contact of radioactive material to patient's body fluid and tissue [88].

The capsule also contains a long silver rod, which is used as an x-ray marker [89]

The isotope iodine-125 has a half-life of about 59 days. It decays by electronic capture with x-rays or gamma-rays emission. The electrons emitted are absorbed by the titanium capsule [89].

Figure 18 shows an example of commercial brachytherapy seed.

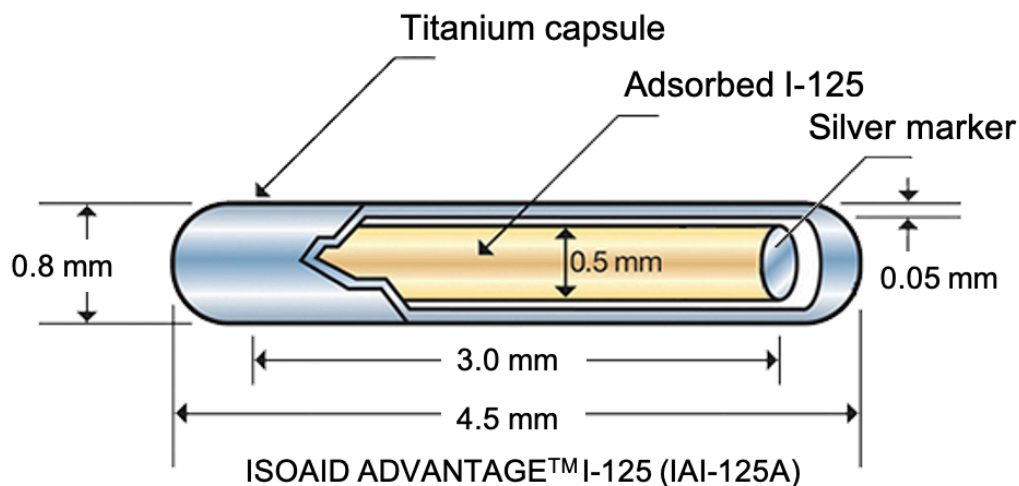


Figure 18: Example of commercial brachytherapy seed [90].

1.5 Conclusions

Bones are the organs of the skeletal system; they support our weight and work together with muscles, producing controlled and precise movements.

The skeleton may be affected by neoplasms which alter the structure of the bone and impair the functionality of the locomotor system. It was estimated that in Italy the annual incidence of new primary malignant bone tumours is around 500 cases.

Despite currently there are many state-of-the-art methods for treating bone cancer, the most widely used techniques are surgical therapy, chemotherapy, and radiation therapy.

Surgical therapy is the treatment of choice for most primary bone malignancies. However, this technique has limitations: usually patients feel pain in the operated part of the body, and sometimes the tumour cannot be removed surgically because of its location and size. In addition, risks of surgery include bleeding, blood clots, damage to nearby tissues, and reactions to the anaesthesia. Among the

materials used to fill bone defects resulting from the surgical removal of bone cancer, autograft emerges, since it is still considered the gold standard of bone grafting, and bioactive glasses stand out, since they have both osteo-conductive and osteo-productive properties.

The efficacy of chemotherapy depends on the type and the stage of cancer, and it is often limited by the toxicity to other tissues in the body. Drug delivery materials allow to overcome the limits of conventional therapy because of their ability to encapsulate the drug and to release it at the target site. Several chemotherapy drug delivery systems were either approved, and many others are in clinical or preclinical development stages.

External radiation therapy, although it is often used for the treatment of bone cancer, damages not only diseased cells, but also healthy tissue. The advantage of brachytherapy, over conventional radiotherapy technique, is the high dose delivered into the tumor, due to the source's proximity to the cancer. Some studies have shown the effectiveness of ^{125}I seed implant brachytherapy in the palliative treatment of bone metastases. Recently, it was found that glasses and glass-ceramics are promising materials to use in brachytherapy due to their bioactive and biocompatible behavior.

References

- [1] F. H. Martini, R. B. Tallitsch, and J. L. Nath, *Human Anatomy*, Ninth. 2018.
- [2] W. H. Ridder, *Anatomy and Physiology*. OpenStax, 2006.
- [3] B. Clarke, “Normal bone anatomy and physiology,” *Clin. J. Am. Soc. Nephrol.*, vol. 3 Suppl 3, no. Suppl 3, 2008.
- [4] G. Anastasi *et al.*, *Trattato di anatomia umana*, vol. 1. .
- [5] S. C. Cowin, *Bone Mechanics Handbook*, Second. 2001.
- [6] J. S. Lowe and P. G. Anderson, *Stevens & Lowe’s Human Histology*, Fourth. 2015.
- [7] E. M. Aarden, P. J. Nijweide, and E. H. Burger, “Function of osteocytes in bone,” *J. Cell. Biochem.*, vol. 55, no. 3, pp. 287–299, 1994.
- [8] L. F. Bonewald and M. L. Johnson, “Osteocytes, mechanosensing and Wnt signaling,” *Bone*, vol. 42, no. 4, pp. 606–615, 2008.
- [9] E. F. Morgan, G. Unnikrisnan, and A. Hussein, “Bone Mechanical Properties in Healthy and Diseased States,” *Annu. Rev. Biomed. Eng.*, vol. 20, pp. 119–143, 2018.
- [10] L. C. Gerhardt and A. R. Boccaccini, “Bioactive glass and glass-ceramic scaffolds for bone tissue engineering,” *Materials (Basel)*, vol. 3, no. 7, pp. 3867–3910, 2010.
- [11] M. R. Allen, J. M. Hock, and D. B. Burr, “Periosteum: Biology, regulation, and response to osteoporosis therapies,” *Bone*, vol. 35, no. 5, pp. 1003–1012, 2004.
- [12] R. Dacquin *et al.*, “Amylin inhibits bone resorption while the calcitonin receptor controls bone formation in vivo,” *J. Cell Biol.*, vol. 164, no. 4, pp. 509–514, 2004.
- [13] L. B. J. Isabel Fernández-Tresguerres Hernández-Gil , Miguel Angel Alobera Gracia , Mariano del Canto Pingarrón, “Physiological bases of bone regeneration II. The remodeling process,” *Med. Oral, Patol. Oral y Cirugía Bucal*, vol. 11, no. 2, pp. 151–157, 2004.
- [14] G. M. Pontieri, *Patologia Generale*, 4th ed., vol. 1. .
- [15] Y. Lin, J. C. Mauro, and G. Kaur, “Bioactive Glasses for Cancer Therapy,” in *Biomedical, Therapeutic and Clinical Applications of Bioactive Glasses*, no. 1, Elsevier Ltd., 2019, pp. 273–312.
- [16] “Tumori benigni e maligni: le differenze.” [Online]. Available: <https://www.fondazioneccmt.it/blog-articolo.asp?idb=188>. [Accessed: 12-Mar-2020].
- [17] F. A. Grassi, U. E. Pazzaglia, G. Pilato, and G. Zatti, *Manuale di ortopedia e traumatologia*. 2012.
- [18] J. C. Aster, *Le basi patologiche delle malattie, Volume 2*, Eight. .
- [19] T. Ibrahim, L. Mercatali, and D. Amadori, “Bone and cancer: The osteoncology,” *Clin. Cases Miner. Bone Metab.*, 2013.
- [20] “Tumori ossei primitivi maligni - Disturbi del tessuto muscoloscheletrico e connettivo - Manuali MSD Edizione Professionisti.” [Online]. Available: <https://www.msmanuals.com/it-it/professionale/disturbi-del-tessuto-muscoloscheletrico-e-connettivo/tumori-di-ossa-e-articolazioni/tumori-ossei-primitivi-maligni>. [Accessed: 08-May-2020].
- [21] “Mieloma multiplo - Ematologia e oncologia - Manuali MSD Edizione Professionisti.” [Online]. Available: <https://www.msmanuals.com/it-it/professionale/ematologia-e-oncologia/disturbi-plasmacellulari/mieloma-multiplo>. [Accessed: 08-May-2020].
- [22] “Myeloma | CDC.” [Online]. Available: <https://www.cdc.gov/cancer/myeloma/index.htm>. [Accessed: 08-May-2020].

- [23] “Bone Cancer Symptoms Signs Causes Treatment | Cancer Signs and Symptoms | Do i have Cancer?- Webmd.” [Online]. Available: <https://signscancersymptoms.com/bone-cancer-symptoms-signs-causes-treatment/>. [Accessed: 16-Jun-2020].
- [24] “Neoplasie ossee osteogeniche.” [Online]. Available: https://www.gastroepato.it/tumore_ossa_osteogenici.htm. [Accessed: 16-Jun-2020].
- [25] C. Fletcher, K. Unni, and F. Mertens, *World Health Organization classification of tumours: Pathology and genetics of tumours of soft tissue and bone*. 2002.
- [26] S. A. Lietman and M. J. Joyce, “Bone sarcomas: Overview of management, with a focus on surgical treatment considerations,” *Cleve. Clin. J. Med.*, vol. 77, no. SUPPL. 1, pp. 8–12, 2010.
- [27] T. Cosker and C. L. M. H. Gibbons, “Surgical management of primary bone sarcomas,” *Orthop. Trauma*, vol. 31, no. 3, pp. 173–179, 2017.
- [28] “Surgery of bone sarcoma.” [Online]. Available: <http://oncolex.org/Sarcoma/Diagnoses/Bone/Procedures/TREATMENT/Kirurgi?lg=procedur eGroup>. [Accessed: 09-May-2020].
- [29] K. I. Ringe, M. Panzica, and C. Von Falck, “Thermoablation of Bone Tumors,” *RoFo Fortschritte auf dem Gebiet der Rontgenstrahlen und der Bildgeb. Verfahren*, vol. 188, no. 6, pp. 539–550, 2016.
- [30] “What is chemotherapy? | Cancer in general | Cancer Research UK.” [Online]. Available: <https://www.cancerresearchuk.org/about-cancer/cancer-in-general/treatment/chemotherapy/what-chemotherapy-is>. [Accessed: 10-May-2020].
- [31] M. J. Lind, “Principles of cytotoxic chemotherapy,” *Medicine (Baltimore)*, vol. 36, no. 1, pp. 19–23, 2008.
- [32] “How chemotherapy works | Cancer in general | Cancer Research UK.” [Online]. Available: <https://www.cancerresearchuk.org/about-cancer/cancer-in-general/treatment/chemotherapy/how-chemotherapy-works>. [Accessed: 10-May-2020].
- [33] B. G. Katzung, *Basic & Clinical Pharmacology*, 14th ed. 2018.
- [34] M. J. Wagner, J. A. Livingston, S. R. Patel, and R. S. Benjamin, “Chemotherapy for Bone Sarcoma in Adults,” *J. Oncol. Pract.*, vol. 12, no. 3, pp. 208–216, 2016.
- [35] “Mieloma Multiplo: sintomi, prevenzione, cause, diagnosi.” [Online]. Available: <https://www.airc.it/cancro/informazioni-tumori/guida-ai-tumori/mieloma-multiplo>. [Accessed: 10-May-2020].
- [36] R. Baskar, K. A. Lee, R. Yeo, and K. W. Yeoh, “Cancer and radiation therapy: Current advances and future directions,” *Int. J. Med. Sci.*, vol. 9, no. 3, pp. 193–199, 2012.
- [37] S. P. Jackson and J. Bartek, “The DNA-damage response in human biology and disease,” *Nature*, vol. 461, no. 7267, pp. 1071–1078, 2009.
- [38] W. C. Dewey, C. C. Ling, and R. E. Meyn, “Radiation-induced apoptosis: Relevance to radiotherapy,” *Int. J. Radiat. Oncol. Biol. Phys.*, vol. 33, no. 4, pp. 781–796, 1995.
- [39] N. Sato *et al.*, “A possible role for centrosome overduplication in radiation-induced cell death,” *Oncogene*, vol. 19, no. 46, pp. 5281–5290, 2000.
- [40] R. Hotchkiss, “Cell death,” *N. Engl. J. Med.*, vol. 9, no. 6, pp. 191–199, 2009.
- [41] A. C. Begg, F. A. Stewart, and C. Vens, “Strategies to improve radiotherapy with targeted drugs,” *Nat. Rev. Cancer*, vol. 11, no. 4, pp. 239–253, 2011.
- [42] “Brachiterapia.” [Online]. Available: <https://www.my-personaltrainer.it/salute-benessere/brachiterapia.html>. [Accessed: 15-May-2020].
- [43] J. R. Jones and A. G. Clare, *Bio-Glasses: An Introduction*. 2012.

- [44] S. Feng *et al.*, “125I Seed Implant Brachytherapy for Painful Bone Metastases After Failure of External Beam Radiation Therapy,” *Medicine (Baltimore)*, vol. 94, no. 31, p. e1253, 2015.
- [45] R. Borges, J. Marchi, and R. D. Aspasio, “Biocompatible Glasses for Cancer Treatment,” *Biocompatible Glas.*, vol. 53, pp. 85–117, 2016.
- [46] “Radiation Therapy for Bone Cancer.” [Online]. Available: <https://www.cancer.org/cancer/bone-cancer/treating/radiation.html>. [Accessed: 10-May-2020].
- [47] S. N. Goldberg, G. S. Gazelle, and P. R. Mueller, “Thermal Ablation Therapy for Focal Malignancy,” *Am. J. Roentgenol.*, vol. 174, no. 2, pp. 323–331, 2000.
- [48] C. Kim, A. P. O’Rourke, D. M. Mahvi, and J. G. Webster, “Finite-element analysis of ex vivo and in vivo hepatic cryoablation,” *IEEE Trans. Biomed. Eng.*, vol. 54, no. 7, pp. 1177–1185, 2007.
- [49] M. R. Callstrom and A. N. Kurup, “Percutaneous ablation for bone and soft tissue metastases-why cryoablation?,” *Skeletal Radiol.*, vol. 38, no. 9, pp. 835–839, 2009.
- [50] T. Moser, X. Buy, G. Goyault, C. H. Tok, F. Irani, and A. Gangi, “Image-guided ablation of bone tumors: Review of current techniques,” *J. Radiol.*, vol. 89, no. 4, pp. 461–471, 2008.
- [51] D. A. Gervais, F. J. McGovern, R. S. Arellano, W. S. McDougal, and P. R. Mueller, “Radiofrequency Ablation of Renal Cell Carcinoma: Part 1, Indications, Results, and Role in Patient Management over a 6-Year Period and Ablation of 100 Tumors,” *Am. J. Roentgenol.*, vol. 185, no. 1, pp. 64–71, 2005.
- [52] T. Sabharwal, K. Katsanos, X. Buy, and A. Gangi, “Image-Guided Ablation Therapy of Bone Tumors,” *Semin. Ultrasound, CT MRI*, vol. 30, no. 2, pp. 78–90, 2009.
- [53] K. I. Ringe, C. Lutat, C. Rieder, A. Schenk, F. Wacker, and H. J. Raatschen, “Experimental evaluation of the heat sink effect in hepatic microwave ablation,” *PLoS One*, vol. 10, no. 7, pp. 1–8, 2015.
- [54] B. D. Skonieczki, C. Wells, E. J. Wasser, and D. E. Dupuy, “Radiofrequency and microwave tumor ablation in patients with implanted cardiac devices: Is it safe?,” *Eur. J. Radiol.*, vol. 79, no. 3, pp. 343–346, 2011.
- [55] R. S. Avedian, G. Gold, P. Ghanouni, and K. B. Pauly, “Magnetic resonance guided high-intensity focused ultrasound ablation of musculoskeletal tumors,” *Curr. Orthop. Pract.*, vol. 22, no. 4, pp. 303–308, 2011.
- [56] C. E. Raposo-Amaral *et al.*, “Is bone transplantation the gold standard for repair of alveolar bone defects?,” *J. Tissue Eng.*, vol. 5, 2014.
- [57] W. Lattanzi *et al.*, “Ex vivo-transduced autologous skin fibroblasts expressing human Lim mineralization protein-3 efficiently form new bone in animal models,” *Gene Ther.*, vol. 15, no. 19, pp. 1330–1343, 2008.
- [58] W. Lattanzi and E. Pola, “Gene therapy for in vivo bone formation: recent advances,” 2005.
- [59] M. F. Pittenger *et al.*, “Multilineage potential of adult human mesenchymal stem cells,” *Science (80-.)*, vol. 284, no. 5411, pp. 143–147, 1999.
- [60] E. M. Horwitz *et al.*, “Clarification of the nomenclature for MSC: The International Society for Cellular Therapy position statement,” *Cytotherapy*, vol. 7, no. 5, pp. 393–395, 2005.
- [61] D. J. Prockop and J. Y. Oh, “Medical therapies with adult stem/progenitor cells (MSCs): A backward journey from dramatic results in vivo to the cellular and molecular explanations,” *J. Cell. Biochem.*, vol. 113, no. 5, pp. 1460–1469, 2012.
- [62] M. Barba *et al.*, “Spinal fusion in the next generation: Gene and cell therapy approaches,” *Sci.*

World J., vol. 2014, 2014.

- [63] V. Campana *et al.*, “Bone substitutes in orthopaedic surgery: from basic science to clinical practice,” *J. Mater. Sci. Mater. Med.*, vol. 25, no. 10, pp. 2445–2461, 2014.
- [64] R. Rajani and P. C. Gibbs, “Treatment of Bone Tumors,” 2012.
- [65] “Bone Grafting | Johns Hopkins Medicine.” [Online]. Available: <https://www.hopkinsmedicine.org/health/treatment-tests-and-therapies/bone-grafting>. [Accessed: 11-May-2020].
- [66] S. T. Kao and D. D. Scott, “A Review of Bone Substitutes,” *Oral Maxillofac. Surg. Clin. North Am.*, vol. 19, no. 4, pp. 513–521, 2007.
- [67] P. V. Giannoudis, H. Dinopoulos, and E. Tsiridis, “Bone substitutes: An update.,” *Injury*, vol. 36 Suppl 3, pp. 20–27, 2005.
- [68] T. J. Cypher and J. P. Grossman, “Biological principles of bone graft healing,” *J. Foot Ankle Surg.*, vol. 35, no. 5, pp. 413–417, 1996.
- [69] W. R. Moore, S. E. Graves, and G. I. Bain, “Synthetic bone graft substitutes,” *ANZ J. Surg.*, vol. 71, no. 6, pp. 354–361, 2001.
- [70] “Newport Biologics™ Bone Graft Putty Mineral-Collagen Composite 0.5cc - Glidewell Direct.” [Online]. Available: <https://glidewelldirect.com/products/bone-graft-putty-mineral-collagen-composit-005cc?variant=43183719763>. [Accessed: 10-May-2020].
- [71] “Exabone Products.” [Online]. Available: <https://exabone.com/products/>. [Accessed: 10-May-2020].
- [72] “MBCP® Synthetic Bone Graft Substitute - Biomatlante.” [Online]. Available: <https://biomatlante.com/en/products/orthopaedics/mbcp-synthetic-bone-graft-substitute>. [Accessed: 10-May-2020].
- [73] “Calcium Sulphate – Science Lab Ltd.” [Online]. Available: <https://www.sciencelab.co.ke/products/calcium-sulphate>. [Accessed: 16-May-2020].
- [74] “Sostituto Osseo | DMR SRL.” [Online]. Available: <https://www.dmrsl.it/dmrsl.iotdb.it/node/1>. [Accessed: 10-May-2020].
- [75] “Bonalive-Granules - Meditech.” [Online]. Available: <https://www.meditech.care/prodotti/bio-materiali/spalla/bonalive/bonalive-granules/>. [Accessed: 11-May-2020].
- [76] “i-FIL - Glass Ionomer Filling Cement.” [Online]. Available: <https://www.i-dental.lt/en/product-category/glass-ionomer-cements/i-fil/>. [Accessed: 11-May-2020].
- [77] H. Oonishi *et al.*, “Quantitative comparison of bone growth behavior in granules of Bioglass®, A-W glass-ceramic, and hydroxyapatite,” *J. Biomed. Mater. Res.*, vol. 51, no. 1, pp. 37–46, 2000.
- [78] D. L. Wheeler, K. E. Stokes, R. G. Hoellrich, D. L. Chamberland, and S. W. McLoughlin, “Effect of bioactive glass particle size on osseous regeneration of cancellous defects,” *J. Biomed. Mater. Res.*, vol. 41, no. 4, pp. 527–533, 1998.
- [79] L. L. Hench, O. Andersson, and A. Akademi, *An Introduction to Bioceramics*. 1969.
- [80] L. L. Hench, “Bioceramics,” *J. Am. Ceram. Soc.*, vol. 81, no. 7, pp. 1705–28, 1998.
- [81] I. D. Xynos, A. J. Edgar, L. D. K. Buttery, L. L. Hench, and J. M. Polak, “Gene-expression profiling of human osteoblasts following treatment with the ionic products of Bioglass® 45S5 dissolution,” *J. Biomed. Mater. Res.*, vol. 55, no. 2, pp. 151–157, 2001.
- [82] A. A. Gorustovich, J. A. Roether, and A. R. Boccaccini, “Effect of bioactive glasses on angiogenesis: a review of in vitro and in vivo evidences,” *Tissue Eng. Part B. Rev.*, vol. 16,

no. 2, pp. 199–207, 2010.

- [83] K. Rezwan, Q. Z. Chen, J. J. Blaker, and A. R. Boccaccini, “Biodegradable and bioactive porous polymer/inorganic composite scaffolds for bone tissue engineering,” *Biomaterials*, vol. 27, no. 18, pp. 3413–3431, 2006.
- [84] H. M. A. Jeewantha, “Systems for the delivery of chemotherapeutic drugs, new approaches and perspective,” *Russ. Open Med. J.*, vol. 6, no. 3, 2017.
- [85] S. Senapati, A. K. Mahanta, S. Kumar, and P. Maiti, “Controlled drug delivery vehicles for cancer treatment and their performance,” *Signal Transduct. Target. Ther.*, vol. 3, no. 1, pp. 1–19, 2018.
- [86] S. Y. Wang, H. Z. Hu, X. C. Qing, Z. C. Zhang, and Z. W. Shao, “Recent advances of drug delivery nanocarriers in osteosarcoma treatment,” *J. Cancer*, vol. 11, no. 1, pp. 69–82, 2020.
- [87] L. Lin, L. Guo, W. Zhang, X. Cai, D. Chen, and X. Wan, “Novel silicone-coated 125I seeds for the treatment of extrahepatic cholangiocarcinoma,” *PLoS One*, vol. 11, no. 2, pp. 1–15, 2016.
- [88] S. B. Awan, M. Hussain, S. A. Dini, and A. S. Meigooni, “Historical review of interstitial prostate brachytherapy,” *Iran. J. Radiat. Res.*, vol. 5, no. 4, pp. 153–168, 2008.
- [89] “Prodotti medicali brachiterapia - IsoSeeds I-125 - Brumola.” [Online]. Available: <http://www.brumola.com/specification/isoseeds-i-125/>. [Accessed: 12-May-2020].
- [90] “I-125 Seeds.” [Online]. Available: <https://www.eyephysics.com/PS/PS6/UserGuide/OrderSeeds.html>. [Accessed: 12-May-2020].

Chapter 2

Bioactive Glasses

The purpose of the present chapter is to provide an overview on bioactive glasses and their clinical applications. Structural and chemical properties will be discussed in relation to the processes currently available for their production. Particular attention will be paid to the potentialities of bioactive glasses in the treatment of bone cancer, focusing on brachytherapy. In the end, bioactive glasses will be presented as promising biomaterials for the realization of three-dimensional porous scaffolds for bone tissue engineering approaches, providing a brief summary on manufacturing processes and structural features.

2.1 Glass and its Components

Glass is an amorphous material with no long-range order and no periodic repetition of atoms in the three-dimensional (3D) space, characterized by a glass transformation region [1].

Glasses are obtained by progressive stiffening of a highly viscous liquid that does not crystallize upon cooling. As the cooling process is very rapid, indeed, glasses are characterized by a highly disordered spatial organization, similar to the liquid from which they originate [2].

Glasses are characterized by a glass transition temperature, called T_g , which indicates the rough temperature at which the supercooled liquid converts to a solid. Typical glass viscosity values at this specific temperature are defined within the range $10^{12.0}$ – $10^{12.5}$ Pa s [3].

Glassy materials are brittle below T_g and ductile above T_g . It should be noted that T_g is not strictly constant, since it depends on the cooling rate [3].

Within the glass network, it is possible to distinguish:

- a. Glass network formers: The glass formers compose the backbone of glass network. Their bond strength ranges between 60 and 80 kcal/mol. Glass formers are characterized by high field strength (1–2) and low coordination number (CN) between 3 and 4 [1].

A glass may be formed of one or more glass formers. Glasses tend to be named after their main formers. The most used oxide glass formers are SiO_2 , B_2O_3 and P_2O_5 [1].

Oxides such as Sb_2O_3 , Al_2O_3 , Ga_2O_3 , V_2O_5 , and Bi_2O_3 behave as glass formers when combined with other oxides, while the most common halide glass formers are ZrF_4 and BeF_4 [1].

In order to produce pure silica glasses, very high melting temperatures are necessary. Thus, fluxes such as Na_2O , PbO , Li_2O , and K_2O are required to reduce the melting temperature [1].

- b. Glass network modifiers: Glass modifiers are randomly positioned in the glass network and alter the network by giving additional oxygen ions. These additional oxygens are known as non-bridging oxygens and they do not belong to polyhedral units. The bond strength for modifiers varies between 30 and 40 kcal/mol. Modifiers are characterized by low field strength and high coordination number, i.e. between 6 and 8 [1].

The glass modifiers such as alkaline and alkaline-earth oxides (e.g. Na_2O , CaO , MgO , K_2O) contribute to reduce the melting temperature of glass and, in the case of biomedical glasses, can greatly increase the reactivity in aqueous media and, thus, their bioactive properties and even solubility. Usually, the modifiers are present in lower concentrations than the formers [1].

- c. Glass network intermediates: Glass intermediates has a double nature as it can either act as network formers or network modifiers. These oxides possess intermediate coordination and field strength, i.e., CN varies from 4 to 8, and field strength ranges between 0.84 and 0.04. Their bond strength varies between 50 and 60 kcal/mol, which is the intermediate range of formers and modifiers [1]. The most common intermediate oxides are Al_2O_3 , ZnO , TiO_2 , ZrO_2 [1].
- d. Fining Agents: Finings agents are present in such small quantities that they do not influence glass features. Fining agents discharge large bubbles, which transport smaller bubbles to the surface and seed over there [1].
The most common fining agents are arsenic and antimony, but also NaCl , CaF_2 , NaF , and Na_3AlF_6 can be found. In any case, they modify the viscosity of the melt [1].
- e. Colorants: Colorants give the glass different colours. They are copper, vanadium, iron, manganese, gold, and silver. Gold and silver colour glass by producing colloids [1].
Occasionally, it is necessary for glass to be free of any unintentional colorants, and so other colorants called decolourants are used to counter their effect [1].

Figure 1 shows the glass structure.

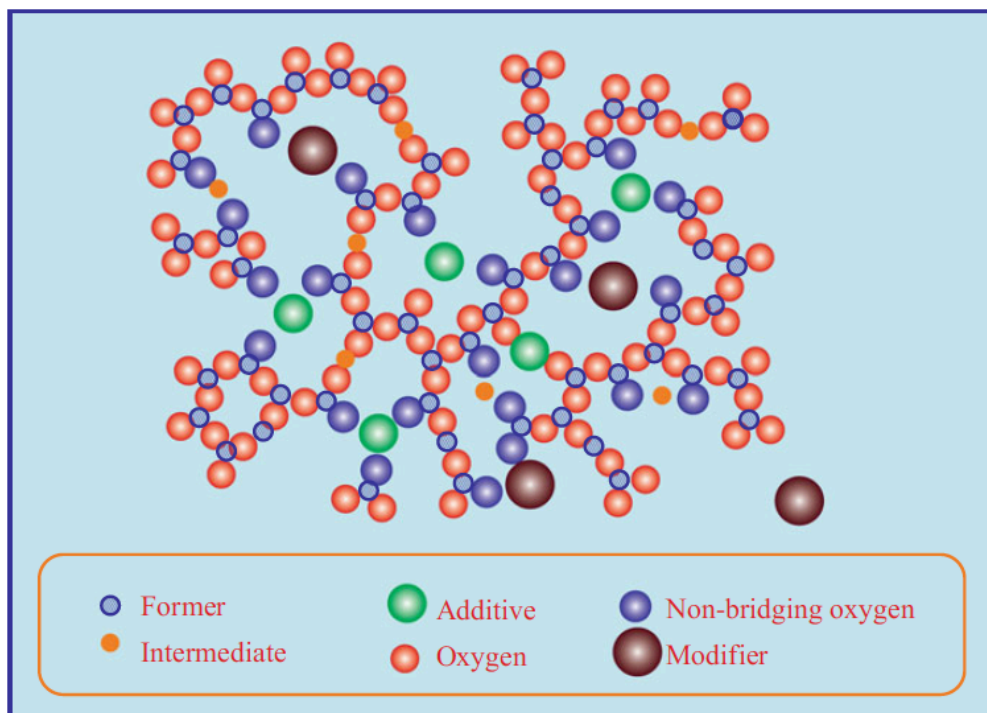


Figure 1: Representation of glass structure. Figure reproduced from Kaur [1].

Since the glassy state is not a state of equilibrium, glass is a thermodynamically unstable substance, which tends to evolve into more stable situations, i.e., to crystallize [2].

In fact, glass and crystals are formed from the same blocks (cation polyhedra) differently arranged; e.g., glasses have broader distributions of bond angles [1].

Amorphous materials can be transformed into a semi-crystalline system or into a crystalline one by applying suitable kinetic and thermodynamic conditions. This phenomenon, called “devitrification”, can occur if the glass is kept for a certain period of time in a temperature range where the crystallization rate is high, leading to the formation of a glass-ceramic material. The transition from the glassy state to the crystalline one cannot occur simultaneously in the whole mass. In fact, it occurs from the formation and the subsequent growth of small clusters of a few hundred atoms, until the crystallization of almost the whole material. The devitrification process of a glass is graphically depicted in Figure 2 [2].

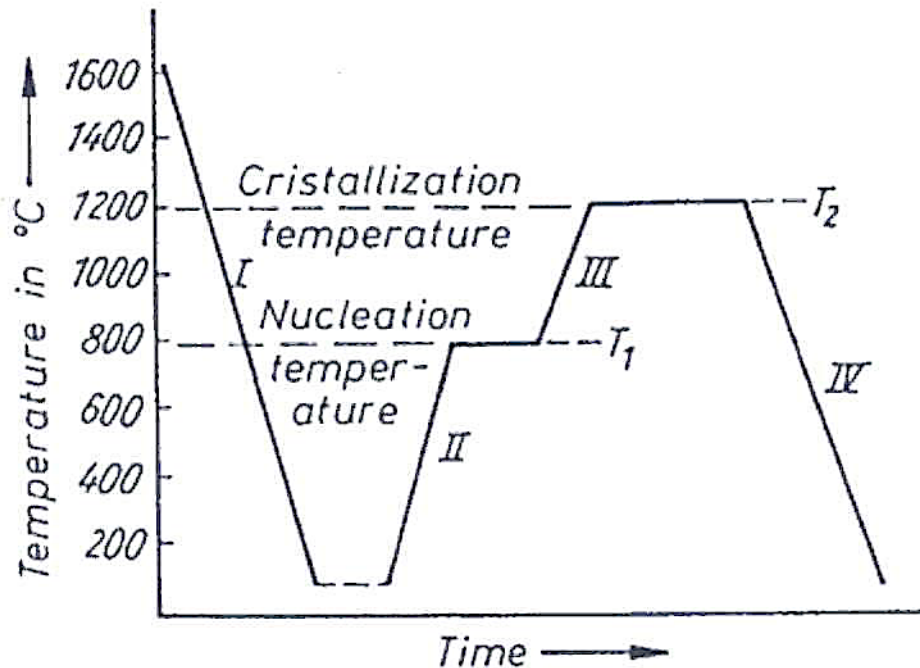


Figure 2: Thermal treatment for the production of glass-ceramic material. The glass undergoes heat treatment at a T_1 temperature, and it is maintained at that temperature for a certain period of time in order to promote the formation of nuclei acting as crystallization centres (nucleation). Subsequently, these nuclei are subjected to a heat treatment which enables them to grow at a temperature $T_2 > T_1$ [2].

Glasses show isotropic properties, because they have no crystallographic planes [4].

From a mechanical point of view, glasses are characterised by brittle behaviour and a short elastic deformation range [3].

Their chemical behaviour depends above all on the oxide composition. For example, silicate glasses exhibit high chemical durability, which is particularly high for pure silica glasses [3].

Glasses are generally transparent to visible light; however, this is not a fundamental requirement for biomedical applications.

2.2 Bioactive Materials

As regards a material intended to be implanted in the human body, the concepts of bioactivity and biocompatibility are closely related. Indeed, excellent biocompatibility could be obtained by

stimulating physiological tissue growth on the surface of the material which needs to bear the physiological expected loads [2].

A bioactive material is defined as: “a material that elicits a specific biological response at the interface of the material, which results in the formation of a bond between the tissue and the material” [5]. The nature of the bond changes according to the material used. The time needed for bonding is a variable depending on the type of material and the bioactivity index (I_B), according to Equation 1 [2]:

$$I_B = 100 / t_{0.5bb} \quad (1)$$

where $t_{0.5bb}$ is the time required for half of the material surface to establish the bond with the tissue [6].

The purpose of a bioactive material is to completely regenerate the tissue in the area where it is implanted.

In the case of bone tissue, an ideal graft material should exhibit the following characteristics: osteo-integration, osteo-conduction, osteo-induction, and osteogenesis [7].

Larry Hench classified materials into two classes of bioactivity on the basis of the degree of interaction with the surrounding tissue that they show after the implantation [8].

- Class A bioactive materials: these materials generate both osteo-conductive and osteo-productive response because of the rapid reaction mechanism that occurs in the surface of the material and which causes the dissolution of critical concentration of soluble silica and Ca^{2+} ions [9].
- Class B bioactive materials: these implants exhibit only osteo-conductive properties, caused entirely by extracellular factors [8].

2.3 The Invention of Bioactive Glass

The first BG was invented in 1969 by Larry L. Hench, a Graduated Research Professor of the Department of Material Science and Engineering at the University of Florida [10].

The idea of making a BG arose during a conversation between Larry Hench and a US Army colonel who had just returned from the Vietnam War in 1967 [10]. The colonel expressed the need to replace the damaged parts of the body of the soldiers returning from the war with new materials, as an alternative to the polymeric and metallic materials that were used at the time. Indeed, since the polymer and metal implants are inert materials, as soon as they come in contact with the physiological environment, they are surrounded by a fibrous capsule of scar tissue that compromises their interaction with the tissues [11].

Hench's BG hypothesis was based on two pillars:

- I. Polymeric and metallic implants provoked a foreign body reaction because they are made up of materials which are completely different from those which are in the human body [11].
- II. In order not to be rejected by the body, a material should form a hydroxyapatite (HA) layer on its surface, because HA is the main component of the bone matrix [11].

From 1969 to 1971, Hench and his collaborators designed and tested various glass composition, on the basis of the Na_2O - CaO - SiO_2 ternary state diagram [10].

The ternary phase diagram SiO_2 , CaO , Na_2O with 6% of P_2O_5 is shown in Figure 3.

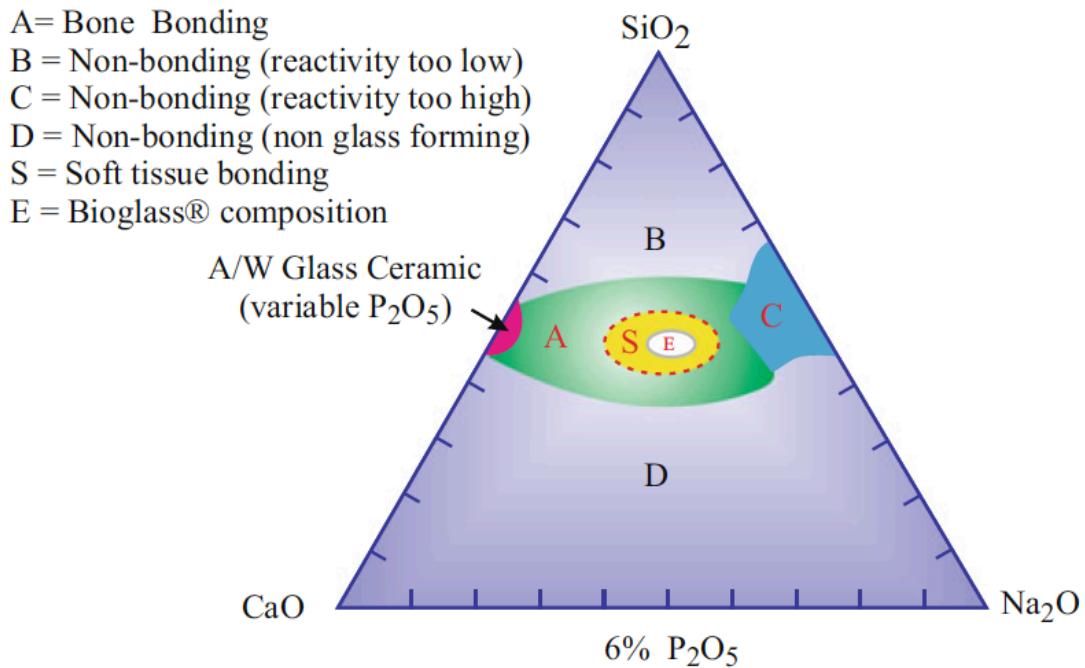


Figure 3: Phase diagram showing the glass-forming area as suggested by Hench. Region E belongs to region S which in turn belongs to region A. Region A is an area of bioactivity where bioactive glasses bond to living tissue and are gene activating. Figure reproduced from Kaur [1].

Glass systems belonging to region A form a bond with bone since a layer of silica gel forms and can precipitate apatite following the Ca^{2+} and PO_4 ions precipitation. Region B includes glasses that are considered bioinert since they do not form bonding because reactivity is too low due to the formation of a hydration layer that is in contact with saline. In region C, the reactivity is so high that it causes a rapid dissolution of silica gel and a gradual dissolution of the glass. Region D includes non-glassy materials. The region S is the class A bioactivity region, typical of osteo-conductive and osteo-productive materials. This region includes glasses capable of forming bonds with bone and soft tissue and that are gene activators. Glasses with the highest level of bioactivity are those within the region E [10].

After several attempts which included 4 oxides: SiO_2 , Na_2O , CaO , P_2O_5 , Hench and his collaborators chose the formulation $45\text{SiO}_2\text{--}24.5\text{Na}_2\text{O--}24.5\text{CaO--}6\text{P}_2\text{O}_5$ wt.%, later named 45S5 and Bioglass® [12], [13]. This composition is characterized by large quantities of Na_2O and CaO , and a high $\text{CaO}/\text{P}_2\text{O}_5$ ratio, which makes the surface of the material very reactive in physiological environment [14]. Furthermore, this composition had the benefit of being very easy to melt because of its closeness to the ternary eutectic [10].

Bioglass® is a silicate glass, i.e. a bioactive glass consisting of a network of silicon dioxide (SiO_2), whose basic unit is the SiO_4 tetrahedron. Each base unit shears up to 4 oxygen atoms leading to the creation of a 3D network, and links to each other by --Si--O--Si-- bridging oxygen bonds. Sodium and calcium act as network modifiers that break up the network making non-bridging oxygen bonds. Bioglass® has a high bioactivity and capacity to encourage stem cell differentiation into an osteoblastic phenotype [15], [16], thus encouraging the creation of an adequately mineralized bone matrix [17].

Bioglass® is a class A bioactive material, that entails to both osteo-conductive and osteo-productive events, because of the fast reactions occurring on the material's surface and which cause the dissolution of soluble silica (SiO₂) and Ca ions [8].

Class A BGs support the establishment of the osteogenic stem cells inside the surgery-derived bone defect that leads to the creation of osteoid bridges between particles. As a result, the matrix mineralizes and mature bone forms. These events cause both an intracellular and an extracellular reaction [9]. In fact, Bioglass® has an intracellular action on the proliferation of bone tissue, due to the delivery of soluble silica, and it has an extracellular action thanks to the high surface area and the porosity of the order of nanometres of the hydrated silica gel and hydroxycarbonate apatite layers which is quickly created [8].

Table 1 summarizes physical and thermal properties of 45S5 Bioglass®.

Table 1: Selected properties of melt derived 45S5 Bioglass®. Table adapted from Jones [18].

Property	Value
Density (ρ)	2.7 g · cm ⁻³
Glass transition temperature (T_g)	538 °C
Glass melting temperature (T_m)	1224-1264 °C
Onset of crystallization (T_x)	677 °C
Thermal expansion coefficient (α)	15.1 × 10 ⁻⁶ °C ⁻¹

A very important limit of Bioglass® is the difficulty of processing into porous 3D scaffolds.

In fact, in order to preserve the amorphous structure, the glass should be thermally treated at a temperature within the sintering window. The sintering window is given as the temperature range limited by T_g (lower limit) and T_x (upper limit) [18].

As can be seen from Table 1, 45S5 Bioglass® is characterized by a sintering window extremely narrow. As a result, it cannot be sintered without undergoing devitrification [19].

The obtaining foam struts are made of loosely bonded particles, and the resulting scaffolds are quite brittle. In addition, the presence of a crystalline phase reduces bioactivity [20].

However, by optimizing the production process, it is possible to obtain both sufficiently strong and bioactive scaffolds [20].

2.3.1 Bioactivity Mechanism

The mechanism of bioactivity first proposed by Hench and still valid for silicate BGs is based on 11 steps, which are divided into two different macro-stages [14]:

1. Formation of the hydroxycarbonate apatite (HCA) layer, which occurs during the first 5 stages of reactions, culminating in the crystallization of the amorphous calcium phosphate film [10].
2. Dissolution of ionic products from BG surface and osteogenesis, leading to the mineralization of the extracellular matrix (ECM) [18].

2.3.1.1 Formation of the HCA Layer

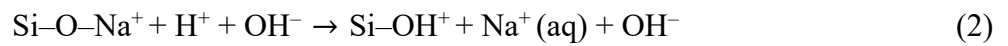
The mechanism of bone bonding is due to the formation of an HCA layer on the glass surface in contact with body fluid. HCA is similar to bone mineral and thus builds a bond [21].

This phenomenon may occur both *in vitro* and *in vivo* on the surface of the material, without any substantial distinctions as regards the deposition mechanism [22].

When the implant comes into contact with the body fluid, a series of chemical reactions take place leading to the formation of the HCA layer [21]. The HCA layer forms following solution-mediated dissolution of the glass [18]. Dissolution products coming from the material accumulate in the environment inducing local variations of physiological pH and variations in the chemical composition of the solution [10], [18], [23], [24].

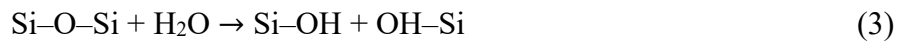
The mechanism of deposition of the HCA layer interposed between implants and biological fluids involves five steps [10], [18], [23], [24]:

1. Ionic exchange among Ca^{2+} and Na^+ ions in the material and H^+ and H_3O^+ ions coming from the environment. Silanol bonds (Si-OH) form on the surface of the glass (Equation 2). The release of alkaline ions increases the solution pH, and a silica-rich layer appears on the surface of the glass. $(\text{PO}_4)^{3-}$ ions are released too, in case they exist in the starting formulation [22].



This reaction happens very quickly, within a few minutes of contact with biological fluids. The surface layer is alkaline cation-depleted and exhibits a net superficial negative charge [22].

2. High local value of pH causes the breaking of O-Si-O bonds conducted by OH^- groups, which determine the breaking of the silica network. Soluble silica is released in the form of $\text{Si}(\text{OH})_4$ and the silanol groups are exhibited on the glass surface, directly in contact with the solution (Equation 3) [22].



It has been reported that the soluble silica released favours the proliferation of cells, leading to the formation of new bone tissue at the implant site [22].

3. Silanol groups condensation and re-polymerization of an amorphous silica-rich layer poor in Na^+ and Ca^{2+} ions. The thickness of this layer is typically between 1 and 2 μm . During leaching the proportion of bridging oxygen increases [22]. The surface is micro-porous, its average pore diameter is between 30 and 50 \AA , and its effective surface area is up to 100 m^2/g [23].
4. Migration to the surface of Ca^{2+} and $(\text{PO}_4)^{3-}$ ions through the SiO_2 -rich layer both from the solution and from the glass inducing the formation of ACP layer on the surface of the SiO_2 -rich layer [24].
5. Incorporation of hydroxyls and carbonate from solution, while the dissolution of the material keeps on starting from the surface [18], [22]. HCA forms from the crystallization of the amorphous layer. The resulting surface resembles the nano-crystalline mineral phase of the physiological bone tissue

both in terms of structure and composition, and this allows the direct attachment of the glass to the living tissue [22].

The thickness of the HCA layer increases over time up to 100 μm [23].

The conformity of the interface is indispensable in mechanical conservation of the bond [22].

Glass composition is the variable that most affects the rate of HCA layer formation and bone bonding. Basically, lower amount of silica implies a less connected silica network, leading to higher dissolution rates and, thus, faster HCA deposition kinetics. However, the connectivity of the network is fundamental and depends on the amount of silica and other cations. In fact, the addition of sodium instead of silicon leads to an increase in dissolution rate, but the replacement of cations, such as sodium and calcium with multivalent ions such as Al^{3+} , Ti^{4+} or Ta^{5+} reduces bioactivity by diminishing solubility [10], [18], [23], [24].

2.3.1.2 Ionic Dissolution Products and Osteogenesis

The reaction phases after the formation of the HCA layer are not yet fully defined [22]. What is clear is that proteins adsorb to the HCA layer, and cells attach, proliferate and differentiate [18]. After differentiating in the appropriate phenotype, the cells are able to synthesize an extracellular matrix that will be subsequently mineralized [18]. More precisely the last five steps are explained below:

6. The absorption of organic species, such as proteins and growth factors, which influences the characteristics of the HCA layer, since it happens at the same time with the first four steps [25].
7. The reaction layer affects the time macrophages need to prepare the implant site and allow tissue regeneration [9].
8. Stem cells colonize the surface of the implant. From the implantation of the glass, the colonization lasts 12 h [23].
9. Stem cells proliferate and differentiate into a mature osteoblastic phenotype [9].
10. Osteoblasts begin to produce different growth factors which trigger the cellular anchorage, mitosis and synthesis of extracellular matrix proteins [9].
11. Mineralization of the matrix. It occurs 6–12 days after the synthesis of extracellular matrix proteins [9].

Table 2 summarizes the bioactivity mechanisms explained above.

Table 2: 45S5 Bioglass[®] reaction stages. Table adapted from Baino et al. [22].

Stage	Reaction Event
11	Crystallization of matrix
10	Cellular attachment
9	Differentiation of steam cells
8	Attachment of steam cells
7	Action of macrophages
6	Adsorption of biological moieties
5	Nucleation and crystallization of calcium phosphate to HCA
4	Precipitation of amorphous calcium phosphate
3-2	Dissolution and re-polymerization of surface silica
1	Ion exchange
0	Initial glass surface

2.3.1.3 Influence of the Ionic Dissolution Products

Key mechanisms inducing new bone growth are related to the controlled release of ionic dissolution products from the degrading bioactive glass, principally critical concentrations of biologically active, soluble silica and calcium ions [10], [26].

Recently, it has been demonstrated that bioactive glasses, along with ionic dissolution products, improve osteogenesis by regulating osteoblast proliferation, differentiation, and gene expression.

In order to regenerate bone, it is crucial that osteoprogenitor cells undergo cell division (mitosis) and receive the right chemical stimuli from their local environment that orient them to enter the active segments of the cell cycle [26].

Sun et al. [27] have found that 45S5 Bioglass[®] triggers human osteoblast proliferation by reducing the growth cycle to pass through G₁ (first growth phase including amino acid synthesis) and S (synthesis) and then enter G₂ (second growth phase, including the mitosis) quickly. In the presence of critical concentrations of Si and Ca ions, in 48 h, the osteoblasts that are able to differentiate into a mature osteocyte phenotype, start to proliferate and regenerate new bone. Furthermore, osteoblasts, that are not in the correct phase of the cell cycle and are not able to differentiate, are led to apoptosis by the ionic dissolution products [27], [28].

Besides, recent studies have shown that controlled release of low concentrations of ionic dissolution products from BGs can promote also angiogenesis [17].

2.4 Categories of Bioactive Glasses

Biomedical glasses are typically classified according to their composition and, more specifically, their former oxide (SiO₂, B₂O₃ or P₂O₅) [29]. The emerging class of biomedical “black glasses” as well as doped bioactive glasses are also shortly described.

2.4.1 Silicate Bioactive Glasses

Silica is the main component of silicate BGs. SiO_4 basic units are connected to each other at the oxygen centres. The presence of non-bridging oxygen ions connected with silicon makes the silica structure open. Furthermore, the opening of silica network structure is also caused by the addition of network modifiers such as Na^+ , K^+ , Ca^{2+} , which substitute bridging oxygens of the network with non-bridging oxygens. It has been shown that the properties of bioactive glass also depend on the amount of modifier ion-oxygen bonds and non-bridging oxygen bonds [13].

Na_2O , CaO , P_2O_5 are the basic oxides required for a silicate glass to achieve bioactivity. Moreover, it should have the following characteristics: the quantity of SiO_2 must be between 45 wt% and 60 wt%, and the amount of CaO and Na_2O should be high, as well as the $\text{CaO}/\text{P}_2\text{O}_5$ ratio. In fact, a quantity of silica higher than recommended reduces the dissolution rate of the glass ions from the surface causing a dramatic reduction in bioactivity. While a lower content of silica leads to completely dissolvable basic SiO_4 units. The quantity of silica affects the formation of hydroxyapatite carbonate (HCA) when the bioactive glass comes into contact with the physiological fluid, favouring the bond with living tissues. As a result, the strength of the bond between bone and soft/hard tissue increases. The high $\text{CaO}/\text{P}_2\text{O}_5$ ratio favours the release of ions from the surface of the glass, when immersed in the body fluid, quickly leading to the formation of a surface layer of HCA [13].

Finally, silicate bioactive glasses support the proliferation and differentiated function of osteoblastic cells [1].

As already mentioned, Bioglass[®] is a silicate bioactive glass [24].

2.4.2 Borate Bioactive Glasses

It has been recently discovered that specific compositions in other glass-forming systems, such as borate glasses, are bioactive too [24].

Borate glasses are highly reactive and have low chemical durability. Accordingly, they totally convert to HA faster than the silicate glasses [1]. Huang et al. [30] gradually replaced SiO_2 with B_2O_3 and have demonstrated a considerable increment in glass conversion to HA in aqueous phosphate solutions [30]. However, borate glasses convert to apatite with a mechanism which is similar to that of silicate glasses, with the development of a borate-rich layer similar to the silicate-rich layer of the previous ones [1].

The remarkable difference in the degradation rate between borate and silicate BGs may be explained considering the glass network structure. Due to its coordination number, indeed, boron is not able to completely form 3D structures, creating less resistant network interconnections [31].

The derived advantage is that the degradation rate can be designed by acting on the glass composition [22]. Therefore, by adjusting the glass composition, it should be possible to match the degradation rate of borate BG with the bone regeneration rate [24].

For the first time in 2005, scaffolds using borate BG were developed by means of soft pressing and sintering treatment [1].

In addition, the fast and controllable reaction of borate BGs has played a key role in soft tissue regeneration, blood vessel formation (angiogenesis) and wound healing [32].

Boron is a trace element, required for bone health. Borate glass leads to higher pH value of the culture medium. *In vitro*, borate BGs stimulate cell proliferation and differentiation, whereas *in vivo* they

improve tissue infiltration [1]. Borate BGs were also used as a substrate for drug release in the treatment of bone infection [24].

The downside of these glasses is the toxicity of boron released into the solution as borate ions, $(\text{BO}_3)^{3-}$ [33]. It has been noted that under conventional static *in vitro* culture conditions, some borate glasses are toxic to cells, but toxicity is much lower under dynamic culture conditions [33].

2.4.3 Phosphate Bioactive Glasses

Phosphate bioactive glasses based on the P_2O_5 as glass network former, and CaO and Na_2O as modifiers were developed for biomedical purpose by several research groups [34], [35], [36], [37], [38].

These glasses present chemical affinity with bone because their constituent ions are present in the organic mineral phase of bone [24].

Phosphate BGs are characterized by the presence of phosphate (PO_4) tetrahedron structural unit, which is highly asymmetric in nature. Due to this asymmetry these glasses have low durability and easy hydration of P-O-P bonds [1].

Since phosphate BGs show an excellent tendency to dissolve spontaneously in aqueous media, they are optimal materials to construct temporary implants [29].

In addition, these glasses were deeply studied as vehicles to release, in a controlled manner, antibacterial ions such as silver, copper, zinc, and gallium [1].

Furthermore, phosphate glass fibres which are obtained from phosphate glasses through the spinning process, are suitable to be used as guides for muscle or nerve repair in soft tissue engineering [1].

As concerns hard tissue engineering, the phosphate BGs are considered as bone tissue regenerative materials in the form of either bulk or powders combined with polymers in composite materials [1].

2.4.4 Black Glasses

Black glasses are based on silicon oxycarbide (Si-O-C) [39]. They form by partial replacement of oxygen ions by carbon ions in an amorphous silica structure [40].

The simplest and the most reliable method to obtain black glasses is the sol-gel route using opportune precursors containing Si-C bonds in their polymeric chains [41].

The Si-C bond is highly durable and remains intact during the entire glass synthesis [41]. Therefore, Si-O and Si-C are the only bonds present in stoichiometric silicon oxycarbide glasses [42].

It could be expected that with the increasing amount of carbon ions in the glass network the properties of the glass will also improve. Therefore, one prefers to design glasses with high contents of carbon. However, the maximum amount of carbon atoms that can be introduced into the silica network is 45% [42].

Black glasses, in addition to Si-C and Si-O bonds, generally contain also the so-called free carbon, which confers them black colour [43], [44].

Functional parameters of black glasses can vary within a wide range, according to the amount of free carbon and isomorphous substitution in the glass structure [45], [46].

2.4.5 Doped Bioactive Glasses

Incorporating different ions into the BGs compositions could improve their physical-chemical properties while conferring specific therapeutic action [47].

This incorporation of particular ions in the composition of glass is called doping process and it was widely employed for the production of BG-based multifunctional products for various clinical applications [47].

A doping element, by definition, is an additional incorporation in the main composition at a very low concentration compared to the main components, ranging from a few ppm to a few percent [47].

Recent studies showed that, in some cases, the controlled introduction of doping elements can lead to increased efficiency in performing a specific therapeutic action (e.g., antibacterial properties, angiogenesis) [48], [49]. In other cases, doping may enhance surface structure of the material or the physical characteristics of it [47].

There is no specific date marking the start of the doping, but around late 1985 incorporating different ions into the bioactive glasses became very common [50].

At the beginning, the dopants were selected according to their similarity in valence with the elements already present, whereas later, the choice of the dopants was made on the basis of the literature about the essential trace elements required in human body and their action [51], [52].

Since metal ions, by acting as an enzyme cofactors, affect signalling pathways and encourage tissue formation, they are considered interesting doping materials in the field of hard and soft tissue engineering [52], [53].

Some ions, such as Sr, Zn, Cu, Mg and B are believed to be promising in improving the bioactivity of implant materials by monitoring the release of specific ions during *in vivo* dissolution.

Bioactive glasses doped with iron and bioactive glasses doped with rare-earth elements, such as yttrium, samarium, holmium and rhenium captured the attention of many researchers, since the doping element make them respectively suited for hyperthermia treatment and brachytherapy. These glasses and their applications will be discussed more thoroughly afterwards.

2.5 Manufacturing Techniques for the Production of BGs

Currently, two methods exist for the production of bioactive glass: melt-quenching route and sol-gel process. They both aim at obtaining glasses with controlled bioactive behaviour, that is the most important requirement in clinical applications [22].

Glasses obtained by these two techniques differ in their porosity, mechanical properties, uniformity, and in bioactive properties. Sol-gel glasses have inherent mesoporous texture, characterized by the presence of pores in the range of 2–50 nm, while the melt-quenched glasses are characterized by better mechanical properties, such as hardness and flexural strength [1].

2.5.1 Melt-Derived Technique

Most of the bioactive glasses as well as the 45S5 Bioglass[®], were obtained by melting a mixture of raw material, followed by their quenching [54], [13].

The choice of high-purity reagents is fundamental in order to avoid contaminations [55], while the composition of the glass has to be designed to facilitate the melting process and guarantee a proper bioactive response [13].

The batch of glasses is prepared by mixing an appropriate mole/weight fraction of initial ingredients [54].

In order to have more uniform powder, the mix of ingredients is ground in ball mill for about two hours in damp substance like acetone [13], [54]. The ball milling is usually made by balls of porcelain or agate in the respective container. Subsequently, the obtained mixture is dried in air so that the acetone evaporates [54].

Then, the mix is moved inside a recrystallized alumina or platinum crucible and melted in a high temperature furnace. The alumina crucible is only used for low-melting temperature glasses, because at high temperatures aluminium ions can diffuse from the crucible into the melted glass (contamination and unpredictable alteration of glass composition with detrimental effect on bioactivity). A platinum crucible is therefore used for high-melting temperatures glasses [54].

Since gaseous substances usually leave the composition at about 500 °C, calcinating the mixture at 500 °C for at least 2 hours is recommended [13].

For some aluminosilicate compositions the furnace temperature can reach 1500 °C, while for the borate and phosphate compositions the furnace reaches lower temperatures, around 1200-1300 °C. Once the melting temperature is reached, the glass mix should remain at this temperature for at least an hour, in order to obtain homogeneous and bubble-free melted material [54].

At this point, two different procedures can be followed: the first is to pour the molten glass into a preheated graphite or brass mould and then to anneal the poured glass slightly below the glass transition temperature of the corresponding glass for 12 h in air in pit furnace. This technique allows obtaining glasses of different shapes and sizes [13].

The second route is to quench the molten glass in a liquid such as water, liquid nitrogen etc. or in air using copper plates. By quenching the glass in a liquid, higher cooling rates are achieved, while air quenching prevents any crystallization [1]. Different shape granules are obtained, and then collected and milled in order to obtain glass powder [13].

The schematization of this process is shown in Figure 4.

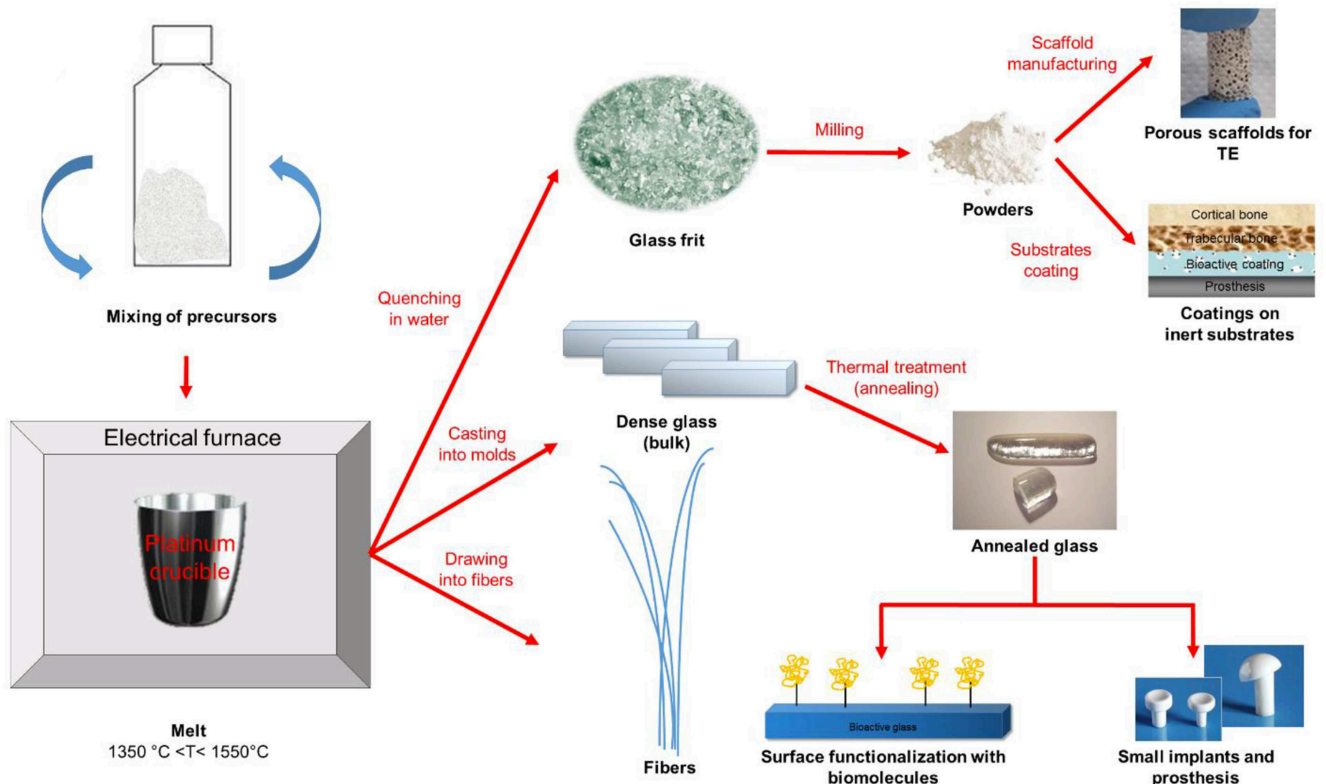


Figure 4: Schematization of melt-derived glass synthesis. Figure adapted from Fiume et al. [56].

The factors that should be considered when producing a glass with the melt-derived technique are viscosity, thermal expansion, and crystallization characteristics [13]. Low viscosity makes the melt homogeneous and bubble-free, facilitating the casting procedure [13].

Moreover, the melting temperature should be higher than liquidus temperature of the compositions [13]. Aboud et al. [57] analysed the effect of temperature rise on crystallization and the phase formation order of various crystals of SiO_2 , P_2O_5 , Al_2O_3 , MgO , Na_2O glasses [57].

Finally, thermal treatments allow obtaining glass with different elastic properties and a range of bioactivity, which could be helpful for developing patient-specific implant [13].

Currently, the melt-derived 45S5, 13-93 and S53P4 composition are approved by the Food and Drug Administration (FDA) for clinical use in human patients [55].

2.5.2 Sol-Gel Technique

The first sol-gel bioactive glasses were developed in the early 1990s by Li et al. [58] and Pereira et al. [59]. Their composition was called 58S (60 mol% SiO_2 , 36 mol% CaO , 4 mol% P_2O_5) and was very similar to the melt-derived compositions developed previously [10].

The sol-gel technique is a chemistry-based synthesis method in which the polymerization reaction of a solution including oxides precursors carries out the gelation of the sol at room temperature [60]. Before explaining the characteristic reaction steps, it is necessary to provide some definitions:

- a sol is a colloidal suspension of solid particles with a diameter in a range of 1–100 nm in a liquid, where the colloids move randomly guided by momentum imparted by collisions with molecules of the suspending medium. This movement is called Brownian motion [13].
- A gel is a rigid network of covalently bonded silica formed of interconnected pores and polymeric chains [13],[54]. Gels can be classified into three groups: alcogels, xerogels and aerogels [61]. Alcogels are characterized by the presence of an alcohol-based pore-liquid, while xerogels are created from thermal remove of pore liquid. Finally, aerogels are low-density gels (80 kg/m^3) with large pore volumes (up to 98%), which are produced by removing pore liquid from the rigid network without collapsing it [13], [54].

According to the classification given by Flory [62], gels can be categorized into four different classes: (i) well-ordered lamellar structures, (ii) disordered covalent polymeric networks, (iii) disordered and physically aggregated polymeric network and (iv) particular disordered structures [62].

There are three different routes necessary to obtain sol-gel monoliths: (i) gelation of solution of colloidal powders; (ii) reactions of hydrolysis and poly-condensation of alkoxide or nitrate precursors, followed by hypercritical drying of the gel; (iii) reaction of hydrolysis and polycondensation of alkoxide precursors to which follows the aging and drying under ambient atmosphere [61].

In order to produce biomedical sol-gel glasses, the third route is usually adopted, which consist of seven steps [63]:

1. Mixing the reagents at room temperatures and formation of strong covalent bonds between the elements [60]. Hydrolysis and poly-condensation reactions are competitive during this step and happen at the same time, until the solution is completely homogeneous under mild reaction conditions [63].
 2. Casting the sol into moulds of different geometries to obtain the final product of the desired shape. Actually, this step is not indispensable if the bowl used for the mixing possess adequate characteristics in terms of shape and material [61].
 3. Gelation, which leads to the formation of a 3D network, and consequently an increase in viscosity. During this step, it is possible to draw the gel into fibres by operating a strict control on the rheological properties of the material [61].
 4. Syneresis/aging of a gel in which the continuous process of polycondensation and re-precipitation of the gel network causes the decrease in porosity, hence the increase in strength. Moreover, this step also includes the phase transformation. The aging process can be accelerated by hydrothermal treatment. The aging process largely influences the physical properties such as pore volume, gel surface and density and thus the resulting glass structure [1], [54].
 5. Drying, by removing the liquid in the pores of the 3D network [61]. As concern the fabrication of monoliths, the main problem is the cracking and the shrinkage which take place during this stage, most often causing the fracture of the material [64].
 6. Dehydration or chemical stabilization, which entails the removal of silanol bonds from the pore network, allowing to obtain a chemically stable solid [61].
 7. Densification of the gel through a high-temperature thermal treatment that removes the pores [61].
- The schematization of the sol-gel process is shown in Figure 5.

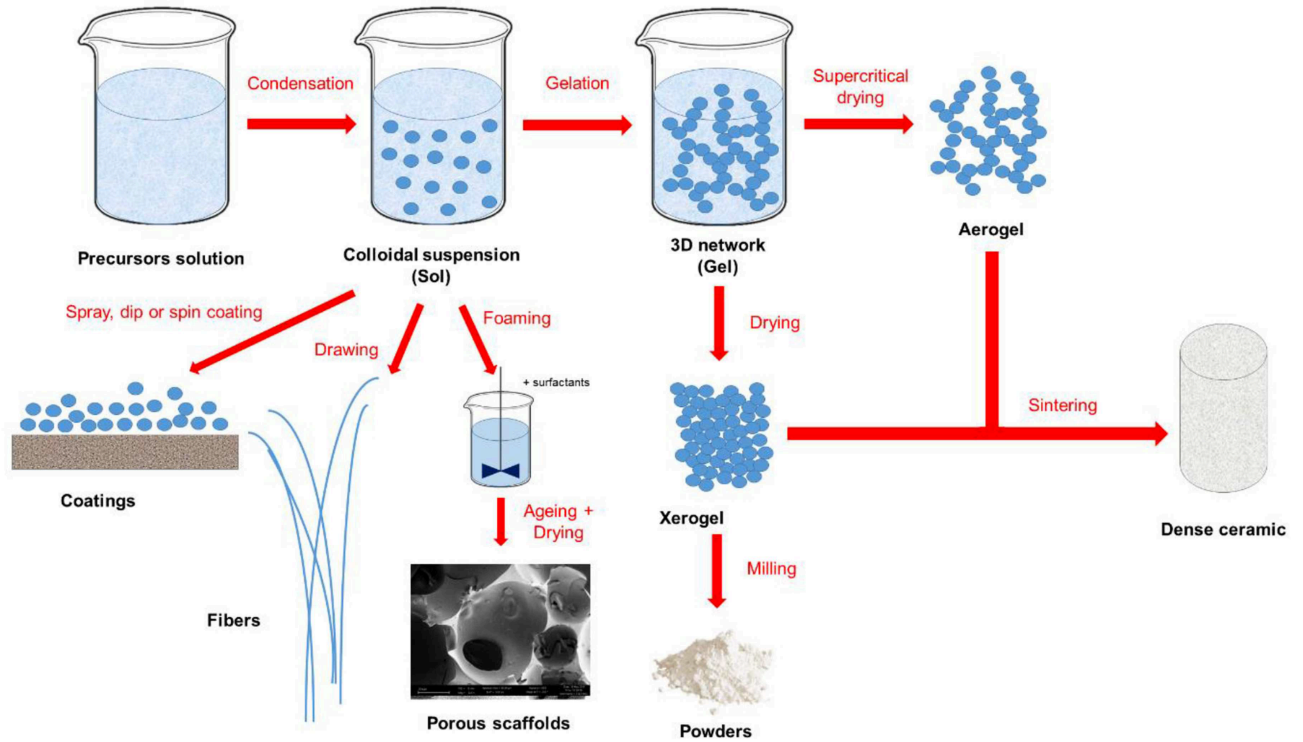


Figure 5: Schematization of sol-gel glass synthesis. Figure adapted from Fiume et al. [56].

2.5.2.1 Hydrolysis and Polycondensation

Silica gels are commonly formed by hydrolysing alkoxide precursors by means of catalysts action, which could be either an acid or a base [65].

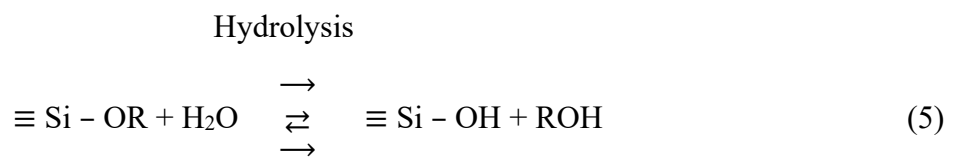
The most frequently used agents to form the network are tetra-functional monomeric alkoxides with general chemical formula $\text{Si}(\text{OR})_n$, where R is the alkyl group, such as ethyl group (C_2H_5) in tetraethyl orthosilicate (TEOS, $\text{Si}(\text{OC}_2\text{H}_5)_4$), and methyl group CH_3 in tetramethoxysilane (TMOS, $\text{Si}(\text{OCH}_3)_4$) [61].

The chemical reaction below describes the production of TEOS, which starts from anhydrous ethanol and tetra-chlorosilane, and produces HCl as a by-product [65].



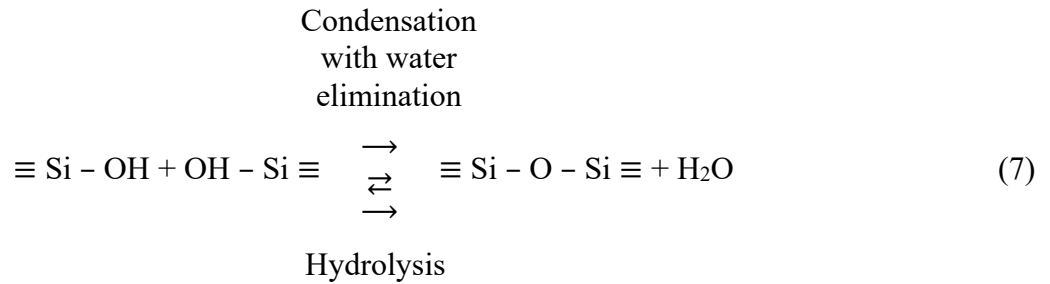
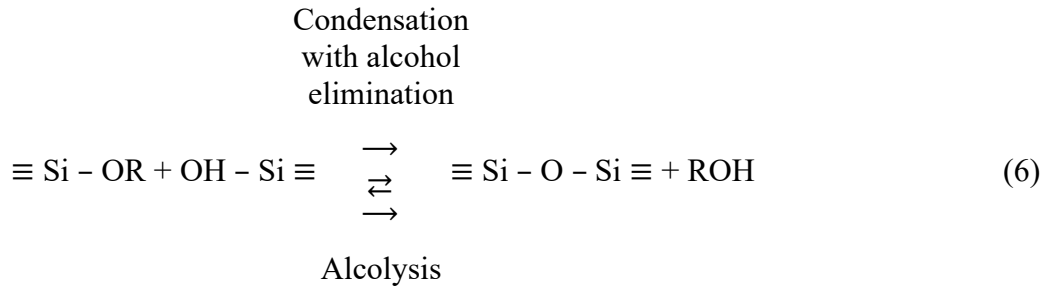
Subsequently, chemical reactions which describe the processes of hydrolysis and poly-condensation involved in sol-gel synthesis are given:

1. Hydrolysis involves nucleophilic attack during which the OH group substitutes the OR group according to the reaction:



Esterification

2. Condensation causes the formation of siloxane bonds and water or alcohols, according to the reactions shown below:



where R represents the alkyl functional group in the form: $\text{C}_x\text{H}_{2x+1}$ [65].

Sol-gel process tends to be particularly sensitive to the following parameters:

- Catalysts: catalysts, both acidic and basic, lower the activation energy causing a faster evolution of hydrolysis and poly-condensation reactions [65].

For the hydrolysis reaction, mineral acids and ammonia are the most used catalysts [65].

As concern the condensation reaction, the use of catalysts is beneficial, but not indispensable. In this case, the most used catalysts are mineral acids, ammonia, alkali metal hydroxides, and fluoride anions [65].

The type of catalysts, for both hydrolysis and condensation reaction, plays a crucial role in setting the gelling time of the system [66], as shown in Table 3.

Table 3: Gelation times and solution pH for TEOS systems employing different catalysts. Table reproduced from Pope et al. [66].

Catalysts	TEOS (mol/L)	Initial pH of the solution	Gelation time (h)
HF	0.05	1.90	12
HCL	0.05	0.05	92
HNO ₃	0.05	0.05	100
H ₂ SO ₄	0.05	0.05	106
HOAc	0.05	3.70	72
NH ₄ OH	0.05	9.95	107
None	-	5.00	1000

- pH: particularly, low pH values induce the protonation of the leaving groups favouring the hydrolysis reaction, while high pH values cause the deprotonation of the -OH groups favouring the condensation reaction [60].

The isoelectric point of silica (pH=2.5) defines the acidic and basic conditions, in fact if the pH is < 2.5 , the reaction advances by acid catalysis, while if the pH is > 2.5 , the conditions of basic catalysis are ensured [60].

Under acidic conditions, mesopores are organized in well-ordered hexagonal structures because hydrolysis occurs faster than condensation. On the contrary, under basic or neutral conditions, a gel-like structure is formed without any mesopores [60].

- Solvent: during the primary stages of reactions, solvents are commonly used to increase the solubility of TEOS in aqueous solutions as well as to control H₂O and silicates concentrations, which define the kinetics of the gelling process. However, it is often preferable to avoid the addition of mutual solvents, because the alcohols deriving from TEOS hydrolysis have the same ability by taking part into the esterification and alcoholysis reaction (reverse reaction) [65].

Four kinds of solvents can be adopted in sol-gel synthesis: polar, nonpolar, protic, and aprotic [65]. The quantity of the solvent concentration affects the gelation kinetics [61].

- H₂O:Si ratio: the H₂O:Si ratio (r) can vary from 1 to 25 [65].
Higher values of r-ratio support the reaching of a complete hydrolysis before achieving advanced phases of the condensation reaction. Anyway, high values of r-ratio combine with a constant solvent:silicate ratio, leading to a decrease in the concentration of silicate, which in turn reduces the silicates' concentration, causing an increasing in gelling time [65].
- Temperature: the chemical kinetics of the several reactions involved in the formation of nanoparticles and the aggregation of them in a gel network is accelerated with temperature, which influences the gelation time. At very low temperatures, gelation slowly occurs, over weeks or months. Contra, at high temperatures, the reactions that bind the nanoparticles to the gel network happens so fast that lumps form. The gelation temperature must be controlled to optimize the reaction time [67].

2.5.2.2 Physical, Chemical and Biological Properties of Sol-Gel Derived Materials

Mesoporous Structure

Sol-gel materials are characterized by porous structure, which is due to the synthesis process [68].

According to IUPAC, based on their pore size, porous materials can be classified into three classes:

1. Microporous materials, with pores size < 2 nm [68].
2. Mesoporous materials, with pores size between 2 and 50 nm [68].
3. Macroporous material, with pores size > 50 nm [68].

The mesopores average size of silicate materials obtained by “conventional” sol-gel method is typically 10-40 nm [69].

In order to obtain smaller mesopores, it is sufficient to use a surfactant as a mesopore template [70]. This approach allows controlling the mesopore size, which is essential when the material is designed as a drug delivery system [71], and is usually applied for the synthesis of the so-called mesoporous bioactive glasses (MBGs) [72].

For the porosity characterization, several aspects must be considered, such as shape of the pores, size distribution and interconnectivity [63].

The control of porosity is fundamental for the manufacture of substitutes of living tissues, since porosity features affect the entity of the interactions with cells and the surrounding environment, and the drug release kinetics in drug delivery systems [63].

Chemical Properties

Chemical composition affects biological activities of BGs in physiological environment [73].

In order to have suitable bioactivity, glasses should have:

- Si-OH (silanol) or R-OH groups on the surface to form nucleation sites for HA/ HCA [73].
- Ca^{2+} and phosphate ions near the material surface to allow HCA crystallization, even though this might be not necessary due to the presence of both Ca and P in body fluids [73].

Due to high specific surface area, sol-gel glasses expose a high density of silanol groups which allow bonding of functional groups on the surface of the glass [60].

Functional groups are generally grafted using two different routes, called stepwise synthesis and one-pot synthesis [60]. These groups enhance adsorption of biomolecules, binding affinity, biocompatibility and load capability for non-polar drugs in controlled and targeted drug delivery devices [63].

Mechanical Properties

Due to their inherent porous structure, sol-gel materials are characterized by poor mechanical performances [60]. This problem is more evident when sol-gel materials are used to develop scaffolds with multiscale porosity [74].

It has been proven that the change of some processing parameters affects mechanical properties of the materials. For example, higher amount of water causes an accelerated hydrolysis reaction, resulting in lower density values [75]. Murtagh et al. [75] showed that the elastic, shear, and bulk moduli of the silica gel decrease as the water content increases from 4:1 to 24:1 [76].

The shrinkage, occurring during the drying process, develops internal stresses, which can cause the catastrophic fracture of sol-gel monoliths. The shrinkage is deeply related to the pH of the sol and lower shrinkages were detected for higher values of solution pH [76].

The precursors utilized during synthesis can also influence the mechanical behaviour of the final material. Therefore, the sintering process could be appropriately optimized in order to improve mechanical properties by diminishing pore size [77]. Nonetheless, there are two types of limitations: first, sintering at high temperature could cause disappearance of the mesopores because of densification, which affects bioactivity and the release of ionic dissolution products, as well as makes the final product unsuitable for drug delivery applications; secondly, if biomolecules are embedded into the material before sintering, the temperature must be kept below a certain threshold, in order to safeguard biological molecules from degradation and prevent undesired crystallization process [60].

Biological Properties

Jones et al. [78] have observed that, since the dissolution of the glass occurs as of the material surface, a higher surface area is generally responsible for faster dissolution rates [78].

In addition, current studies have proved the beneficial effect of high surface area and pore volume in accelerating the apatite-forming ability of sol-gel BGs. On the other hand, the significant pH changes produced by the fast dissolution kinetics of the glass may be a problem for biomedical applications because it can lead to toxicity [63].

Summary and Differences between Melt-derived and Sol-gel derived BGs

The most interesting characteristics of sol-gel glasses are shown below:

1. Intrinsic nanoporosity, which is reflected in a higher surface area, which in turn leads to enhanced cellular response as well as higher solubility and reactivity in aqueous environments [79].
2. Basic composition, because addition oxides are not necessary to facilitate the processing of the material [80].
3. Possibility to obtain nano-porous powders, monoliths and nanoparticles by changing pH conditions [81].
4. Possibility to control the pore size distribution by adjusting precursors and pH conditions. Usually pores between 2 and 30 nm in diameters (mesoporous range) are obtained [63].
5. Possibility to adapt the oxide composition by adding appropriate precursors during the sol's mixing [18].

The main difference between sol-gel and melt-derived bioactive glasses is that sol-gel glasses are intrinsically nano-porous, whereas melt-derived glasses are dense [18]. This means that the specific surface area of the sol-gel glasses is two orders of magnitude higher than for similar compositions of melt-derived glass, which results in greater dissolution rate, and hence higher cellular response [18], [13].

From a chemical point of view, sol-gel glasses with composition containing up to 90 mol% SiO₂ can still be bioactive [82]. This can be explained considering the reduction in network connectivity because of the presence of hydroxyl groups along with the inherent glass nanoporosity. On the contrary, melt-derived glasses require <60 wt% of SiO₂ to maintain their bioactivity [58].

The composition of melt-derived glasses is more complex than that of sol-gel glasses as additional components are necessary to foster the processing of the material. For example, Na₂O is used to lower the melting point in melt-derived glass, improving its workability; while, it is not required in sol-gel glasses, due to the absence of melting. However, sol-gel glasses with a composition similar to that of 45S5 were produced [18].

Contra, melt-derive glasses are more suitable to produce scaffolds for hard tissue engineering because they have higher mechanical performances than sol-gel glasses [13].

2.6 Clinical Applications of Bioactive Glasses

The extraordinary versatility of bioactive glasses, which primarily depends on the flexibility of their composition, makes these biomaterials suitable for various clinical applications [83].

Since their discovery, BGs were principally used for the healing of bone defects deriving from trauma, tumour removal, and congenital disease [18].

In recent years, encouraging results were achieved regarding the neo-cartilage formation, and several studies showed the great potential of BGs in soft tissue repair applications [22].

In the most recent investigation, the potential of bioactive glasses for cancer therapy emerged.

2.6.1 Bone Repair and Orthopaedic Surgery

Classical applications of bioactive glasses include bioactive coatings on orthopedic implants, bone filling materials, small bone implants and dental applications [84].

Bioactive glass, since its discovery, has mainly been used for coating of metallic implant because the metal is bioinert, i.e. it is characterized by poor bonding ability to bone tissue, while the BG is a remarkable osteogenic agent. On the other hand, BG has poor mechanical properties leading to its limited application in load-bearing implants where metallic alloys are still the materials of choice. BG coating ensures primary stability through the formation of a bonding interface between the bioactive coating and the host tissue [13]. BG coating also have the function of protecting the metal from corrosion, and, in some cases, to prevent the release of potentially toxic metal ions [85]. Under these circumstances the degradation rate of BGs should be carefully controlled, since too high bioactivity could cause a too much fast dissolution of the coating, leading to a failure of the treatment [85]. The thermal expansion coefficient of the glass must match that of the metal to avoid the glass detaching from the metal during manufacturing [13].

The most important application of bioactive glass is the healing of bone defects, which may result from trauma, congenital defects or disease such as osteoporosis or tumour removal [18].

Bone is one of the most transplanted tissues, second only to blood [18]. In fact, 2.2 million bone grafts are used annually in orthopaedic operations worldwide [60]. An overview of bone grafts was provided in Chapter 1. However, bone grafts have several disadvantages which led to the development of synthetic bone substitutes, such as bioactive glass grafts.

45S5 Bioglass[®] was used in more than a million patients to repair bone defects in the jaw and in orthopedics [86].

Subsequently, also other bioactive glass compositions were used as bone substitutes in orthopedic field [87].

In addition, some bioactive glasses were clinically used as bone substitutes to restore bone loss from periodontal disease in infrabony defects. Other ones were used as bone substitutes in tooth extraction sites and alveolar ridge augmentation [87].

Moreover, bioactive glass blocks were successfully used as a bone graft expander, since they resist drilling and shaping, but they may fracture in the process [7].

Some BGs were clinically used as ossicular reconstruction prostheses, and endosseous ridge maintenance implants [87].

It is also worth remembering that the main commercial use of bioactive glass is in toothpaste. Bioactive glasses were also used in the polishing procedure to whiten teeth [88].

2.6.2 Chondrogenesis and Osteochondral Tissue Engineering

While the ability of BG to promote osteogenesis is well known, only recently it was found that the soluble products of BG degradation may also promote chondrogenesis which leads to the neocartilage formation [24].

Recent *in vitro* studies have shown that the silicate 13-93 bioactive glass ionic degradation products modulate chondrocyte biosynthesis, thus promoting neocartilage tissue formation [89]. These results show the potential benefits of BG on chondral tissue formation in engineered cartilage [89]. Tissue-engineered osteochondral grafts are thus considered as one of the most promising approaches for repairing full-thickness articular cartilage defects [90].

Recent *in vivo* study has shown promising outcomes as regards the use of 13-93 bioactive glass as a substrate for tissue engineered osteochondral grafts [91].

Despite the *in vivo* results of tissue-engineered osteochondral grafts were long investigated, the action of the subchondral support material on graft integration and cell survival is still unclear [91].

2.6.3 Soft Tissue Repair

Until 1981 it was believed that only calcified tissues would form a bond to bioactive materials [10]. Dr. June Wilson and his research team were the first to demonstrate that soft connective tissues could also form a bond to 45S5 Bioglass[®] if the interface was immobile. In particular, they emphasized the strong dependence existing between the nature of the established bond and compositional factors [10].

Referring to the phase diagram shown in Figure 3, it was found that only BGs with higher reactivity (class A) were able to form bonds with soft tissues whereas glasses characterized by a SiO₂ content within 52–60 wt% were able to form bonds only with calcified tissues [10].

In 1982, Bioglass[®] was used to reconstruct the ossicles chain of the middle ear exhibiting for the first time the *in vivo* bond between BGs and soft tissue [23]. Since then, new studies regarding BGs in soft tissue repair were conducted. Recent works have shown the BGs ability to promote angiogenesis, the healing of soft tissue wounds, and nerve regeneration [24].

Angiogenesis

Angiogenesis consists of the formation of new blood vessels from pre-existing ones under the action of mechanical and chemical stimuli such as growth factors, signal molecules and proteins of the extracellular matrix. This process is a crucial step in any tissue-engineering strategy, because new tissue requires appropriate oxygenation and the right amount of nutrients, which are indispensable to avoid tissue necrosis [92]. Although angiogenesis is indeed important in the context of bone regeneration as bone is a vascularized tissue, its role in some soft-tissue applications (e.g. wound healing) is even more fundamental.

The most common methods to stimulate angiogenesis include the delivery of growth factors, such as vascular endothelial growth factor (VEGF) and basic fibroblast growth factor (bFGF), gene therapy and cell-based therapy [93]. Nonetheless, growth factors are expensive, the release kinetics is unknown, and the reproducibility of the procedure is low [94].

An alternative approach may be represented by the ability of bioactive glass to induce angiogenesis [94]. The angiogenic effect of BG was first reported in 2004 by Day et al. [95]. Subsequent *in vitro* and *in vivo* studies have found that the dissolution products release from the bioactive glasses produce increased secretion of VEGF and VEGF gene expression in fibroblasts, the proliferation of endothelial cells and formation of endothelial tubules *in vitro*, as well as enhancement of vascularization *in vivo* [94]. Further investigations have shown that the bioactive glass dissolution products that most affect angiogenesis are boron, copper and cobalt [96], [97], [98].

Wound Healing

In case of large skin harm caused by injury, disease or nonhealing wounds, such as diabetic skin ulcers, particular care is required in order to concurrently repair damaged tissue, prevent infection, and remove excessive tissue exudates that might impede healing [92].

Clinical and animal studies have found that nanofibrous BG medications and ointments containing BG particles of various compositions respectively speed healing and enhance the quality of the forming tissue [92].

Although the exact mechanism of action of BGs in wound care is still unknown, it has been demonstrated that bioactive glasses activate the expression of genes involved in the healing processes such a VEGF and bFGF and vascular cell adhesion protein. Furthermore, BGs have shown to preserve endothelial cells and improve gap junction communication, which increases vascularization and as a result accelerates wound healing [99].

Silicate-based BGs meet the need to prevent wound infections because their dissolution products, such as silver, boron, copper, increase local pH causing an antibacterial effect [99].

Nerve Regeneration

Peripheral neuropathies deriving from serious injuries cannot always be treated by suturing, and even in circumstances where suturing is opportune, they may cause limited nerve function [100].

The gold standard, regarding the treatment of damaged nerves that have a gap larger than 4 mm, is the use of autografts. However, the limited availability and possible secondary effects showed the need for alternative way for nerve repair [100].

Flexible bioactive glass fibres were found to be suitable materials for this purpose. In view of this, Bunting et al. [101] developed a nerve regeneration scaffold by incorporating 45S5 Bioglass® fibres within silicone conduits and tested them in adult rats [101]. Further studies suggest that BG fibres are promising materials as regard nerve regeneration [102], [103], [104]. However, some aspects need to be improved, such as the material choice for the tubular conduit that accommodate these fibres, and the amount and composition of bioactive glass [84].

2.6.4 Cancer Therapy

Cancer remains leading cause of death globally, and its prevalence is continuously increasing over the world [105].

New scientific discoveries are changing this scenario, and new cancer treatment techniques are included in the clinical practice every day. Among these, mesoporous BGs, hyperthermia and brachytherapy show a great potential [106].

In this section, biocompatible glasses for cancer treatment are introduced. Mesoporous bioactive glasses are presented, highlighting the characteristics that make them excellent drug delivery systems. The main compositions of BGs used in hyperthermia are discussed concerning their magnetic and bioactive properties. Finally, several glasses with suitable radiological and biological properties for brachytherapy are described.

2.6.4.1 Mesoporous Bioactive Glasses for Targeted Tumour Therapy

A very promising approach to treat a cancer in a targeted manner is to introduce a local drug release system into the malignant tumour [107]. This treatment is very beneficial for patients due to high delivery efficiency, the continuity of the release and the reduced toxicity compared to systemic administration of chemotherapy drugs [108].

Mesoporous materials are particularly suitable for this purpose owing to their large surface area (600-1000 m²/g), high pore volume (0.6-1.0 mL/g), and narrow mesoporous structure, which allows adsorbing drug molecules and releasing them from the meso-structured matrices with a sustained profile [109].

Vallet-Regí et al. [110] were the first who develop a mesoporous bioactive glass that combines effective drug delivery and exceptional bioactivity (Figure 6) [110].

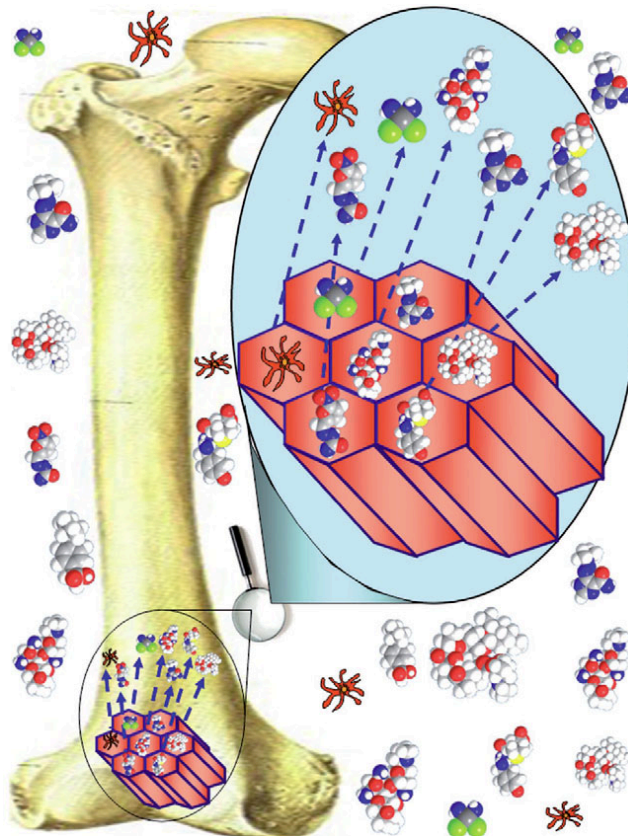


Figure 6: The concept of MBG for drug delivery and bone regeneration. Figure reproduce from Vallet-Regí [111].

In 2004, Yan et al. [112] produced highly ordered mesoporous BGs by using non-ionic block copolymers as structure-directing agents through an evaporation-induced self-assembly (EISA) process with superior *in vitro* bone-forming bioactivity [112].

In the following years, mesoporous BGs with different compositions and obtained by various manufacturing techniques, were studied as drug delivery systems.

Mesoporous BGs are characterized by regularly sized pores, in the range of 15–100 Å, which allow encapsulation of a variety of hydrophobic and hydrophilic antineoplastic agents, and by a high surface area, able to host targeting groups. These properties make mesoporous bioactive glass able to deliver therapeutic agents to the desired place [113].

Mesoporous bioactive glass morphologies considerably affect the loading and release of drugs and growth factors, which means that also the preparation methods along with the mesopore structures influence the drug delivery [114].

Table 4 summarizes the drug/growth factor category for the various shapes of mesoporous bioactive glass.

Table 4: The drug/growth factor category for mesoporous bioactive glass. Table reproduced from Wu et al. [114].

Mesoporous Bioactive Glass	Composition	Drug/Growth Factor	Loading Efficiency (%)	Burst Release (%) at Day 1	Delivery Time
Particles	58Si36Ca6P 80Si15Ca5P 80Si15Ca5P	Gentamicin Ibuprofen Ipriflavone	36-48 35 1-11	28-60 25-45, 90	> 10 days
Discs	100Si 90Si5Ca5P 80Si15Ca5P 70Si25Ca5P	Tetracycline Metoclopramide Phenanthrene	10-18 15-45 5.15	15-30 40-55 70	> 5 days
Spheres	100Si 85Si10Ca5P	Triclosan Ibuprofen Bovine serum albumin	9.1-10.7 20 4-16	30 100 2.5-25	> 14 days
Fibres	70Si25Ca5P	Gentamicin	5.5-14.4	60-80	> 4 days
Scaffolds	80Si15Ca5P 80Si15Ca5P 80Si15Ca5P 100Si	Gentamicin Dexamethasone VEGF BMP	11 16 90 -	70 20-50 0.2 -	> 7 days
Composites	80Si15Ca5P 80Si15Ca5P	Gentamicin/naproxen Dexamethasone	1.1 5.4	30-50 50	> 10 days

Since in some cases a constant release rate of the drug is required, while in other case it is preferred a burst release followed by sustained release [114], it is of paramount importance to adjust the mesopore structure according to the specific clinical case.

In order to demonstrate that mesoporous bioactive glasses are applicable in clinical practice for the diagnosis and treatment of cancer, loading efficiency and release kinetics were studied.

The loading efficiency of drug and growth factors in mesoporous BG is considerably higher than that in conventional BGs. The drug release kinetics in mesoporous BG is lower than that in conventional BGs [113].

Zhao et al. [115] have shown that as CaO content increase in in the mesoporous bioactive glass, the loading efficiency increases and the drug release rate and burst effect decrease [115].

This is probably due to the fact that the drugs may be chelated with calcium on the pore wall, thus making it complicated to be released [115].

Another probable reason is that mesoporous BG has greater apatite mineralization ability in biological solutions with respect to conventional mesoporous SiO₂ materials [115]. The apatite forming on the surface of MBG materials could enhance the drug-loading efficiency and decreasing the burst release and release rate [115].

In support of the fact that the CaO content in mesoporous bioactive glass influences the drug release, Zhao et al. [115] have proved that 58S MBG has slower release kinetics than 77S mesoporous bioactive glass [115].

Zhu et al. [116] have found that the dissolution of mesoporous BG affects drug release and the drug release from this material is mostly controlled by a Fickian diffusion mechanism [116].

Mesoporous BGs allow both the early detection of cancer cells and the delivery of the chemotherapeutic drugs to the tumour area [117].

Ideally, mesoporous BGs should restrain drug molecules for a long period of time as they circulate, extravasate into the cancer tissue, and release the drug in the tumour, causing the reduction or destruction of the tumour [117].

Despite the underlying mechanisms of cancer cell death caused by mesoporous bioactive glass-mediated drug delivery are not yet fully understood, it is believed that mesoporous bioactive glass will be a promising biomaterial for anticancer application in the future since its therapeutic efficacy is better than drugs alone. The combination of efficient drug delivery and inherent bioactivity of mesoporous bioactive glass will represent a valid option to treat cancer clinically [113].

2.6.4.2 Magnetic Bioactive Glasses for Hyperthermia Treatment

Magnetic bioactive glasses are accounted suitable materials for hyperthermia treatment of malignant tumours, in particular for deep-regional cancers such as bone cancer [113].

The potential of these materials lies in being able to support hyperthermic treatment and to augment the formation of new bone tissue at the same time [113].

After placing the magnetic biocompatible glass in the tumour region, an alternating magnetic field is applied, and the heat from glass raises the surrounding temperature (Figure 7) [106].

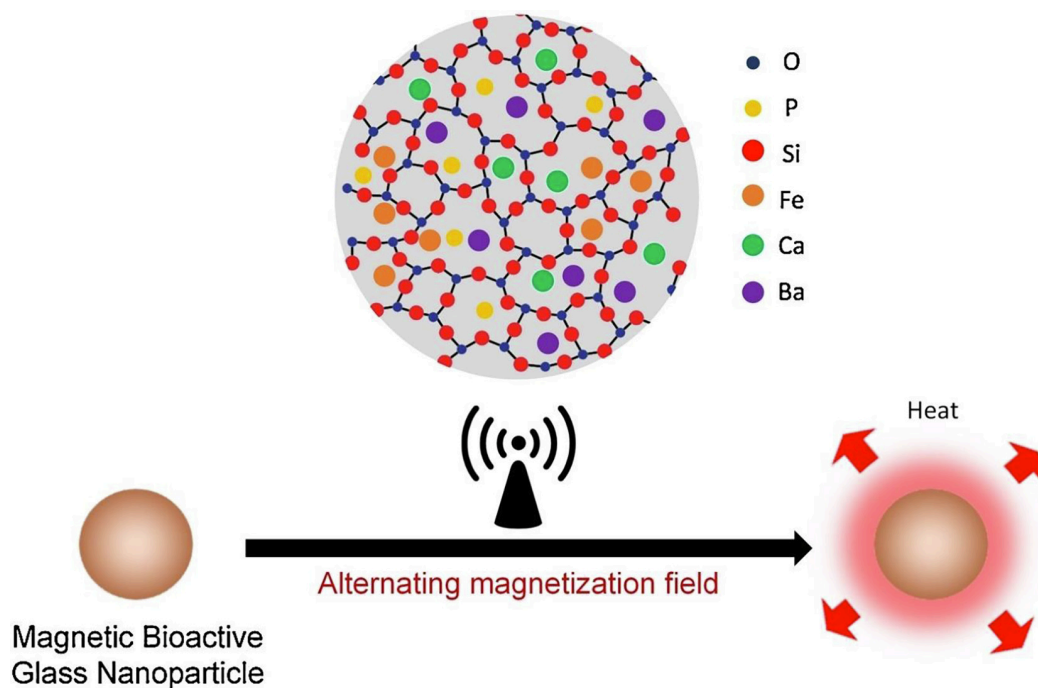


Figure 7: Schematic representation of magnetic BGs developed for hyperthermia cancer therapy. Figure reproduced from Yazdanpanah et al. [118].

Malignant cells are selectively killed when exposed to temperatures within 41–47 °C due to their intrinsic microenvironment comprising low pH, whereas healthy cells can survive at even higher temperatures. Tumours tend to be more intensively heated compared to surrounding healthy tissues because their vascular network, being poorly structured, cannot dissipate heat adequately [105].

After tumour shrinkage, the malignant cells can remain around the tumour site, causing tumour recurrence. These malignant cells can be destroyed to prevent tumour recurrence by re-heating the implanted material when necessary [119].

In order to make a magnetic BG, it is necessary to incorporate magnetic phases, e.g. magnetite (Fe_3O_4), in the glass network [106].

The magnetic phase of the magnetic biocompatible glasses can be obtained through heat treatment of the glass system for the crystallization of magnetic phases or by the incorporation of magnetic nanoparticles in the glass matrix [106].

The incorporation of magnetic nanoparticles is advantageous because their higher superficial contact area leads to a better magnetization than the magnetic phase crystallized by heat treatment. Besides it allows a better control of the magnetic phase morphology. However, since magnetic nanoparticles tend to aggregate, the uniform incorporation of these nanoparticles into the matrix is difficult to achieve [106].

Research in the field of magnetic biocompatible glasses started in 1991, when Kokubo et al. [120] produced glasses in the $\text{CaO-SiO}_2\text{-B}_2\text{O}_3\text{-P}_2\text{O}_5$ system doped with iron oxides II and III through melting-quenching method. From these glasses, by means of heat treatment, glass ceramics with the formation of β -wollastonite ($\text{CaO}\cdot\text{SiO}_2$) and magnetite (Fe_3O_4) were formed. These were the first biocompatible glasses with magnetic properties that could be used to cancer treatment by hyperthermia [120].

Since then, various studies investigated glasses on similar systems.

It has been shown that magnetic properties depend on the composition of the system. In particular, magnetization increases with the concentration of the magnetic phase. However, higher concentration of magnetic phase decreases the bioactivity of the biomaterial; hence combining the desired bioactivity with sufficient magnetization is one of the main challenges in magnetic biocompatible glasses development [106]

For the first time ever, Li et al. [121] prepared magnetic $\text{SiO}_2\text{-CaO-P}_2\text{O}_5$ mesoporous bioactive glass by introducing iron nitrate in the sol; as a result, MBG powders containing a homogeneous dispersion of Fe_3O_4 nanoparticles were made [121].

MBG scaffolds, obtained by adopting various methods, have the twofold function of enhancing osteogenic activity, due to bioactivity, and inducing hyperthermia, thanks to the magnetic phase [113].

Successively, magnetic bioactive formulations including 58S sol-gel glass and different amounts of melt-derived $\text{SiO}_2\text{-CaO-Fe}_2\text{O}_3$ glass-ceramics have been found able to induce *in vitro* effective hyperthermia on human osteosarcoma (Saos-2) cells with reduction in cell proliferation and viability [122].

In this context, using sol-gel bioactive glass rather than melt-derived is advantageous, as it shows higher bioactivity [122].

Recently, it was found that other elements besides Fe can confer magnetic properties to MBGs. Koohkan et al. [123] studied the bioactive and magnetic properties of $\text{SiO}_2\text{-CaO-P}_2\text{O}_5$ MBGs doped with Fe, Cu or co-doped with both, and have proved that adding Cu to the MBG composition causes a better entry of Fe_2O_3 into the glass structure and, thereby, a better formation of Fe_3O_4 after calcination and higher saturation magnetization [123].

These materials also showed other favourable characteristics due to the local release of Cu^{2+} ions, such as antibacterial action and incentive to angiogenesis, along with considerable biocompatibility with mesenchymal stem cells [123].

Polymer/magnetic bioactive glass composites, resulting in a magnetic drug delivery carrier, combining hyperthermia and the drug delivery, deserve a mention [113].

Jayalekshmi et al. [124] developed a system of chitosan-gelatine with magnetic BG nanoparticles as a suitable device for drug delivery and hyperthermia, obtained by a sol-gel route. The drug likely to be dispersed in the polymer matrix [124].

Current studies on the use of MBGs for hyperthermic treatment of bone cancer are limited to *in vitro* assays, but the results are hopeful and motivate further research in animal models [105].

The main aspects, that need to be considered in the future, are the right material dosage necessary to obtain a therapeutic effect *in vivo*, the duration and the parameters to apply for the clinical treatment (e.g., frequency and amplitude of the alternating magnetic field) [105].

2.6.4.3 Bioactive Glasses Applied in Brachytherapy

As already mentioned in Chapter 1, brachytherapy is a kind of radiotherapy for cancer treatment, which consists in placing the radiation source inside the tumour area in order to deliver a therapeutic dose β radiation emission into the cancerous tissue *in situ* without damaging the nearby healthy tissue [125].

Most commercialized seeds are composed of a metallic capsule containing Iodine-125 as a radioactive element [126]. However, as the metallic capsule is inert in biological environment, a second invasive surgery for removal is required. Moreover, ^{125}I has a long half-life (59.49 days) [127].

Yttrium-90 (^{90}Y) is an attractive alternative radioisotope for this purpose since it could be obtained by neutron activation of ^{89}Y which is abundant in nature, has a shorter half-life of 64.2 hours, and the emitted β radiation have an average range in soft tissue of only 2.5 mm [128], [129]. Thanks to this short-range radiation, the radiation reaching healthy tissues was minimized [128].

In Table 5, physical features of the most currently used β -emitting radionuclides are summarized.

Table 5: Characteristics of various β -emitting radionuclides. Table reproduced from Hadadi et al. [129].

Radionuclide	Half-life ($T_{1/2}$)	Maximum Energy (MeV)	Average Energy (MeV)	Abundance of Parent (%)	γ Emissions (keV)	Thermal Neutron Cross Section of Parent (b)
^{90}Y	64.0 hours	2.284 (100%)	0.934	100	Brems	1.28
^{90}Sr	29.1 years	0.546 (100%)	0.196	-	Brems	-
^{32}P	14.3 days	1.710 (100%)	0.695	100	Brems	0.172
^{186}Re	90.6 hours	1.076 (73%)	0.35	37.4	137 (8.65%)	112
^{188}Re	17.0 hours	2.119 (71.6%)	0.764	62.6	155 (14.9%)	76.4
^{153}Sm	46.7 hours	0.817 (21%)	0.228	26.75	103 (28.3%)	206
^{142}Pr	19.1 hours	2.159 (96.3%)	0.809	100	1580 (3.7%)	11.5
^{177}Lu	6.71 days	0.497 (78.6%)	0.133	2.59	208 (11%)	2090
^{166}Ho	26.8 hours	1.856 (51%)	0.667	100	80.6 (6.2%)	64.7

Radioactive microspheres can be delivered to a target organ either through the bloodstream or by direct injection in the tumour area [128].

In 1960s, polymer microspheres coated with radioactive ^{90}Y were used to treat liver cancers *in situ*. The radioactive microspheres were used to be injected into the hepatic artery. Shortly afterwards this application was suspended because the radionuclide ^{90}Y could not be confined [128].

In order to overcome these issues and consequently to increase the life expectancy of the patients, new materials were studied [130], [24].

Bioactive glasses are interesting materials for this application since they are characterized by high biocompatibility, controlled biodegradability, and by the ability to promote the growth of new healthy tissues at the same time or after the treatment with radionuclides [130], [24].

The idea is to incorporate radioactive seeds into the bioactive glass matrix for the use of brachytherapy in the medical application field [131].

There are two procedures to prepare a radioactive glass for *in vivo* use. The first method consists in mixing the radioactive substance with the batch material and process these materials. In this way the radioisotope become an integral part of the glass. The main disadvantage is that particular safety measures must be taken to manage radioactive materials during the processing [131].

The second way is to produce a glass using non-radioactive materials, and then, as the last step in the fabrication process, to make the glass radioactive by neutron activation. This method simplifies the processing of the glass, but limits the chemical composition of the glass, because oxide glass composed of Na, K, and Ca should be avoided as they could become radioactive by neutron activation [131].

Despite the great potential exhibited by glasses in radiotherapy, research is still at the very early stage of development. This is due to the fact that few research groups around the world have nuclear facilities to study biocompatible glasses containing radioisotopes. In fact, the main experimental procedure involved in the nuclear characterization of these materials, is the neutron activation, whose

principle of operation is shown in Figure 8. This procedure consists in using a nuclear reactor to generate neutrons and exposing the material containing the desired isotope to these neutrons. Radioisotopes and β and/or γ rays are obtained as reaction products [132].

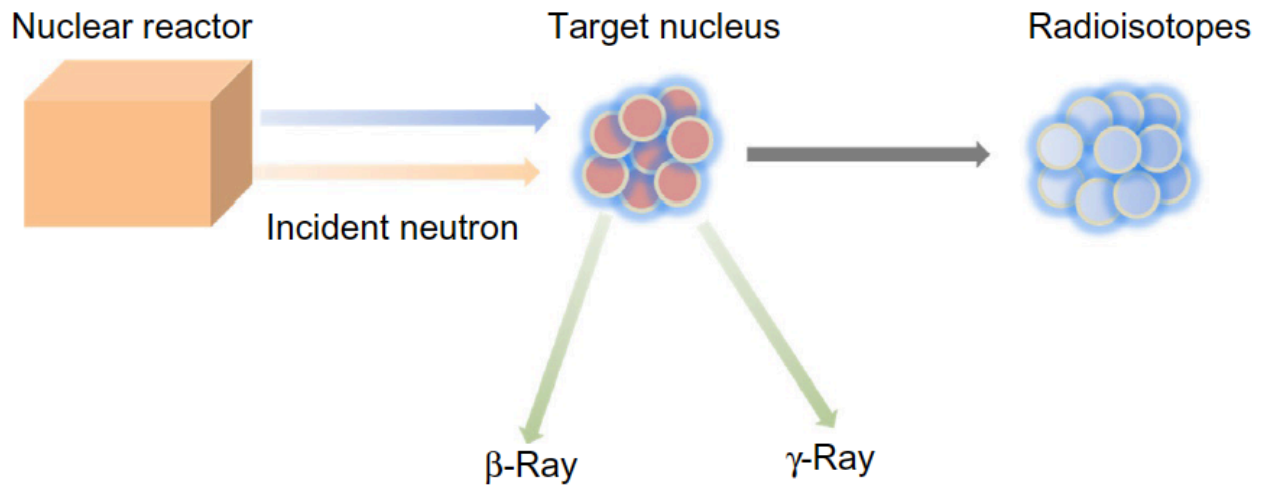


Figure 8: Schematic representation of nuclear reaction between a target nucleus and an incident neutron, leading to the formation of a radioisotope and the emission of β and/or γ rays. Figure reproduced from Borges et al. [106].

The concentration of the neutron-activable element in the glass must be high enough to grant the level of specific activity recommended for the chosen treatment and changes with the element being activated, the organ being treated, and the neutron flux and activation time [128].

In order to be used for the brachytherapy of cancers, bioactive glass must satisfy three requirements:

1. Biocompatibility [128].
2. Chemical durability of the glass matrix and resistance to body fluids to avoid radioisotope release in body [128].
3. Absence of other elements able to form undesired radioisotopes during the neutron activation process [128].

Since high bioactivity involves fast dissolution rates of all ions in a physiological environment, the quantity of radionuclides released from a highly bioactive composition might also exceed safe limits for brachytherapy treatments. For this reason, it is necessary to investigate the influence of radionuclides incorporation on bioactivity and degradation kinetics in physiological environment [130].

Cacaina et al. [133], [134] have demonstrated that BGs containing ~ 5 mol% yttria preserved their bioreactivity while releasing relatively small amounts of yttrium into simulated body fluid, which, in accordance with what was discussed above, are beneficial characteristics, thus proving the general suitability of BGs as yttrium vectors in brachytherapy [130], [133], [134].

In addition, they proposed that yttrium incorporation increases the durability of BG. Actually, this conclusion was reached by analysing the rate of dissolution of BGs containing significantly different silica molar fractions, where the yttrium influence would be outweighed by the heavy dependence of

the BG durability on silica molar fractions. Indeed, lower-silica BG compositions were found to release significantly higher amounts of yttrium and soluble silica in simulated body fluid [128].

Non Degradable Glasses

The need to use neutron activation and to have a glass with high chemical durability rejects the most common BGs because they form undesirable radioisotopes during neutron activation [128].

Thus, rare earth aluminosilicate (REAS) glasses are considered suitable for this application. They are composed of only three oxides: alumina (Al_2O_3), silica (SiO_2), and the neutron activatable rare earth oxide (RE_2O_3). During neutron activation, radioisotopes from aluminium (Al), silicon (Si) and oxygen (O) are also formed, but they decay very quickly, with no adverse consequence for the human body [131].

Regions that allow the formation of the glass for various families of REAS glasses which melt below 1600 °C are shown in Figure 9 [131].

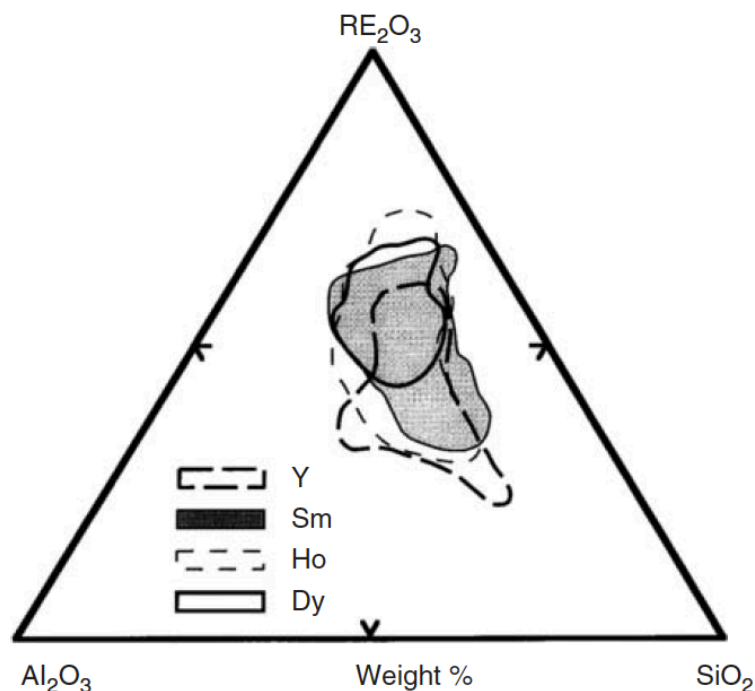


Figure 9: The compositional diagram shows the glass formation range for rare earth aluminosilicate (REAS) compositions that melt below 1600 °C. Yttrium, while not rigorously a RE, is comprised in the Figure because it has similar properties to those for the RE elements [131].

REAS glasses can contain from a low of 32 wt% to a high of 69 wt% of RE oxide. REAS glass properties depend on the RE elements, and the density of the REAS glasses increases with increasing RE_2O_3 concentration. These glasses are characterized by an exceptional chemical durability in the biological environment, that generally does not allow the loss or release of a radioisotope [131].

The most common shape of a glass radiation delivery vehicle is a microsphere ranging from 10 to 30 μm in diameter, although glass seeds or fibres are used too (Figure 10).

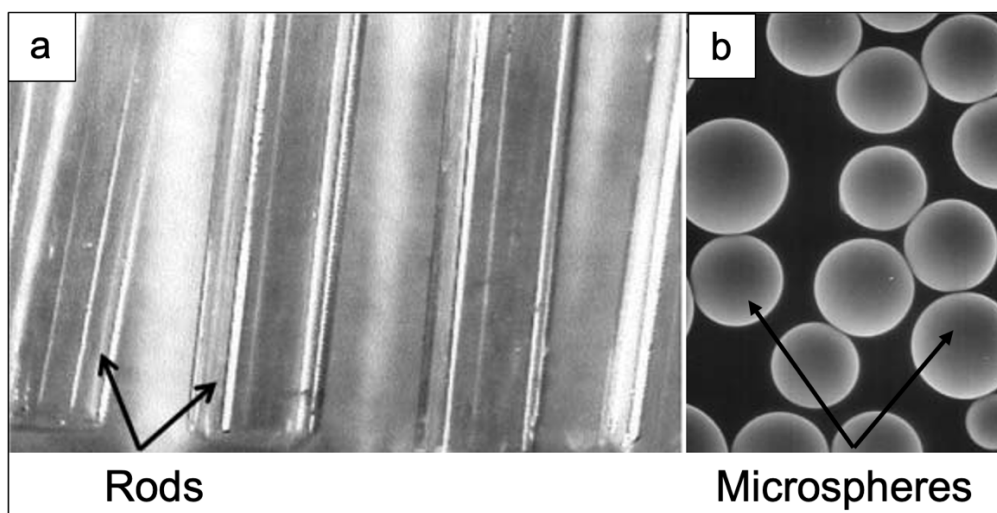


Figure 10: RE aluminosilicate glasses with different shapes: (a) rods and (b) microspheres, used in brachytherapy. The rods in (a) and the glass microspheres in (b) are composed of 46.8 wt% Sm_2O_3 , 18.2 wt% Al_2O_3 , and 35 wt% SiO_2 , and 55 wt% Y_2O_3 , 20 wt% Al_2O_3 , and 25 wt% SiO_2 , respectively. The rods in (a) have a diameter of 1 mm, and the white bar in (b) is 10 μm [131].

The use of microspheres is preferred both in intravenous administration and direct injection at the target site [131].

The surface of the glass microspheres, indeed, is smooth, their size is controlled, and can be tailor-made for a particular organ. In this way the microsphere can pass the capillary bed of the target organ, but they can't cross it entirely [131].

REAS microspheres incorporating beta-emitting ^{90}Y , ^{153}Sm , ^{165}Dy , ^{166}Ho , and $^{186}\text{Re}/^{188}\text{Re}$ were tested on animal models [131].

Two animal experiments show that *in situ* beta radiation from REAS glass carrying ^{166}Ho or ^{90}Y has a dual function, both preventing the tumour growth and reducing its size [131].

The effectiveness of *in situ* radiation depends on the tumour features, the range and energy of the radiation, the half-life and quantity of the radioisotope [131].

REAS glasses are prepared by using the most effecting beta-emitting radioisotope in order to treat a specific type of tumour or organ [131].

To date, only REAS glasses containing a single type of radioisotope were used for the *in situ* irradiation of a target organ. However, combining different neutron activatable radioisotopes into a single glass microsphere, could lead to some advantages regarding the optimization of the irradiation of tumours of different sizes and the delivery of the radiation dose over a period of time not obtainable with a single radioactive isotope. Another option is to mix two or more REAS glasses, each containing a distinct neutron activatable element, and the resulting delivered dose is a combination of radiation type, energy and half-life [131].

An example of REAS glasses are yttria-alumina-silica (YAS) glasses [128]. Since it was found that YAS glasses compositions (up to 55 wt% Y_2O_3) have an excellent chemical durability, glass microspheres of 25–35 μm were developed by flame spheroidization method [128], [130], [135].

In 1988, Day et al. [136] got the first patent regarding the ^{90}Y biocompatible glass microspheres, which enabled the development of a new treatment for liver cancer, combining radiation and embolization effects of the capillaries [136].

The ^{90}Y microspheres safely deliver a much larger dose of radiation to the tumour, and approximately 2–8 million glass microspheres, in a common injection, deposit in the capillaries, thus reducing the blood flow to the malignant tumour [128], [135].

Moreover, animal studies have shown that YAS glass with a nominal composition of $40\text{Y}_2\text{O}_3$ - $20\text{Al}_2\text{O}_3$ - 40SiO_2 wt% did not release detectable amount of ^{90}Y [135].

After FDA approval in 1999, ^{90}Y microspheres were marketed under the name TheraSphere® [128]. It is used commercially at over 200 sites worldwide to treat inoperable liver cancer [135]. Compared to other cancer treatments, TheraSphere® results in fewer side effects, causing flu-like symptoms such as fatigue, a slight fever, or abdominal pain for a few days in a few patients [135]. In addition, the survival rates of the patients are hopeful [128].

Biodegradable Glasses

The first biodegradable glass used as radioisotope vector dates back to 2003. It was developed by Campos et al. [132] in order to replace ^{125}I seeds used in prostate cancer treatment by brachytherapy. The underlying assumption was that a biodegradable glass would be better for brachytherapy, because the ^{125}I seeds are temporary, and a second surgery is necessary to remove them. For this reason, they developed glass based on SiO_2 - CaO system incorporated with samarium (Sm) [132]. The purpose was to obtain glasses incorporating ^{153}Sm radioisotope after neutron activation. ^{153}Sm was selected because it has a shorter half-life than ^{125}I (46.27 h and 54.9 days, respectively) and so proving its suitability for being coupled with a resorbable material with chemical durability lower than 7 months. However, in order to achieve the same activity as the ^{125}I seeds, it was necessary to incorporate a Sm concentration between 4.5 and 11.5 wt.% in the glass structure [132].

In 2008, Campos et al. [137] investigated the degradation of ^{153}Sm seeds implanted in a rabbit's liver, using X-ray radiography images to control the glass durability *in vivo*. After seven months, there was no evidence of glass in radiography images, because the seeds had been absorbed in the liver [137]. Furthermore, alkali borate (B_2O_3) and borosilicate glasses deserve to be mentioned. They degrade progressively in the body within hours or weeks once they are no longer radioactive [131]. An amazing feature of these glasses is that even though the glass is degrading in the body, the radioisotope of RE elements, reacting with the phosphate and other anions in the body fluids, forms an insoluble phosphate material, which contains the radioisotope to the target organ [138].

Borate glass microspheres incorporating beta-emitting ^{90}Y , ^{153}Sm , ^{165}Dy , ^{166}Ho , and $^{186}\text{Re}/^{188}\text{Re}$ were tested on animals [131]. However, these glasses are still not available for commercial use [131].

In addition, Campos et al. [139] investigated a bioactive glass structure containing Zr, Ba and Ho. The Zr and Ba allow a better view of the seeds by radiography once these elements are apt contrast agents. Ho was used because it emits higher energy than Sm, thus allowing to reduce the content of dopant in the BG structure, or to develop a device that emits higher energy for the treatment of small tumours in shorter time [139].

Chemical and nuclear characterization analysis have shown that ^{166}Ho radionuclides are homogeneously distributed in the seeds [139]. The biodegradation process is facilitated by neutron activation, which elicits deformation in the surface structure of the seeds [139].

Recently, Nogueira et al. [140] demonstrated that the Zr nuclide significantly increases the mass attenuation coefficient of the HoZr seeds. Thus, HoZr bioactive glass seeds offered a superior radiological response compared to that of Ho bioactive glass seeds, increasing the radiological contrast [140].

Another recent work developed by Sadeghi et al. [141] explains the interesting features of ^{153}Sm in prostate brachytherapy when inserted within a biodegradable glass structure. The scientists performed computational simulations, through Monte Carlo code, in order to analyse the dose rate in function of distance for a material doped with ^{153}Sm . ^{142}Pr beta emitter source was used as a benchmark to validate the simulation method accuracy and dose calculation. It was also inserted data about other materials based on ^{32}P and $^{90}\text{Sr}/^{90}\text{Y}$ beta emitter for comparative purposes. It is possible to conclude that beta doses using ^{153}Sm has a shorter distance effectiveness and a higher initial dose rate than the other ones. These data denote that ^{153}Sm would enable a less radiation effect on healthy tissues, reducing the side effects of radiotherapy, and also decreasing the treatment time due to the higher initial dose [141].

Hosseini et al. [142] performed similar Monte Carlo code simulations to evaluate the beta dose of ^{166}Ho -based biodegradable glass seed [142]

Khorshidi et al. [143] evaluated ^{188}Re -based biodegradable glasses seed with the same method [143]. These researchers used the same parameters as Sadeghi et al. [141], and they focused on hepatic cancer treatment. They concluded that both ^{166}Ho and ^{188}Re have a shorter dose distance, and a slightly higher initial dose, as presented in the Figure 11.

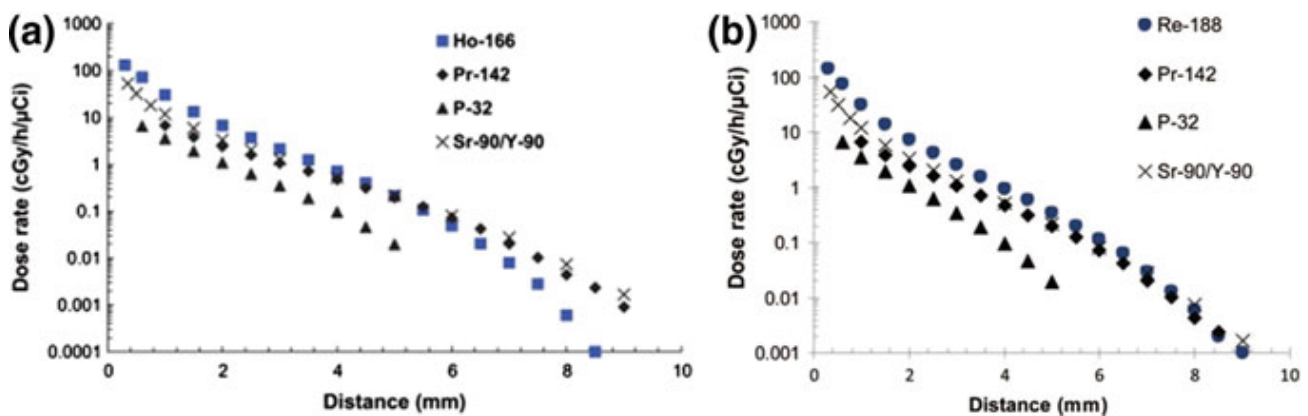


Figure 11: Comparison the dose rate in function of distance for different beta emitters. Figure adapted from Hosseini et al. [142], [143].

In 2011 Christie et al. [130] studied through molecular dynamics simulations how yttrium in the high-silica BG structure can influence the surface reactivity of the glass [130].

Their purpose was to encounter a highly bioactive glass which releases small amount of yttrium, in order to prevent the release of radionuclides into the bloodstream [130].

Their outcomes demonstrated that a low rate of yttrium leaching is related to high site-selectivity and clustering, which are believed to reduce the rate of yttrium transfer and release from the glass surface. At the same time, the limited network connectivity of the BG promotes the dissolution of the soluble species and enhances the glass network degradation [130].

For example, a satisfactory procedure may result from the incorporation of yttrium in some of the less bioactive, higher-silica compositions. Y_2O_3 incorporation causes network fragmentation, which could offset the strong union between the silica fragments in the presence of yttrium, resulting in a glass composition with suitable bioactivity [130].

Meanwhile, Christie et al. [144] evaluated the effect of incorporating higher yttria amounts in the glass. The results illustrated the possibility of obtaining BGs incorporating yttrium having enough biological activity to allow new tissues growth and which are able to deliver higher radiation doses through a higher yttria content [144].

2.6.5 Clinical Products based on Bioactive Glasses: a Historical Overview

It was calculated that, starting from FDA approval in 1985 up to 2016, Hench's original 45S5 Bioglass[®] was implanted in 1.5 millions of patients to repair bone and dental defects [88].

The first 45S5 Bioglass[®] implant approved for clinical use in the USA had the purpose of substituting the small bones of the middle ear in order to treat conductive hearing losses [145]. In fact, this bioactive glass, produced with melt derived synthesis, allowed sound conduction from the eardrum to the internal structures of the ear. After FDA approval in 1985, this device was marketed under the name of "Bioglass[®] Ossicular Reconstruction Prosthesis" or "Middle Ear Prosthesis" MEP[®] [146]. Although the short- and medium-term performance of this implant was good, in the long term the 45S5 Bioglass[®] was susceptible to dissolution and fragmentation [147]. For this reason, this device was taken off the market in 2000 [83].

45S5 Bioglass[®] was also used to hold cochlear implants to the temporal bone of totally deaf patients who suffered from irreversible damage to their cochlea. This device was commercialized as Bioglass[®]-EPI (Extracochlear Percutaneous Implant) about 30 years ago [148]. 45S5 Bioglass[®]-EPI was taken off the market because it degraded over time [149].

In 1988, Endosseous Ridge Maintenance Implant (ERMI[®]) was put on the market and still today, it is applied in periodontal surgery. This implant consists of a 45S5 Bioglass[®] cone that is inserted into fresh tooth extraction area, in order to replace tooth roots and give a constant support to dentures [150].

Subsequently, several clinical products for bone repair based on bioactive glasses were developed.

In particular, in 1993, 45S5 Bioglass[®] particulate, for repairing jawbone defects associated to periodontal diseases, was approved by the FDA, known under the trade name PerioGlas[®] [151].

It is also worth mentioning NovaBone[®] (NovaBone Products LLC), a particulate of 45S5 Bioglass[®] used to repair bone defects in maxillofacial or orthopedic non-load-bearing sites [151].

Besides 45S5 Bioglass[®], other FDA-approved or CE-marked BGs are available on the market [83].

Most of commercial BGs are characterized by a SiO₂-based composition, containing some additional modifiers which increase the bioactivity or confer other characteristics to the bioactive glass [83].

For example, a BG powder comprised of 70SiO₂-30CaO mol% and obtained by the sol-gel process, elicited a fast bone healing because of its inherent nanoporosity. This device is known by the trade name of TheraGlass[®] [83].

Furthermore, 45S5 Bioglass[®] was also commercialized as porous glass-ceramic sintered blocks [152]. In fact, the sinterability window of 45S5 Bioglass[®] is so tight that it cannot be sintered without suffering devitrification [20].

Recently, 45S5 Bioglass[®] was also used to make oral hygiene products [83].

In 2004 NovaMin[®], a 45S5 Bioglass[®] particulate was added to a toothpaste in order to treat dental hypersensitivity, which nowadays affects about one-third of world population [153], [154]. The aim of NovaMin[®] is to occlude dentinal tubules and remineralize the tooth surface, thus eliminating the cause of the disease [155]. This device was also employed for tooth whitening treatments [156].

Interest in bioactive glass increased since it was discovered that its ion dissolution products stimulate angiogenesis, which, as already said, plays an important role in wound healing and certain eye diseases. Currently, there are only two BG-based commercial products having a relevant angiogenic function [83].

One of this is trade-named as DermaFuse™/Mirragen™. It consists of BG nanofibers, whose composition is $53\text{B}_2\text{O}_3\text{--}6\text{Na}_2\text{O--}12\text{K}_2\text{O--}5\text{MgO--}20\text{CaO--}4\text{P}_2\text{O}_5$ wt%. They are aimed at accelerating wound healing by imitating the microstructure of a fibrin clot [157].

The other one is called “RediHeal”, and it is a bioactive glass which was doped with copper in order to enhance the angiogenetic function. It is currently available in veterinarian medicine, while FDA approval for clinical use in humans is pending [83].

In 2002, an orbital implant which was made of polyethylene coated with NovaBone® particles was approved by the FDA and, since then, it was marketed as Medpor®- Plus™ [83].

Other BG-based products to be applied in both wound healing and peripheral nerve regeneration are resorbable Ag-doped phosphate glasses combined either with a polymeric adhesive for wound care film dressing or with alginate for topical powders. Their trade name are respectively Antimicrobial Arglaes® film and Arglaes® powder. They control infections by constantly releasing silver, which is a strong antibacterial element [158].

Furthermore, a tube of resorbable glass composed of $\text{Na}_2\text{O--CaO--P}_2\text{O}_5$ glass, named Corglaes®, was tested for the repair of a divided facial nerve of sheep as an alternative to the end-to-end suturing [158].

Finally, biocompatible radioactive glasses for cancer treatment aroused great interest among researchers [159], [131]. As previously discussed, glass microspheres having ternary composition, $\text{Y}_2\text{O}_3\text{--Al}_2\text{O}_3\text{--SiO}_2$, were approved by the FDA in 1999 and were marketed under the name of TheraSphere®. They are clinically used for the treatment of hepatocellular carcinoma and metastatic liver cancer in many specialized centres in North America and Europe [83].

Figure 12 shows several examples of commercial products based on bioactive glasses.



Figure 12: Examples of BG-based products available on the market. Figure reproduced from Baino et al. [83].

2.7 Bioactive Glass Scaffolds for Bone Tissue Engineering

Tissue engineering (TE) has been defined as a technological field in biomedical practice since the mid-1980s, but its first official definition was provided only in 1993 as “an interdisciplinary field that applies the principles of engineering and life science toward the development of biological substitutes that restore, maintain or improve the tissue function” [160].

The key elements required for the implementation of TE and regenerative medicine approach are shortly described below, while the most commonly used procedure is shown in Figure 13 [161].

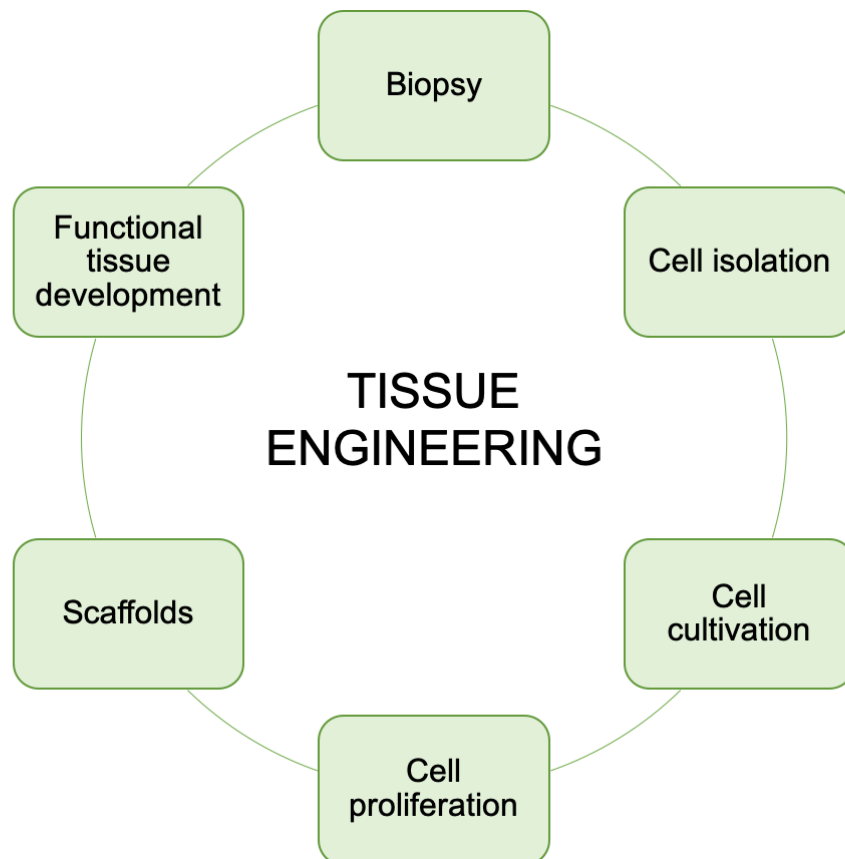


Figure 13: Schematization of a tissue engineering approach starting from the biopsy and concluding with the implant of the tissue substitute. Figure adapted from Fiume et al. [22].

- **Cells** are essential for the synthesis of new tissues [161].
Commonly, in order to avoid the risk rejection arising from immune response, autologous cells are used. They are collected from the site of interest by biopsy [161].
Another option is to use the stem cells, which are able to evolve to multiple cell lines by appropriate stimuli. Currently, multipotent stem cells are used, which are easily found in the human body. They are collected mainly from bone marrow or other tissues, such as the adipose one [161].
- **Scaffolds** are 3D porous structure which encourage cell attachment, differentiation and proliferation [162].
Both natural and synthetic scaffolds are currently available. Natural scaffolds derive from ECM extracted by the patient or by donors or are made of biopolymers. Synthetic scaffolds are made of materials carefully designed in order to mimic the features of physiological tissue [161].

- **Signals** can be biological, chemical or physical-mechanical. Specific stimulation procedures are able to affect cell pathways during the processes of proliferation and differentiation by fostering the evolution towards specific phenotypes. These signals are fundamental because they are able to guarantee cell survival and, therefore, it is required that all the cells in the scaffold are influenced by them likewise [161].

The main advantage offered by TE is the opportunity to avoid organ and tissue transplantation, which still today is a critical procedure due to problems of rejection and transmission of pathologies, along with difficult application caused by shortage of available organs and very long waiting lists for their receiving [163].

Since the late 1990s, a great potential has been attributed to the application of BGs in TE and regenerative medicine since they are materials suitable for producing functional 3D scaffolds for the regeneration of both hard and soft tissues [162].

In particular, BGs are biomaterials of choice for bone tissue engineering (BTE) scaffolds because of their ability to react very effectively with the physiological environment by forming a strong bonding interface comprised of a bone-like HA layer, inducing a stable fixation of the material to the host tissue [162].

A scaffold is a 3D device which owns specific physical, chemical and biological properties to promote cell infiltration, adhesion, colonization and differentiation until the formation of a mature and functional tissue [22].

In order to correctly design a scaffold, it is necessary to fully comprehend the biological processes and the features of the tissues, because the scaffold requires characteristics optimized according to the type of tissue that needs to be regenerated [22].

The main requirements of a scaffold necessary to stimulate bone tissue growth are:

1. **Biocompatibility and bioactivity:** the scaffold must not release toxic deliverables within the human body, and it must be able to stimulate the adhesion of the osteogenic cells that induce the formation of new bone tissue. After implantation, the scaffold must generate a negligible immune response in order to avoid it triggering such a serious inflammatory response that it might slow down the healing or induce rejection by the body [163]. In addition, as the scaffold degrades over time, the material used should own adapted bioactivity and dissolution kinetics comparable to the rate of tissue's recovery, so that cells can generate the new extracellular matrix by themselves, thereby regenerating the tissue as the scaffold degrades [24].
2. **Ability to form a bond with the living bone** without the formation of fibrous tissue at the interface [18].
3. **Porous and interconnected structure**, in order to simplify nutrient exchange and waste product expulsion, cell migration and adhesion, and the creation of a vascular network to permit tissue oxygenation [164]. The porosity of the scaffold should be greater than 90%, however the minimum porosity value admitted is 50 vol%, which allows satisfying minimum requirements for tissue ingrowth [162], [24]. Pore diameters should vary in the range 10-500 μm [162]. The ideal would be a bimodal distribution of the pore in order to mimic the trabecular bone as best as possible. In fact, pores below 50 μm stimulate the interaction between cells and materials and osteo-integration, while pore of 100-500 μm favourite new bone formation, bone ingrowth, and capillaries formation [162].
4. **Versality in shape and size** to totally fill bone defects [18].

5. Suitable degradation rate matching the time necessary for bone tissue regeneration and osteoclastic remodelling [18].
6. Preservation of mechanical properties during degradation, remodelling, and load sharing with the living tissue. Furthermore, a scaffold should have mechanical properties compatible with the anatomical site of interest [18].
7. Easy production that can be up-scalable for mass fabrication [18].
8. Sterilization and compliance with the rules for the use of biomedical devices [18].

Currently, an ideal scaffold for bone tissue regeneration does not exist [22].

For example, from a mechanical point of view, highly-performant materials are required to provide support during the whole healing process. On the one hand, stiff materials are the ones exhibiting the best mechanical performances, on the other, their high values of rigidity could cause tissue resorption because of the lack of loads transmission between the scaffold and the bone tissue [20].

As regard the elastic modulus of the scaffold, it should be comparable to that of the tissue to be replaced, in order to favour load transfer and minimize stress shielding, reducing the problems of bone resorption [165].

There is a linear correlation between porosity and elastic modulus of BG scaffold (Figure 14). In particular, the value of elastic modulus decrease as the scaffold porosity increases [166].

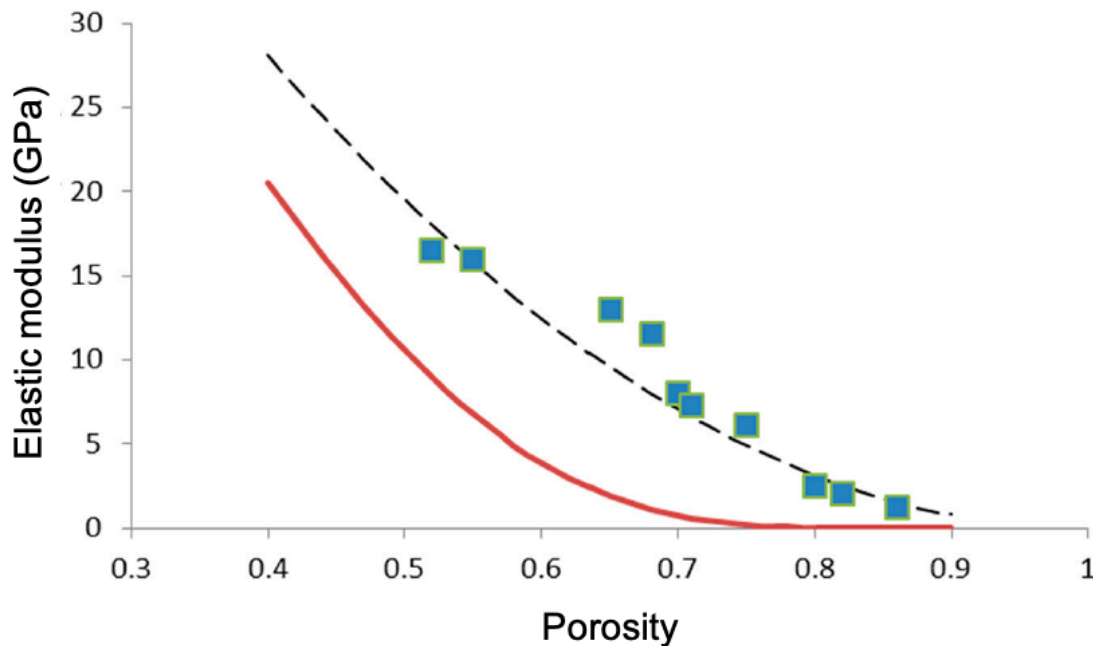


Figure 14: Porosity dependence of elastic modulus in 45S5 glass-derived foams with data interpolation by applying the Gibson–Ashby power-law model (dashed line) and the Pabst–Gregorova exponential relation (solid line). Figure reproduced from Baino et al. [166].

Despite these difficulties, several research groups were successful in producing glass scaffolds showing comparable mechanical properties to that of the human bone [167], as shown in Figure 15.

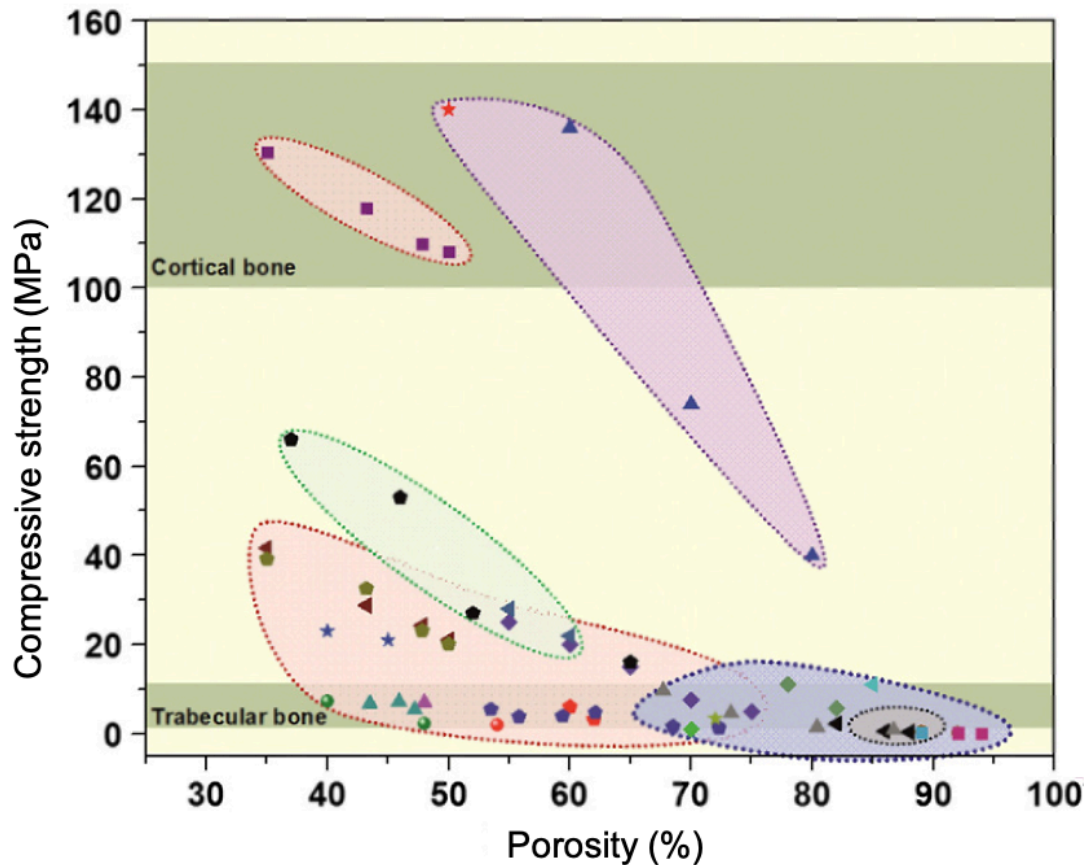


Figure 15: Porosity vs compressive strength of different glass scaffold compared with the human bone. Grey: sol-gel, pink: thermally bonding of particles, blue: polymer foam replication, green: freeze casting and purple: solid freeform fabrication. Figure adapted from Tomsia et al. [167].

In particular, scaffolds with high mechanical properties can be obtained by solid free form fabrication which allows controlling both pores orientation and dimension [167].

Scaffold porosity is a key parameter when designing a scaffold for tissue engineering application as it defines mass transportation properties, cell colonization and tissue ingrowth [162].

However, the porous structure of the scaffolds is often cause for a reduction in mechanical performances (Figure 15), thereby a balance should be found [162].

Mechanical properties could be improved by increasing the sintering temperature during heat treatment, which is an essential step to obtain the scaffold. In fact, the increase in temperature causes greater glass densification, which entails a reduction in porosity and consequently, an improvement in mechanical strength [162]. The drawback is that the use of a high temperature can lead to the formation of a crystalline phase in the material [162].

Scaffolds implanted in load-bearing bone defects are normally subjected to cyclic loading; thus, besides elastic modulus and strength, fracture toughness is also crucial [167].

Due to its low fracture toughness, glass is extremely sensitive to the presence of small defects ($\sim 10 \mu\text{m}$) and it can fail when subject to tensile or flexural stresses much lower than its compressive strength [167]. This criticality cannot be totally controlled, but it can be minimized through an optimization of the design and execution phase [162]. An alternative is the production of composite

scaffolds. In fact, the use of another material in addition to bioactive glass could improve the performance of the scaffolding despite the presence of small defects [162].

2.7.1 Fabrication Techniques

The first attempt to develop a bioactive glass-based scaffold was made in 2002 by Sepulveda et al. [168]. The manufacturing method was based on a sol-gel process combined with *in situ* foaming in order to obtain a macroporous structure [168].

Since then, many research groups had conducted several studies aimed at improving bone TE scaffolds properties, according to the critical requirements discussed above [29].

Here, a brief overview of scaffold fabrication techniques is provided, with a particular attention on methods, materials and processing parameters.

2.7.1.1 Foaming Methods

These techniques involve the use of a foaming agent in addition to bioactive glass which can be melt-derived or sol-gel [29].

Commonly, the foaming agent is added to the slurry or sol in order to create air bubbles which originate porosity [29].

Pores in the scaffolds can be produced by the following methods: direct injection of gases, vigorous agitation, gas generation through a chemical reaction, or thermal decomposition of peroxides [29].

Gel-Cast Foaming

This approach consists of mixing melt-derived glass powders into a solution of organic monomers. The resulting slurry is poured into a mould and the polymerization initiator and catalyst are added. Therefore, the polymerization reaction takes place in the mould [29].

The polymer gel is extracted from the mould maintaining the mould shape, and the solvent and the polymeric phase are removed [29].

The most suitable solvent is water, because it can be eliminated by drying [29].

Finally, the green body is thermally treated to remove the organic phase and sinter the structure [29]. In order to fabricate a porous scaffold, a foaming stage has to be introduced during the gelation step. The foam may be obtained by mechanical frothing or by gas injection. In both cases, a surfactant is required to stabilize the air bubbles [29].

The porosity of the scaffold can be adjusted by acting on the induction period, also known as idle time, which is the time that occurs between the addition of the polymerization initiator and the catalyst to the slurry and the polymerization beginning [29].

Wu et al. [169] fabricated gel-cast BG foams with a modal pore size of 379 μm and modal interconnect size of 141 μm , which are suitable value for BTE. They were characterized by a compressive strength close to the lower limit of spongy bone and the ability to form HA *in vitro* [169].

Sol-Gel Foaming

In order to develop the first bioactive glass scaffold, Sepulveda et al. [168] used the sol-gel foaming [168].

Hierarchically porous structure was obtained by adding a proper foaming agent during the sol-gel synthesis of the glass. Once all the reagents are completely dissolved within the sol, a surfactant and a gelation catalyst are added under vigorous agitation. When the gel reaches the right viscosity, it is poured into a mould [29]. Then the gel is subjected to aging and drying processes, to remove the liquid by-product and to calcination process to remove organic residuals and thus obtaining the final 3D scaffold (Figure 22a) [167].

Most of sol-gel bioactive glass foams are based on simple binary ($\text{SiO}_2\text{--CaO}$) or ternary compositions ($\text{SiO}_2\text{--CaO--P}_2\text{O}_5$) [170], [171].

The obtained scaffolds have a hierarchical pore architecture, consisting of interconnected macropores (10–500 μm) deriving from the foaming process, and mesopores (2–50 nm) that result from the sol-gel process. This hierarchical pore architecture is considered advantageous to stimulate the reaction of the scaffold to cells, because it imitates the hierarchical structure of natural tissues thus simulating the physiological environment [167].

Sol-gel derived scaffolds have usually a high surface area (100–200 m^2/g) due to the presence of mesopores. Consequently, interaction with the physiological environment are favoured, leading to a faster conversion to HA and better bioactive response [167].

The downside of these scaffolds is that they have low compression strength (0.3–2.3 MPa), and therefore they can substitute defects in low-load sites only [167].

H₂O₂ Foaming

This technique allows to obtain porous scaffold using peroxide solution. By heating the peroxide solution to 60 °C, water vapour and oxygen are released. They act as foaming agents producing bubbles and therefore pores in the structure [29].

Navarro et al. [172] mixed powders of phosphate glass with different amounts of H_2O_2 solution. The resulting slurry was poured into a mould, foamed at 60 °C, and subjected to drying and sintering. They found that the amount H_2O_2 is the principal factor affecting scaffold porosity. In particular, an increase in H_2O_2 content led to an increase in porosity, pore interconnectivity and pore size [172].

2.7.1.2 Thermal Consolidation of Particles

These methods consist in the mixing/incorporation of sacrificial particles/template in the green body that is commonly sintered [29].

Bioactive glass scaffolds with a large range of formulations were produced through these methods (Figure 22b) [167].

The main upsides of these techniques are the ease and non-need for complex machinery. While the main disadvantage is the difficult to achieve high levels of porosity and pore interconnectivity [167].

Scaffold Manufacturing without the Use of Porogen Particles

This method requires that no sacrificial components are added to the glass or ceramic particles used to fabricate the green body [29].

The porosity of the scaffold can be modified by varying the particle size and acting on the sintering process. Indeed, in order to fabricate a porous scaffold, the sintering process must be stopped as soon as enough sintering necks are formed between the particles to ensure suitable mechanical properties for the final scaffold [29].

This approach is very easy, but it allows to produce only scaffolds with low levels of porosity (usually < 50 vol%) [29].

For example, the scaffolds developed by Fu et al. [173] with 13-93 glass showed 40% porosity and high compressive strength (22MPa) [173].

Borate glass-based scaffolds obtained by Liang et al. [174] also had a porosity of less than 40%, thus confirming the limit of the technique of producing scaffolds with sufficient porosity [174].

Scaffold Manufacturing with the Use of Porogen Particles

A pore-forming agent can be added to the glass or ceramic particles before molding in order to increase the scaffold porosity and to better control the shape and size of the pores [29].

Pore-forming agents are generally polymers of natural (eg, starch, rice husk) or synthetic origin (eg, polyethylene particles) [29].

These agents must be eliminated before sintering because their presence can lead to the formation of black char (organic combustion residue) on the surface of the green body, hindering sintering and reducing the bioactivity of the material [29].

Starches of different plants were used as porogens by Vitale-Brovarone et al. [175] to produce scaffolds based on a 50SiO₂–25CaO–16Na₂O–9MgO (mol%) glass system. Corn starch grains due to their low dimensions resulted in scaffolds with too small pore size. While potato and rice starches allowed to obtain scaffolds with well interconnected pores between 50 and 100 µm and a compressive strength of 6 MPa, which falls in the range of that of spongy bone [175].

Wu et al. [176] used rice husk as a porogen agent to produce 45S5 Bioglass®-based scaffolds. The scaffolds were characterized by a lower porosity (43-49 vol%) than that of bone, while the compressive strength (5-7 MPa) was suitable for bone substitution [176].

Brovarone et al. [177] used polyethylene powders as organic filler for fabrication of melt-derived BG scaffolds. Varying the size and amount of polyethylene particles, a total porosity from 50% to 70% was obtained with well interconnected pores within 100-200 µm or above 200 µm. By using small amounts and sizes of polyethylene particles a maximum compressive strength of 6 MPa was obtained. In addition, these scaffolds exhibited micropores < 10 µm due to the presence of β-wollastonite crystals [177].

2.7.1.3 Freeze-Drying

These techniques take advantage of the formation of ice crystals to create the porous structure of the scaffold [29].

Freeze-Casting of Suspensions

This approach consists of pouring a colloidal suspension of glass particles into a mould and quickly freezing it. Oriented and elongated ice crystals are formed because usually the cooling rate is not homogeneous in all directions [29].

The frozen solvent is removed by sublimation in vacuum conditions at slightly cold temperature (around $-20\text{ }^{\circ}\text{C}$). This step is very critical because if the solvent is removed uncontrollably, the porous structure of the scaffold could be destroyed [29].

After complete removal of the solvent, the scaffold is thermally treated in order to sinter the inorganic particles [29].

The scaffolds obtained with this technique have a rather high compressive strength due to the oriented microstructure of the pores [29].

However, the use of water as the only solvent does not allow obtaining scaffold with appropriate pore dimensions for bone tissue engineering applications, because the range of pore sizes that can be obtained is $10\text{--}40\text{ }\mu\text{m}$, which is too low compared to spongy bone (well above $100\text{ }\mu\text{m}$) [29].

The addition of other solvents such as 1,4-dioxane or camphene in the solution allows a larger pore size to be obtained [29]. In fact, these solvents cause a change in the microstructure from lamellar to columnar, and an increase in the pore size [167].

Bioactive glass (13-93) scaffolds with columnar microstructures and pore diameters of $100\text{--}150\text{ }\mu\text{m}$ were produced by Fu et al. [178] (Figure 22c, d). They were characterized by high mechanical strength, the skill to promote cell proliferation and differentiation *in vitro*, as well as tissue infiltration *in vivo* [178].

Ice-Segregation-Induced Self-Assembly Combined with The Sol-Gel Method

This technique consists of immersing the sol in liquid nitrogen at a controlled rate. This involves the rapid freezing of the sol and then the sublimation of the frozen solvent [29].

The resulting microstructure can be controlled by adjusting the following parameters: the nature and concentration of the solute, the solvent composition, the cooling rate and the temperature gradient [29].

Minaberry and Jobbagy [179] fabricated a porous scaffold by this technique using a bioactive sol-gel-derived glass. At the end the process, the green body was subjected to annealing in order to remove residuals such as organic phases, acid and salts and to consolidate the structure. This structure showed pores $\leq 20\text{ }\mu\text{m}$ and low compressive strength ($<0.2\text{ MPa}$), thus suggesting the non-suitability of this scaffold for BTE approaches [179].

2.7.1.4 Foam Replica Method

The foam replica method was first used a long time ago to create macroporous ceramics, while more recently it was adopted to produce porous glass scaffolds [167].

In particular, scaffolds of silicate, borosilicate, and borate bioactive glass were obtained [167].

This technique allows fabricating highly porous glass scaffolds with open and interconnected porosity in the range $40\text{--}95\%$. The scaffold microstructure is similar to that of dry human trabecular bone (Figure 22e) [167].

Anyway, these scaffolds possess a low strength, usually in the lower range of that of trabecular bone, which limits its application to the repair of low-load bone areas [167].

In Chapter 3 the polymer foam replica method will be described with particular attention to the process parameters. In addition, the main features and the mechanical properties of the scaffolds obtained by this method will be discussed.

2.7.1.5 Solid Freeform Fabrication

Solid Free Form (SFF) techniques allow the fabrication of a design-controlled scaffold manufacturing process [22].

The final 3D structure is adjusted by changing the processing parameters [22].

SFF techniques rely on layer-wise manufacturing technologies, since the final 3D scaffold is obtained by subsequent deposition of material following a bottom-up process [22].

This technique allows the creation of customized devices through the precise virtual reconstruction of the bone defect, obtained from clinical images acquired by CT and MRI [22].

The technique generally involves four steps:

1. creation of a computer-generated model of the desired geometry by the use of a computer-aided design (CAD) software;
2. segmentation of the model into cross-sections;
3. implementation of the data;
4. creation of the physical model [180].

SFF techniques include both direct SFF and indirect SFF [22].

Direct SFF consists in the direct production of the scaffold from the biomaterial [22].

In indirect SFF, the biomaterial is cast into moulds that are later removed through the use of an opportune solvent [22].

Direct SFF techniques are highly reproducible because of the intrinsic automation of the process, even if they are very difficult to implement due to the compatibility required between apparatus and biomaterials; when glass slurries are printed to create a layer-wise scaffold, a typical problem is the risk of nozzle occlusion in the printing head [22].

The most common SFF techniques are selective laser sintering (SLS), stereolithography (SL), fused deposition modelling (FDM), ink-jet printing, three-dimensional printing (3DP) and robocasting (Figure 22f) [167].

Selective Laser Sintering

SLS employs a CO₂ laser or a Nd: YAG to selectively sinter successive layers of powder materials, thus creating a 3D object [181], [182].

As shown in Figure 16, the set up consist of the laser, the scanner system and two different chambers. One of the two chambers is intended for the preparation of the powder feedstock. A roller transfers the powders from one chamber to another and as soon as it finishes preparing the layer, the laser beam sinters the powders. Subsequently, the roller creates another layer and so on [181], [182].

During manufacturing process, the structure is surrounded and supported by non-sintered powders. Once the structure is completed, it is extracted from the powders [181].

A material is suitable to be processed by SLS if it absorbs light in the laser wavelength range and if it is formed by flowable powders to form the bed correctly. Ideally, the particles should be between 10 and 150 μm in size [29].

The porosity of SLS-produced scaffolds can be controlled by adjusting the SLS process parameters such as laser energy density, scanning speed, and the hatching distance, which is the distance between two lines scanned by the laser [181], [29].

In 2012 Liu et al. [183] produced the first Bioglass[®] scaffold via SLS. They optimized the laser power to obtain a good sintering and densification and as a result good mechanical property. Indeed, they found that if too high a laser power is used, the material melts and starts flowing through the layers below creating holes and voids in the glass layer [183].

Although SLS was developed as a direct technique, it was also used as an indirect method in order to reduce the laser power and to achieve better dimensional accuracy [29].

In indirect SLS, a binder is added to the powders; then, the laser melts the binder, which holds together the glass particles [29]. After SLS, debinding and sintering processes are necessary to remove the binder and to sinter the glass, respectively [182].

For example, Kolan et al. [184] produced 13-93 glass scaffolds by indirect SLS using stearic acid as a binder. The surface roughness and the presence of micropores due to SLS increased the surface area of the scaffold improving bioactivity and cell attachment and proliferation. In addition, these scaffolds were characterized by a compressive strength comparable to that of spongy bone [184].

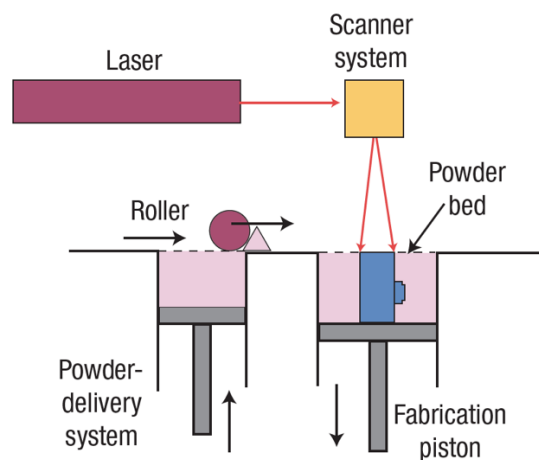


Figure 16: Schematic diagram of SLS. Figure reproduced by Hollister [185].

Stereolithography

SL is based on spatially controlled solidification of liquid-based resins by photopolymerization to produce a 3D structure [186].

Ultraviolet (UV) light is irradiated on the photosensitive resin surface in a precise pattern, which is defined by CAD files [186].

Free radicals and other reactive species, which are formed upon excitation of photoinitiator molecules by UV light, cause resin polymerization and formation of a material solid phase [186].

A build platform is used to provide support for structure during the manufacturing process. Therefore, the first layer of photopolymerized polymer is adhered to this platform and, once it is polymerized,

the platform is moved a defined distance for polymerization of the subsequent layer [186]. This procedure is repeated until the 3D structure is obtained [186].

Figure 17 shows this system.

For the application of SL in glass or ceramic production, it is necessary to combine the liquid photopolymer with glass or ceramic particles. Once the 3D structure is obtained, an heat treatment is necessary to eliminate the organic component and achieve greater densification [187].

In 2012 SL was applied for the first time for the production of Bioglass® based scaffolds. These scaffolds were characterized by arbitrary porosity and pore sizes of about 500 μm , which is similar to the pore sizes in spongy bone [188]. Therefore, this technique represents an innovative method to fabricate scaffolds for BTE applications.

Subsequently, also dense structures of bioactive glass and glass ceramic were fabricated by SL [189].

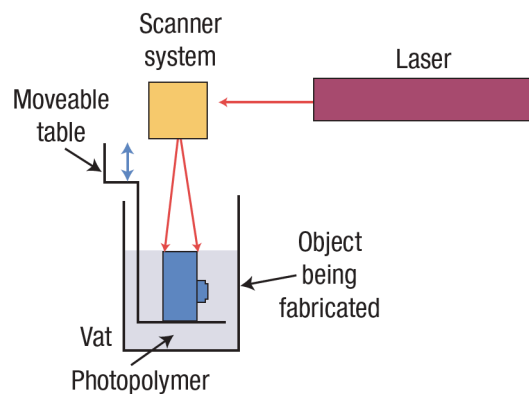


Figure 17: Schematic diagram of SL. Figure reproduced by Hollister [185].

Fused Deposition Modelling

FDM employs the melt extrusion process to deposit a parallel series of material fibres, thus forming a material layer [181].

A heated liquefier head melts the filament material (generally thermoplastics), which is extruded by a nozzle with a small orifice [181]. The first extruded filament adheres to the support platform and solidifies as it cools. Subsequently, the support platform is lowered a distance equal to the thickness of the new layer. The extrusion and lowering process is repeated until the structure is completed [190].

Figure 18 shows this system.

This technique allows to obtain scaffolds with highly uniform internal honeycomb-like structures, controllable pore morphology and complete pore interconnectivity by modifying the material deposition direction for consecutively layers and the space between the material fibres [181].

FDM allows to develop also scaffolds with overhanging features by depositing removable supporting structures alongside the scaffold [181].

In order to apply FDM in ceramic fabrication, filaments composed of ceramic particles and binder thermoplastic polymers should be prepared. After obtaining the green body by FDM, debinding and sintering processes are necessary to get the ceramic sample [190].

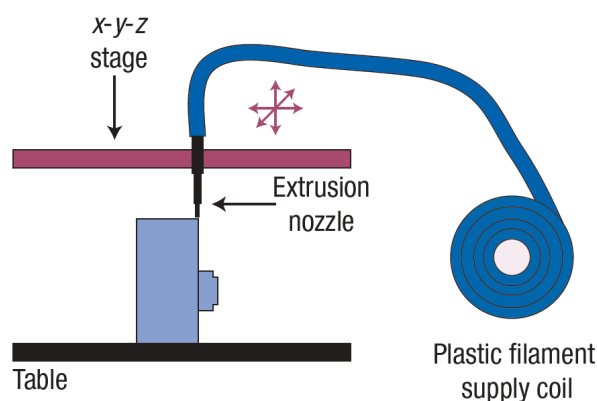


Figure 18: Schematic diagram of FDM. Figure reproduced by Hollister [185].

Ink-Jet Printing

Ink-jet printing employs micrometre-sized printhead nozzles to dispense liquid-phase materials in a controlled manner. The liquid-phase material, also known as ink, is dispensed in form of droplets onto a surface. The ink dries by creating a thin layer of the ink residue. Subsequently, other layers are placed on top of the previous ones in order to form a multilayer 3D structure [187].

The ink-jet printing technique can use two different ink delivery methods: continuous inkjet (CIJ) or drop-on-demand (DOD) printing, as shown in Figure 19.

In the CIJ method, a drops stream is dispensed by a controllable micronozzle. Afterwards, an electrostatic field influences the formed droplets and deviates their trajectories to print on a surface or allows them to reach the collector for reuse. Just a few drops are printed on a substrate and the largest number of drops is recycled. Therefore, CIJ is a non-economical material process [187].

The DOD method is more economical than CIJ method because it produces ink droplets when and where is required. In addition, it is more suitable for printing 3D structures due to the small size of droplets and the high positioning accuracy. In DOD method the ink droplets can be formed by piezoelectric effect or thermal excitation in the printing nozzle head [187].

Ink-jet printing can be used to print a wide range of materials. To date, this technique was used to produce scaffolds based on natural and synthetic polymers as well as on calcium phosphates [191]. Hard ceramics cannot be processed in a molten state because of their high melting temperature; therefore, in order to obtain an adequate ink a binder is added to them. In this case, once the 3D structure is fabricated, a thermal treatment is necessary to eliminate the binder and sinter the ceramic material [192].

Ink-jet printing allows multiple nozzles to be used simultaneously to speed up the printing process for each layer and to obtain composite structures by using different inks [192].

There is no publication about inkjet printing of bioactive glasses so far [182]. While, silica-based sol-gel-derived materials were inkjet-printed for biosensor applications [193].

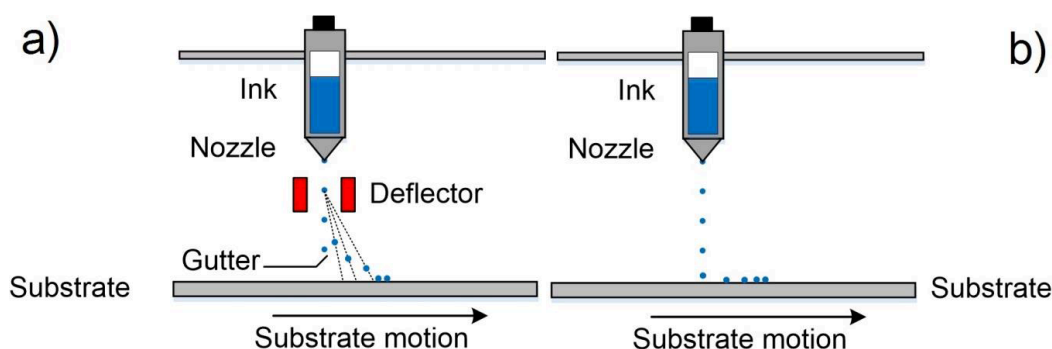


Figure 19: Schematic diagrams of printing methods used in ink-jet printing; (a) continuous inkjet and (b) drop-on-demand. Figure reproduced from Solis Pinargote [187].

Three-Dimensional Printing

The 3DP technique has a set up similar to that of the SLS (Figure 20). In fact, there is a first chamber where a powder bed is created, and a printing chamber where the actual printing process takes place. The powders are transferred from one room to another by a set of rollers [29].

3DP technique incorporates ink-jet printing technology for processing powder materials [194], [181]. As common ink-jet printer, it allows to use two different ink delivery: CIJ or DOD [29].

A binder is ejected by a jet head, which moves in accordance with the object's profile generated by the system computer, onto thin layers of powder [194], [181]. The binder dissolves and joins adjacent powder particles. The piston chamber is lowered and filled with another layer of powder and the process repeated [194]. After several process cycles, the complete structure of the desired object is created [181]. The completed object is incorporated inside unbound powders and is extracted by brushing away the powders [181].

Before starting printing, the parameters of the powder bed and ink delivery system should be optimized in order to achieve good final scaffold. The powders must have a good packaging capacity and sufficient flowability to be transferred from the feed bed to the printing one. These aspects depend primarily on particle shape, size, size distribution and roughness. Other important parameters are the wettability of the powders and ink droplets [29].

3D-printed ceramic and glass structures must be heat treated after the moulding process. The heat treatment comprises two phases: the debinding and the sintering phase [182]. Crystalline phase(s) may form during the sintering process [29].

HA, several kinds of calcium phosphates, 45S5 Bioglass®, 13-93 glass and MBGs were used to produce 3D-printed scaffolds. All of them exhibited low porosity (<50 vol%) and a compressive strength up 70 MPa, thus proving to be suitable for load-bearing applications [182].

Recently, Mancuso et al. [195] produced porous silicate glass-ceramic scaffolds by 3DP having mechanical properties comparable to cortical bone and dimensions of several centimetres [195].

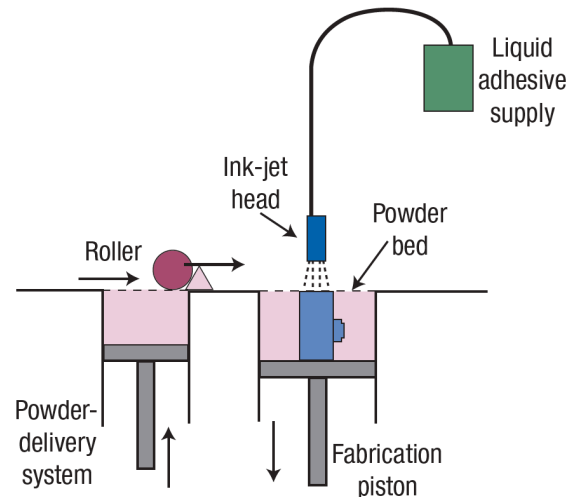


Figure 20: Schematic diagram of 3DP. Figure reproduced by Hollister [185].

Robocasting

Robocasting is an extrusion-based technique. A moving controlled nozzle extrudes the ink in order to form a bidimensional pattern [187]. Once a layer is printed, the support platform is lowered of the same distance of the new-layer thickness. A new layer is extruded on the top of the previous one. Therefore, through a layer by layer procedure, the 3D structure is formed [187].

Figure 21 shows this system.

The ink is a colloidal slurry composed of glass or ceramic particles and a binder [29].

In order to be used for robocasting, the ink should:

1. Be pseudoplastic. Indeed, it should flow through the nozzle by applying a small pressure [29].
2. Setup into a nonflowable mass. It should preserve the rod-like shape once extruded on the support platform [29].
3. Be strong enough to bear the weight of the overlying layers without deformation [29].

Extrusion can occur directly in the air or in a nonwetting oil bath [29].

Extrusion in air can cause uneven shrinkage due to several air flows in the structure. In addition, the feed rate must be coordinated with the drying kinetics to obtain sufficiently resistant layers [29].

These problems are overcome by extrusion in an oil bath. This approach prevents drying of the structure at first. Then the sample is extracted and is dried in a controlled environment. In addition, this type of extrusion prevents clogging of the nozzle [29].

In robocasting, the ink can be delivered in two different ways:

1. Constant displacement: the ink is extruded at a constant flow rate by moving in a mechanical way the cartridge plunger through changing the pressure as needed [196].
2. Constant pressure: pressurized air, which is maintained at a constant pressure, moves the plunger [196].

In addition to the intrinsic properties of the ink, other factors influence the final structure. For example, the nozzle diameter along with the air pressure and printing speed determine the final diameter of the extruded rod. The space between the various layers is crucial to achieve good adhesion between the layers and good mechanical properties. The initial substrate has to be plane, should allow the ink attachment and the easily detachment of the final scaffold [29].

Glasses or ceramics were extensively used to fabricate scaffolds by robocasting for BTE. Debinding and sintering post-process are necessary to produce a glass or ceramic scaffolds without organic components [187].

Robocasting was first used for fabrication scaffolds of bioceramic by Franco et al. [197] in 2010. They used an ink containing calcium phosphates (HA and β -TCP) and Pluronic as a binder [197].

Also Fu et al. [198] used Pluronic to fabricate the first bioactive glass (13-93)-based robocast scaffold. Pluronic F-127 is one of the most frequently used binders for robocasting in BTE, along with ethyl cellulose/PE glycol and carboxymethyl cellulose [29].

Eqtesadi et al. [199] produced 45S5 Bioglass[®] scaffolds by robocasting using carboxymethyl cellulose as binder. All the scaffolds, including those sintered at temperatures below T_x , exhibited interconnected porosities ranging from 60 to 80% and compressive strength comparable to that of spongy bone. Therefore, robocasting is the first technique that allows to obtain vitreous 45S5 Bioglass[®] scaffolds with suitable mechanical properties for practical applications [199].

Recently, robocasting was successfully used to produce hierarchical scaffolds based on MBGs. Wu et al. [200] robocast $\text{SiO}_2\text{--CaO--P}_2\text{O}_5$ MBG powders using poly(vinyl alcohol) as a binder. They obtained macromesoporous scaffolds characterized by a compressive strength of 16 MPa and a great mineralization capacity and sustained drug release property [200].

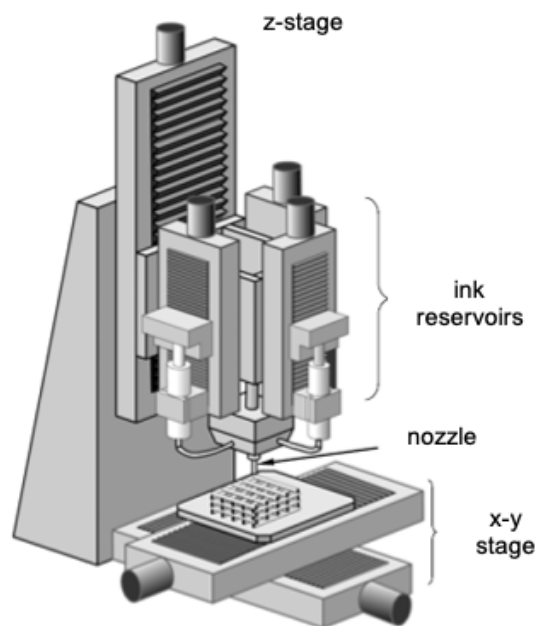


Figure 21: Schematic representation of robocasting. Figure adapted from Smay [201].

Table 6 summarizes the main characteristics of currently available SFF techniques.

Table 6: Capabilities and limitations of SFF techniques.

Technique	Achievable pore size (μm)	Advantages	Limitations	Ref.
SLS	45-100	High porosity. High surface area to volume ratio. Complete pore interconnectivity. Macro shape control. Independent control of porosity and pore size. Wide range of materials. Solvent Free.	High processing temperature. Limited to small pore sizes.	[181]
SL	≥ 70	Control over the internal and external geometry of the structure. Well-defined pore sizes, pore geometries, and porosities. Good compressive strengths. High resolution. Wide range of materials.	Limited number of resins commercially available.	[186], [202]
FDM	250-1000	High porosity. High surface area to volume ratio. Complete pore interconnectivity. Macro shape control. Independent control of porosity and pore size. Good compressive strengths. Solvent free.	High processing temperatures. Limited material range. Inconsistent pore opening in x-, y and z-directions. Pore occlusion at boundaries. Requires support structures for irregular shapes.	[181]
Ink-jet printing	Customer-based	High resolution. Good surface finish. Good mechanical properties. Controllable porosity and pore geometry. Can integrate with cells and growth factors.	Limited to the production of miniaturized structures. Limited material range. Use of solvent. High cost.	[187], [203]
3DP	45-100	Easy process. High porosity. High surface area to volume ratio. Complete pore interconnectivity. Macro shape control. Independent control of porosity and pore size. Suitable for many kinds of materials.	Use of toxic organic solvents. Lack of mechanical strength. Limited to small pore sizes.	[181], [202]
Robocasting	300-500	Simple, flexible, and inexpensive approach. Suitable for many kinds of materials. Low cost. Fast.	Need for an ink with appropriate rheological properties.	[187], [204]

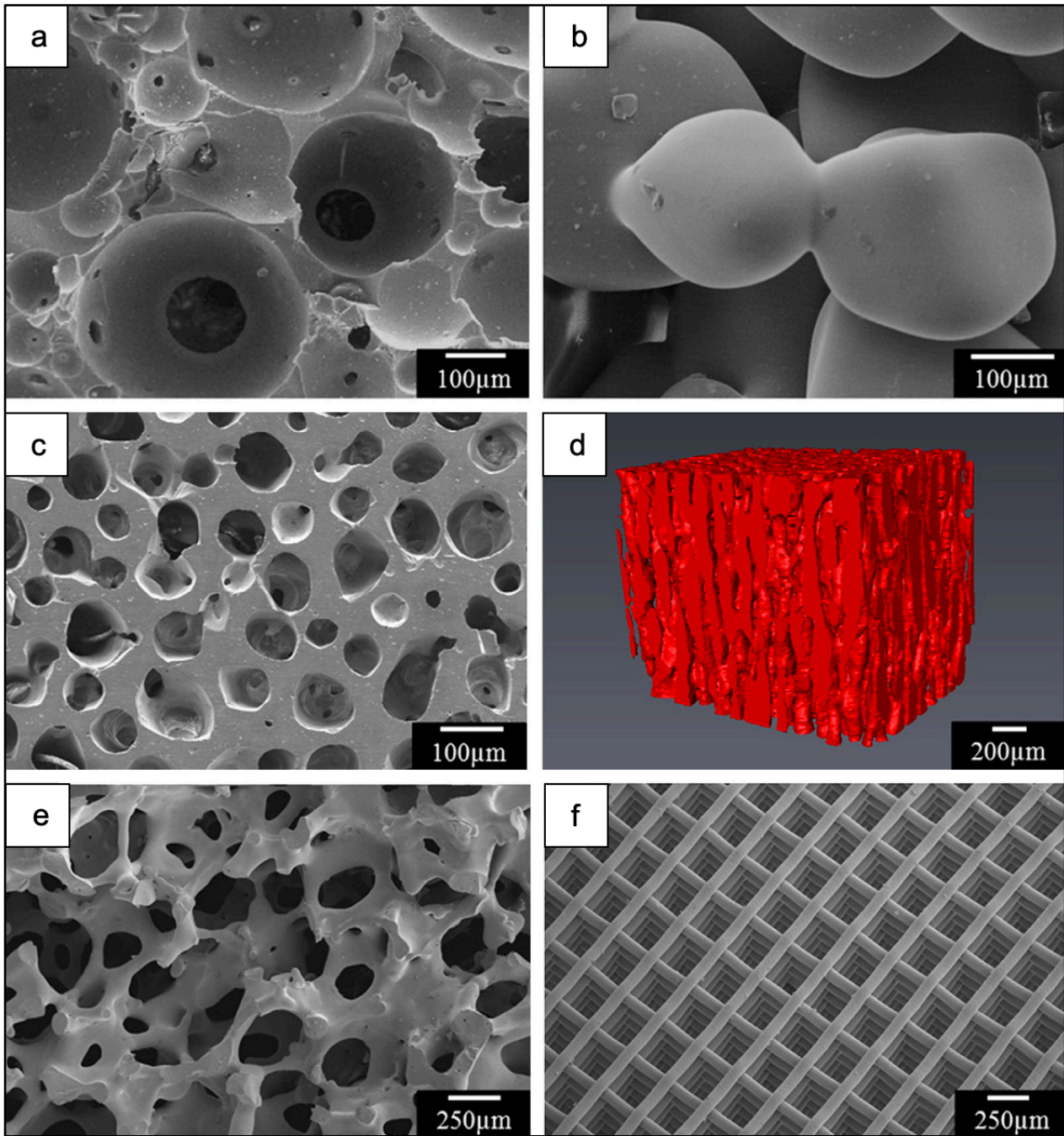


Figure 22: Microstructures of bioactive glass scaffolds made through different fabrication techniques: (a) sol-gel; (b) thermal bonding of particles (microspheres); (c) oriented microstructure produced by unidirectional freezing of suspensions (plane perpendicular to the orientation direction); (d) Micro-computed tomography image of the oriented scaffolds in (c); (e) ‘trabecular’ microstructure obtained through polymer foam replication technique; (f) grid-like microstructure fabricated by Robocasting. Figure adapted from Tomsia et al. [167].

2.8 Conclusions

Bioactive glasses refer to amorphous materials that have a bioactive behaviour, i.e. the capability to create a stable bonding interface with living tissues by the progressive deposition of a calcium phosphate layer chemically analogous to the mineral phase of natural bone.

The term “bioactive” was coined by Hench in 1969, when he and his colleagues invented Bioglass[®], the first material able to bond to living bone and to stimulate osteogenesis through the release of biologically active ions.

According to the production method used, bioactive glasses could be characterized by chemical and microstructural features varying in a wide range. In particular glasses produced by melt-quenching technique are dense, while sol-gel process allows the production of nano-textured materials exhibiting higher reactivity in contact with body fluids.

BG-based products were successfully implanted in millions of patients worldwide, mainly to repair bone and dental defects and, over the years, many other bioactive glass compositions were proposed for innovative biomedical applications, such as and osteochondral tissue engineering and soft tissue repair.

Bioactive glasses are very promising materials in the treatment of cancer, as they provide therapeutic effect and promote new bone tissue formation at the same time.

In particular, mesoporous bioactive glasses are especially suitable for drug delivery due to their large surface area, high pore volume and narrow mesoporous structure.

Magnetic bioactive glasses were evaluated as potential materials for treatment of bone cancer by hyperthermia since they have the dual action of magnetic properties and bioactivity.

Finally, bioactive glasses are interesting materials as radioisotope vectors for cancer treatment by brachytherapy. The features that make them so attractive are high biocompatibility, controlled biodegradability, and the ability to promote the growth of new healthy tissues after the treatment with radionuclides. Since 1988 ⁹⁰Y biocompatible glass microspheres are used in clinical practice to treat liver cancer.

Currently, no one else bioactive glass device for bone cancer treatment has been commercialized, yet. However, the results of recent studies are encouraging and motivate further investigation.

In addition, bioactive glasses were designed to act as 3D scaffolds able to promote bone tissue regeneration and remodeling. Scaffold properties can be adjusted by acting on the glass composition and scaffold fabrication technique. Recently, there were tremendous progress in the field of manufacturing of BG scaffolds. However, the foam replica method still remains one of the most popular, cheapest and easiest method to fabricate 3D porous BG structure which resemble spongy bone.

References

- [1] G. Kaur, *Bioactive glasses - Potential Biomaterials for Future Therapy*. 2017.
- [2] E. Verné, “Notes of the course ‘Material for Bioengineering’ (Politecnico di Torino).” Turin, 2018.
- [3] J. M. Fernández-Navarro and M. Á. Villegas, “What is Glass?: An Introduction to the Physics and Chemistry of Silicate Glasses,” *Mod. Methods Anal. Archaeol. Hist. Glas. Vol. I*, vol. 1, pp. 1–22, 2013.
- [4] H. Ylänen, “Materials and Mechanical Properties of Bioactive Glass,” in *Bioactive Glasses: Materials, Properties and Applications*, 2011.
- [5] L. L. Hench, O. Andersson, and A. Akademi, *An Introduction to Bioceramics*. 1969.
- [6] Z. Strnad and J. Sestak, “Bio-Compatible Ceramics as mimetic material for bone tissue substitution,” *Proc. 2nd Int. Conf. Intell. Process. Manuf. Mater. IPMM 1999*, vol. 1, pp. 431–436, 1999.
- [7] P. V. Giannoudis, H. Dinopoulos, and E. Tsiridis, “Bone substitutes: An update,” *Injury*, vol. 36 Suppl 3, pp. 20–27, 2005.
- [8] H. Oonishi *et al.*, “Quantitative comparison of bone growth behavior in granules of Bioglass®, A-W glass-ceramic, and hydroxyapatite,” *J. Biomed. Mater. Res.*, vol. 51, no. 1, pp. 37–46, 2000.
- [9] L. L. Hench, “Chronology of Bioactive Glass Development and Clinical Applications,” *New J. Glas. Ceram.*, vol. 03, no. 02, pp. 67–73, 2013.
- [10] L. L. Hench, “The story of Bioglass®,” *J. Mater. Sci. Mater. Med.*, vol. 17, no. 11, pp. 967–978, 2006.
- [11] L. L. Hench, R. J. Splinter, W. C. Allen, and T. K. Greenlee, “Bonding mechanisms at the interface of ceramic prosthetic materials,” *J. Biomed. Mater. Res.*, vol. 5, no. 6, pp. 117–141, 1971.
- [12] J. Wilson, G. H. Pigott, F. J. Schoen, and L. L. Hench, “Toxicology and biocompatibility of bioglasses,” *J. Biomed. Mater. Res.*, vol. 15, no. 6, pp. 805–817, 1981.
- [13] S. K. Nandi, A. Mahato, B. Kundu, and P. Mukherjee, “Doped Bioactive Glass Materials in Bone Regeneration,” *Intech*, 2016.
- [14] L. L. Hench, “Bioceramics: from concept to clinic,” *J. Am. Ceram. Soc.*, vol. 74, pp. 1487–1510, 1991.
- [15] R. Detsch *et al.*, “Osteogenic differentiation of umbilical cord and adipose derived stem cells onto highly porous 45S5 Bioglass®-based scaffolds,” *J. Biomed. Mater. Res. - Part A*, vol. 103, no. 3, pp. 1029–1037, 2015.
- [16] O. Tsigkou, J. R. Jones, J. M. Polak, and M. M. Stevens, “Differentiation of fetal osteoblasts and formation of mineralized bone nodules by 45S5 Bioglass® conditioned medium in the absence of osteogenic supplements,” *Biomaterials*, vol. 30, no. 21, pp. 3542–3550, 2009.
- [17] I. D. Xynos, A. J. Edgar, L. D. K. Buttery, L. L. Hench, and J. M. Polak, “Gene-expression profiling of human osteoblasts following treatment with the ionic products of Bioglass® 45S5 dissolution,” *J. Biomed. Mater. Res.*, vol. 55, no. 2, pp. 151–157, 2001.
- [18] J. R. Jones, “Review of bioactive glass : From Hench to hybrids,” *Acta Biomater.*, vol. 9, no. 1, pp. 4457–4486, 2013.
- [19] Q. Chen, F. Bairo, S. Spriano, N. M. Pugno, and C. Vitale-Brovarone, “Modelling of the

- strength-porosity relationship in glass-ceramic foam scaffolds for bone repair,” *J. Eur. Ceram. Soc.*, vol. 34, no. 11, pp. 2663–2673, 2014.
- [20] Q. Z. Chen, I. D. Thompson, and A. R. Boccaccini, “45S5 Bioglass - derived glass – ceramic scaffolds for bone tissue engineering,” *Biomaterials*, vol. 27, pp. 2414–2425, 2006.
- [21] J. R. Jones, E. Gentleman, and J. Polak, “Bioactive Glass Scaffolds for Bone Regeneration,” 2007.
- [22] E. Fiume, J. Barberi, E. Vern, and F. Baino, “Bioactive Glasses : From Parent 45S5 Composition to Scaffold-Assisted Tissue-Healing Therapies,” 2018.
- [23] D. C. Greenspan, “Bioactive glass: mechanisms of bone bonding,” *Tandläkartidningen Årk*, vol. 91, no. 8, pp. 1–32, 1999.
- [24] M. N. Rahaman *et al.*, “Bioactive glass in tissue engineering,” *Acta Biomater.*, vol. 7, no. 6, pp. 2355–2373, 2011.
- [25] E. A. Abou Neel, D. M. Pickup, S. P. Valappil, R. J. Newport, and J. C. Knowles, “Bioactive functional materials: A perspective on phosphate-based glasses,” *J. Mater. Chem.*, vol. 19, no. 6, pp. 690–701, 2009.
- [26] L. L. Hench and A. J. Edgar, “Gene activating glasses,” *J. Inorg. Mater.*, 2002.
- [27] J.-Y. Sun, Y.-S. Yang, J. Zhong, and D. C. Greenspan, “The effect of the ionic products of Bioglass® dissolution on human osteoblasts growth cycle in vitro,” *J. Tissue Eng. Regen. Med.*, pp. 281–286, 2007.
- [28] L. L. Hench, I. D. Xynos, and J. M. Polak, “Bioactive glasses for in situ tissue regeneration,” *J. Biomater. Sci. Polym. Ed.*, vol. 15, no. 4, pp. 543–562, 2004.
- [29] F. Baino *et al.*, “Processing methods for making porous bioactive glass-based scaffolds—A state-of-the-art review,” *Int. J. Appl. Ceram. Technol.*, 2019.
- [30] W. Huang, D. E. Day, K. Kittiratanapiboon, and M. N. Rahaman, “Kinetics and mechanisms of the conversion of silicate (45S5), borate, and borosilicate glasses to hydroxyapatite in dilute phosphate solutions,” *J. Mater. Sci. Mater. Med.*, vol. 17, no. 7, pp. 583–596, 2006.
- [31] A. C. Wright, G. Dalba, F. Rocca, and N. M. Vedishcheva, “Borate versus silicate glasses: Why are they so different?,” *Phys. Chem. Glas. Eur. J. Glas. Sci. Technol. Part B*, vol. 51, no. 5, pp. 233–265, 2010.
- [32] P. Balasubramanian, T. Büttner, V. Miguez Pacheco, and A. R. Boccaccini, “Boron-containing bioactive glasses in bone and soft tissue engineering,” *J. Eur. Ceram. Soc.*, vol. 38, no. 3, pp. 855–869, 2018.
- [33] R. F. Brown, M. N. Rahaman, A. Dwilewicz, W. Huang, D. E. Day, and Y. Li, “Conversion of borate glass to hydroxyapatite and its effect on proliferation of MC3T3-E1 cells,” vol. 88, no. A, pp. 392–400, 2009.
- [34] M. Uo, M. Mizuno, Y. Kuboki, A. Makishima, and F. Watari, “Properties and cytotoxicity of water soluble Na₂O-CaO-P₂O₅ glasses,” *Biomaterials*, vol. 19, no. 24, pp. 2277–2284, 1998.
- [35] K. Franks, I. Abrahams, and J. C. Knowles, “Development of soluble glasses for biomedical use part I: In vitro solubility measurement,” *J. Mater. Sci. Mater. Med.*, vol. 11, no. 10, pp. 609–614, 2000.
- [36] V. Salih, K. Franks, M. James, G. W. Hastings, J. C. Knowles, and I. Olsen, “Development of soluble glasses for biomedical use part II: The biological response of human osteoblast cell lines to phosphate-based soluble glasses,” *J. Mater. Sci. Mater. Med.*, vol. 11, no. 10, pp. 615–620, 2000.
- [37] I. Ahmed, M. Lewis, I. Olsen, and J. C. Knowles, “Phosphate glasses for tissue engineering:

- Part 1. Processing and characterisation of a ternary-based P2O5-CaO-Na 2O glass system,” *Biomaterials*, vol. 25, no. 3, pp. 491–499, 2004.
- [38] I. Ahmed, M. Lewis, I. Olsen, and J. C. Knowles, “Phosphate glasses for tissue engineering: Part 2. Processing and characterisation of a ternary-based P2O5-CaO-Na 2O glass fibre system,” *Biomaterials*, vol. 25, no. 3, pp. 501–507, 2004.
- [39] C. G. Pantano, A. K. Singh, and H. Zhang, “Silicon oxycarbide glasses,” *J. Sol-Gel Sci. Technol.*, vol. 14, no. 1, pp. 7–25, 1999.
- [40] M. Gaweda *et al.*, “Bioactive layers based on black glasses on titanium substrates,” *J. Am. Ceram. Soc.*, vol. 101, pp. 590–601, 2018.
- [41] H. J. Kleebe and Y. D. Blum, “SiOC ceramic with high excess free carbon,” *J. Eur. Ceram. Soc.*, vol. 28, no. 5, pp. 1037–1042, 2008.
- [42] H. Zhang and C. G. Pantano, “Synthesis and characterization of silicon oxycarbide glasses,” *J. Am. Ceram. Soc.*, vol. 73, no. 4, pp. 958–963, 1990.
- [43] G. D. Sorarù, Q. Liu, L. V. Interrante, and T. Apple, “Role of precursor molecular structure on the microstructure and high temperature stability of silicon oxycarbide glasses derived from methylene-bridged polycarbosilanes,” *Chem. Mater.*, vol. 10, no. 12, pp. 4047–4054, 1998.
- [44] S. Trassl, G. Motz, E. Rössler, and G. Ziegler, “Characterisation of the free-carbon phase in precursor-derived SiCN ceramics,” *J. Non. Cryst. Solids*, vol. 293–295, no. 1, pp. 261–267, 2001.
- [45] J. Latournerie, P. Dempsey, D. Hourlier-Bahloul, and J. P. Bonnet, “Silicon oxycarbide glasses: Part 1-thermochemical stability,” *J. Am. Ceram. Soc.*, vol. 89, no. 5, pp. 1485–1491, 2006.
- [46] M. A. Mazo, A. Nistal, A. C. Caballero, F. Rubio, J. Rubio, and J. L. Oteo, “Influence of processing conditions in TEOS/PDMS derived silicon oxycarbide materials. Part 1: Microstructure and properties,” *J. Eur. Ceram. Soc.*, vol. 33, no. 6, pp. 1195–1205, 2013.
- [47] J. M. Nedelec *et al.*, “Materials doping through sol-gel chemistry: A little something can make a big difference,” *J. Sol-Gel Sci. Technol.*, vol. 46, no. 3, pp. 259–271, 2008.
- [48] P. Saravanapavan, J. R. Jones, R. S. Pryce, and L. L. Hench, “Bioactivity of gel-glass powders in the CaO-SiO2 system: A comparison with ternary (CaO-P2O5-SiO2) and quaternary glasses (SiO2-CaO-P2O5-Na2O),” *Bioactivity of gel-glass powders*, pp. 110–119, 2003.
- [49] C. Wu and J. Chang, “Multifunctional mesoporous bioactive glasses for effective delivery of therapeutic ions and drug/growth factors,” *J. Control. Release*, vol. 193, pp. 282–295, 2014.
- [50] A. Krajewski, A. Ravaglioli, B. Fabbri, and C. B. Azzoni, “Doping influence on the interaction between a bioactive glass and a simulated physiological solution: Chemical and EPR tests,” *J. Mater. Sci.*, vol. 22, no. 4, pp. 1228–1234, 1987.
- [51] P. D. Saltman and L. G. Strause, “The role of trace minerals in osteoporosis,” *J. Am. Coll. Nutr.*, vol. 12, no. 4, pp. 384–389, 1993.
- [52] J. H. Beattie and A. Avenell, “Trace Element Nutrition and Bone Metabolism,” *Nutr. Res. Rev.*, vol. 5, no. 1, pp. 167–188, 1992.
- [53] Zhi Lin Sun, J. C. Wataha, and C. T. Hanks, “Effects of metal ions on osteoblast-like cell metabolism and differentiation,” *J. Biomed. Mater. Res.*, vol. 34, no. 1, pp. 29–37, 1997.
- [54] G. Kaur, G. Pickrell, N. Sriranganathan, V. Kumar, and D. Homa, “Review and the state of the art: Sol-gel and melt quenched bioactive glasses for tissue engineering,” *J. Biomed. Mater. Res. - Part B Appl. Biomater.*, 2015.
- [55] H. Ylänen, *Bioactive Glasses: Materials, Properties and Applications, 2nd Edition*. 2015.

- [56] S. Kargozar, M. Montazerian, E. Fiume, and F. Baino, "Multiple and Promising Applications of Strontium (Sr)-Containing Bioactive Glasses in Bone Tissue Engineering," *Front. Bioeng. Biotechnol.*, 2019.
- [57] T. Aboud and L. Stoch, "Crystallization behavior in the glass system SiO₂-P₂O₅-Al₂O₃-MgO-Na₂O," *J. Non. Cryst. Solids*, vol. 219, pp. 149–154, 1997.
- [58] R. Li, A. E. Clark, and L. L. Hench, "An investigation of bioactive glass powders by sol-gel processing," *J. Appl. Biomater.*, vol. 2, no. 4, pp. 231–239, 1991.
- [59] M. M. Pereira, A. E. Clark, and L. L. Hench, "Calcium phosphate formation on sol-gel-derived bioactive glasses in vitro," *J. Biomed. Mater. Res.*, vol. 28, no. 6, pp. 693–698, 1994.
- [60] G. J. Owens *et al.*, "Sol-gel based materials for biomedical applications," *Prog. Mater. Sci.*, vol. 77, pp. 1–79, 2016.
- [61] L. L. Hench and J. K. West, "The Sol-Gel Process," *Chem. Rev.*, vol. 90, no. 1, pp. 33–72, 1990.
- [62] P. Flory, *Principles of polymer chemistry*. 1953.
- [63] F. Baino, E. Fiume, M. Miola, and E. Vern, "Bioactive sol-gel glasses: Processing, properties, and applications," no. December 2017, pp. 841–860, 2018.
- [64] A. M. Siouffi, "Silica gel-based monoliths prepared by the sol-gel method: facts and figures," *J. Chromatogr. A*, vol. 1000, no. 1–2, pp. 801–818, 2003.
- [65] C.J. Brinker; G. W. Scherer, *Sol-Gel Science -The physics and chemistry of sol-gel processing*. 1990.
- [66] E. J. A. Pope and J. D. Mackenzie, "Sol-gel processing of silica. II. The role of the catalyst," *J. Non. Cryst. Solids*, vol. 87, no. 1–2, pp. 185–198, 1986.
- [67] G. Valverde Aguilar, "Introductory Chapter: A Brief Semblance of the Sol-Gel Method in Research," in *Sol-Gel Method - Design and Synthesis of New Materials with Interesting Physical, Chemical and Biological Properties*, 2019.
- [68] B. D. Zdravkov, J. J. Čermák, M. Šefara, and J. Janků, "Pore classification in the characterization of porous materials: A perspective," *Cent. Eur. J. Chem.*, vol. 5, no. 2, pp. 385–395, 2007.
- [69] J. R. Jones, P. D. Lee, and L. L. Hench, "Hierarchical porous materials for tissue engineering," *Philos. Trans. R. Soc. A*, vol. 364, pp. 263–281, 2006.
- [70] J. S. Kresge, C. T., Leonowicz, M. E., Roth, W. J., Vartuli, J. C., Beck, "Ordered mesoporous molecular sieves synthesized by a liquid-crystal template mechanism," *Lett. to Nat.*, vol. 359, pp. 710–712, 1992.
- [71] M. Vallet-Regí and D. Arcos, "Bioceramics for drug delivery," *Acta Mater.*, vol. 61, pp. 890–911, 2013.
- [72] B. G. Trewyn, I. I. Slowing, S. Giri, H. T. Chen, and V. S. Y. Lin, "Synthesis and functionalization of a mesoporous silica nanoparticle based on the sol-gel process and applications in controlled release," *Acc. Chem. Res.*, vol. 40, pp. 846–853, 2007.
- [73] M. Łączka, K. Cholewa-Kowalska, and A. M. Osyczka, "Bioactivity and osteoinductivity of glasses and glassceramics and their material determinants," *Ceram. Int.*, no. 13, pp. 14313–14325, 2016.
- [74] F. Baino and C. Vitale-Brovarone, "Three-dimensional glass-derived scaffolds for bone tissue engineering: Current trends and forecasts for the future," *J. Biomed. Mater. Res. - Part A*, vol. 97 A, pp. 514–535, 2011.
- [75] M. J. MURTAGH, E. K. GRAHAM, and C. G. PANTANO, "Elastic Moduli of Silica Gels

- Prepared with Tetraethoxysilane,” *J. Am. Ceram. Soc.*, vol. 69, no. 11, pp. 775–779, 1986.
- [76] T. Woignier, G. W. Scherer, and A. Alaoui, “Stress in aerogel during depressurization of autoclave: II. Silica gels,” *J. Sol-Gel Sci. Technol.*, vol. 3, pp. 141–150, 1994.
 - [77] G. Poologasundarampillai, P. D. Lee, C. Lam, A. M. Kourkouta, and J. R. Jones, “Compressive Strength of Bioactive Sol–Gel Glass Foam Scaffolds,” *Int. J. Appl. Glas. Sci.*, vol. 7, no. 2, pp. 229–237, 2016.
 - [78] P. Sepuvela, J. R. Jones, and L. L. Hench, “In vitro dissolution of melt-derived 45S5 and sol-gel derived 58S bioactive glasses,” *Key Eng. Mater.*, 2011.
 - [79] P. Sepulveda, J. R. Jones, and L. L. Hench, “Characterization of Melt-Derived 45S5 and sol-gel-derived 58S Bioactive Glasses Pilar,” *J. Biomed. Mater. Res.*, 2001.
 - [80] M. Vallet-Regí and D. Arcos, “Sol-gel silica-based biomaterials and bone tissue regeneration,” *Acta Biomater.*, pp. 2874–2888, 2010.
 - [81] S. Labbaf, O. Tsigkou, K. H. Müller, M. M. Stevens, A. E. Porter, and J. R. Jones, “Spherical bioactive glass particles and their interaction with human mesenchymal stem cells in vitro,” *Biomaterials*, vol. 32, no. 4, pp. 1010–1018, 2011.
 - [82] M. M. Pereira, A. E. Clark, and L. L. Hench, “Effect of Texture on the Rate of Hydroxyapatite Formation on Gel-Silica Surface,” *J. Am. Ceram. Soc.*, vol. 78, no. 9, pp. 2463–2468, 1995.
 - [83] F. Baino, S. Hamzehlou, and S. Kargozar, “Bioactive Glasses : Where Are We and Where Are We Going ?,” *Funct. Biomater.*, 2018.
 - [84] V. Miguez-Pacheco, L. L. Hench, and A. R. Boccaccini, “Bioactive glasses beyond bone and teeth: Emerging applications in contact with soft tissues,” *Acta Biomater.*, vol. 13, pp. 1–15, 2015.
 - [85] F. Baino and E. Verne, “Glass-based coatings on biomedical implants: A state-of-the-art review,” *Biomed. Glas.*, vol. 3, no. 1, pp. 1–17, 2017.
 - [86] L. L. Hench, “Bioactive materials for gene control,” in *New materials and technologies for healthcare*, 2011, pp. 25–48.
 - [87] M. Montazerian and E. D. Zanotto, “Bioactive and inert dental glass-ceramics,” *J. Biomed. Mater. Res. - Part A*, vol. 105, no. 2, pp. 619–639, 2017.
 - [88] J. R. Jones, D. S. Brauer, L. Hupa, and D. C. Greenspan, “Bioglass and Bioactive Glasses and Their Impact on Healthcare,” *Int. J. Appl. Glas. Sci.*, vol. 7, no. 4, pp. 423–434, 2016.
 - [89] E. B. Hunziker, “The elusive path to cartilage regeneration,” *Adv. Mater.*, vol. 21, no. 32–33, pp. 3419–3424, 2009.
 - [90] L. E. Freed, G. C. Engelmayr, J. T. Borenstein, F. T. Moutos, and F. Guilak, “Advanced material strategies for tissue engineering scaffolds,” *Adv. Mater.*, vol. 21, no. 32–33, pp. 3410–3418, 2009.
 - [91] B. Sonny Bal *et al.*, “In vivo outcomes of tissue-engineered osteochondral grafts,” *J. Biomed. Mater. Res. - Part B Appl. Biomater.*, vol. 93, no. 1, pp. 164–174, 2010.
 - [92] V. Miguez-Pacheco, D. Greenspan, L. L. Hench, and A. R. Boccaccini, “Bioactive glasses in soft tissue repair,” *Am. Ceram. Soc. Bull.*, vol. 94, no. 6, pp. 27–31, 2015.
 - [93] P. Carmeliet, “Manipulating angiogenesis in medicine,” *J. Intern. Med.*, vol. 255, no. 5, pp. 538–561, 2004.
 - [94] A. A. Gorustovich, J. A. Roether, and A. R. Boccaccini, “Effect of bioactive glasses on angiogenesis: a review of in vitro and in vivo evidences,” *Tissue Eng. Part B. Rev.*, vol. 16, no. 2, pp. 199–207, 2010.
 - [95] R. M. Day *et al.*, “Assessment of polyglycolic acid mesh and bioactive glass for soft-tissue

- engineering scaffolds,” *Biomaterials*, vol. 25, no. 27, pp. 5857–5866, 2004.
- [96] L. A. Haro Durand *et al.*, “Angiogenic effects of ionic dissolution products released from a boron-doped 45S5 bioactive glass,” *J. Mater. Chem. B*, vol. 3, no. 6, pp. 1142–1148, 2015.
- [97] S. Zhao *et al.*, “Wound dressings composed of copper-doped borate bioactive glass microfibers stimulate angiogenesis and heal full-thickness skin defects in a rodent model,” *Biomaterials*, vol. 53, pp. 379–391, 2015.
- [98] S. Kargozar *et al.*, “Strontium- and cobalt-substituted bioactive glasses seeded with human umbilical cord perivascular cells to promote bone regeneration via enhanced osteogenic and angiogenic activities,” *Acta Biomater.*, vol. 58, pp. 502–514, 2017.
- [99] S. Naseri, W. C. Lepry, and S. N. Nazhat, “Bioactive glasses in wound healing: hope or hype?,” *J. Mater. Chem. B*, vol. 5, no. 31, pp. 6167–6174, 2017.
- [100] X. Yu and R. V. Bellamkonda, “Tissue-engineered scaffolds are effective alternatives to autografts for bridging peripheral nerve gaps,” *Tissue Eng.*, vol. 9, no. 3, pp. 421–430, 2003.
- [101] S. Bunting, L. Di Silvio, S. Deb, S. Hall, and S. Standring, “Bioresorbable glass fibres facilitate peripheral nerve regeneration,” *J. Hand Surg. Am.*, vol. 30, no. 3, pp. 242–247, 2005.
- [102] Y.-P. Kim, G.-S. Lee, and J.-W. Kim, “Phosphate glass fibres promote neurite outgrowth and early regeneration in a peripheral nerve injury model,” *Ann. Am. Thorac. Soc.*, vol. 12, no. 3, pp. 181–204, 2010.
- [103] G. Novajra, C. Tonda-Turo, C. Vitale-Brovarone, G. Ciardelli, S. Geuna, and S. Raimondo, “Novel systems for tailored neurotrophic factor release based on hydrogel and resorbable glass hollow fibers,” *Mater. Sci. Eng. C*, vol. 36, no. 1, pp. 25–32, 2014.
- [104] L. M. Marquardt, D. Day, S. E. Sakiyama-Elbert, and A. B. Harkins, “Effects of borate-based bioactive glass on neuron viability and neurite extension,” *J. Biomed. Mater. Res. - Part A*, vol. 102, no. 8, pp. 2767–2775, 2014.
- [105] S. Kargozar, M. Mozafari, S. Hamzehlou, H. W. Kim, and F. Baino, “Mesoporous bioactive glasses (MBGs) in cancer therapy: Full of hope and promise,” *Mater. Lett.*, vol. 251, pp. 241–246, 2019.
- [106] R. Borges, J. Marchi, and R. D. Aspasio, “Biocompatible Glasses for Cancer Treatment,” *Biocompatible Glas.*, vol. 53, pp. 85–117, 2016.
- [107] J. B. Wolinsky, Y. L. Colson, and M. W. Grinstaff, “Local drug delivery strategies for cancer treatment: Gels, nanoparticles, polymeric films, rods, and wafers,” *J. Control. Release*, vol. 159, no. 1, pp. 14–26, 2012.
- [108] C. Wu and J. Chang, “Bioactive Scaffolds with Multifunctional Properties for Hard Tissue Regenerations,” in *Biomaterials for implants and scaffolds*, 2017.
- [109] M. Caldorera-Moore, N. Guimard, L. Shi, and K. Roy, “Designer nanoparticles: Incorporating size, shape and triggered release into nanoscale drug carriers,” *Expert Opin. Drug Deliv.*, vol. 7, no. 4, pp. 479–495, 2010.
- [110] M. Vallet-Regi, A. Rámila, R. P. Del Real, and J. Pérez-Pariente, “A new property of MCM-41: Drug delivery system,” *Chem. Mater.*, vol. 13, no. 2, pp. 308–311, 2001.
- [111] M. Vallet-Regi, “Ordered mesoporous materials in the context of drug delivery systems and bone tissue engineering,” *Chem. - A Eur. J.*, vol. 12, no. 23, pp. 5934–5943, 2006.
- [112] X. Yan, C. Yu, X. Zhou, J. Tang, and D. Zhao, “Highly ordered mesoporous bioactive glasses with superior in vitro bone-forming bioactivities,” *Angew. Chemie - Int. Ed.*, vol. 43, no. 44, pp. 5980–5984, 2004.
- [113] Y. Lin, J. C. Mauro, and G. Kaur, “Bioactive Glasses for Cancer Therapy,” in *Biomedical*,

Therapeutic and Clinical Applications of Bioactive Glasses, no. 1, Elsevier Ltd., 2019, pp. 273–312.

- [114] C. Wu and J. Chang, “Mesoporous bioactive glasses: Structure characteristics, drug/growth factor delivery and bone regeneration application,” *Interface Focus*, vol. 2, no. 3, pp. 292–306, 2012.
- [115] L. Zhao *et al.*, “Mesoporous bioactive glasses for controlled drug release,” *Microporous Mesoporous Mater.*, vol. 109, no. 1–3, pp. 210–215, 2008.
- [116] Y. Zhu and S. Kaskel, “Comparison of the in vitro bioactivity and drug release property of mesoporous bioactive glasses (MBGs) and bioactive glasses (BGs) scaffolds,” *Microporous Mesoporous Mater.*, vol. 118, no. 1–3, pp. 176–182, 2009.
- [117] L. Pasqua and A. Leggio, “Mesoporous Silica Nanoparticles in Cancer Therapy: Relevance of the Targeting Function,” *Mini Rev. Med. Chem.*, vol. 16, pp. 743–753, 2016.
- [118] A. Yazdanpanah and F. Moztarzadeh, “Synthesis and characterization of Barium–Iron containing magnetic bioactive glasses: The effect of magnetic component on structure and in vitro bioactivity,” *Colloids Surfaces B Biointerfaces*, vol. 176, pp. 27–37, 2019.
- [119] G. Li, S. Feng, and D. Zhou, “Magnetic bioactive glass ceramic in the system CaO-P 2O 5-SiO 2-MgO-CaF 2-MnO 2-Fe 2O 3 for hyperthermia treatment of bone tumor,” *J. Mater. Sci. Mater. Med.*, vol. 22, no. 10, pp. 2197–2206, 2011.
- [120] T. Kokubo, “Bioactive glass ceramics: properties and applications,” *Biomaterials*, vol. 12, 1991.
- [121] X. Li, X. Wang, Z. Hua, and J. Shi, “One-pot synthesis of magnetic and mesoporous bioactive glass composites and their sustained drug release property,” *Acta Mater.*, vol. 56, no. 13, pp. 3260–3265, 2008.
- [122] M. Alcaide *et al.*, “In vitro evaluation of glass-glass ceramic thermoseed-induced hyperthermia on human osteosarcoma cell line,” *J. Biomed. Mater. Res. - Part A*, vol. 100 A, no. 1, pp. 64–71, 2012.
- [123] R. Koohkan, T. Hooshmand, D. Mohebbi-Kalhari, M. Tahriri, and M. T. Marefati, “Synthesis, Characterization, and in Vitro Biological Evaluation of Copper-Containing Magnetic Bioactive Glasses for Hyperthermia in Bone Defect Treatment,” *ACS Biomater. Sci. Eng.*, vol. 4, no. 5, pp. 1797–1811, 2018.
- [124] A. C. Jayalekshmi, S. P. Victor, and C. P. Sharma, “Magnetic and degradable polymer/bioactive glass composite nanoparticles for biomedical applications,” *Colloids Surfaces B Biointerfaces*, vol. 101, pp. 196–204, 2013.
- [125] W. Ngwa *et al.*, “Targeted radiotherapy with gold nanoparticles: Current status and future perspectives,” *Nanomedicine*, vol. 9, no. 7, pp. 1063–1082, 2014.
- [126] S. H. Goudreau, J. P. Joseph, and S. J. Seiler, “Preoperative radioactive seed localization for nonpalpable breast lesions: Technique, pitfalls, and solutions,” *Radiographics*, vol. 35, no. 5, pp. 1319–1334, 2015.
- [127] C. Richmond and J. Findlay, “Half-life of Iodine-125,” *Heal. Phys*, 1966.
- [128] L. L. Hench, D. E. Day, W. Höland, and V. M. Rheinberger, “Glass and Medicine,” *Int. J. Appl. Glas. Sci.*, vol. 1, no. 1, pp. 104–117, 2010.
- [129] A. Hadadi, M. Sadeghi, D. Sardari, A. Khanchi, and A. Shirazi, “Monte Carlo characterization of biocompatible beta-emitting 90Y glass seed incorporated with the radionuclide 153Sm as a SPECT marker for brachytherapy applications,” *J. Appl. Clin. Med. Phys.*, vol. 14, no. 5, pp. 90–103, 2013.

- [130] J. K. Christie, J. Malik, and A. Tilocca, "Bioactive glasses as potential radioisotope vectors for in situ cancer therapy: Investigating the structural effects of yttrium," *Phys. Chem. Chem. Phys.*, vol. 13, pp. 17749–17755, 2011.
- [131] J. R. Jones and A. G. Clare, *Bio-Glasses: An Introduction*. 2012.
- [132] W. dos S. Roberto, M. M. Pereira, and T. P. R. de Campos, "Analysis of Bioactive Glasses Obtained by Sol-Gel Processing for Radioactive Implants," *Mater. Res.*, vol. 6, no. 2, pp. 123–127, 2003.
- [133] D. Cacaina, H. Ylänen, M. Hupa, and S. Simon, "Study of yttrium containing bioactive glasses behaviour in simulated body fluid," *J. Mater. Sci. Mater. Med.*, vol. 17, no. 8, pp. 709–716, 2006.
- [134] D. Cacaina, H. Ylänen, S. Simon, and M. Hupa, "The behaviour of selected yttrium containing bioactive glass microspheres in simulated body environments," *J. Mater. Sci. Mater. Med.*, vol. 19, no. 3, pp. 1225–1233, 2008.
- [135] J. E. White and D. E. Day, "Rare earth aluminosilicate glasses for in vivo radiation delivery," *Mech. Corros. Prop. Ser. A, Key Eng. Mater.*, vol. 94–95, pp. 181–208, 1994.
- [136] D. E. Day, "Glass microspheres US 4789501 A," 1988.
- [137] T. P. R. Campos, J. P. L. Andrade, I. T. Costa, and C. H. T. Silva, "Study of the Sm-153 seeds degradation and evaluation of the absorbed dose in rabbit's liver implants," *Prog. Nucl. Energy*, vol. 50, pp. 757–766, 2008.
- [138] S. D. Conzone, R. F. Brown, D. E. Day, and G. J. Ehrhardt, "In vitro and in vivo dissolution behavior of a dysprosium lithium borate glass designed for the radiation synovectomy treatment of rheumatoid arthritis," *J. Biomed. Mater. Res.*, vol. 60, no. 2, pp. 260–268, 2002.
- [139] L. B. Nogueira and T. P. R. Campos, "Nuclear Characterization of Radioactive Bioglass Seed for Brachytherapy Studies," *Int. Conf. Math. Comput. Methods Appl. to Nucl. Sci. Eng.*, pp. 1–9, 2011.
- [140] L. B. Nogueira and T. P. R. Campos, "Synthesis, chemical characterization and radiological response of Ho and HoZr bioglass seeds," *J. Sol-Gel Sci. Technol.*, vol. 77, no. 3, pp. 688–698, 2016.
- [141] M. Sadeghi, F. Taghdiri, S. Hamed Hosseini, and C. Tenreiro, "Monte Carlo calculated TG-60 dosimetry parameters for the β -Emitter ^{153}Sm brachytherapy source," *Med. Phys.*, vol. 37, no. 10, 2010.
- [142] S. H. Hosseini, M. Enferadi, and M. Sadeghi, "Dosimetric aspects of ^{166}Ho brachytherapy biodegradable glass seed," *Appl. Radiat. Isot.*, vol. 73, pp. 109–115, 2013.
- [143] A. Khorshidi, M. Ahmadinejad, and S. H. Hosseini, "Evaluation of a proposed biodegradable ^{188}Re source for brachytherapy application: A review of dosimetric parameters," *Med. (United States)*, vol. 94, no. 28, pp. 1–7, 2015.
- [144] J. K. Christie and A. Tilocca, "Integrating biological activity into radioisotope vectors: Molecular dynamics models of yttrium-doped bioactive glasses," *J. Mater. Chem.*, vol. 22, pp. 12023–12031, 2012.
- [145] G. E. Merwin, "Bioglass middle ear prosthesis: Preliminary report," *Ann. Otol. Rhinol. Laryngol.*, vol. 95, no. 1, pp. 78–82, 1986.
- [146] L. L. Hench and D. C. Greenspan, "Interactions between bioactive glass and collagen: A review and new perspectives," *J. Aust. Ceram. Soc.*, vol. 49, no. 2, pp. 1–40, 2013.
- [147] F. Bahmad and S. N. Merchant, "Histopathology of ossicular grafts and implants in chronic otitis media," *Ann. Otol. Rhinol. Laryngol.*, vol. 116, no. 3, pp. 181–191, 2007.

- [148] R. Reck, S. Storkel, and A. Meyer, "Bioactive Glass-Ceramics in Middle Ear Surgery an 8 year review," *Ann. New York Acad. Sci.*, vol. 523, pp. 100–106, 1988.
- [149] P. D. R. Spraggs, "A Bone-Anchored Percutaneous Connector System for Neural Prosthetic Applications," 1997.
- [150] H. Stanley, M. Hall, and A. Clark, "Using 45S5 bioglass cones as endosseous ridge maintenance implants to prevent alveolar ridge resorption: a 5-year evaluation," *Int. J. Oral Maxillofac. Implants*, vol. 12, no. 1–19, 1997.
- [151] L. L. Hench, D. C. Greenspan, and J. w Hench, "Bioglass: a short history and bibliography," *J. Aust. Ceram. Soc.*, vol. 40, no. 1, pp. 1–42, 2004.
- [152] "Novabone." [Online]. Available: <http://novabone.com/>. [Accessed: 08-Jun-2020].
- [153] D. G. Gillam, J. Y. Tang, N. J. Mordan, and H. N. Newman, "The effects of a novel Bioglass® dentifrice on dentine sensitivity: a scanning electron microscopy investigation," *J. Oral Rehabil.*, vol. 29, no. 4, pp. 305–313, 2002.
- [154] B. J. Tai *et al.*, "Anti-gingivitis effect of a dentifrice containing bioactive glass (NovaMin®) particulate," *J. Clin. Periodontol.*, vol. 33, pp. 86–91, 2006.
- [155] M. Vahid Golpayegani, A. Sohrabi, M. Biria, and G. Ansari, "Remineralization Effect of Topical NovaMin Versus Sodium Fluoride (1.1%) on Caries-Like Lesions in Permanent Teeth," *J. Dent. (Tehran)*, vol. 9, no. 1, pp. 68–75, 2012.
- [156] A. Banerjee, M. Hajatdoost-Sani, S. Farrell, and I. Thompson, "A clinical evaluation and comparison of bioactive glass and sodium bicarbonate air-polishing powders," *J. Dent.*, vol. 38, no. 6, pp. 475–479, 2010.
- [157] S. B. Jung and D. E. Day, "Treatment of non-healing diabetic venous stasis ulcers with bioactive glass nanofibers," *Wound Repair Regen.*, vol. 19, 2011.
- [158] T. Gilchrist *et al.*, "In vitro nerve repair - in vivo. The reconstruction of peripheral nerves by entubulation with biodegradable glass tubes - a preliminary report," *Br. J. Plast. Surg.*, vol. 51, no. 3, pp. 231–237, 1998.
- [159] E. Day and G. J. Ehrhardt, "Therapeutic Use of 90Y Microspheres," vol. 14, no. 3, pp. 233–242, 1987.
- [160] J. P. Vacanti and R. Langer, "Tissue engineering: The design and fabrication of living replacement devices for surgical reconstruction and transplantation," *Lancet*, 1999.
- [161] R. Lanza, R. Langer, and J. Vacanti, *Principles of Tissue Engineering*. 2011.
- [162] L. C. Gerhardt and A. R. Boccaccini, "Bioactive glass and glass-ceramic scaffolds for bone tissue engineering," *Materials (Basel)*, vol. 3, no. 7, pp. 3867–3910, 2010.
- [163] F. J. O'Brien, "Biomaterials & scaffolds for tissue engineering," *Mater. Today*, vol. 14, no. 3, pp. 88–95, 2011.
- [164] K. C. Dee and B. Engineering, "Engineering of Materials for Biomedical Applications," *Mater. Today*, pp. 7–10, 1988.
- [165] H. M. Frost, "Could some biomechanical effects of growth hormone help to explain its effects on bone formation and resorption?," *Bone*, vol. 23, no. 5, pp. 395–398, 1998.
- [166] F. Baino and E. Fiume, "Elastic mechanical properties of 45S5-based bioactive glass-ceramic scaffolds," *Materials (Basel)*, vol. 12, no. 19, 2019.
- [167] Q. Fu, E. Saiz, M. N. Rahaman, and A. P. Tomsia, "Bioactive glass scaffolds for bone tissue engineering: state of the art and future perspectives," *Mater. Sci. Eng. C*, vol. 31, no. 7, pp. 1245–1256, 2011.
- [168] P. Sepulveda, J. R. Jones, and L. L. Hench, "Bioactive sol-gel foams for tissue repair," *J.*

Biomed. Mater. Res., no. 2, pp. 340–348, 2002.

- [169] Z. Y. Wu, R. G. Hill, S. Yue, D. Nightingale, P. D. Lee, and J. R. Jones, “Melt-derived bioactive glass scaffolds produced by a gel-cast foaming technique,” *Acta Biomater.*, vol. 7, no. 4, pp. 1807–1816, 2011.
- [170] J. R. Jones, L. M. Ehrenfried, and L. L. Hench, “Optimising bioactive glass scaffolds for bone tissue engineering,” *Biomaterials*, vol. 27, no. 7, pp. 964–973, 2006.
- [171] S. Midha, T. B. Kim, W. Van Den Bergh, P. D. Lee, J. R. Jones, and C. A. Mitchell, “Preconditioned 70S30C bioactive glass foams promote osteogenesis in vivo,” *Acta Biomater.*, vol. 9, no. 11, pp. 9169–9182, 2013.
- [172] M. Navarro *et al.*, “New macroporous calcium phosphate glass ceramic for guided bone regeneration,” *Biomaterials*, vol. 25, no. 18, pp. 4233–4241, 2004.
- [173] Q. Fu, M. N. Rahaman, B. S. Bal, W. Huang, and D. E. Day, “Preparation and bioactive characteristics of a porous 13-93 glass, and fabrication into the articulating surface of a proximal tibia,” *J. Biomed. Mater. Res. - Part A*, vol. 82, no. 1, pp. 222–229, 2007.
- [174] W. Liang, M. N. Rahaman, D. E. Day, N. W. Marion, G. C. Riley, and J. J. Mao, “Bioactive borate glass scaffold for bone tissue engineering,” *J. Non. Cryst. Solids*, vol. 354, no. 15–16, pp. 1690–1696, 2008.
- [175] C. Vitale-Brovarone, E. Vernè, M. Bosetti, P. Appendino, and M. Cannas, “Microstructural and in vitro characterization of SiO₂-Na₂O-CaO-MgO glass-ceramic bioactive scaffolds for bone substitutes,” *J. Mater. Sci. Mater. Med.*, vol. 16, no. 10, pp. 909–917, 2005.
- [176] S. C. Wu, H. C. Hsu, S. H. Hsiao, and W. F. Ho, “Preparation of porous 45S5 Bioglass®-derived glass-ceramic scaffolds by using rice husk as a porogen additive,” *J. Mater. Sci. Mater. Med.*, vol. 20, no. 6, pp. 1229–1236, 2009.
- [177] C. V. Brovarone, E. Verné, and P. Appendino, “Macroporous bioactive glass-ceramic scaffolds for tissue engineering,” *J. Mater. Sci. Mater. Med.*, vol. 17, no. 11, pp. 1069–1078, 2006.
- [178] Q. Fu, M. N. Rahaman, B. S. Bal, and R. F. Brown, “Preparation and in vitro evaluation of bioactive glass (13-93) scaffolds with oriented microstructures for repair and regeneration of load-bearing bones,” *J. Biomed. Mater. Res. - Part A*, vol. 93, no. 4, pp. 1380–1390, 2010.
- [179] Y. Minaberry and M. Jobbágy, “Macroporous bioglass scaffolds prepared by coupling sol-gel with freeze drying,” *Chem. Mater.*, vol. 23, no. 9, pp. 2327–2332, 2011.
- [180] E. Sachlos, J. T. Czernuszka, S. Gogolewski, and M. Dalby, “Making tissue engineering scaffolds work. Review on the application of solid freeform fabrication technology to the production of tissue engineering scaffolds,” *Eur. Cells Mater.*, vol. 5, pp. 29–40, 2003.
- [181] K. F. Leong, C. M. Cheah, and C. K. Chua, “Solid freeform fabrication of three-dimensional scaffolds for engineering replacement tissues and organs,” *Biomaterials*, vol. 24, no. 13, pp. 2363–2378, 2003.
- [182] R. Gmeiner *et al.*, “Additive manufacturing of bioactive glasses and silicate bioceramics,” *J. Ceram. Sci. Technol.*, vol. 6, no. 2, pp. 75–86, 2015.
- [183] J. Liu, H. Hu, P. Li, C. Shuai, and S. Peng, “Fabrication and characterization of porous 45S5 glass scaffolds via direct selective laser sintering,” *Mater. Manuf. Process.*, vol. 28, no. 6, pp. 610–615, 2013.
- [184] K. C. R. Kolan, M. C. Leu, G. E. Hilmas, R. F. Brown, and M. Velez, “Fabrication of 13-93 bioactive glass scaffolds for bone tissue engineering using indirect selective laser sintering,” *Biofabrication*, vol. 3, no. 2, 2011.

- [185] S. J. Hollister, "Porous scaffold design for tissue engineering," *Nat. Mater.*, vol. 5, no. 7, p. 590, 2006.
- [186] S. A. Skoog, P. L. Goering, and R. J. Narayan, "Stereolithography in tissue engineering," *J. Mater. Sci. Mater. Med.*, vol. 25, no. 3, pp. 845–856, 2014.
- [187] N. W. Solís Pinargote, A. Smirnov, N. Peretyagin, A. Seleznev, and P. Peretyagin, "Direct Ink Writing Technology (3D Printing) of Graphene-Based Ceramic Nanocomposites: A Review," *Nanomaterials*, vol. 10, no. 7, p. 1300, 2020.
- [188] P. Tesavibul *et al.*, "Processing of 45S5 Bioglass® by lithography-based additive manufacturing," *Mater. Lett.*, vol. 74, pp. 81–84, 2012.
- [189] R. Gmeiner, G. Mitteramskogler, J. Stampfl, and A. R. Boccaccini, "Stereolithographic ceramic manufacturing of high strength bioactive glass," *Int. J. Appl. Ceram. Technol.*, vol. 12, no. 1, pp. 38–45, 2015.
- [190] G. M. Shashi, M. A. R. Laskar, H. Biswas, and A. K. Saha, "A Brief Review of Additive Manufacturing with Applications," *Proc. 14th Glob. Eng. Technol. Conf.*, no. December, 2017.
- [191] S. Preethi Soundarya, A. Haritha Menon, S. Viji Chandran, and N. Selvamurugan, "Bone tissue engineering: Scaffold preparation using chitosan and other biomaterials with different design and fabrication techniques," *Int. J. Biol. Macromol.*, vol. 119, pp. 1228–1239, 2018.
- [192] M. Guvendiren, J. Molde, R. M. D. Soares, and J. Kohn, "Designing Biomaterials for 3D Printing," *ACS Biomater. Sci. Eng.*, vol. 2, no. 10, pp. 1679–1693, 2016.
- [193] M. R. N. Monton, E. M. Forsberg, and J. D. Brennan, "Tailoring sol-gel-derived silica materials for optical biosensing," *Chem. Mater.*, vol. 24, no. 5, pp. 796–811, 2012.
- [194] J. F. Bredt, "THREE DIMENSIONAL PRINTING SYSTEM," 1998.
- [195] E. Mancuso *et al.*, "Three-dimensional printing of porous load-bearing bioceramic scaffolds," *Proc. Inst. Mech. Eng. Part H J. Eng. Med.*, vol. 231, no. 6, pp. 575–585, 2017.
- [196] J. A. Lewis, J. E. Smay, J. Stuecker, and J. Cesarano, "Direct ink writing of three-dimensional ceramic structures," *J. Am. Ceram. Soc.*, vol. 89, no. 12, pp. 3599–3609, 2006.
- [197] J. Franco, P. Hunger, M. E. Launey, A. P. Tomsia, and E. Saiz, "Direct write assembly of calcium phosphate scaffolds using a water-based hydrogel," *Acta Biomater.*, vol. 6, no. 1, pp. 218–228, 2010.
- [198] Q. Fu, E. Saiz, and A. P. Tomsia, "Direct ink writing of highly porous and strong glass scaffolds for load-bearing bone defects repair and regeneration," *Acta Biomater.*, vol. 7, no. 10, pp. 3547–3554, 2011.
- [199] S. Eqtesadi, A. Motealleh, P. Miranda, A. Pajares, A. Lemos, and J. M. F. Ferreira, "Robocasting of 45S5 bioactive glass scaffolds for bone tissue engineering," *J. Eur. Ceram. Soc.*, vol. 34, no. 1, pp. 107–118, 2014.
- [200] C. Wu, Y. Luo, G. Cuniberti, Y. Xiao, and M. Gelinsky, "Three-dimensional printing of hierarchical and tough mesoporous bioactive glass scaffolds with a controllable pore architecture, excellent mechanical strength and mineralization ability," *Acta Biomater.*, vol. 7, no. 6, pp. 2644–2650, 2011.
- [201] J. E. Smay, G. M. Gratson, R. F. Shepherd, J. Cesarano, and J. A. Lewis, "Directed colloidal assembly of 3D periodic structures," *Adv. Mater.*, vol. 14, no. 18, pp. 1279–1283, 2002.
- [202] J. W. Lee, P. X. Lan, B. Kim, G. Lim, and D. W. Cho, "Fabrication and characteristic analysis of a poly(propylene fumarate) scaffold using micro-stereolithography technology," *J. Biomed. Mater. Res. - Part B Appl. Biomater.*, vol. 87, no. 1, pp. 1–9, 2008.
- [203] Y. Zhang, C. Tse, D. Rouholamin, and P. J. Smith, "Scaffolds for tissue engineering produced

by inkjet printing,” *Cent. Eur. J. Eng.*, vol. 2, no. 3, pp. 325–335, 2012.

- [204] A. Nommeots-Nomm, P. D. Lee, and J. R. Jones, “Direct ink writing of highly bioactive glasses,” *J. Eur. Ceram. Soc.*, vol. 38, no. 3, pp. 837–844, 2018.

Chapter 3

Production of Bioactive Glass Scaffolds by Foam Replica Method

Foam replica method is recognized to be a valuable technique for the production highly porous bioactive glass scaffolds with architecture comparable to that of trabecular bone. In the present chapter, a detailed description of the method will be provided, together with an accurate comparative analysis of scaffold properties in relation with process parameters. In particular, scaffold morphology, mechanical and mass transport properties will be reviewed and the relation with sacrificial template features and porosity will be discussed in detail. In the end, a comprehensive overview on *in vivo* studies will be provided, in order to put an emphasis on scaffolds performances in a complex three-dimensional environment.

3.1 The Foam Replica Method

The foam replica method was developed by Schwartzwalder and Somers in 1963 for the manufacturing of ceramic foams [1]. In 2006, Chen et al. [2] and Legeros et al. [3] were the first to use this technique in bone tissue engineering for the development of bioactive glass scaffolds. Since that moment, the foam replica method was considerably used by several research groups to obtain porous glass scaffolds for bone regeneration.

The process is based on the replication of the porous structure of a sacrificial template, which could be both of natural and synthetic origin, in order to obtain its positive replica made of glass or glass-ceramic particles sintered around the organic template.

In a typical process, the foam is dipped in a slurry consisting of glass powders suspended into a binder solution, in order to obtain a consistent coating on the foam struts [4][5]. The coating thickness is adjustable according to the number of consecutive immersions performed and the particles content within the slurry composition [6], [5]. The excess of slurry is removed by squeezing the foams, which are then left to dry in order to obtain the so called green bodies [6], [5]. After drying, the foam is burned out by thermal treatments at high temperature, typically between 300 and 600 °C, in order to minimize microstructure damage of the porous glass coating [6], [5]. Once the foam is removed, the glass struts are densified by sintering at 600–1000 °C, depending on the composition and particle size of the glass [6], [5].

Frequently, the foam burning out and the glass sintering are combined in a single treatment. It is carried out by maintaining a very low heating rate uphill in order to burn out the foam without damaging the glass coating. Then the treatment involves keeping the sample at the chosen sintering temperature for a few hours in order to sinter the glass struts [7], [8].

Figure 1 provides a schematization of the process.

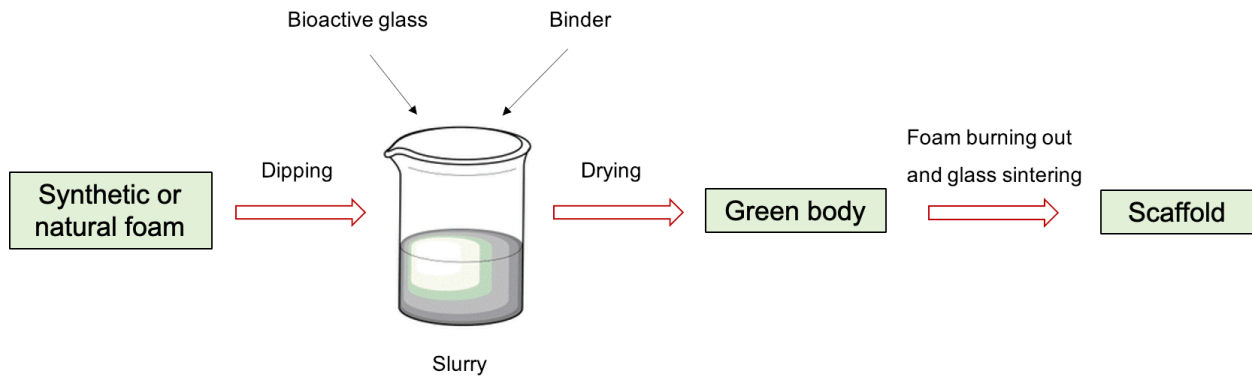


Figure 1: Schematic representation of foam replica technique.

Currently, foam replica method is one of the most popular, affordable, relatively easy and effective techniques for the development of highly porous and interconnected 3D bone-like scaffolds [9].

The success of this method is also attributed to its versatility, which relies upon the possibility to use a wide variety of sacrificial templates both of synthetic (e.g., commercial polymeric sponges [2]) and natural (e.g., marine sponges [10]) origin, as well as the opportunity of processing both traditional melt-derived glasses and sol-gel materials.

As an example, foam replica method was used in combination with evaporation-induced self-assembly (EISA) [11] to fabricate hierarchical porous BG (HPBG) scaffolds, where a polyurethane foam and a surfactant are used as co-templates for scaffold macropores and mesopores, respectively [12], [13].

Moreover, in the last years, the use natural biological materials as macroporous templates was particularly appreciated due to their easy availability and low-cost, thus leading to the possibility of obtaining diverse and environment-friendly structures [14].

One limitation of the foam replica method is that a good reproducibility of the process can only be achieved for relatively small and simple samples, since for very large samples, with complex geometry, phenomena that are difficult to control occur [6].

In addition, it is not possible to achieve pore architecture and porosity tailored to the patient using this technique [15].

3.2 Variants of the Process and Impact on the Morphological Properties

Morphological properties refer to the 3D architecture of scaffolds, in particular to the shape, size and interconnectivity of pores.

These properties are mainly influenced by the structure of the sacrificial template and process parameters. Some process parameters, such as sintering temperature, in turn, are intimately linked to glass composition, which determines the thermal response of the glass and thus the devitrification kinetics and the scaffolds densification upon thermal treatments.

In the following section, morphological properties of scaffolds produced from different sacrificial templates will be discussed in detail, paying particular attention to the open cell architecture.

3.2.1 Replica of Synthetic Templates

Both Chen et al. [2] and Legeros et al. [3] developed bioactive glass scaffolds for BTE using polyurethane (PU) sponges as sacrificial templates. Since then, PU sponges became the most widely used sacrificial templates for the production of glass-based bone-like structures. Indeed, their morphological similarity to trabecular bone in terms of open-cell architectures and high interconnectivity between adjacent pores make them very appealing templates for the manufacturing of synthetic bone grafts; besides, they are low-cost and are easily available.

This section provides an overview of the bioactive glass scaffolds produced by foam replica method using the polyurethane sponges as sacrificial templates.

In more detail, Chen et al. [2] developed 45S5 Bioglass[®] based scaffolds by using totally reticulated polyester-based polyurethane foams of 60 pores per inch (ppi) from Recticel UK (Corby) as sacrificial templates (Figure 2a, b) [2].

The slurry was obtained by adding melt-derived 45S5 Bioglass[®] powders (particle size $\sim 5\ \mu\text{m}$) to polyvinyl alcohol (PVA)-based binder solution [2].

Three different sintering conditions were used: 900 °C/5 h; 950 °C/0–5 h; and 1000 °C/0–2 h to investigate the effect of the thermal treatment on scaffold microstructure and mechanical properties. The heating and cooling rates were 2 and 5 °C/min, respectively [2].

The macroporous network and the microstructure of the scaffolds obtained under different sintering conditions are shown in Figure 2c-h.

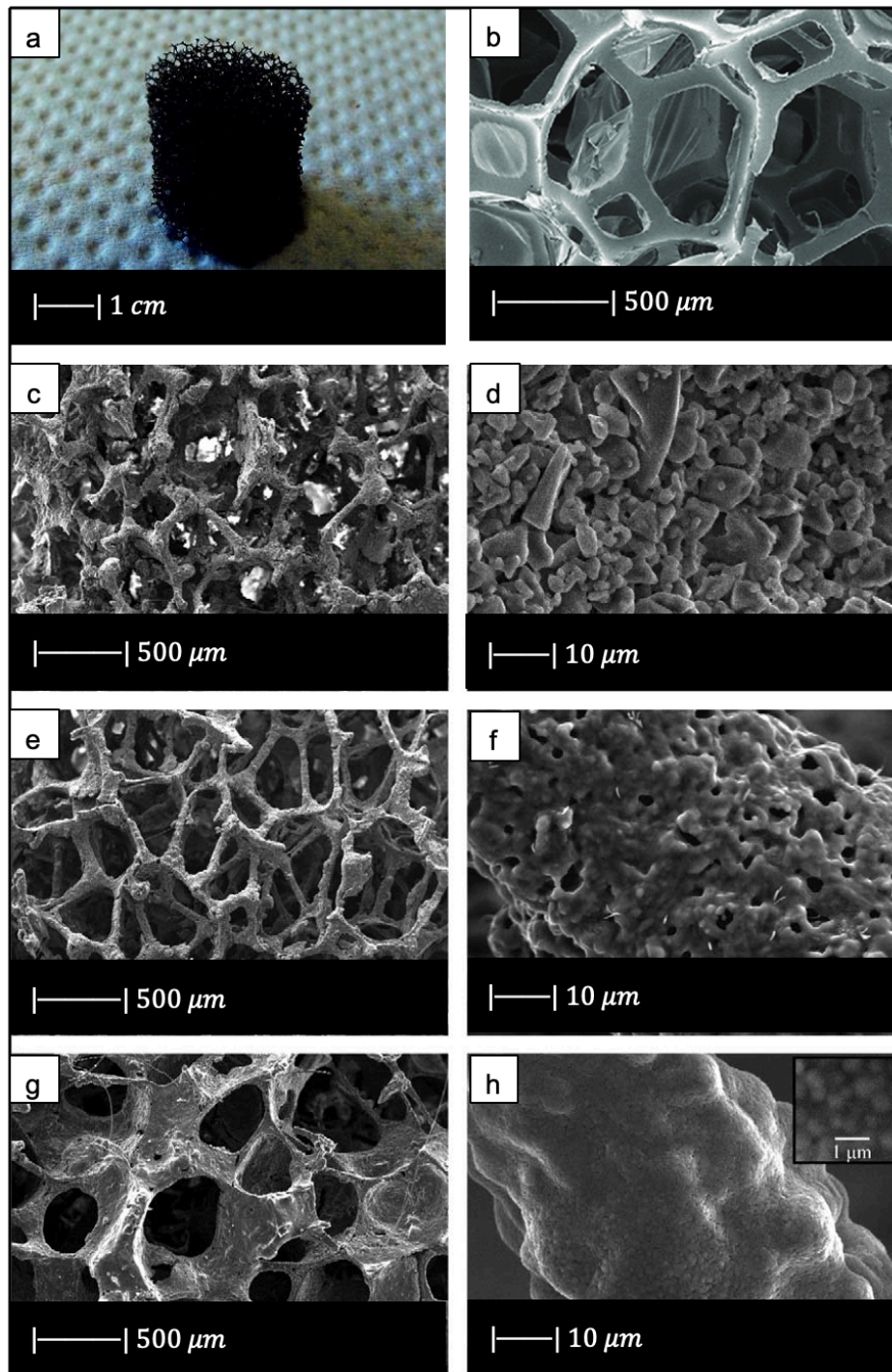


Figure 2: (a) Digital camera image of PU foam [10]. (b) SEM image of the PU foam [16]. (c-f) Pore structure and strut microstructure of 45S5 Bioglass[®]- derived foams sintered at (c), (d) 900 °C for 5 h, (e), (f) 950 °C for 2 h, and (g), (h) 1000 °C for 1 h. Figure adapted from Chen et al. [2].

For all the samples produced, the total porosity was $\sim 90\%$ and macropores were in the range of 510-720 μm , regardless of the sintering conditions [2].

Comparing Figures 2c, 2e and 2g, it was observed that cell struts were much thicker when sintered at 1000 °C for up to 1 h than at 900–950 °C for 2–5 h because reaching a higher temperature allowed for greater densification of the glass [2].

Images at higher magnification show that in the scaffold thermally treated at 900 °C (Figure 2d) a low sintering was achieved. Indeed, it was still possible to observe the presence of glass particles. While the scaffolds thermally treated at 950 °C (Figure 2f) exhibited greater sintering and ones treated at 1000 °C (Figure 2h) were fully sintered; in the latter, glass particles were no longer distinguishable, and the scaffold surface appeared smooth and round. Indeed, as the temperature increased, the viscosity decreased and the viscous flow sintering is enhanced [2].

In scaffolds sintered at 1000 °C (Figure 2h), fine crystalline grains of 0.5 µm in diameter were observed [2].

XRD analysis revealed that crystallization occurred in all the scaffolds [2]. This result confirmed what previously reported by Clupper and Hench [33], i.e. the occurrence of a broad crystallisation before a significant viscous flow sintering in 45S5 Bioglass® and other bioactive glasses [2]. As already mentioned in Chapter 2, Bioglass® crystallizes before sintering because it has a very narrow sintering window [17].

In addition, due to the limited viscous flow or diffusion in 45S5 Bioglass®, voids resulting from the burnout of the PU foam were not filled and remained as triangular-shaped pores in the struts (Figure 3) [4]. Analogous morphologies were obtained for several ceramic foams fabricated by the polymer-sponge method [18].

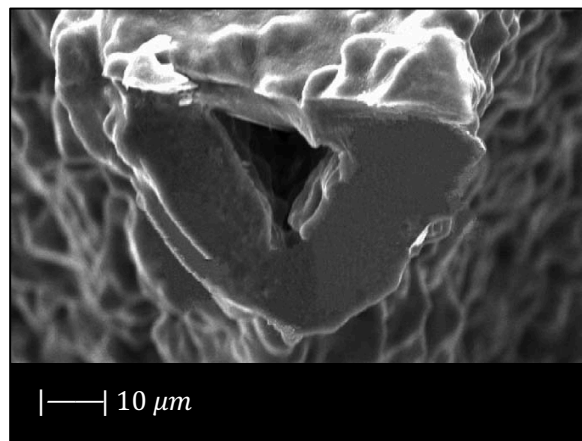


Figure 3: The hollow center of a single strut in a Bioglass® derived foam sintered at 1000 °C for 1 h. Figure adapted from Chen et al. [2].

Subsequently, Bairo et al. [19] have succeeded in obtaining well densified Bioglass® scaffolds without template-derived voids. This achievement was reached by sintering Bioglass® at the temperature at which the powders began to melt. Despite the high sintering temperature used, the scaffolds were characterised by a porosity of 70 %, which is sufficient for BTE applications, and a pore size of between 100 and 600 µm [19].

In the same study Bairo et al. [19] used CEL2 glass to fabricate bioactive glass-ceramic scaffolds. CEL2 is a silicate glass with composition 45SiO₂-3P₂O₅-26CaO-7MgO-15Na₂O-4K₂O mol% originally developed and investigated by Vitale-Brovarone et al. [20] at Politecnico di Torino.

The composition of the system influences the thermal behaviour of the material. Indeed, in CEL2 glass, the viscous flow sintering starts at the glass transition temperature and is totally completed when crystallization begins. For this reason, CEL2 glass allowed obtaining scaffolds with higher degree of sintering compared to Bioglass® scaffolds [19].

In addition, these scaffolds exhibited well-interconnected pores of 100-500 μm in size [19]. CEL2 scaffolds with similar morphology were obtained by Vitale-Brovarone [21]. In this study it was found that particle size represents an important factor to obtain an open and interconnected porosity. Indeed, CEL2 particles with a diameter 30 μm led to a lot of closed porosity in the final scaffold, while ones sieved below 30 μm gave the best sponge impregnation [21]. By reversing the molar quantities of SiO_2 and P_2O_5 in CEL2, phosphate glass ICEL2 glass was obtained [7]. This glass is characterized by a narrower sintering window than CEL2 glass, and consequently a lower degree of sintering was reached in ICEL2 scaffolds (Figure 4) developed by Baines et al. [7] respect to CEL2 scaffolds. However, ICEL2 structures exhibited an effective densification of the pore struts [7]. As far as pore size is concerned, there was no difference between CEL2 and ICEL2 scaffolds [7].

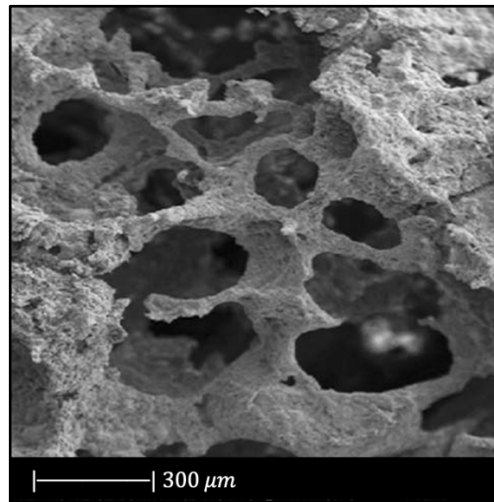


Figure 4: SEM image of ICEL2 scaffold. Figure adapted from Baines et al. [7].

The first calcium phosphate glass scaffold was developed by Legeros et al. [3]. They used a glass in the system of $\text{CaO-CaF}_2\text{-P}_2\text{O}_5\text{-MgO-ZnO}$ and a reticulated polyurethane ester sponge as sacrificial template. This sponge had 500 three-dimensionally interconnected open pores per each linear mm [3].

The slurry was composed of calcium phosphate glass powders, distilled water and organic additives such as binder, dispersant and a drying chemical control additive (DCCA). PVA, PEG and dimethyl formamide were chosen as binder, dispersant and drying chemical control additive, respectively [3]. Before the dipping process, the surface layer of the sponge was treated in a 2% NaOH solution ultrasonically to increase its hydrophilicity [3].

Finally, the glass was sintered for 2h at different temperatures between 650 $^{\circ}\text{C}$ and 850 $^{\circ}\text{C}$ [3].

This procedure was repeated twice to thicken the framework of the scaffolds and as a result to obtain an increased compressive strength [3].

Figure 5 shows the obtained scaffolds after sintering at 850 $^{\circ}\text{C}$ (a) once and (b) twice.

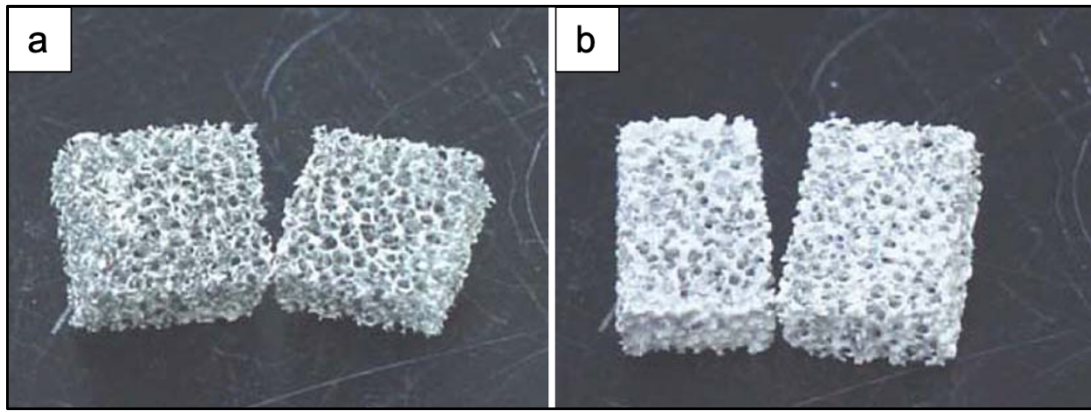


Figure 5: Photographs of PU ester sponge foams after sintering at 850 °C (a) once and (b) twice. Figure adapted from Legeros et al. [3].

The scaffolds obtained under different sintering conditions are shown in Figure 6.

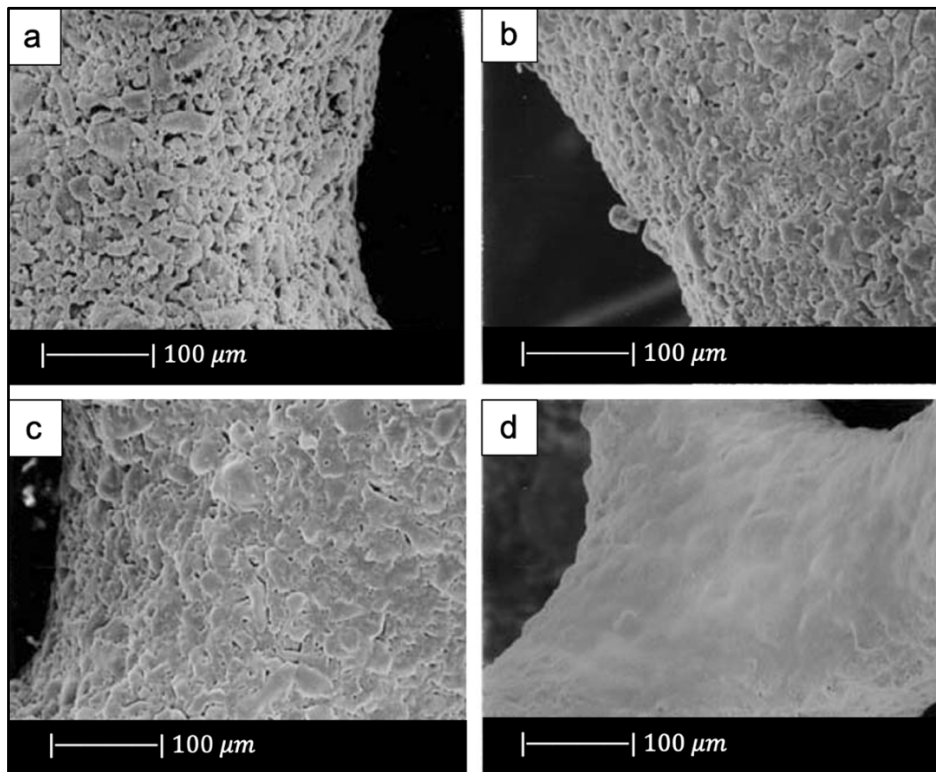


Figure 6: SEM images of the scaffolds sintered at (a) 650 °C, (b) 700 °C, (c) 800 °C, (d) 850 °C. Figure adapted from Legeros et al. [3].

The scaffolds thermally treated at 650 °C showed grey colour while the ones sintered at 850 °C were white. The grey colour was due to sponge remains and additives still present in the sample due to the low sintering temperature used [3].

The glass powders sintered at 650 °C had just started to bond with each other (Figure 6a). As sintering temperature increased, the voids between the powders were reduced in number and size (Figure 6b, c). Scaffolds sintered at 850 °C showed a dense microstructure without voids and cracks (Figure 6d) [3].

The heating rate proved to be one of the most important factors to obtain successful scaffolds. Indeed, the use of a heating rate above 3 °C/min resulted in very weak or locally collapsed scaffolds. This was probably due to the removal of the sponge before the formation of necks between particles and to an insufficient binding strength of the particles. While, by using a heating rate lower than 1 °C/min, a more resistant 3D structure with interconnected open pores was obtained [3].

The macropores in these scaffolds were about 500~800 µm [3].

Later, Lee et al. [22] fabricated calcium phosphate glass scaffolds having the same morphological properties of those developed by Legeros et al. [3]. This similarity is justified by the fact that both the scaffolds were made from the same glass, were sintered at the same temperature and undergone a double coating and double sintering process.

In another study, Bairo and Vitale-Brovarone [23] using an experimental silicate glass with composition 57SiO₂-34CaO-6Na₂O-3Al₂O₃ (mol%), named SCNA, obtained scaffolds with a bimodal pore size distribution: pores > 100 µm and pores < 10-20 µm, which makes them suitable for BTE applications [23]. Indeed, as already mentioned in Chapter 2, pores of 100-500 µm favour new bone formation, bone ingrowth, and capillaries formation, and pores below 50 µm spur the interaction between cells and materials and osteo-integration [24].

A silicate glass widely used for the production of scaffolds is 13-93 glass, whose composition is 53SiO₂-20CaO-6Na₂O-12K₂O-5MgO-4P₂O₅ wt%. This glass is characterized by a larger sintering window compared to 45S5 Bioglass[®], which leads to beneficial viscous flow characteristics and in turns to a greater densification [25].

For example, 13-93 scaffolds fabricated by Fu et al. [25] were fully dense, with a smooth surface and pores of 100-500 µm [25]. In addition, the triangular voids, typical of Bioglass[®], resulting from decomposition of the PU foam, were not present in 13-93 scaffolds, because they were filled by facile viscous flow of the this glass during sintering [25].

13-93 BG scaffolds with similar morphology were produced by Liu et al. [26]. This resemblance is attributable to the fact that Liu, besides the same glass composition, also used the same slurry composition and sintering temperature used by Fu et al [25].

In the same study, Liu et al. used the same glass (13-93 BG) to create also scaffolds with oriented microstructure by unidirectional freezing of camphene-based suspensions. The oriented scaffolds had a lower porosity (50%) and pore size (50-150 µm) compared to the trabecular one [26].

In another study Fu et al. [27] developed scaffolds of borate glass by replacing all the SiO₂ in 13-93 with B₂O₃. This glass composition, called 13-93B3, fully converts to hydroxyapatite at a rate that is three to four times faster compared to silicate 13-93 scaffolds thus paving the way for new applications [27]. The replacement of silicon oxide with boron oxide did not lead to significant differences in the final structure of the scaffold since 13-93 and 13-93B3 scaffolds had approximately the same microstructure and the same pores size (100-500 µm) (Figure 7) [27]. It should be noted that due to the different glass composition (13-93 and 13-93B3), a different sintering temperature was used; each sintering temperature was appropriate to densify the glass without crystallizing it [25], [27].

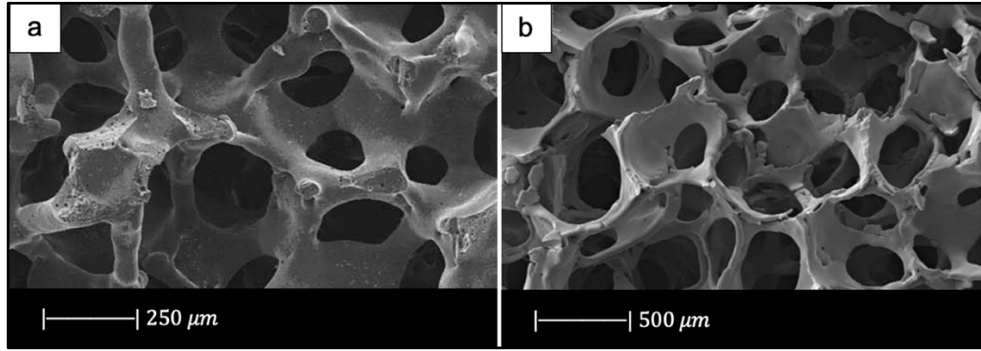


Figure 7: Microstructure of (a) 13-93 BG scaffold [25] and (b) 13-93B3 scaffold [27]. Figures reproduced from Fu et al. [25], [27].

Bi et al. [28] fabricated scaffolds of 13-93B3 glass and Cu-doped 13-93B3 glass with three different microstructures described as trabecular, oriented, and fibrous (Figure 8) [28].

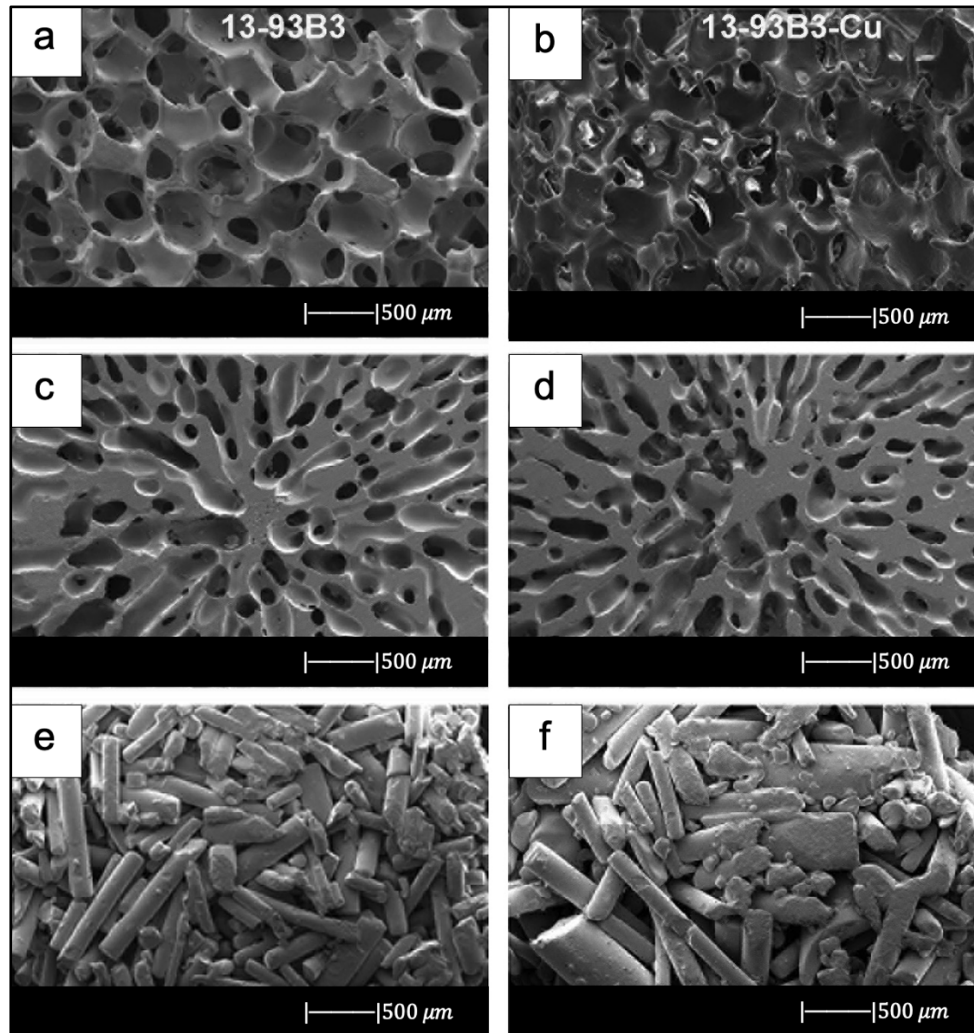


Figure 8: SEM images of 13-93B3 bioactive glass scaffolds (left) and Cu-doped 13-93B3 scaffolds (right) with three different microstructures used in this study: (a, b) trabecular; (c, d) oriented, with the pores are oriented in the radial direction; (e, f) fibrous [28].

The scaffolds with trabecular microstructure were prepared by polymer foam replication technique, the scaffolds with oriented microstructure were fabricated by unidirectional freezing of camphene-based suspensions, and the scaffolds with fibrous microstructure were prepared by thermally fusing randomly oriented short fibres [28].

Generally, the microstructure and the pore size of the undoped scaffolds were similar to the corresponding doped ones, thus suggesting the independence of morphological properties from CuO presence (The difference between Figure 8a and b is due to the use of two different SEM devices) [28].

The trabecular scaffolds were characterized by a porosity of $77 \pm 5\%$ and pore sizes of 200–400 μm . The fibrous scaffolds showed a porosity of $50 \pm 2\%$ and pore sizes of 50–500 μm . The oriented scaffolds exhibited a porosity of $62 \pm 5\%$ and columnar pores with diameters between 60 and 200 μm [28]. Therefore, the foam replica method allows to obtain scaffolds with greater porosity and pore size than scaffolds produced with unidirectional freezing of camphene-based suspensions and thermally fusing randomly oriented short fibres.

13-93B3 scaffolds are limited to the repair of non-loaded bone defects due to their rapid degradation rate.

This limit is exceeded by 13-93B1 borosilicate glass with the composition $6\text{Na}_2\text{O}-8\text{K}_2\text{O}-8\text{MgO}-22\text{CaO}-18\text{B}_2\text{O}_3-36\text{SiO}_2-2\text{P}_2\text{O}_5$ (mol%), obtained by replacing one-third of the molar concentration of SiO_2 in 13-93 glass with B_2O_3 . This glass degrades and converts faster to HA than silicate 13-93 glass but slower than borate 13-93B3.

The scaffolds fabricate by Gu et al. [29] with 13-93B1 glass exhibited a trabecular microstructure with a porosity of $78 \pm 8\%$, and a pore size of 400–650 μm [29].

Since there are no significant differences between the scaffolds produced with 13-93, 13-93B1 and 13-93B3 glass, it is reasonable to assume that the partial or total replacement of SiO_2 with B_2O_3 does not affect the morphological properties of the structure.

By reversing the molar quantities of SiO_2 and B_2O_3 in 13-93B1 glass, the borosilicate glass designated as double alkali borate (D-Alk-B) glass is obtained. Also this glass produces adequate viscous flow during sintering that allows to obtain dense and smooth struts [30].

For example, Liu et al. [30], by sintering this glass at an appropriate temperature between the T_g and T_x , have obtained scaffolds characterized by a very smooth surface and dense struts [30].

The pore size (200–300 μm) was slightly smaller than that typical of scaffolds manufactured using this method [30].

Wang et al. by loading D-Alk-B glass with CuO [31], Fe_3O_4 [32], and ZnO [33] in three different studies respectively, have obtained scaffolds with similar morphology. The similarity between these 3D structure is due to the fact that they were all manufactured using a sponge of 50 ppi and were sintered at about the same temperature [29], [31]–[33]. Furthermore, the fact that these scaffolds all had the same morphology suggested that the doping element did not affect the microstructure.

In the past several years, mesoporous bioactive glasses attracted significant attention for bone regeneration due to their high specific surface area, bioactivity and drug delivery properties [34]. Therefore, MBG were used by several researchers to develop scaffolds, through foam replica method, for bone tissue engineering applications.

For example, Zhang et al. [35], [36] produced MBG scaffolds containing strontium by using co-templates of nonionic block polymer EO20-PO70-EO20 (P123) as mesoporous template and PU sponge as macroporous template [35], [36].

These scaffolds exhibited a well ordered and uniform mesoporous channel structure with pores of 4.5–5 nm and a large-pore structure in the range of 300–500 μm [35], [36].

Moreover, it was noted that the presence of strontium caused a reduction in well-ordered mesoporous structures [35], [36].

In another study, Sui et al. [37] developed MBG scaffold using $^{45}\text{CaCl}_2$. The obtained scaffolds had a mesoporous-macroporous cross-linked structure with mesopores of approximately 6.40 nm and macropores in the range of 300–500 μm and [37].

More recently, foam replica method was also used to make glass/polymer composite scaffolds.

The idea of developing composite scaffolds stems from the need to obtain structure with better mechanical properties.

It is known that bone is a composite material, and the high tensile strength and fracture toughness of bone are largely due to the presence of the collagen fibres [38]. Based on this knowledge, BG scaffolds can be combined with polymers in order to improve their mechanical behaviour [38].

For example, Bretcanu et al. [39] produced composite scaffolds by coating 45S5 Bioglass[®]- foams with bacteria-derived P(3HB) polymer [39].

Firstly, 45S5 Bioglass[®] scaffolds were fabricated by the foam replica method. During heat treatment up to 1100 °C the glass crystallized, resulting in glass-ceramic scaffolds. Then, the obtained structures were immersed into P(3HB) solution for a fixed time and left to dry [39].

An important result is that the samples maintained a highly porous structure with interconnected pores despite the polymer coating [39].

Balasubramanian et al. [40] developed composite scaffolds that imitated osteochondral region composed of a highly bioactive, porous bone side, and a collagen containing fibrillar cartilage portion [40].

Foam replica method fabricated highly porous 45S5 Bioglass[®]- based scaffolds similar to the cancellous bone structure. Dip-coating by PCL considerably improved the mechanical behaviour of the scaffolds. Electrospinning created a layer of submicrometric collagen-PCL fibrous mesh over the Bioglass[®] scaffolds [40].

These layers showed alignment of the fibres in between the struts, which is believed to be beneficial for the flattening, elongation, and attachment of chondrocytes [40].

Composite scaffolds were also manufactured with other glasses than 45S5 Bioglass[®].

For example, Erol et al. [41] developed boron-containing silicate glass scaffolds coated with alginate cross-linked with copper ions [41].

Alginate formed a uniform coating on the surface of the scaffold without clogging the pores, whose size ranged from 100 μm to 500 μm [41].

The struts appeared well densified and the voids resulting from the sponge burn-out were not present. This result suggests that the sintering conditions were correctly chosen, leading to an extensive densification by viscous flow without the formation of crystalline phases [41].

The study of Wu et al. [34] offers an example of composite scaffold produced by using a mesoporous bioactive glass [34]. This research group used P123 as mesoporous template and PU sponge as macroporous template to produce the scaffold. Then, the scaffold was modified with silk solution in order to improve the mechanical properties [34].

The resulting structure exhibited a smooth silk film on the surface of the pores. The silk modification improved the continuity and homogeneity of pore network and did not affect the pore size (200–400 μm) [34].

Recently, hierarchical porous scaffolds, that allowed transportation on various scales, gained the attention of several researchers.

For example, Tang et al. [42] produced a trimodal macro/micro/nano-porous scaffold (TMS) by using $\text{EO}_{106}\text{PO}_{70}\text{EO}_{106}$ (F127) as mesoporous template, methyl cellulose as microporous template, and PU sponge as macroporous template. The mesoporous structure was tailored for the recombinant human bone morphogenetic protein-2 (rhBMP-2) entrapment [42].

TMS showed interconnected macropores of 200-500 μm in size, micropores $< 10 \mu\text{m}$ and rhBMP-2 entrapped mesopores of 7.5 nm [42].

3.2.2 Replica of Natural Templates

In recent years, natural structures were a source of inspiration for biomedical researchers [43] [44], in the attempt to improve mechanical and biological performance of bioactive glass scaffolds supporting bone healing and regeneration.

3.2.2.1 Replica of Marine Sponges

The replication of PU foams created highly porous and interconnected structures that however were characterized by low mechanical properties, which limited their suitability for clinical applications. As a consequence, marine sponges were investigated as sacrificial templates in order to obtain scaffolds with reduced total porosity and, as a result, increased mechanical properties without losing pores interconnectivity, required for considerable bone ingrowth [10].

Cunningham et al. [45] were the first to use marine natural sponges as sacrificial templates in place of PU foams for the development of hydroxyapatite-based scaffolds [45]. The obtained scaffolds showed high porosity and pores between 0 and 200 μm , which proved to be sufficient for the full integration of the foam in natural tissue [45].

Later, natural marine sponges were used by Boccardi et al. [10] to develop Bioglass[®] based scaffolds by the replica technique. They used *Spongia Agaricina* (SA) and *Spongia Lamella* (SL) harvested respectively from the Indo-Pacific Ocean (Pure Sponges, UK) and Mediterranean Sea (Hygan Products Limited, UK) belonging to the ‘Elephant Ear’ family [10]. These sponges, due to the millenarian evolution for water filtration, that led to the formation of an interconnected porous structure, are promising materials in the development of bone tissue engineering scaffolds [46].

The SA and SL showed a vase or fan shaped growth and a surface composed by fine fibres [10]. It was possible to identify two different structures, as reported by Pronzato and Manconi [46]: an inhalant (Figure 9a and c) and an exhalant (Figure 9b and d) surface, depending on the directionality of water flow in the sponges in their natural habitat [10]. Architectural properties of natural marine sponges are summarized in Table 1 [10].

Table 1: Summary of natural marine sponge architecture properties. Table adapted from Boccardi et al. [10].

Property	SL	SA
Pore dimension inhalant surface	1.0 ± 0.1 mm	590 ± 50 μ m
Pore dimension exhalant surface	1.7 ± 0.2 mm	920 ± 90 μ m
Pore wall thickness	540 ± 80 μ m	400 ± 40 μ m

As regard the scaffolds production, the replica technique was used according to the method proposed by Chen et al. [2]. The melt-derived 45S5 Bioglass[®] powder (particle size ~ 5 μ m) was added to PVA-water solution to obtain the slurry [10]. The SL was immersed in the Bioglass[®] powder slurry three times, while SA only required two coating cycles. The burn-out and sintering conditions were 400 °C/1 h and 1050°C/1 h respectively, and the heating and the cooling down rates were 2 and 5 °C min⁻¹ respectively [10].

SEM images of the SA and SL replica foams (BG-SA and BG-SL respectively) obtained are shown in Figure 9e-h.

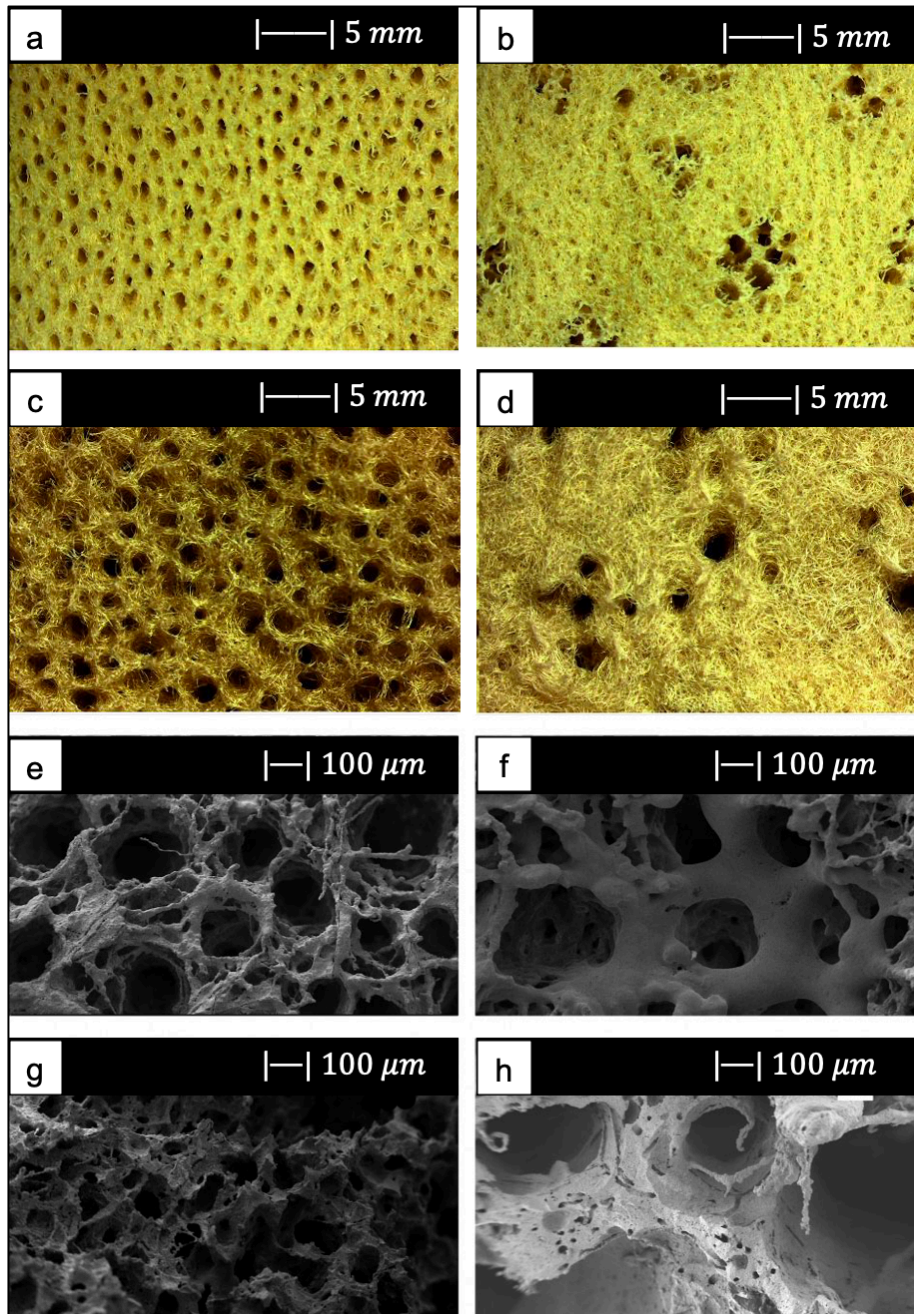


Figure 9: (a) Inhalant surfaces and (b) exhalant surface of SA sponge. (c) Inhalant surfaces and (d) exhalant surface of SL sponge. (e) Inhalant surfaces and (f) exhalant surface of SA replica foam (BG-SA). (g) Inhalant surfaces and (h) exhalant surface of SL replica foam (BG-SL). Figure adapted from Boccardi et al. [10].

SEM images showed that almost all the spaces between the fibres of the marine sponges were filled with the Bioglass® particles, and the macroporous structure was optimally replicated. Indeed, it was still possible to distinguish the inhalant and exhalant surfaces of both kinds of sponge [10].

Small sized pores connecting the larger pores were observed, creating highly interconnected porous structure (>99.5%) [10].

Overall pore size was in the range 0–600 μm and 0–900 μm and the an average pore size was 215 ± 20 μm and 265 ± 120 μm for the BG-SA and BG-SL respectively [10]. In particular, the marine sponge

foams were characterized by a large number of pores in the range of 0–200 μm , and in the range 200–500 μm [10].

The presence of a large number of pores in the range of 0–200 μm is fundamental for the complete colonization of the scaffolds by cells, as it improves the flow of biological fluids also inside the porous structure, and fosters the complete integration with the surrounding tissue [47], [48]. Whereas pores in the range of 200–500 μm are important for bone integration and neovascularization [47], [48].

The total porosity of BG-SL and BG-SA was $76\pm 2\%$ and $68\pm 0.2\%$ respectively. Hence, the marine sponges foam replicas had a lower total porosity than PU foam replicas, but at the same time these foams had a considerable microporosity, which was almost totally absent in the PU foam replicas [10].

The achievement of improved mechanical properties, which will be discussed later, combined with the high pore interconnectivity and wide pore size distribution, confirmed the chance of using natural marine sponges as porous precursors for fabrication of bone tissue scaffolds [10].

3.2.2.2 Replica of Bread

Fiume et al. [8] used for the first time stale bread as a sacrificial template for the fabrication of scaffolds for BTE. The choice fell on stale bread, since it offers several advantages such as easy availability, contribution to food waste disposal and cost effectiveness of the production process [8]. They used industrial bread obtained from industrial wastes (Roberto Industria Alimentare S.r.l., Treviso, Italy) [8].

SEM images showed that the industrial bread had a trabecular morphology (Figure 10a, b) which resembled that of cancellous bone [8]. The bread was indeed characterized by pores of regular size and shape, homogeneously distributed and well interconnected. Both large macropores within 100–300 μm and smaller ones between 10–20 μm were observed [8].

For scaffold production, 47.5 B glass with composition $47.5\text{SiO}_2\text{-}20\text{CaO-}10\text{MgO-}2.5\text{P}_2\text{O}_5\text{-}10\text{K}_2\text{O-}10\text{Na}_2\text{O}$ (mol%) [49], produced by melt-derived technique, was used as starting material.

The slurry was prepared by adding the glass to water-PVA solution. The green bodies were thermally treated at 750 $^{\circ}\text{C}$ for 3 h (heating rate 5 $^{\circ}\text{C}/\text{min}$). The sintering temperature was set above the crystallization onset, which was detected at $T_x=700$ $^{\circ}\text{C}$, because of the brittleness of the scaffolds sintered at lower temperatures, as assessed in the early tests [8].

Figure 10c, d shows the SEM images of the scaffolds obtained.

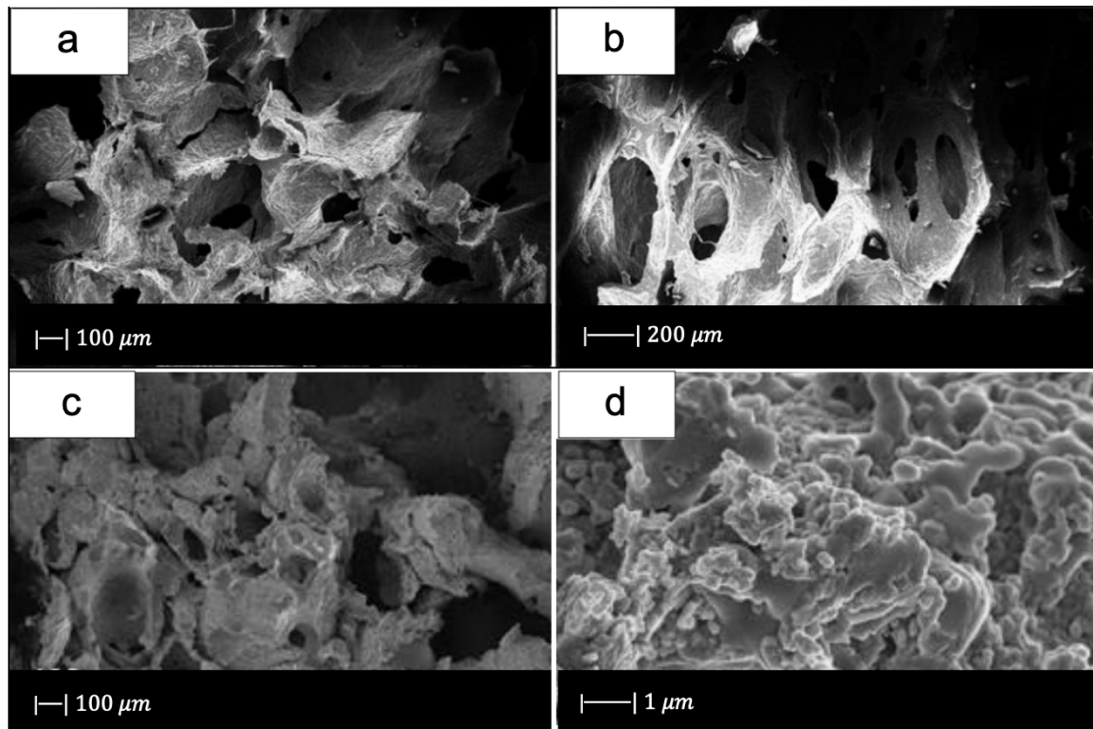


Figure 10: SEM micrographs of (a, b) bread used, and (c,d) glass scaffold. Figure adapted from Fiume et al. [8].

Upon sintering, the sample underwent notable changes regarding the morphology and pore size distribution in comparison with the starting template. However, the morphology of the original bread template was still clearly distinguishable (Figure 10c) [8].

Particularly, the densification that occurred during sintering process caused a decrease in pore size [8]; however, they still had a suitable size for TE purposes. Indeed, inter-pore windows of 20–100 μm are sufficient to allow the vascularization of the scaffold [50].

From the images obtained at higher magnifications (Figure 10d), it could be observed in the scaffold the same the wrinkled surface of the bread template, which is beneficial for the cell-implant interactions. Indeed, it was found that micrometric roughness on the device surface can foster protein-mediated cell adhesion [51].

In addition, from the SEM images, some voids were detected inside the structure. Probably this was due to a poor impregnation of the sacrificial template [8].

The scaffolds had a porosity of 72 ± 1.5 vol% which lies in the range of spongy bone [8].

The outcomes exhibited great promise and supported the use of stale bread as sacrificial template for the development of highly sustainable BTE approaches.

3.2.2.3 Replica of Vegetal and Fungal Templates

Corn stalks, cattail stems and mushroom stalks were used as macroporous templates to fabricate HPBG scaffolds [14], [52], [53].

Replica of Corn Stalk

Jiang et al. [14] used foam replica method in combination with EISA in order to produce hierarchical porous TiO₂-bioglass scaffolds [14].

They used a plant corn stalk as macroporous template and P123 as mesoporous template [14].

They first prepared the precursor solution using P123. Later, the corn stalks were soaked in the precursor solution for 1 day, and then the samples were dried at room temperature for 12 h. The process of dipping and drying was repeated twice for each scaffold. Finally, the samples were thermally treated at 550 °C for 5 h in air to burn out the corn stalk templates [14].

SEM photographs of the corn stalks and the obtained scaffold are given in Figure 11.

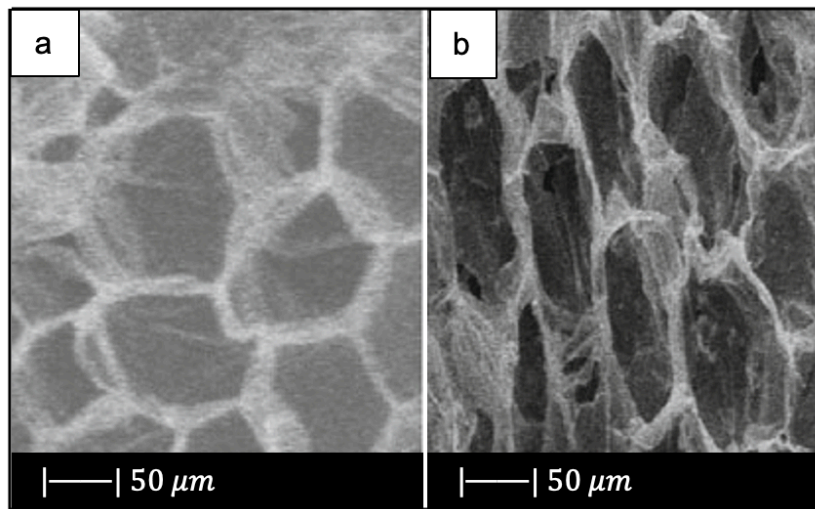


Figure 11: SEM images of (a) the corn stalk and (b) TiO₂-glass scaffold. Figure adapted from Jiang et al. [14].

As can be seen, the scaffold replicated perfectly the original morphology and structure of the corn stalk, exhibiting a 2D ordered macroporous structure characterized by a pore size of about 30–50 μm [14].

Macropores >10 μm not only increase the contact surface and flow resistance for cell adhesion, but also carry the blood and the large size matter to a new tissue. In addition, they promote free penetration of cells and intracellular fluid [54].

As regard the nanoporous structure, the sample had a pore volume of approximately 0.16 cm³/g, a mesopore size of 4.4 nm, and a surface area of 153 m²/g [14].

Replica of Cattail Stem

Also Ma et al. [52] used foam replica method in combination with EISA in order to produce HPBG scaffolds [52].

They used a cattail stem as a macroporous template and P123 as mesoporous template. The cattail stem was characterized by pores from 40 to 60 μm, as shown in Figure 12a [52].

At first, the precursor solution was prepared by using P123, then the cattail stem was soaked in the precursor solution for 1 day, and the plant templates were dried at room temperature for 12 h. These processes were repeated twice. After all, the sample was calcined at 550 °C for 6 h [52].

SEM images of the obtained HPBG scaffold are given in Figure 12b.

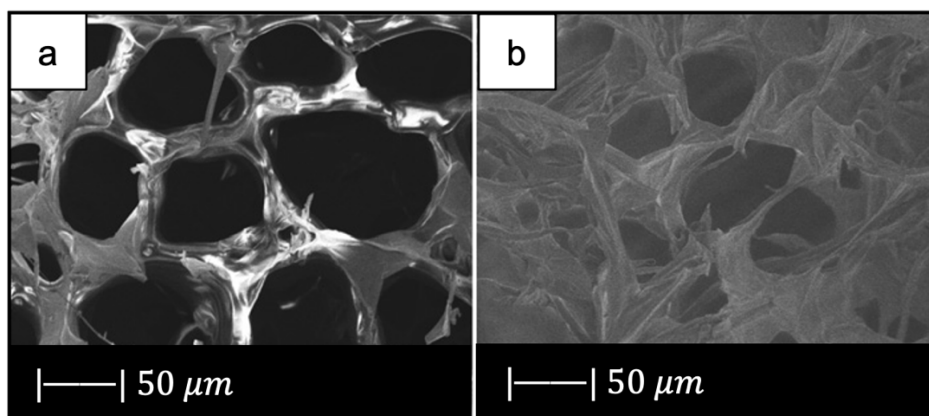


Figure 12: SEM images of (a) plant template cattail stalks, and (b) the scaffold obtained. Figure adapted from Ma et al. [52].

Figure 12b shows that the material approximately copied the macropores structure of cattail stem [52].

The scaffold was characterized by the presence of macropores of 30–50 μm in size. The pore size was smaller than that of the cattail stem due to the high temperature treatment [52].

As mentioned in Chapter 2, pores below 50 μm stimulate the interaction between cells and materials, and osteo-integration [24].

The hierarchical porous glass had a pore volume of 0.137 cm³/g, a mesopore size of 3.86 nm, and a surface area of 154.22 m²/g [52].

Thus, the HPBG obtained by Ma et al. [52] with macroporous structures and mesoporous structures were found to be suitable for bone tissue engineering and drugs delivery [52].

Replica of Mushroom Stalk

Han et al. [53] fabricated hierarchical porous bioactive glass (SiO₂–CaO–P₂O₅) scaffolds by using a dual-template method [53].

Mushroom stalk was used as the macroporous template, and P123 was used as the mesoporous template. The choice of the macroporous template fell on the mushroom stalk because of its unique three-dimensional mycelium and high pore volume. Mycelium is the vegetative part of mushrooms, composed of a mass of branching, thread-like hyphae. It is characterized by a 3D porous structure with 20–40 μm in size, as shown in Figure 13a [53].

As regard the scaffolds production, Han et al. [53] prepared a mesoporous bioactive glass precursor (MBG-p) solution using P123 as mesoporous template. Then, the mushroom stalks were soaked in MBG-p solution for 1 day, and then the sample were dried at room temperature for 12 h. This process of dipping and drying was repeated twice for each scaffold. Finally, the samples were thermally treated at 550 °C for 5 h in air to burn out the mushroom stalk templates. The obtained hierarchical porous materials were named MRBG [53].

Figure 13b shows a representative SEM image of MRBG [53].

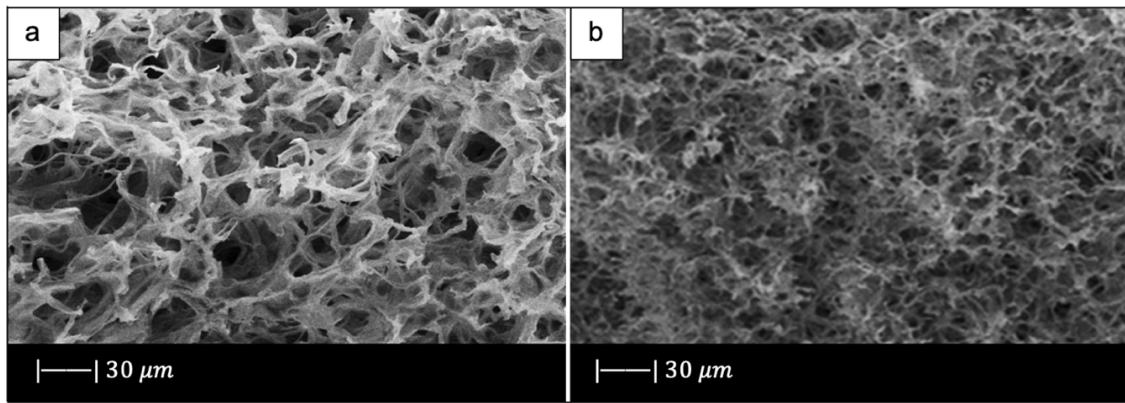


Figure 13: SEM images of (a) mycelium and (b) MRBG. Figure adapted from Han et al. [53].

The obtained scaffold showed the reticulate structure of the vegetal template with a pore size of 10–30 μm . Therefore, the three-dimensional structure of the mycelium was replicated perfectly. However, MRBG showed decreased diameter compared to mycelium due to the high temperature treatment [53].

As concern the nanoporous structure, the MRBG had a pore volume of approximately $0.14 \text{ cm}^3/\text{g}$, a mesopore size of 3.4 nm, and a surface area of $107.28 \text{ m}^2/\text{g}$ [53].

Due to both the macroporous and mesoporous structure, MRBG exhibited good biomineralization, cell attachment and controlled drug delivery ability. These aspects made the obtained scaffold a promising material for tissue regeneration [53].

3.2.2.4 Replica of Demineralized Bone Matrix

Using bone matrix as sacrificial template could be a valuable strategy to replicate the most peculiar morphological features of trabecular bone [55].

However, calcined bone matrix allows duplicating only the macroporous bone structure, because the fine microstructure cannot be properly reproduced [56], [57].

On the contrary, demineralized bone matrix (DBM) is an excellent sacrificial template because it retains also the ordered microporous structure of natural bone thanks to the removal of well-assembled hydroxyapatite nanoclusters from the bone matrix. Besides, the intrinsic elasticity of organic matrix facilitates the infiltration of the ceramic/glass suspensions, thus allowing a complete impregnation of the template [55].

Demineralized cancellous bone matrix was used by Xia et al. [55] as sacrificial template to developed a biomorphic bioactive glass-gelatin composite scaffold having both structure and mechanical behaviour similar to cancellous bone [55].

As starting materials for the scaffolds manufacture, 58-S sol-gel glass and gelatin (Sinopharm, China) were used [58].

In particular, bones from bovine femoral distal condyles and from bovine femoral heads were selected, and DBM was prepared according to published procedures [56], [57].

The demineralized bone matrix templates were soaked in the glass slurry and the obtained samples were calcined at 700°C for 3 h at a heating rate of $1^\circ\text{C}/\text{min}$ to remove the organic matrix. Then, the obtained bioactive glass scaffold was immersed into gelatin solution to make gelatin solution enter

into the gaps of the pore walls of the BG scaffold. The obtained composite scaffold was then dried at room temperature [55].

Figure 14 shows the optical images of a bioactive glass scaffold and its corresponding composite scaffold, as well as SEM images of biomimetic bioactive glass scaffold and natural calcined spongy bone [55].

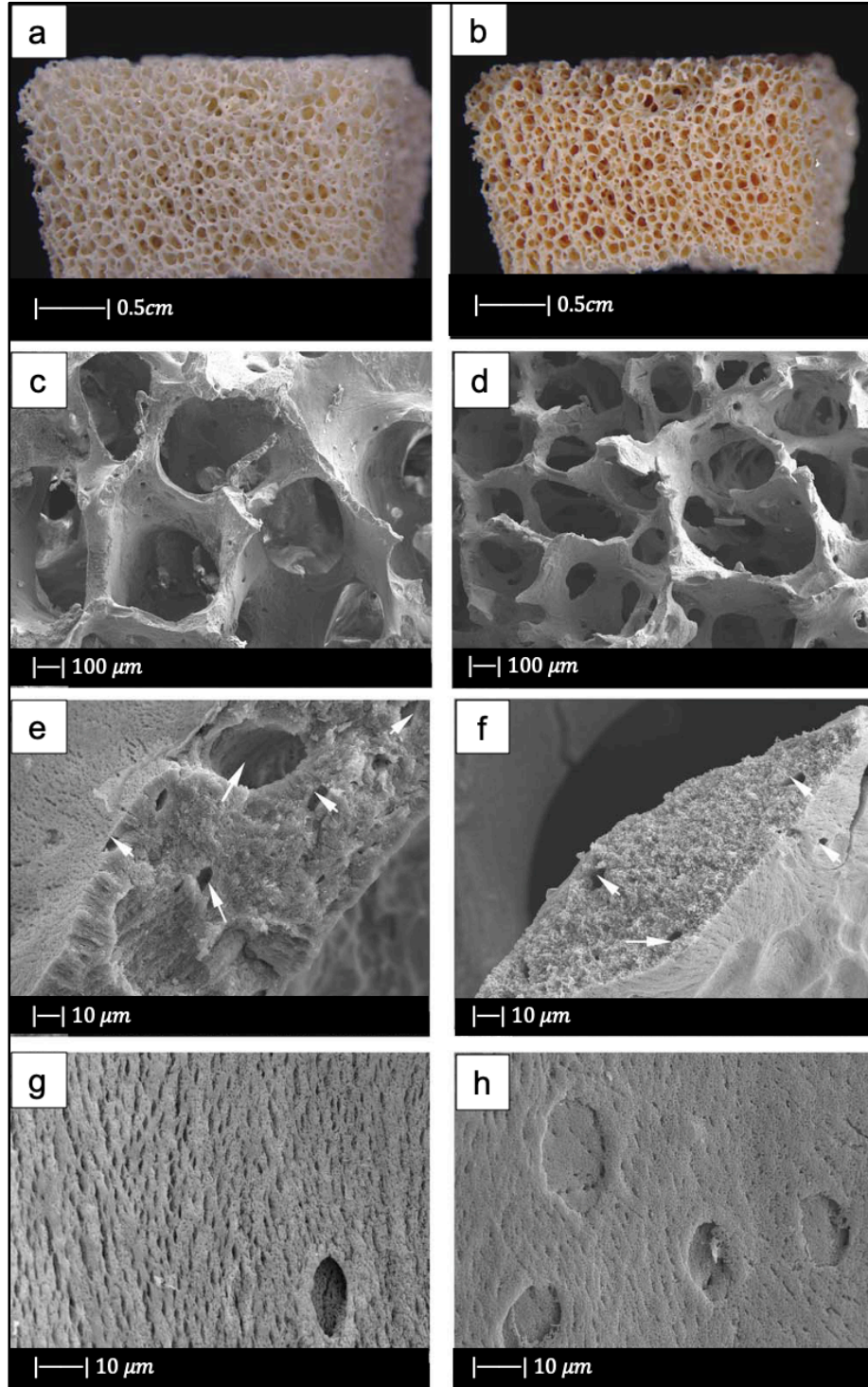


Figure 14: (a) Bioactive glass scaffold. (b) Bioactive glass/gelatin composite scaffold. SEM images of (c,e, g) biomimetic bioactive glass scaffold, and (d,f, h) natural calcined cancellous bone. Figure adapted from Xia et al. [55].

Both the BG scaffold and the bioactive glass/gelatin composite scaffold were characterized by high porosity and good pore connection (Figure 14a, b) [55].

It can be noticed that the BG scaffold had similar macroscopic and microscopic structures to calcined cancellous bone (Figure 14c-h) [55].

The macrostructure of the bioactive glass scaffold (Figure 14c) was characterized by pores of 300-700 μm and an excellent pore interconnections [55].

Figure 14e shows that the bioactive glass scaffold perfectly replicated the microporous structure of the calcined spongy bone matrix (Figure 14f) [55].

As can be seen from Figure 14g, bioactive glass particles in the pore walls had a well-oriented arrangement. In addition, between the glass particle bunches, ordered bunches of holes can be observed. Similar holes, which connected between macropores on the pore wall, were also present in the calcined spongy bone (Figure 14h) [55].

The porosities of DBM, calcined spongy bone, and BG scaffold were $77.1\% \pm 2.1\%$, $86.6\% \pm 1.5\%$, and $89.3\% \pm 2.0\%$, respectively. The porosity of bioactive glass/gelatin composite scaffold was around 88% [55]. These porosities lie in the range of porosity of the spongy bone, which is between 50% and 95%, as mentioned in Chapter 1 [59].

Therefore, by using DBM as template, a biomorphic scaffold with highly porous macrostructure and fine microstructure was produced. The most interesting aspect of the composite scaffold was its excellent mechanical properties, which will be discussed later [55].

3.3 Mechanical Properties

Just like morphological properties, also the mechanical behaviour of the scaffold is influenced by the sacrificial template; indeed, as mentioned in Chapter 2, compressive strength is affected by scaffold porosity and 3D architecture, which, in turn, depends on the template used.

Other factors that influence mechanical properties are the composition both of the glass and the slurry, the number of times the template is immersed into the slurry and the immersion duration.

In addition, the mechanical performances are also affected by process parameters, such as the sintering temperature and the heating rate.

The mechanical properties of the scaffolds are mainly evaluated in terms of stress-strain curve as well as compressive strength.

The stress-strain curve is a reliable and complete source for the evaluation of mechanical properties of scaffolds for BTE [2].

A typical compressive stress-strain curve concerning a scaffold fabricated by foam replica method is shown in Figure 15 [2].

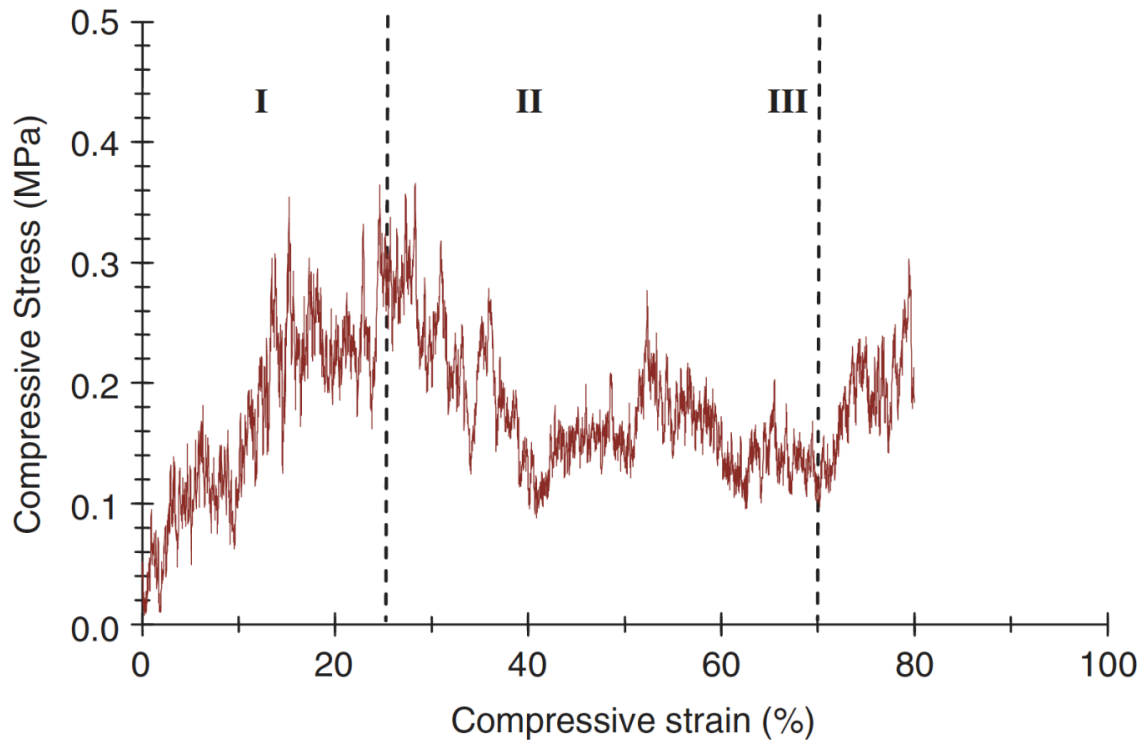


Figure 15: A typical compressive stress-strain curve of the 45S5 Bioglass[®]-based foams sintered at 1000 °C for 1 h. (The porosity of the foam was 91%). Figure adapted from Chen et al. [2].

It can be observed that the stress-strain curve is “jagged”, i.e. characterized by the presence of multiple peaks, which are typical of cellular ceramic materials under compression conditions. As soon as the load is applied, the scaffold tends to crack in thin struts at stress-concentrating sites, causing a temporary decline of apparent stress. However, the overall structure still has the ability to bear increasing loads, thus determining the increase in stress values [2].

As can be seen in Figure 15, a typical stress-strain curve of a glass-based scaffold is characterized by three distinct areas.

In stage I, the stress-strain curve shows a positive slope until a maximum stress is reached. This maximum stress causes the thick struts of the foam to fracture, so that the stress-strain curve shows a negative slope in stage II. In stage III, fractured foam densifies as stress increases, which is the typical behavior of scaffold under compression [2].

A matter of fundamental importance for the successful achievement of a scaffold for load-bearing applications is the need to find a balance between the porosity and the mechanical properties [60]. As already mentioned in Chapter 2, a highly interconnected porous structure with a minimum porosity value of 50 vol% is necessary for the scaffold to fully integrate once implanted. However, porosity affects the mechanical competence of the scaffold, as strength and stiffness progressively decrease when the volume fraction of porosity increases [61].

Figure 16 shows theoretical and experimental compressive strength vs porosity of Bioglass[®]-based scaffolds developed by Chen et al. [2] and those of hydroxyapatite-based foams reported in literature [62]–[64].

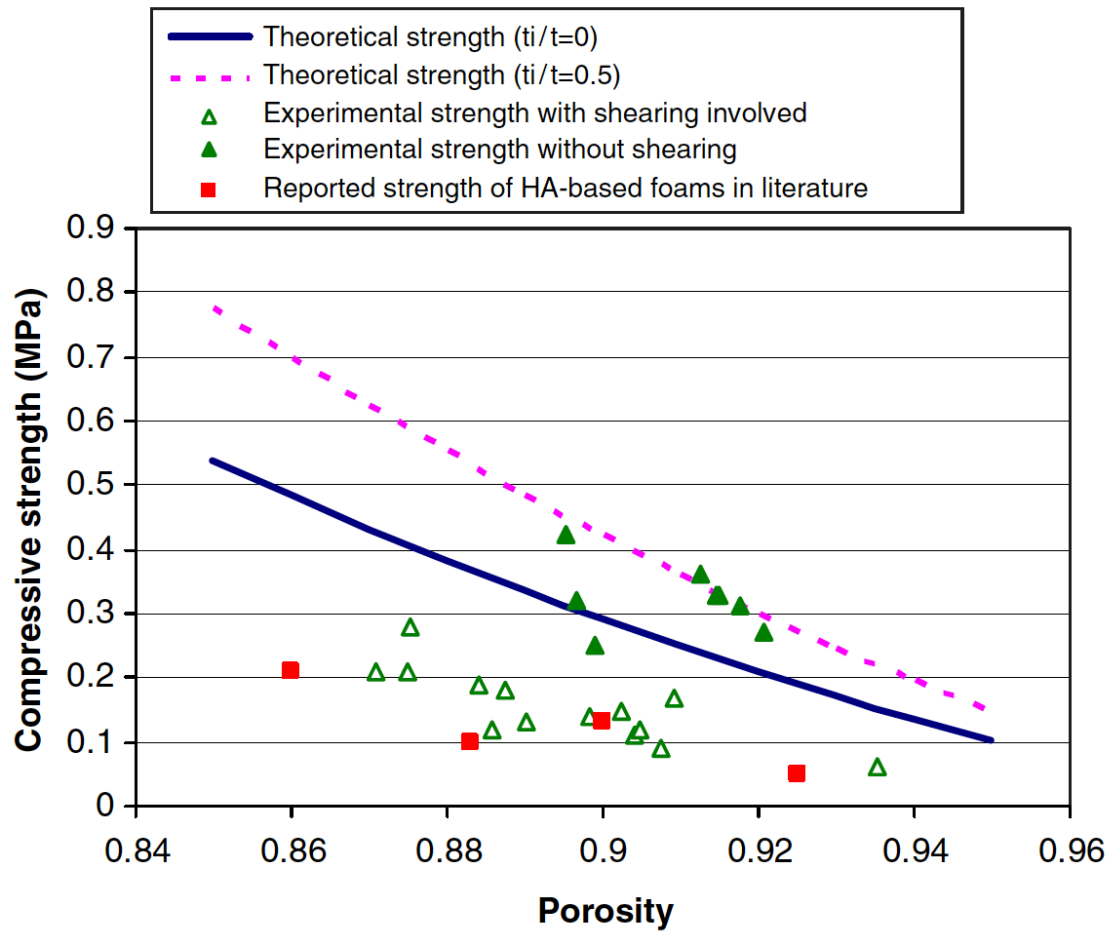


Figure 16: Theoretical and experimental compressive strength values of Bioglass[®]-based scaffolds fabricated by Chen et al. [2], and those of hydroxyapatite- based foams reported in literature [62], [63], [64] (The foams with porosity lower than 89% were prepared by double coating). Figure adapted from Chen et al. [2].

Mechanical properties, pore size and porosity of several bioactive glass scaffolds produced by the foam replica method are summarized in Table 2.

All studies reported in Table 2 have already been reviewed from a morphological point of view in the section 3.2 (Variants of the process and impact on the morphological properties) of this chapter.

Table 2: Pore characteristics and compressive strength of several bioactive glass scaffolds produced by foam replica method.

Glass System	Template	Pore Size (µm)	Porosity (%)	Compressive Strength (MPa)	Reference
45S5 Bioglass® : 45SiO ₂ -24.5CaO-24.5Na ₂ O-6P ₂ O ₅ wt%	PU	510-720	~90	0.3–0.4	Chen [2]
45S5 Bioglass® : 45SiO ₂ -24.5CaO-24.5Na ₂ O-6P ₂ O ₅ wt%	PU	100-600	~70	~2.5	Baino [19]
45S5 Bioglass® : 45SiO ₂ -24.5CaO-24.5Na ₂ O-6P ₂ O ₅ wt%	SA sponge	0–600	68±0.2	1.8±0.3	Boccardi [10]
45S5 Bioglass® : 45SiO ₂ -24.5CaO-24.5Na ₂ O-6P ₂ O ₅ wt%	SL sponge	0–900	76±2	4±0.4	Boccardi [10]
47.5. B : 47.5SiO ₂ -20CaO-10MgO-2.5P ₂ O ₅ -10K ₂ O-10Na ₂ O mol%	Bread	-	72±1.5	0.62±0.2	Fiume [8]
CEL2 : 45SiO ₂ -3P ₂ O ₅ -26CaO-7MgO-15Na ₂ O-4K ₂ O mol%	PU	100-600	66.4±2	4.5±0.9	Baino [19]
CEL2 : 45SiO ₂ -3P ₂ O ₅ -26CaO-7MgO-15Na ₂ O-4K ₂ O mol%	PU	100-500	~70	1±0.4	Vitale-Brovarone [21]
I-CEL2 : 3SiO ₂ -45P ₂ O ₅ -26CaO-7MgO-15Na ₂ O-4K ₂ O mol%	PU	100-500	82±6.7	0.4 ± 0.2	Baino [7]
CaO-CaF ₂ -P ₂ O ₅ -MgO-ZnO	Polyurethane ester	500-800	-	~1.5	Legeros [3]
SCNA : 57SiO ₂ -34CaO-6Na ₂ O-3Al ₂ O ₃ mol%	PU	~240	56±6	18±5	Baino-Vitale Brovarone [23]
13-93 : 53SiO ₂ -20CaO-6Na ₂ O-12K ₂ O-5MgO-4P ₂ O ₅ wt%	PU	100–500	85±2	11±1	Fu [25]
13-93B3 : 6Na ₂ O-7.9K ₂ O - 7.7MgO-22.1CaO-54.6B ₂ O ₃ -1.7P ₂ O ₅ mol%	PU	100-500	82±3	5±0.5	Fu [27]
D-Alk-B : 6Na ₂ O-8K ₂ O-8MgO-22CaO-18SiO ₂ -2P ₂ O ₅ -36B ₂ O ₃ mol%	PU	100-500	67.7±2.6	9.7±1.3	Liu [30]
45S5 Bioglass® : 45SiO ₂ -24.5CaO-24.5Na ₂ O-6P ₂ O ₅ wt%	PU	~470	85±2	~1.5	Bretcanu [39]
45S5 Bioglass® : 45SiO ₂ -24.5CaO-24.5Na ₂ O-6P ₂ O ₅ wt%	PU	400-700	79±1	0.24±0.06	Balasubramanian [40]
65SiO ₂ -15CaO-18.4Na ₂ O-0.1MgO-1.5B ₂ O ₃ wt%	PU	110-550	82±2	1±0.3	Erol [41]
58S : 58SiO ₂ -33CaO-9P ₂ O ₅ wt%	DBM	300–700	89.3±2.0	0.16±0.05	Xia [55]
58S-Gelatin : 58SiO ₂ -33CaO-9P ₂ O ₅ wt%, gelatin > 10 wt%	DBM	300–700	87.7±1.1	4.9±0.2	Xia [55]
5.0Silk-MBG : SiO ₂ -CaO-P ₂ O ₅	PU	200–400	~94	~0.25	Wu [34]

As can be seen, most of the scaffolds produced by foam replica method have porosity levels and a compressive strength comparable to those of spongy bone and thus are potentially suitable to be used in BTE applications. Indeed, the scaffolds reported show a level of porosity between 56 to 94 % which fall within the typical range of spongy bone (50-95 vol%). In addition, their compressive

strength is found to be between 0.16 to 18 MPa, again within the typical values reported for human trabecular bone (0.1–16 MPa).

The low compressive strength exhibited by 45S5 Bioglass[®] scaffolds developed by Chen [2] was due to the highly narrow sintering window of this glass [17]. Indeed, 45S5 Bioglass[®] suffers from limited viscous flow and crystallizes prior to densification [25]. Accordingly, the voids resulting from the burnout of the PU foam are not easily filled and remain as triangular-shaped pores in the struts; these pores cause a decrease in the strength of the scaffold [4].

In addition, it should be considered that 45S5 Bioglass[®] scaffolds developed by Chen [2] are the most porous of all the scaffolds analysed in Table 2. As already mentioned, generally a high porosity is responsible for low mechanical performance [61].

Since it was found that the compressive strength of a HA scaffold considerably increases *in vivo* due to tissue ingrowth, it might not be required to develop a scaffold with a mechanical strength equal to bone, because cultured cells on the scaffold and new tissue formation *in vitro* form a biocomposite and considerably increase the time-dependent strength of the foam [65].

However, an ideal scaffold should have at least an appropriate strength and fracture toughness in order to be handled for tissue engineering applications and to ensure an initial stability of the implant. In view of this, 45S5 Bioglass[®]-based scaffolds possessed a suitable mechanical competence [2].

Baino et al. [19] obtained more resistant 45S5 Bioglass[®]-scaffolds compared to those fabricated by Chen [2]. They achieved this result by sintering the glass at higher temperature (1180 °C) [19] than the one used by Chen (1000 °C) [2].

An increment of sintering temperature led to an increase in mechanical properties for two reasons: (1) sintering at higher temperature involves a greater volumetric shrinkage of the scaffold, entailing in turns a lower porosity in the final structure; (2) by using a higher sintering temperature, an improved densification of scaffold trabeculae is obtained [19].

Despite the high sintering temperature used, these scaffolds had a porosity level (70 %) sufficient for BTE applications [19].

Equally resistant 45S5 Bioglass[®]-scaffolds were obtained from the replica of marine sponges. Indeed, the reduced porosity of the natural marine sponges made it possible to create scaffolds with reduced porosity, and as a result, with high compressive strength [10].

Moreover, natural marine sponges were characterized by interconnected porous structures, which resulted in 45S5 Bioglass[®] - based scaffolds with high pore interconnectivity and wide pore size distribution [10].

Not only marine sponges were used as natural-sacrificial template, but also stale bread.

The bread-derived scaffolds of 47.5B produced by Fiume et al. [8] had a compressive strength about two times higher than that of PU-derived 45S5 Bioglass[®] scaffolds fabricated by Chen et al. [2].

CEL2-derived-scaffolds fabricated by Baino et al. [19] had twice the mechanical strength of Bioglass[®] - derived scaffolds also produced by Baino et al. [19].

The different compressive strength cannot be only due to almost negligible decrease of porosity; but it was attributed mainly to the different sintering windows of the two glass [19]. Indeed, as already stated, due to the narrow sintering window, Bioglass[®] crystallizes before the occurrence of a significant viscous flow sintering; while in CEL2 glass the viscous flow sintering begins at T_g and is fully completed when crystallization begins. Therefore, the CEL2 glass reached a higher densification compared to Bioglass[®] and as a result, it was more resistant [19].

In addition, the different mechanical behaviour of the two types of scaffolds was also due to the different crystalline phases in the materials. The densities of CEL2-scaffold crystalline phases were higher in comparison to that of Bioglass® scaffold. Since higher the density of a material, higher is its mechanical strength, the crystalline phases of CEL2 scaffolds gave the structure higher mechanical strength in comparison to that conferred to Bioglass® scaffolds [19].

CEL2 scaffolds produced by Vitale Brovarone et al. [21] were characterized by a lower compression strength than CEL2 scaffolds produce by Baino et al. [19]. It is plausible to attribute this phenomenon to the use of a lower sintering temperature. Indeed, the used sintering temperatures were 950 °C for 3 h [21] and 1000 °C for 3 h [19].

The low compressive strength of the CEL2 scaffolds produced by Vitale Brovarone et al. [21] was also due to the presence of a large number of pores that reduced the resistant section and to the collapse of the structure in some inner parts of the scaffold, which may be attributed to a deficient glass coating in the inner part of the sponge [21].

Scaffolds based on ICEL2 [7], which is a phosphate glass obtained by modifying the chemical composition of CEL2, showed a lower compressive strength than CEL2 scaffolds [19].

This can be attributed both to the different pores content, which was higher in ICEL2 scaffolds than in CEL2 ones and to a lower degree of sintering reached in ICEL2 scaffolds with respect to CEL2 ones due to the narrower sintering window [7].

The first produced scaffolds of calcium phosphate glass had higher compressive strength [3] compared to ICEL2 scaffolds [7]. This was attributed to the repeated slurry coating/sintering process, which led to thickening of struts, and to the use of a lower heating rate. Indeed, as mentioned above, the use of a heating rate lower than 1 °C/min involved removing the sponge only after the formation of necks between the particles and the creation of sufficient binding strength between the particles.

In addition, phosphate glass scaffolds exhibited a dense microstructure without voids and cracks, which was responsible for high mechanical properties [3].

In addition to CEL2 silicate glass, also SCNA and 1393 silicate glasses have a suitable thermal behaviour for obtaining mechanically performing scaffolds.

SCNA-based scaffolds having the mechanical suitability for load-bearing bone repair were successfully produced by Baino and Vitale-Brovarone [23]. The elastic modulus of the obtained scaffolds, 380 ± 172 MPa, was within the range assessed for spongy bone (50-500 MPa), and the compressive strength was above the range of the cancellous bone compressive strength; however a higher value than that of the bone may cause bone resorption [23].

The high mechanical behaviour is attributable to the suitable sintering temperature used, which led to a great densification of scaffold trabeculae and a high volumetric shrinkage of the structure resulting in a reduced porosity [23]. The porosity value of the final scaffold was however above the minimum value required (50%) for tissue ingrowth [24], [66].

13-93 based-scaffolds fabricated by Fu et al. [25] had approximately the same porosity of 45S5 Bioglass® scaffolds but a compressive strength of almost 20 times the value for the latter. This difference in strength was due mostly to the different sintering window of the two glasses [4]. Indeed, as already mentioned, 13-93 glass is characterized by a larger sintering window in comparison to 45S5 Bioglass®, which involves beneficial viscous flow features and in turns a higher densification, thus causing an increase in the compressive strength of the scaffold [25].

Scaffolds of 13-93B3 glass, which are obtained by replacing all the SiO₂ in 13-93 with B₂O₃, had roughly the same porosity as 13-93 scaffolds but only half the compression strength. The decrease in

compressive strength is attributable to the presence of boron oxide. Indeed, it was found that the compressive strength decreased with increasing content of boron oxide [27].

In support of this, the D-Alk-B glass scaffolds produced by Liu et al. [30], composed of a smaller amount of B_2O_3 than 13-93B3, exhibited a higher compressive strength than 13-93B3 scaffolds [27], and a lower compressive strength compared to 13-93 glass scaffold [25].

The high mechanical behavior of the D-Alk-B glass scaffolds was reached also thanks to thicker coated green bodies, thus switching the load-bearing units from the trabeculae to the pore walls [30].

The different mechanical behaviour between glass (or glass-ceramic) scaffolds and bone is mainly due to the fact that the glass is an inorganic material, while bone is a composite material, composed of inorganic and organic substances. Therefore, a composite scaffold made of bioactive glass and polymer, having intermediate properties between those of glass and polymer, should better imitate the behaviour of bone.

For this reason, several research groups developed bioactive glass/polymer composite scaffolds [67]. For example Bretcanu et al. [39] produced 45S5 Bioglass[®]/ P(3HB) composite scaffolds.

P(3HB) is a natural thermoplastic polymer produced by several types of microorganisms [68].

The work of fracture of the scaffolds is greatly increased after coating with P(3HB). It is believed that the polymer layer have covered and filled the microcracks located on the surfaces of the struts, improving the mechanical stability of the scaffold [69].

Furthermore, the polymer coating did not influence the pores interconnectivity [39].

Not only P(3HB) coating, but also the coating of PCL, increased 45S5 Bioglass[®] mechanical properties [40]. According to Hum et al. [70] PCL-coating increases the scaffold stiffness by 58% in comparison with uncoated scaffolds [70]. In addition, it was found that PCL coating did not clog the micropores which are necessary for effective cell seeding and bone tissue in-growth [40].

Polymeric coatings improved the mechanical behaviour also of scaffolds obtained with other glass than 45S5 Bioglass[®].

For example, the coating with alginate cross-linked with copper ions increased the compressive strength of boron-containing silicate glass scaffolds produced by Erol et al. [41].

The alginate layer covered the struts and filled microcracks on the struts surface, increasing the mechanical stability of the scaffolds [41]. This is in agreement with the research of Mouriño et al. [71] and with previous investigation in the field of polymer-coated porous ceramics [72], [69].

In addition, it was observed that the compressive strength values increased with copper content. This phenomenon could be due to increased cross-linking density; however, this hypothesis was not demonstrated [41].

As well as alginate, also gelatin proved to be effective in improving the mechanical properties of bioactive glass scaffolds.

Indeed, 58S-gelatin composite scaffolds, produced by Xia et al. [55] using DBM as sacrificial template, before adding gelatin showed a low strength. After compounding the BG scaffolds with gelatin, the compressive strength considerably increased. More specifically, the compressive strength doubled after adding 1 wt% gelatin solution. By increasing the concentration of gelatin, the compressive strength continued to increase. Once gelatin concentration became higher than 10 wt%, the average compressive strength was close to 5 MPa, which is about 30 times the strength of the scaffold before compounding with gelatin [55].

In addition, the gelatin gave the scaffolds a high resistance to deformation and an excellent shape restoration property [55].

The potential of these glass-gelatin composite scaffolds is that the mechanical properties of the scaffolds greatly increased although the porosity was the same as before the addition of gelatin [55]. Since generally polymers increase the mechanical properties of the scaffolds while preserving their porosity, they proved useful in the field of mesoporous bioactive glass scaffolds.

As mentioned above, pure MBG scaffolds have many advantages, such as high bioactivity and drug-loading ability. However, their applicability is limited by their inherent brittleness, which results in non-continuous and collapsed pore network, and low mechanical strength.

For example, Wu et al. [34] used silk to improve the mechanical behaviour of MBG scaffolds.

The addition of silk greatly increased mechanical strength, leading it within the range of the compressive strength of spongy bone, and maintained high porosity [34].

There are two possible reasons why silk addition enhanced the mechanical behaviour of the MBG scaffolds: (1) silk may have created a more uniform and continuous pore network within the MBG scaffolds, which led to higher compression strength; or (2) silk, which has higher mechanical strength than any other traditional polymer [73], may have formed an intertexture within the MBG scaffolds, connecting the inorganic phases together and strengthening the scaffolds [72].

3.4 Mass Transport Properties

In tissue engineering, the use of scaffolds is mainly aimed at providing a suitable environment to favour cell adhesion, proliferation, migration, and thus, the formation of new tissues [74].

Specifically, scaffold microstructure is crucial to proper cell infiltration within the whole 3D volume as well as tissue vascularization, nutrient supply and waste removal [75].

Particularly, several studies reported that an appropriate nutrient transport through the scaffold is required for cell cultures [76]–[79], both in static and dynamic conditions. Accordingly, the ability of the scaffolds to be permeated by nutrients and metabolites, i.e., the easiness with which biological species and fluids migrate through the scaffold [80], strongly affects TE processes [81]–[84].

Mass transport phenomena through scaffolds occur at different scales, including the molecular level (nanoscale), the single-pore dimension level (microscale) and the whole-sample level (macroscale) [85].

Typically, scaffold microstructure is investigated in terms of pore size and distribution, porosity, pore tortuosity and surface area. However, considering these parameters, sometimes, could lead to confusion while characterizing mass transport properties of scaffolds [86].

For example, despite scaffolds with high porosity are believed to have better mass transport properties if compared to those with lower porosity, it was also found that scaffolds characterized by the same porosity do not necessarily exhibit similar transport of nutrients [87].

Moreover, it is worth mentioning that an uncontrolled micro architecture, resulting in heterogeneous pore size and distribution, as well as the presence of isolated and dead pores may determine an uneven distribution of cells within the volume, thus hindering cellular penetration and new matrix formation [88].

Furthermore, determining pore tortuosity is usually a challenging issue due to clear difficulties in measuring the real route length of porous microchannels [86].

On the other hand, the assessment of intrinsic permeability is quite easy and allows appraising mass and species transport through the scaffold, and to define its topological characteristics [75].

Permeability quantifies the ability of a porous structure to be crossed by a fluid when subjected to a pressure gradient. Thus, in tissue engineering applications, permeability is a useful parameter to qualitatively evaluate the nutrient flow to cells within the scaffolds.

Several studies state that cell growth within 3D scaffolds depends on how well nutrients can permeate through the porous medium during cell culture process [76]–[78], or after implantation.

Permeability is a macroscale property that significantly influences biophysical stimuli at the microscale due to the effect of fluid flowing through the scaffold during physiological mechanical loading [83]. In addition, permeability influences the pressure magnitude and shear forces within structure, denoted as potential stimuli for cellular differentiation or functional adjustment [89], [90], [91] for the effectiveness of cell seeding [92], [93] and for the formation of new tissue *in vivo* [94]. Furthermore, permeability affects the degradation rate of biodegradable scaffolds [95], [96].

Permeability is commonly evaluated by the Darcy's law. At the macroscale, Darcy flow transport model defines the fluid flow through a porous structure as the consequence of a proportionality between the fluid velocity and the applied pressure difference (forcing term) (Equation 1) [97]:

$$-\frac{\partial P}{\partial x} = \frac{\mu}{k} U \quad (1)$$

where:

x : flow direction [97].

$\frac{\partial P}{\partial x}$: pressure gradient [97].

μ : fluid dynamic viscosity [97].

k : intrinsic permeability of the porous medium [97].

The intrinsic permeability depends entirely on the scaffold pore structure [97].

In particular, the intrinsic permeability is a function of the pore morphology, interconnection, and pore size, as well as overall porosity [98].

In first approximation, intrinsic permeability is directly proportional to the porosity of the scaffold. However, scaffolds characterized by the same porosity may have different values of the intrinsic permeability because of differences in pore size, morphology and architecture [98].

It is also worth mentioning that with increasing porosity, the apparent scaffold stiffness decreases according to the square of porosity [99]. Thus, a scaffold should have a suitable porosity allowing sufficiently high permeability for waste removal and nutrients supply and appropriate stiffness to bear the loads conveyed to the scaffold from the surrounding healthy bone [98].

In addition, cells attachment and migration to the scaffold surface are influenced by the bulk biomaterial stiffness [100] and the available specific surface. The specific surface is in turn related to permeability as a function of the microstructural design of the scaffold and porosity, which determine the overall permeability, as stated above [98].

Therefore, in the scaffold design, it is crucial to take into account permeability, since it is an important parameter which affects others and accordingly the final success of the scaffold [98].

In light of what was said, in order to quantitatively evaluate the resemblance of a BG scaffold pore interconnectivity with that of spongy bone, it is instructive to compare the values of permeability of the two structures [98].

Regarding the spongy bovine bone, values between $k = 2 \times 10^{-9}$ and $9.5 \times 10^{-9} \text{ m}^2$ were reported [101] in the range of porosities 80-90%. Moreover, values of $k = 7.22 \times 10^{-9}$ and $5.13 \times 10^{-9} \text{ m}^2$ were presented for human spongy bone of the vertebra body and proximal femur [102].

Ochoa et al. [98] measured the permeability of porous-Bioglass[®] scaffolds produced by foam replica method. These scaffolds were characterized by porosity of 90–95% [98].

The assays were carried out in apposite equipment designed for permeability tests to measure intrinsic permeability in the Darcy's linear region [98].

The measured intrinsic permeability, $k = 1.96 \times 10^{-9} \text{ m}^2$, fell within the range of the reported experimental data for human cancellous bone. This confirmed that Bioglass[®] scaffolds, produced by foam replica method, had transport properties and pore structure similar to those of spongy bone, and thereby, represented interesting artificial extracellular matrix structures for the BTE applications [98].

3.5 *In Vivo* Studies

Nowadays, *in vitro* studies on BG-based scaffolds are considered an essential step having the purpose to provide a preliminary evaluation of the biological response induced by the material [15].

However, despite their undeniable scientific and ethical importance, *in vitro* tests are intrinsically limited by the reduced complexity of the environment, able only to approximate the performance of the scaffolds *in vivo*. During *in vitro* experiments, indeed, immune or inflammatory response do not take place, as well as the cascade of events arising from *in vivo* implantation, e.g., the interaction with blood components, clot formation, vascularization and cell recruitment for wound healing processes [103].

In vitro toxicity levels of materials are generally overstated, and since the cultured cells have a relatively short lifespan, the *in vitro* studies allow evaluating only the acute toxicity [104].

Moreover, *in vitro* studies are commonly performed in 2D, on planar or curved surfaces, which do not resemble the 3D surroundings typical of biological tissues and organs [15].

For all these reasons, *in vitro* assessment of biomaterials has questionable clinical relevance [15].

In vivo animal studies enable to understand and assess materials' performance in the complex physiological environment and represent an inevitable stage before clinical trials. They allow to evaluate the biomaterials under various loading conditions, for long periods of time, in several tissue qualities (e.g. healthy or osteopenic bone) and age [15].

However, *in vivo* animal studies also have limits; for example, an animal model that has physiological and pathophysiological similarities with humans must be chosen, and the operation must be controllable. In addition, the implant size, number of implants per animal and test duration should follow the international standards. Other limits include animal availability, costs of purchase and care, the animal's ability to withstand testing and social acceptability [105].

Figure 17 provides a schematization of *in vivo* studies on bioactive glass scaffolds.

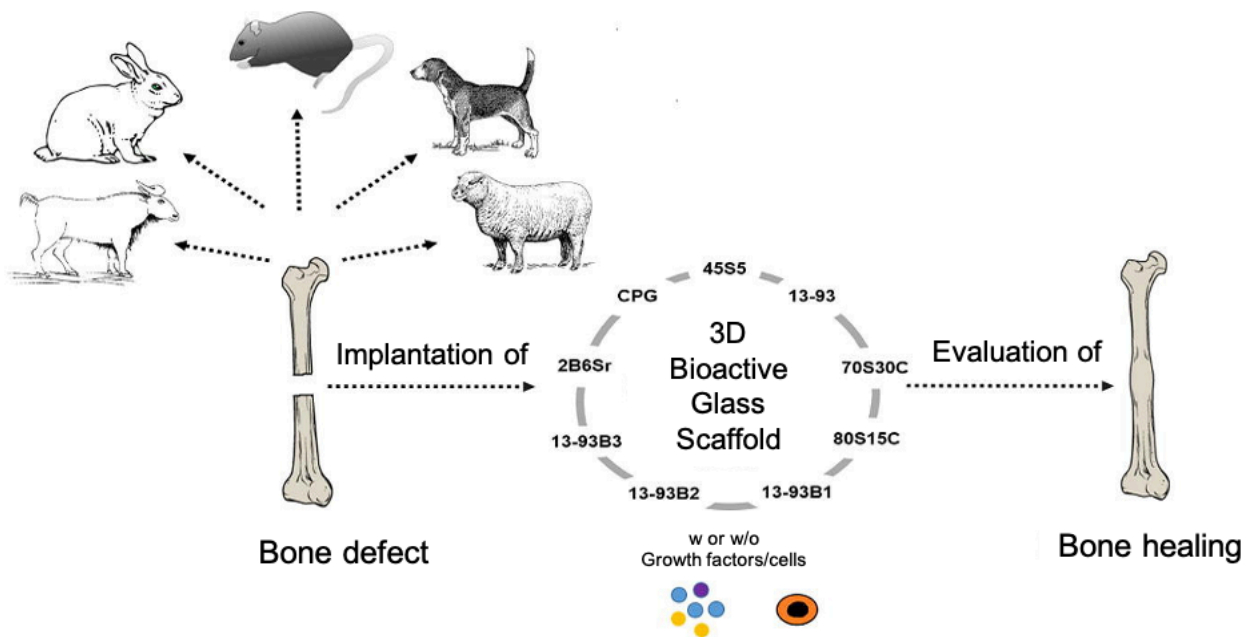


Figure 17: Schematization of *in vivo* studies on bioactive glass scaffolds. Figure adapted from El-Rashidy [15].

The bone defect model chosen as implant site for the scaffold should be a good representation of the designed clinical application. Bone defect models include calvarial, long bone or maxillofacial defects; they can be classified into non-critical and critical sized bone defects, and are used to test osteocompatibility and osteogenesis, respectively [106].

The calvarial defect is generally used as a non-load-bearing model for studying scaffolds with inferior mechanical properties to bone. While load-bearing long bone defect models (e.g., femur, tibia, radius, and humerus) are commonly used for investigating scaffolds with similar properties to bone [106].

The following is a summary of the most significant *in vivo* studies according El-Rashidy [15] regarding bioactive glass scaffolds produced by foam replica method.

The scaffolds whose *in vivo* behaviour is discussed below, have all already been analysed from a morphological point of view in the section 3.2 (Variants of the process and impact on the morphological properties) of this chapter.

Most of the scaffolds analysed below was tested on calvarial models of rats. Indeed, rat is the first choice for *in vivo* testing of biomaterials for BTE due to its small size and easy handling and housing [105].

For example, in the study of Liu et al. [26], 13-93 BG scaffolds with two different microstructure (oriented and trabecular) were compared for their capacity to regenerate bone and osteointegration in a rat calvarial defect models [26]

Both the oriented and trabecular scaffolds were able to support bone regeneration in rat calvarial defects, but the microstructure greatly affected the way in which new bone infiltrated the scaffold and the integration between the scaffolds and the host bone (Figure 18) [26].

12 weeks after implantation, new bone formed principally on the dural (bottom) side of the oriented scaffolds, and only a small amount of bone ingrowth into the periphery (edge) of the scaffolds. At 24 weeks, total bone regeneration enhanced, as well as bone infiltration into the periphery of the scaffolds and integration with host bone (Figure 18a, b) [26].

While the trabecular scaffolds exhibited bone regeneration mainly into the implant periphery and greater integration with host bone than the oriented scaffolds at 12 weeks (Figure 18c, d) [26].

The different bone infiltration in the two kinds of scaffolds (the dural side vs. at the periphery) may be attributed to the different architecture of the scaffolds [26].

It was found that besides porosity and pore size, other factors, such as pore interconnectivity, the size of the aperture between close pores, permeability and microstructural anisotropy of the structure influence bone infiltration [107], [108]. Indeed, even though the trabecular scaffolds had a higher porosity and pore size, the more tortuous pore channels may have constrained bone formation to the periphery. While, although the oriented scaffolds had a lower porosity and pore size, the pores were more connected, and the pore channels were less tortuous, which may have fostered bone ingrowth inside the implant [26].

New bone formation in the oriented scaffolds based on the available pore area (volume) was $55 \pm 5\%$ in comparison with $46 \pm 13\%$ for the trabecular scaffolds. Less new bone formed in the trabecular scaffolds, thus suggesting again that the pore channels tortuosity played a crucial role in adjusting bone infiltration in the scaffolds [26].

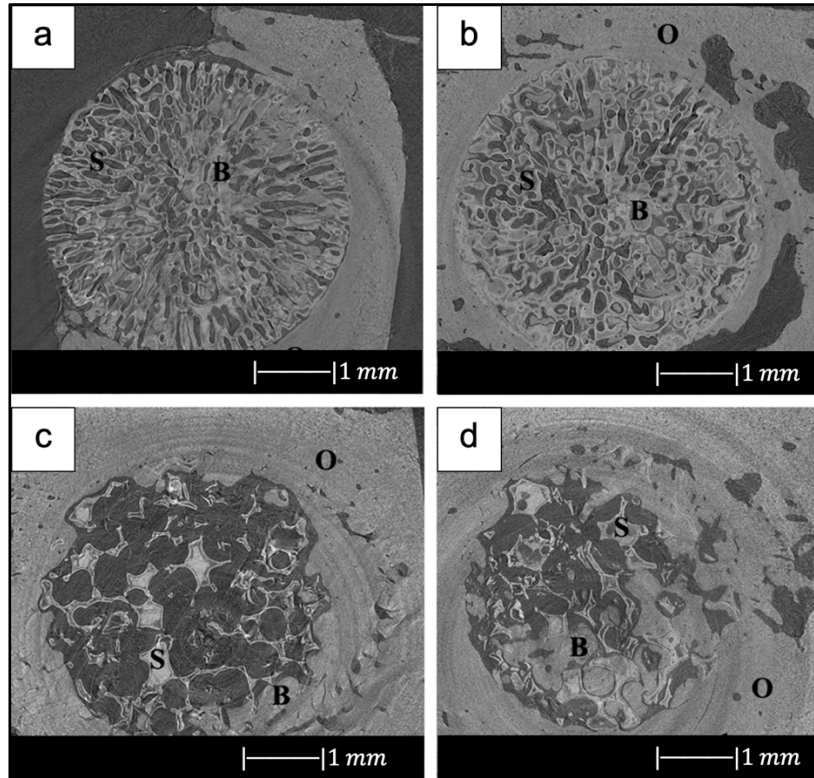


Figure 18: Synchrotron micro-computed x-ray tomography images of 13-93 BG oriented scaffold after implantation for (a) 12 weeks and (b) 24 weeks, and 13-93 BG trabecular scaffold after implantation for (c) 12 weeks and (d) 24 weeks. The distribution of old bone (O), new bone (B) and the bioactive glass scaffold (S) is given. Figure adapted from Liu et al. [26].

Also Bi et al. [28] studied the effect of the microstructure of the scaffolds on bone regeneration by using a rat calvarial model [28].

Scaffolds of 13-93B3 glass and Cu-doped 13-93B3 glass fabricated with three different microstructures, described as trabecular, oriented, and fibrous, were implanted in rat calvarial defect models and compared [28].

The trabecular scaffolds of 13-93B3 glass exhibited a higher quantity of new bone growth, and greater osteoinductive ability in comparison to the oriented or fibrous scaffolds of the same glass [28]. This difference in bone formation may be attributed to the higher porosity (77%) and larger pore size (200–400 μm) of trabecular scaffolds in comparison to the other scaffolds. Indeed, large and interconnected pores in the scaffold may have led to increased bone in-growth, since their presence may have allowed greater migration and proliferation of mesenchymal cells, osteoblasts and neovascularization, resulting in a higher oxygen tension and nutrient supply. While, the lower porosity, as well as pores of size $<100\text{ }\mu\text{m}$ may have impeded tissue penetration into the oriented or fibrous scaffolds [50].

The new bone either penetrated from the edge of the defect, or grew along the dural side of the defect, or formed by a combination of both [50]. Unlike in the previous study by Liu et al. [26], in this study bone growth in the trabecular scaffold was not limited to the periphery of the implant [28]. This is attributable to the different tortuosity of the scaffold pore channels.

Numerous literature studies have shown that Cu ions accelerate angiogenesis [109], [110] and angiogenesis and bone regeneration ability are interrelated. Indeed, an enhanced angiogenesis leads to a better bone regeneration ability because it is believed that the new formed vessels provide a rapid blood supply, offering the cell more nutrition for new bone formation [31].

However, in the present investigation, the Cu-doped 13-93B3 scaffolds did not show a significant increase in total new bone growth compared with 13-93B3 scaffolds. A considerable difference was found only between the Cu-doped and undoped scaffolds with fibrous microstructure [28].

A significant achievement is that, with the exception of 13-93B3 fibrous scaffolds, the amount of new bone formed in the rat calvarial model implanted with 13-93B3 and Cu-doped 13-93B3 scaffolds was larger than in the defects implanted with particles of 45S5 Bioglass[®] which were used as positive control [28]. This is in accordance with the results of the previous study of Bi et al. [111] which exhibited that bioactive borate glass scaffolds had a higher bone regeneration ability than bioactive silicate glass scaffolds [111].

Not only 13-93B3 borate glass was tested *in vivo* in a rat calvarial defect model, but also D-Alk-B borate glass [31], [32], [33].

D-Alk-B borate glass was doped with copper in order to enhance angiogenesis [31]. Contrary to the previous study of Bi et al. [28], in which no differences were found in bone growth between Cu-containing and Cu-free scaffolds, in the present study Cu-doped D-Alk-B scaffolds exhibited a greater ability to stimulate angiogenesis and regenerate bone in comparison to the undoped glass scaffolds (Figure 19) [31].

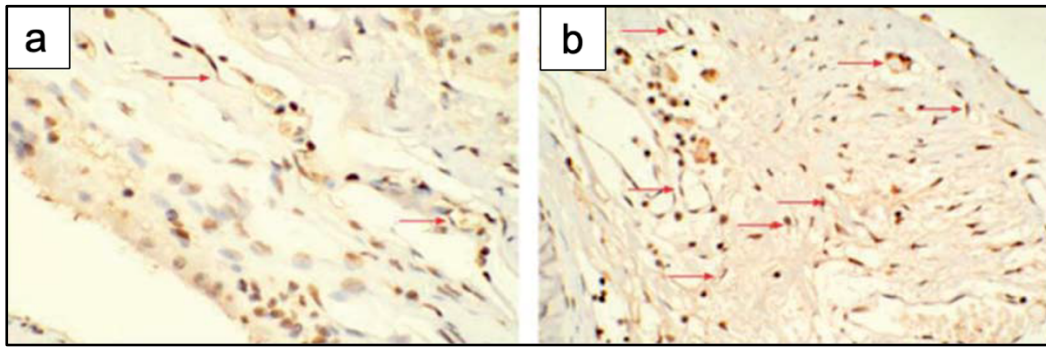


Figure 19: Immunohistochemical staining for CD31 in rat calvarial defects implanted with (a) BG scaffolds and (b) Cu-doped BG scaffolds at 8 weeks post implantation. There were more new blood vessels (red arrows) in the defects implanted with the Cu-doped BG scaffolds. Figure adapted from Wang et al. [31].

The same research group tested also D-Alk-B scaffolds loaded with Fe_3O_4 [32] and ZnO [33] *in vivo* in rat calvarial defect models.

The outcomes showed a higher quantity of new bone in the defects implanted with scaffolds loaded with Fe_3O_4 magnetic nanoparticles (MNPs) than ones implanted with scaffolds alone (Figure 20) [32].

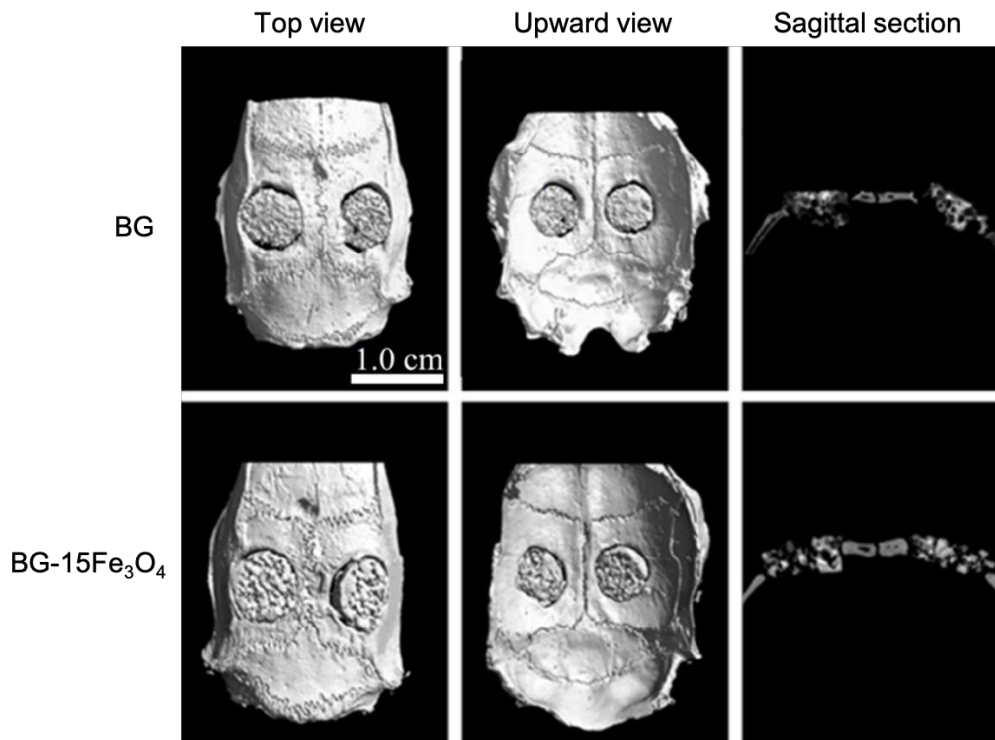


Figure 20: Micro-CT evaluation of bone regeneration in the rat calvarial defects implanted with borosilicate BG scaffolds and borosilicate BG scaffolds loaded with Fe_3O_4 MNPs. Figure adapted from Wang et al. [32].

Indeed, the presence of Fe_3O_4 MNPs probably resulted in many miniature magnetic forces in the scaffold under the external magnetic field, thus steadily spurring osteoblastic cell proliferation,

differentiation, osteogenic gene expression, and secretion of new natural extracellular matrices. In addition, free iron released into cytoplasm could have led to a better cell cycle progression *in vivo* [32]. Also Zn-doped D-Alk-B scaffolds showed an improved bone regeneration compared to the non-doped scaffolds (Figure 21). This finding proved that Zn-doped scaffolds have high osteogenic ability making them promising materials for bone tissue repair and regeneration [33].

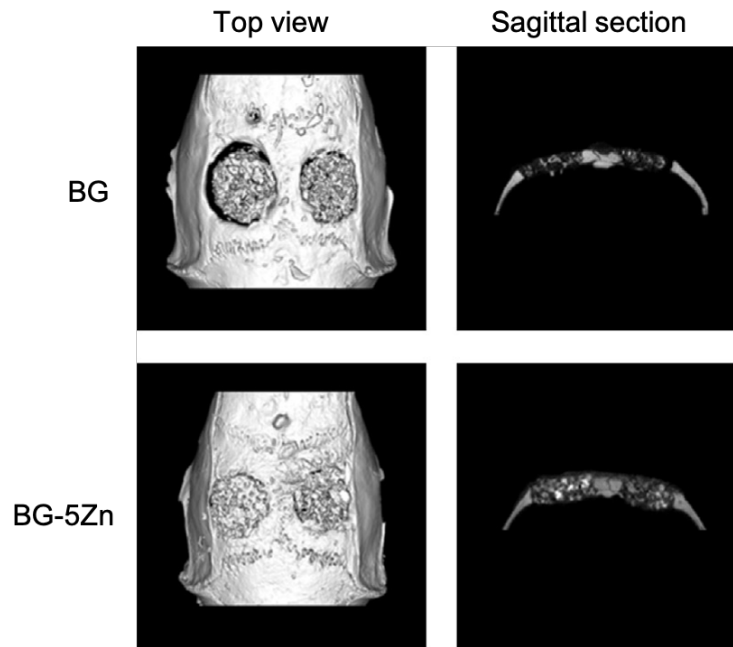


Figure 21: Micro-CT evaluation of bone regeneration in the rat calvarial defects implanted with the borosilicate BG scaffolds and Zn-doped borosilicate BG scaffolds at 8 weeks post-implantation. Figure adapted from Wang et al. [33].

The rat was also chosen for *in vivo* testing of mesoporous bioactive glass scaffolds [35]–[37]. Zhang et al. [35] incorporated strontium into mesoporous bioactive glass (Sr-MBG) scaffolds in order to combine the therapeutic action of Sr^{2+} ions on osteoporosis with the bioactivity of MBG to regenerate osteoporotic-related fractures [35].

MBG scaffolds and Sr-MBG scaffolds were implanted in critical sized femur defects of ovariectomised rats to study *in vivo* regeneration of osteoporotic bone defects [35].

Sr-MBG scaffolds showed greater new bone formation than MBG scaffolds alone. Moreover, incorporation of Sr into MBG scaffolds led to much more mineralization and density (Figure 22) [35]. Indeed, it was found that Sr-MBG scaffolds spurred a more effective osteoconductive and anti-osteoporotic phenotype, which increased the speed and quality of bone regeneration and remodeling and change of trabecular morphology from a more rod-like aspect to the plate-like appearance with retrieve of trabecular connectivity [35].

The results also showed that Sr release in blood was maintained at a very low level which might suggest a slightest chance of side effects on overall health. In addition, the Sr, Si, Ca ions in urine were higher than those in blood, meaning that the ionic products from Sr-MBG scaffolds can be metabolized and excreted by urine [35].

Therefore, these findings suggested that Sr-MBG scaffolds are suitable biomaterials for regenerating osteoporosis-related fractures by the release of Sr-containing ionic products [35].

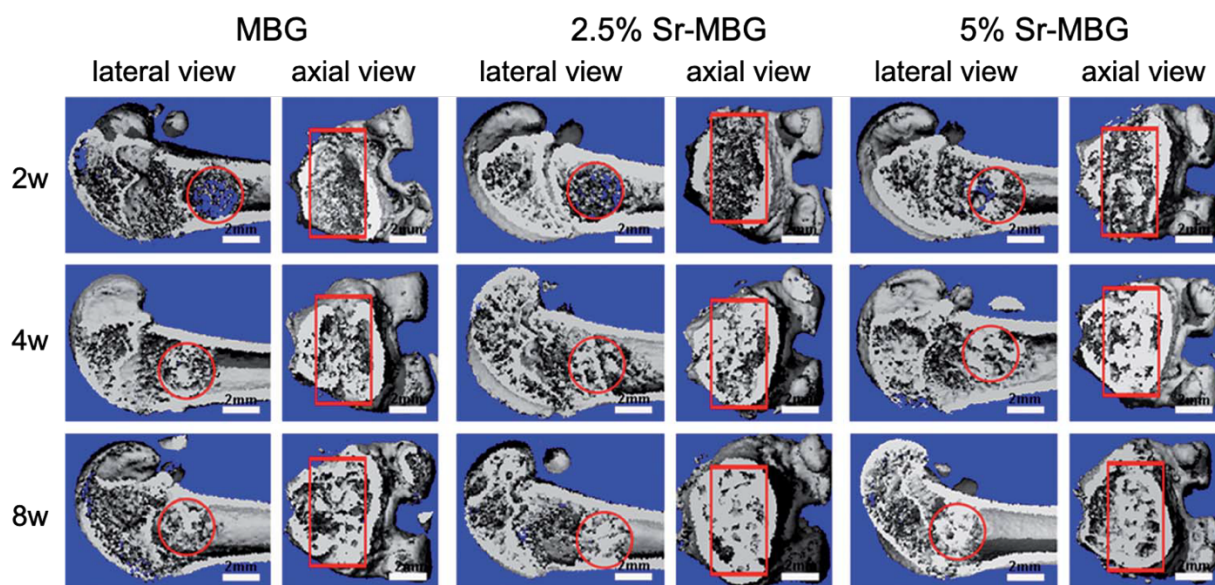


Figure 22: 3D reconstruction of longitudinal section and cross-section images by micro-CT at 2-, 4- and 8-weeks post-implantation of MBG scaffolds and MBG scaffolds containing strontium in the critical femoral defect. The red circle and rectangle indicate the boundary of the defects. Figure adapted from Zhang et al. [35].

In another study, the same research group investigated if the Sr-containing MBG scaffolds were also advantageous for the repair of alveolar bone defects created in periodontal tissues of ovariectomised rats [36].

The outcomes showed that Sr-MBG increased alveolar bone regeneration in periodontal tissues in ovariectomised rats when compared to MBG alone [36].

For the first time, the capacity of scaffolds containing strontium to promote bone formation in periodontal tissue *in vivo* was demonstrated [36].

The release of Sr^{2+} ions was able to enhance osteoblast function by augmenting new bone formation. In addition, it was also found that the number of multi-nucleated osteoclasts was substantially reduced when Sr was added in MBG scaffolds [36]. This finding is in agreement with literature studies that proved that Sr is able to suppress osteoclastogenesis [112].

Taken together, these findings proposed that the implant of Sr containing scaffolds may lead to a better healing of periodontal defects caused by osteoporosis [36].

Besides Sr-MBG [35], also the ^{45}Ca -MBG scaffolds produced by Sui et al. [37] were implanted in critical-sized rat femur defects [37].

The outcomes showed that after scaffold implantation the mesoporous structure sped up the local ion exchange. Reactive ions such as Si and Ca released from MBG fostered bone regeneration *in vivo*. However, it was found that only a small quantity of MBG-released calcium ions was transformed into calcium components of the new bone matrix [37].

The rat model has several limits, such as the small size that makes it unsuitable for testing multiple implants [104]. In addition, the long bone of rats are small and characterized by slim and weak cortices and do not exhibit haversian-type cortex remodeling, as in bigger animals [15].

An alternative to the rat model is the rabbit model. In particular, New Zealand white rabbit is considered the second animal model of choice to test *in vivo* biomaterials for musculoskeletal investigations [105]. Indeed, it is easily available, it has small size which makes it of easy handling

and housing. Moreover, similarities in bone mineral density and fracture toughness of mid-diaphyseal bone between humans and rabbits were found [113].

For instance, Gu et al. [29] evaluated the ability of 13-93B1 scaffold to promote bone regeneration *in vivo* using a non-critical sized defects created in the femoral head of rabbits [29].

Figure 23 exhibits the defects implanted with the 13-93B1 scaffolds after 4 and 8 weeks and the unfilled defects at 8 weeks. The defects implanted with the scaffolds presented better bone healing than the unfilled defects. Moreover, as the scaffold's implantation time increased, bone healing is increased. These results suggest that the trabecular structure of 13-93B1 scaffold produced in the present study is favorable for bone ingrowth [29].

In particular, the results showed that 8 weeks post-implantation the scaffolds were partly converted to HA and they were well integrated with newly formed bone [29].

It is well known that 13-93B1 glass converts to HA faster than the silicate 13-93 glass and slower than the borate 13-93B3 glass [27]. Accordingly, scaffolds of 13-93B1 might offer an excellent combination of conversion to hydroxyapatite and retention of the strength which is difficult to achieve with glass 13-93 or 13-93B3 [29].

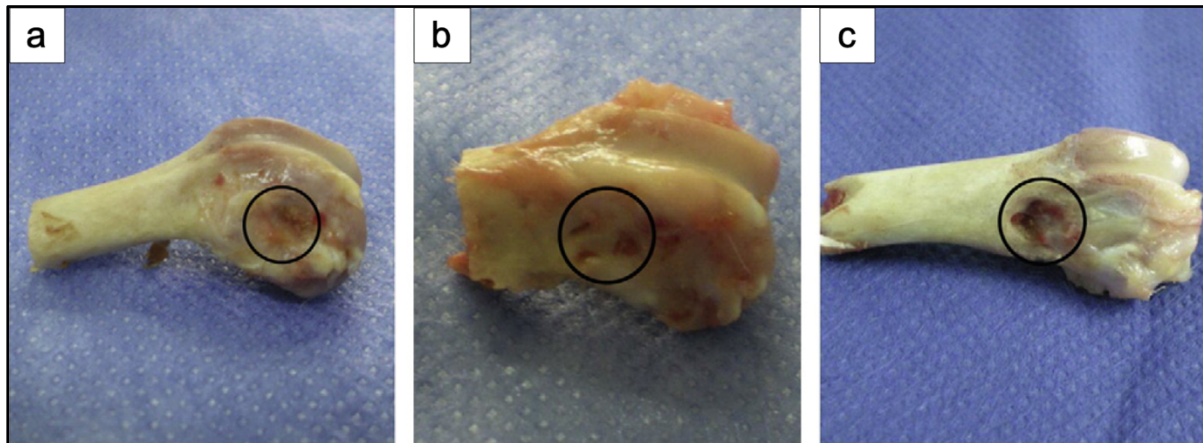


Figure 23: Gross appearance of rabbit femoral head defects implanted with 13-93B1 scaffolds for (a) 4 weeks, and (b) 8 weeks; (c) unfilled defect at 8 weeks. Figure adapted from Gu et al. [29].

Then, 13-93B1 scaffolds were loaded with platelet-rich plasma (PRP), and both the loaded scaffolds and the unloaded ones were implanted in segmental defects in the diaphysis of rabbit radii to evaluate their ability to support bone regeneration *in vivo* [29].

Figure 24 exhibits the segmental defects in the rabbit radii implanted with 13-93B1 scaffolds, 13-93B1 scaffolds loaded with PRP, and the unfilled defects at 8 weeks [29].

Both kinds of scaffolds integrated with host bone, and the formation of callus seems to be started from both the defect ends (Figure 24a, b). On the contrary, no new bone was present in the unfilled defect (Figure 24c) [29].

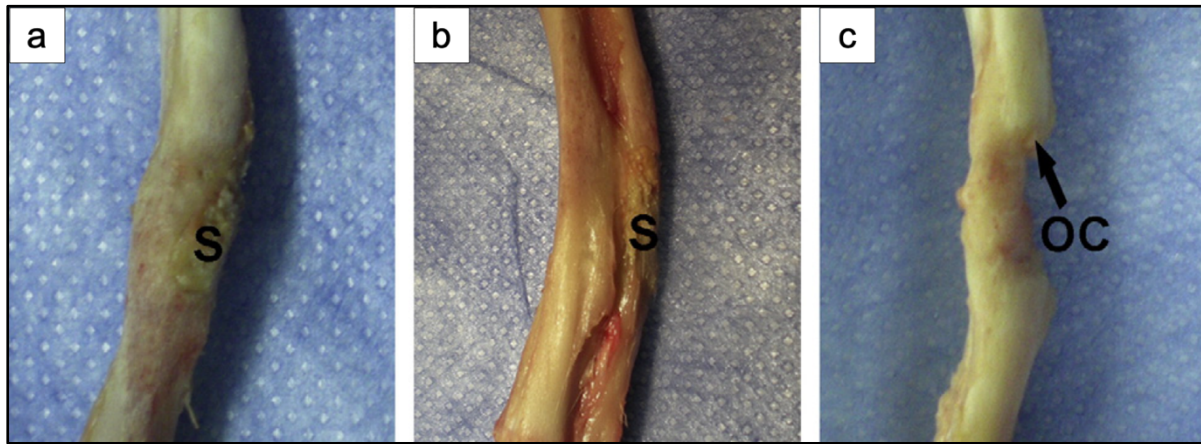


Figure 24: Gross appearance of segmental defect sites in rabbit radii after implantation for 8 weeks with (a) 13-93B1 scaffolds, and (b) 13-93B1 scaffolds loaded with PRP; (c) unfilled defect at 8 weeks. S: scaffold; OC: osseous callus. Figure adapted from Gu et al. [29].

These findings suggested that both kinds of scaffolds supported new bone formation in rabbit defects. However, the scaffolds loaded with PRP exhibited an increased ability to support the healing and the bone formation in comparison with the unloaded ones [29].

Indeed, PRP contains several growth factors, such as transforming growth factor β 1, vascular endothelial growth factor, and insulin-like growth factor, which are known to stimulate the proliferation and differentiation of osteoblastic cells. Therefore, it is believed that the growth factors impart the osteoinductive property to PRP-loaded scaffolds, besides the inherent osteoconductive property of the porous scaffolds themselves [29].

The 13-93B1 scaffold used in the present study was proved to be an effective vector for PRP, which, being characterized by limited stability and a short life span, has to be released in a controlled manner. Like PRP, also the recombinant human bone morphogenetic protein-2 (rhBMP-2) is known to increase the bone formation capacity [114].

This was also proved by Tang et al. [42] who developed trimodal macro/micro/nano-porous scaffolds loaded with rhBMP-2 (TMS/rhBMP-2) [42].

TMS/rhBMP-2 was implanted in thigh muscle pouches of mice and in rabbit radius critical size defect to evaluate *in vivo* the osteogenic performance of this structure [42].

The outcomes showed that TMS/rhBMP-2 had a great bone regeneration ability. Particularly, this scaffold resulted in the extensive regeneration of critical size defect with rapid medullary cavity reunion and sclerotin maturity [42].

In accordance with the theories of endochondral bone formation [115], [116], the regeneration process in this work could be divided into three phases: inflammation and cartilage formation (0–2 weeks), primary bone formation (2–4 weeks), and bone remodeling (after 4 weeks).

Since over 90% of the scaffold degraded by week 8, it was assumed that the osteogenic promotion of TMS/rhBMP-2 especially took place in the first 8 weeks after implantation [42].

On the basis of these outcomes, TMS/rhBMP-2 is considered a promising bone substitute for clinical applications [42].

The rabbit model suffers of limitations including the high bone turnover rate and the fast-skeletal transformations, which make it difficult to use the achievements obtained from rabbit investigations to humans [15].

Larger animals are more like humans. For example, pigs are the animals with bone regeneration processes more similar to human ones. However, no reports on the *in vivo* study of the bone regenerative ability of bioactive glass scaffolds in pigs was found. This may be due to the high body weight and growth rate of the pig and its difficult management [105], [104].

Dogs are the most frequently used animals for musculoskeletal and dental investigation [117]. However, dogs' bones have higher bone mineral density, fracture toughness and different microstructure compared to human bones [113]. In addition, the use of dogs for *in vivo* studies also involves ethical problems since the dog is considered a pet [118].

However, Lee et al. [22] implanted calcium-phosphate-glass scaffolds in 1-wall intra-bony defects of beagle dogs to evaluate the *in vivo* bone regeneration ability [22].

The defects implanted with calcium phosphate glass scaffold and chitosan membrane showed a much larger amount of new cementum and alveolar bone regeneration compared to empty controls, treated with chitosan membrane alone. These findings exhibited that calcium phosphate glass is a promising material for new bone and cementum regeneration [22].

3.6 Conclusions

Since 2006, foam replica method was extensively used to fabricate scaffolds for bone tissue engineering application. The high versatility of the method, together with the ease of execution and the cost-effectiveness, make this technique one of the most appealing manufacturing methods to produce porous and trabecular-like 3D structures resembling natural bone.

As reported by numerous literature studies, scaffold produced by foam replica not only exhibit an exceptional morphological similarity with spongy bone, but also mechanical strength and mass transport properties perfectly matching those of human bone tissue.

Moreover, numerous *in vivo* studies performed on several animal models confirm the exceptional potential of porous scaffolds produced by foam replica method in the regeneration of bone defects in different anatomical sites.

However, additional efforts towards the standardization of the process are strongly required in order to improve the reproducibility and the reliability of foam replicated scaffolds to enable their clinical application in the management of bone defects.

References

- [1] A. W. Somers, "Method of Making Ceramic Articles," 1963.
- [2] Q. Z. Chen, I. D. Thompson, and A. R. Boccaccini, "45S5 Bioglass - derived glass – ceramic scaffolds for bone tissue engineering," *Biomaterials*, vol. 27, pp. 2414–2425, 2006.
- [3] Y. S. Park *et al.*, "Feasibility of three-dimensional macroporous scaffold using calcium phosphate glass and polyurethane sponge," *J. Mater. Sci.*, vol. 41, no. 13, pp. 4357–4364, 2006.
- [4] Q. Fu, E. Saiz, M. N. Rahaman, and A. P. Tomsia, "Bioactive glass scaffolds for bone tissue engineering: state of the art and future perspectives," *Mater. Sci. Eng. C*, vol. 31, no. 7, pp. 1245–1256, 2011.
- [5] Q. Z. Chen and A. R. Boccaccini, "Chapter 6: Tissue Engineering Scaffolds from Bioactive Glass and Composite Materials," in *Topics in Tissue Engineering, Vol. 4.*, 2008.
- [6] F. Baino *et al.*, "Processing methods for making porous bioactive glass-based scaffolds—A state-of-the-art review," *Int. J. Appl. Ceram. Technol.*, 2019.
- [7] C. Vitale-Brovarone, F. Baino, O. Bretcanu, and E. Verné, "Foam-like scaffolds for bone tissue engineering based on a novel couple of silicate-phosphate specular glasses: synthesis and properties," *J. Mater. Sci. Mater. Med.*, vol. 20, no. 11, pp. 2197–2205, 2009.
- [8] E. Fiume, G. Serino, C. Bignardi, E. Vernè, and F. Baino, "Bread-Derived Bioactive Porous Scaffolds: An Innovative and Sustainable Approach to Bone Tissue Engineering," *Molecules*, vol. 24, 2019.
- [9] F. Baino, S. Caddeo, G. Novajra, and C. Vitale-Brovarone, "Using porous bioceramic scaffolds to model healthy and osteoporotic bone," *J. Eur. Ceram. Soc.*, vol. 36, no. 9, pp. 2175–2182, 2016.
- [10] E. Boccardi, A. Philippart, J. A. Juhasz-Bortuzzo, G. Novajra, C. Vitale-Brovarone, and A. R. Boccaccini, "Characterisation of Bioglass based foams developed via replication of natural marine sponges," *Adv. Appl. Ceram.*, vol. 114, no. March 2016, pp. S56–S62, 2015.
- [11] C. J. Brinker, Y. Lu, A. Sellinger, and H. Fan, "Evaporation-Induced Self-Assembly: Nanostructures Made Easy," *Adv. Mater.*, vol. 11, no. 7, 1999.
- [12] Y. Zhu *et al.*, "Preparation, characterization and in vitro bioactivity of mesoporous bioactive glasses (MBGs) scaffolds for bone tissue engineering," *Microporous Mesoporous Mater.*, vol. 112, no. 1–3, pp. 494–503, 2008.
- [13] Y. Zhu and S. Kaskel, "Comparison of the in vitro bioactivity and drug release property of mesoporous bioactive glasses (MBGs) and bioactive glasses (BGs) scaffolds," *Microporous Mesoporous Mater.*, vol. 118, no. 1–3, pp. 176–182, 2009.
- [14] P. Jiang, H. Lin, R. Xing, J. Jiang, and F. Qu, "Synthesis of multifunctional macroporous-mesoporous TiO₂- bioglasses for bone tissue engineering," *J. Sol-Gel Sci. Technol.*, vol. 61, no. 2, pp. 421–428, 2012.
- [15] A. A. El-Rashidy, J. A. Roether, L. Harhaus, U. Kneser, and A. R. Boccaccini, "Regenerating bone with bioactive glass scaffolds: A review of in vivo studies in bone defect models," *Acta Biomater.*, vol. 62, pp. 1–28, 2017.
- [16] X. Zhang *et al.*, "Template-assisted, sol-gel fabrication of biocompatible, hierarchically porous hydroxyapatite scaffolds," *Materials (Basel)*, vol. 12, no. 8, 2019.
- [17] Q. Chen, F. Baino, S. Spriano, N. M. Pugno, and C. Vitale-Brovarone, "Modelling of the

- strength-porosity relationship in glass-ceramic foam scaffolds for bone repair,” *J. Eur. Ceram. Soc.*, vol. 34, no. 11, pp. 2663–2673, 2014.
- [18] L. Montanaro, Y. Jorand, G. Fantozzi, and A. Negro, “Ceramic foams by powder processing,” *J. Eur. Ceram. Soc.*, vol. 18, no. 9, pp. 1339–1350, 1998.
- [19] F. Baino, M. Ferraris, O. Bretcanu, E. Verné, and C. Vitale-Brovarone, “Optimization of composition, structure and mechanical strength of bioactive 3-D glass-ceramic scaffolds for bone substitution,” *J. Biomater. Appl.*, vol. 27, no. 7, pp. 872–890, 2011.
- [20] C. Vitale-Brovarone, E. Verné, L. Robiglio, G. Martinasso, R. A. Canuto, and G. Muzio, “Biocompatible glass-ceramic materials for bone substitution,” *J. Mater. Sci. Mater. Med.*, vol. 19, no. 1, pp. 471–478, 2008.
- [21] C. Vitale-Brovarone *et al.*, “Development of glass-ceramic scaffolds for bone tissue engineering: Characterisation, proliferation of human osteoblasts and nodule formation,” *Acta Biomater.*, vol. 3, no. 2, pp. 199–208, 2007.
- [22] Y.-K. Lee and S.-H. Choi, “Novel Calcium Phosphate Glass for Hard-Tissue Regeneration,” *J. Korean Acad. Periodontol.*, vol. 38, pp. 273–298, 2008.
- [23] F. Baino and C. Vitale-Brovarone, “Mechanical properties and reliability of glass-ceramic foam scaffolds for bone repair,” *Mater. Lett.*, vol. 118, pp. 27–30, 2014.
- [24] L. C. Gerhardt and A. R. Boccaccini, “Bioactive glass and glass-ceramic scaffolds for bone tissue engineering,” *Materials (Basel)*, vol. 3, no. 7, pp. 3867–3910, 2010.
- [25] Q. Fu, M. N. Rahaman, B. Sonny Bal, R. F. Brown, and D. E. Day, “Mechanical and in vitro performance of 13-93 bioactive glass scaffolds prepared by a polymer foam replication technique,” *Acta Biomater.*, vol. 4, no. 6, pp. 1854–1864, 2008.
- [26] X. Liu, M. N. Rahaman, and Q. Fu, “Bone regeneration in strong porous bioactive glass (13-93) scaffolds with an oriented microstructure implanted in rat calvarial defects,” *Acta Biomater.*, vol. 9, no. 1, pp. 4889–4898, 2013.
- [27] Q. Fu, M. N. Rahaman, H. Fu, and X. Liu, “Silicate, borosilicate, and borate bioactive glass scaffolds with controllable degradation rate for bone tissue engineering applications. I. Preparation and in vitro degradation,” *J. Biomed. Mater. Res. - Part A*, vol. 95, no. 1, pp. 164–171, 2010.
- [28] L. Bi *et al.*, “Effect of bioactive borate glass microstructure on bone regeneration, angiogenesis, and hydroxyapatite conversion in a rat calvarial defect model,” *Acta Biomater.*, vol. 9, no. 8, pp. 8015–8026, 2013.
- [29] Y. Gu *et al.*, “Biodegradable borosilicate bioactive glass scaffolds with a trabecular microstructure for bone repair,” *Mater. Sci. Eng. C*, vol. 36, no. 1, pp. 294–300, 2014.
- [30] X. Liu *et al.*, “Bioactive borosilicate glass scaffolds: Improvement on the strength of glass-based scaffolds for tissue engineering,” *J. Mater. Sci. Mater. Med.*, vol. 20, no. 1, pp. 365–372, 2009.
- [31] H. Wang *et al.*, “Evaluation of borate bioactive glass scaffolds as a controlled delivery system for copper ions in stimulating osteogenesis and angiogenesis in bone healing,” *J. Mater. Chem. B*, vol. 2, no. 48, pp. 8547–8557, 2014.
- [32] H. Wang *et al.*, “Biocompatibility and osteogenic capacity of borosilicate bioactive glass scaffolds loaded with Fe₃O₄ magnetic nanoparticles,” *J. Mater. Chem. B*, vol. 3, no. 21, pp. 4377–4387, 2015.
- [33] H. Wang *et al.*, “Three-dimensional zinc incorporated borosilicate bioactive glass scaffolds for rodent critical-sized calvarial defects repair and regeneration,” *Colloids Surfaces B*

Biointerfaces, vol. 130, pp. 149–156, 2015.

- [34] C. Wu, Y. Zhang, Y. Zhu, T. Friis, and Y. Xiao, “Structure-property relationships of silk-modified mesoporous bioglass scaffolds,” *Biomaterials*, vol. 31, no. 13, pp. 3429–3438, 2010.
- [35] Y. Zhang *et al.*, “Strontium-incorporated mesoporous bioactive glass scaffolds stimulating in vitro proliferation and differentiation of bone marrow stromal cells and in vivo regeneration of osteoporotic bone defects,” *J. Mater. Chem. B*, vol. 1, no. 41, pp. 5711–5722, 2013.
- [36] Y. Zhang, L. Wei, C. Wu, and R. J. Miron, “Periodontal regeneration using strontium-loaded mesoporous bioactive glass scaffolds in osteoporotic rats,” *PLoS One*, vol. 9, no. 8, pp. 1–6, 2014.
- [37] B. Sui, G. Zhong, and J. Sun, “Evolution of a mesoporous bioactive glass scaffold implanted in rat femur evaluated by ⁴⁵Ca labeling, tracing, and histological analysis,” *ACS Appl. Mater. Interfaces*, vol. 6, no. 5, pp. 3528–3535, 2014.
- [38] X. Wang, R. A. Bank, J. M. TeKoppele, and C. Mauli Agrawal, “The role of collagen in determining bone mechanical properties,” *J. Orthop. Res.*, vol. 19, no. 6, pp. 1021–1026, 2001.
- [39] O. Bretcanu, S. Misra, I. Roy, R. Chiara, F. Fiori, and A. R. Boccaccini, “In vitro biocompatibility of 45S5 Bioglass®-derived glass–ceramic scaffolds coated with poly(3-hydroxybutyrate),” *J. Tissue Eng. Regen. Med.*, vol. 3, pp. 139–148, 2009.
- [40] P. Balasubramanian, J. A. Roether, D. W. Schubert, J. P. Beier, and A. R. Boccaccini, “Bi-layered porous constructs of PCL-coated 45S5 bioactive glass and electrospun collagen-PCL fibers,” *J. Porous Mater.*, vol. 22, no. 5, pp. 1215–1226, 2015.
- [41] M. M. Erol *et al.*, “Copper-releasing, boron-containing bioactive glass-based scaffolds coated with alginate for bone tissue engineering,” *Acta Biomater.*, vol. 8, no. 2, pp. 792–801, 2012.
- [42] W. Tang *et al.*, “Bioinspired trimodal macro/micro/nano-porous scaffolds loading rhBMP-2 for complete regeneration of critical size bone defect,” *Acta Biomater.*, vol. 32, pp. 309–323, 2016.
- [43] C. Bignardi, M. Petraroli, and N. M. Pugno, “Nanoindentations on conch shells of gastropoda and bivalvia molluscs reveal anisotropic evolution against external attacks,” *J. Nanosci. Nanotechnol.*, vol. 10, no. 10, pp. 6453–6460, 2010.
- [44] M. Yu, E. Fiume, E. Verné, T. Saunders, M. J. Reece, and F. Baino, “Bioactive sol-gel glass-coated wood-derived biocarbon scaffolds,” *Mater. Lett.*, vol. 232, pp. 14–17, 2018.
- [45] E. Cunningham and N. Dunne, “Comparative Characterisation of 3-D Hydroxyapatite Scaffolds Developed Via Replication of Synthetic Polymer Foams and Natural Marine Sponges,” *J. Tissue Sci. Eng.*, vol. s1, no. 1, pp. 1–9, 2011.
- [46] R. Pronzato and R. Manconi, “Mediterranean commercial sponges: Over 5000 years of natural history and cultural heritage,” *Mar. Ecol.*, vol. 29, no. 2, pp. 146–166, 2008.
- [47] S. Yang, K. F. Leong, Z. Du, and C. K. Chua, “The design of scaffolds for use in tissue engineering. Part I. Traditional factors,” *Tissue Eng.*, vol. 7, no. 6, pp. 679–689, 2001.
- [48] M. Mastrogiacomo *et al.*, “Role of scaffold internal structure on in vivo bone formation in macroporous calcium phosphate bioceramics,” *Biomaterials*, vol. 27, no. 17, pp. 3230–3237, 2006.
- [49] E. Verné *et al.*, “Early stage reactivity and in vitro behavior of silica-based bioactive glasses and glass-ceramics,” *J. Mater. Sci. Mater. Med.*, vol. 20, no. 1, pp. 75–87, 2009.
- [50] V. Karageorgiou and D. Kaplan, “Porosity of 3D biomaterial scaffolds and osteogenesis,” *Biomaterials*, vol. 26, no. 27, pp. 5474–5491, 2005.
- [51] K. Anselme, P. Davidson, A. M. Popa, M. Giazson, M. Liley, and L. Ploux, “The interaction

of cells and bacteria with surfaces structured at the nanometre scale,” *Acta Biomater.*, vol. 6, no. 10, pp. 3824–3846, 2010.

- [52] J. Ma, H. Lin, X. Li, C. Bian, D. Xiang, and F. Qu, “Synthesis of hierarchical porous bioactive glasses for bone tissue regeneration,” *IET Nanobiotechnology*, vol. 8, no. 4, pp. 216–221, 2014.
- [53] X. Han *et al.*, “Hierarchical meso-macroporous bioglass for bone tissue engineering,” *J. Sol-Gel Sci. Technol.*, vol. 70, no. 1, pp. 33–39, 2014.
- [54] J. Will, L. C. Gerhardt, and A. R. Boccaccini, “Bioactive Glass-Based Scaffolds for Bone Tissue Engineering,” *Adv. Biochem. Eng. Biotechnol.*, vol. 126, pp. 195–226, 2011.
- [55] W. Xia and J. Chang, “Bioactive glass scaffold with similar structure and mechanical properties of cancellous bone,” *J. Biomed. Mater. Res. - Part B Appl. Biomater.*, vol. 95 B, no. 2, pp. 449–455, 2010.
- [56] D. C. Tancred, B. A. O. McCormack, and A. J. Carr, “A synthetic bone implant macroscopically identical to cancellous bone,” *Biomaterials*, vol. 19, no. 24, pp. 2303–2311, 1998.
- [57] H. Li, K. Lin, and J. Chang, “Preparation of macroporous polymer scaffolds using calcined cancellous bone as a template,” *J. Biomater. Sci. Polym. Ed.*, vol. 16, no. 5, pp. 575–584, 2005.
- [58] D. W. Hutmacher, “Scaffold design and fabrication technologies for engineering tissues - State of the art and future perspectives,” *J. Biomater. Sci. Polym. Ed.*, vol. 12, no. 1, pp. 107–124, 2001.
- [59] E. F. Morgan, G. Unnikrisnan, and A. Hussein, “Bone Mechanical Properties in Healthy and Diseased States,” *Annu. Rev. Biomed. Eng.*, vol. 20, pp. 119–143, 2018.
- [60] C. Vitale-Brovarone, F. Baino, and E. Verné, “High strength bioactive glass-ceramic scaffolds for bone regeneration,” *J. Mater. Sci. Mater. Med.*, vol. 20, no. 2, pp. 643–653, 2009.
- [61] L. J. Gibson, “Modelling the mechanical behavior of cellular materials,” *Mater. Sci. Eng. A*, vol. 110, no. C, pp. 1–36, 1989.
- [62] S. Callcut and J. C. Knowles, “Correlation between structure and compressive strength in a reticulated glass-reinforced hydroxyapatite foam,” *J. Mater. Sci. Mater. Med.*, vol. 13, no. 5, pp. 485–489, 2002.
- [63] H. W. Kim, J. C. Knowles, and H. E. Kim, “Hydroxyapatite porous scaffold engineered with biological polymer hybrid coating for antibiotic Vancomycin release,” *J. Mater. Sci. Mater. Med.*, vol. 16, no. 3, pp. 189–195, 2005.
- [64] S. Ahmadzadeh-Asl, S. Hesarak, and A. Zamanian, “Preparation and characterisation of calcium phosphate-Hyaluronic acid nanocomposite bone cement,” *Adv. Appl. Ceram.*, vol. 110, no. 6, pp. 340–345, 2011.
- [65] J. R. Jones and L. L. Hench, “Regeneration of trabecular bone using porous ceramics,” *Curr. Opin. Solid State Mater. Sci.*, vol. 7, pp. 301–307, 2003.
- [66] M. N. Rahaman *et al.*, “Bioactive glass in tissue engineering,” *Acta Biomater.*, vol. 7, no. 6, pp. 2355–2373, 2011.
- [67] F. Baino and C. Vitale-Brovarone, “Three-dimensional glass-derived scaffolds for bone tissue engineering: Current trends and forecasts for the future,” *J. Biomed. Mater. Res. - Part A*, vol. 97 A, pp. 514–535, 2011.
- [68] Y. Doi and A. Steinbuchel, “Polyesters III,” in *Biopolymers*, vol. 4, 2000.
- [69] D. Mohamad Yunus, O. Bretcanu, and A. R. Boccaccini, “Polymer-bioceramic composites for tissue engineering scaffolds,” *J. Mater. Sci.*, vol. 43, no. 13, pp. 4433–4442, 2008.
- [70] J. Hum *et al.*, “Stiffness improvement of 45S5 bioglass®-based scaffolds through natural and

- synthetic biopolymer coatings: An ultrasonic study,” *Strain*, vol. 49, no. 5, pp. 431–439, 2013.
- [71] V. Mouriño, P. Newby, and A. R. Boccaccini, “Preparation and characterization of gallium releasing 3-D alginate coated 45S5 bioglass® based scaffolds for bone tissue engineering,” *Adv. Eng. Mater.*, vol. 12, no. 7, pp. 283–291, 2010.
 - [72] C. Wu, Y. Ramaswamy, P. Boughton, and H. Zreiqat, “Improvement of mechanical and biological properties of porous CaSiO₃ scaffolds by poly(D,L-lactic acid) modification,” *Acta Biomater.*, vol. 4, no. 2, pp. 343–353, 2008.
 - [73] C. Vepari and D. L. Kaplan, “Silk as a biomaterial,” *Prog. Polym. Sci.*, vol. 32, no. 8–9, pp. 991–1007, 2007.
 - [74] D. W. Hutmacher and J. T. Schantz, “State of the art and future directions of scaffold-based bone engineering from a biomaterials perspective,” *J. Tissue Eng. Regen. Med.*, vol. 1, pp. 245–260, 2007.
 - [75] F. Pennella *et al.*, “A survey of methods for the evaluation of tissue engineering scaffold permeability,” *Ann. Biomed. Eng.*, vol. 41, no. 10, pp. 2027–2041, 2013.
 - [76] E. A. Botchwey, M. A. Dupree, S. R. Pollack, E. M. Levine, and C. T. Laurencin, “Tissue engineered bone: Measurement of nutrient transport in three-dimensional matrices,” *J. Biomed. Mater. Res. - Part A*, vol. 67, no. 1, pp. 357–367, 2003.
 - [77] M. J. Grimm and J. L. Williams, “Measurements of permeability in human calcaneal trabecular bone,” *J. Biomech.*, vol. 30, no. 7, pp. 743–745, 1997.
 - [78] S. Li, J. R. De Wijn, J. Li, P. Layrolle, and K. De Groot, “Macroporous biphasic calcium phosphate scaffold with high permeability/porosity ratio,” *Tissue Eng.*, vol. 9, no. 3, pp. 535–548, 2003.
 - [79] M. Radisic, M. Euloth, L. Yang, R. Langer, L. E. Freed, and G. Vunjak-Novakovic, “High-density seeding of myocyte cells for cardiac tissue engineering,” *Biotechnol. Bioeng.*, vol. 82, no. 4, pp. 403–414, 2003.
 - [80] S. T. Ho and D. W. Hutmacher, “A comparison of micro CT with other techniques used in the characterization of scaffolds,” *Biomaterials*, vol. 27, no. 8, pp. 1362–1376, 2006.
 - [81] M. L. Knothe Tate and U. Knothe, “An ex vivo model to study transport processes and fluid flow in loaded bone,” *J. Biomech.*, vol. 33, no. 2, pp. 247–254, 2000.
 - [82] J. Mansour and V. Mow, “The permeability of articular cartilage under compressive strain and at high pressures,” *J. Bone Jt. Surg.*, vol. 58, no. 4, pp. 509–516, 1976.
 - [83] P. A. Netti, D. A. Berk, M. A. Swartz, A. J. Grodzinsky, and R. K. Jain, “Role of extracellular matrix assembly in interstitial transport in solid tumors,” *Cancer Res.*, vol. 60, no. 9, pp. 2497–2503, 2000.
 - [84] C. A. Znati *et al.*, “Irradiation Reduces Interstitial Fluid Transport and Increases the Collagen Content in Tumors,” *Clin. Cancer Res.*, vol. 9, no. 15, pp. 5508–5513, 2003.
 - [85] S. Succi, *The lattice Boltzmann equation: for fluid dynamics and beyond*. 2001.
 - [86] M. V Chor and W. Li, “A permeability measurement system for tissue engineering scaffolds,” *Meas. Sci. Technol.*, vol. 18, no. 1, 2007.
 - [87] T. S. Karande, J. L. Ong, and C. M. Agrawal, “Diffusion in musculoskeletal tissue engineering scaffolds: Design issues related to porosity, permeability, architecture, and nutrient mixing,” *Ann. Biomed. Eng.*, vol. 32, no. 12, pp. 1728–1743, 2004.
 - [88] K. F. Leong, C. M. Cheah, and C. K. Chua, “Solid freeform fabrication of three-dimensional scaffolds for engineering replacement tissues and organs,” *Biomaterials*, vol. 24, no. 13, pp. 2363–2378, 2003.

- [89] M. V. Hillsley and J. A. Frangos, "Review: Bone tissue engineering: The role of interstitial fluid flow," *Biotechnol. Bioeng.*, vol. 43, no. 7, pp. 573–581, 1994.
- [90] I. Owan, "Mechanotransduction in bone: osteoblasts are more responsive to fluid forces than mechanical strain," *Am. J. Physiol.*, vol. 273, pp. C810–C815, 1997.
- [91] S. Truscello, G. Kerckhofs, S. Van Bael, G. Pyka, J. Schrooten, and H. Van Oosterwyck, "Prediction of permeability of regular scaffolds for skeletal tissue engineering: A combined computational and experimental study," *Acta Biomater.*, vol. 8, no. 4, pp. 1648–1658, 2012.
- [92] S. Impens, Y. Chen, S. Mullens, F. Luyten, and J. Schrooten, "Controlled cell-seeding methodologies: A first step toward clinically relevant bone tissue engineering strategies," *Tissue Eng. - Part C Methods*, vol. 16, no. 6, pp. 1575–1583, 2010.
- [93] S. Van Bael *et al.*, "The effect of pore geometry on the in vitro biological behavior of human periosteum-derived cells seeded on selective laser-melted Ti6Al4V bone scaffolds," *Acta Biomater.*, vol. 8, no. 7, pp. 2824–2834, 2012.
- [94] P. W. Hui, P. C. Leung, and A. Sher, "Fluid conductance of cancellous bone graft as a predictor for graft-host interface healing," *J. Biomech.*, vol. 29, no. 1, pp. 123–132, 1996.
- [95] C. M. Agrawal, J. S. McKinney, D. Lancot, and K. A. Athanasiou, "Effects of fluid flow on the in vitro degradation kinetics of biodegradable scaffolds for tissue engineering," *Biomaterials*, vol. 21, no. 23, pp. 2443–2452, 2000.
- [96] C. G. Jeong and S. J. Hollister, "Mechanical, permeability, and degradation properties of 3D designed poly(1,8 Octanediol-co-Citrate) scaffolds for soft tissue engineering," *J. Biomed. Mater. Res. - Part B Appl. Biomater.*, vol. 93, no. 1, pp. 141–149, 2010.
- [97] J. Bear, *Dynamics of fluids in porous media*. Dover, New York, 1972.
- [98] I. Ochoa, J. A. Sanz-Herrera, J. M. García-Aznar, M. Doblaré, D. M. Yunos, and A. R. Boccaccini, "Permeability evaluation of 45S5 Bioglass®-based scaffolds for bone tissue engineering," *J. Biomech.*, vol. 42, no. 3, pp. 257–260, 2009.
- [99] J. A. Sanz-Herrera, C. Kasper, M. Van Griensven, J. M. Garcia-Aznar, I. Ochoa, and M. Doblaré, "Mechanical and flow characterization of Sponceram® carriers: Evaluation by homogenization theory and experimental validation," *J. Biomed. Mater. Res. - Part B Appl. Biomater.*, vol. 87, no. 1, pp. 42–48, 2008.
- [100] D. E. Discher, P. Janmey, and Y. L. Wang, "Tissue cells feel and respond to the stiffness of their substrate," *Science (80-.)*, vol. 310, no. 5751, pp. 1139–1143, 2005.
- [101] S. S. Kohles, J. B. Roberts, M. L. Upton, C. G. Wilson, L. J. Bonassar, and A. L. Schlichting, "Direct perfusion measurements of cancellous bone anisotropic permeability," *J. Biomech.*, vol. 34, no. 9, pp. 1197–1202, 2001.
- [102] E. A. Nauman, K. E. Fong, and T. M. Keaveny, "Dependence of Intertrabecular Permeability on Flow Direction and Anatomic Site," *Ann. Biomed. Eng.*, vol. 27, no. 4, pp. 517–524, 1999.
- [103] B. D. Ratner, A. S. Hoffman, F. J. Schoen, and J. E. Lemons, *Biomaterials science: an introduction to materials in medicine*. 2012.
- [104] A. I. Pearce, R. G. Richards, S. Milz, E. Schneider, and S. G. Pearce, "Animal models for implant biomaterial research in bone: A review," *Eur. Cells Mater.*, vol. 13, no. 0, pp. 1–10, 2007.
- [105] Y. Li, S. K. Chen, L. Li, L. Qin, X. L. Wang, and Y. X. Lai, "Bone defect animal models for testing efficacy of bone substitute biomaterials," *J. Orthop. Transl.*, vol. 3, no. 3, pp. 95–104, 2015.
- [106] J. O. Hollinger, *An Introduction to Biomaterials*. 2011.

- [107] A. C. Jones, C. H. Arns, D. W. Hutmacher, B. K. Milthorpe, A. P. Sheppard, and M. A. Knackstedt, "The correlation of pore morphology, interconnectivity and physical properties of 3D ceramic scaffolds with bone ingrowth," *Biomaterials*, vol. 30, no. 7, pp. 1440–1451, 2009.
- [108] B. Otsuki, M. Takemoto, S. Fujibayashi, M. Neo, T. Kokubo, and T. Nakamura, "Pore throat size and connectivity determine bone and tissue ingrowth into porous implants: Three-dimensional micro-CT based structural analyses of porous bioactive titanium implants," *Biomaterials*, vol. 27, no. 35, pp. 5892–5900, 2006.
- [109] C. Wu *et al.*, "Copper-containing mesoporous bioactive glass scaffolds with multifunctional properties of angiogenesis capacity, osteostimulation and antibacterial activity," *Biomaterials*, vol. 34, no. 2, pp. 422–433, 2013.
- [110] J. Barralet, U. Gbureck, P. Habibovic, E. Vorndran, C. Gerard, and C. J. Doillon, "Angiogenesis in calcium phosphate scaffolds by inorganic copper ion release," *Tissue Eng. - Part A*, vol. 15, no. 7, pp. 1601–1609, 2009.
- [111] L. Bi *et al.*, "Evaluation of bone regeneration, angiogenesis, and hydroxyapatite conversion in critical-sized rat calvarial defects implanted with bioactive glass scaffolds," *J. Biomed. Mater. Res. - Part A*, vol. 100 A, no. 12, pp. 3267–3275, 2012.
- [112] E. Bonnelye, A. Chabadel, F. Saltel, and P. Jurdic, "Dual effect of strontium ranelate: Stimulation of osteoblast differentiation and inhibition of osteoclast formation and resorption in vitro," *Bone*, vol. 42, no. 1, pp. 129–138, 2008.
- [113] X. Wang, J. D. Mabrey, and C. M. Agrawal, "An interspecies comparison of bone fracture properties," *Biomed. Mater. Eng.*, vol. 8, no. 1, pp. 1–9, 1998.
- [114] E. B. Hunziker, L. Enggist, A. Küffer, D. Buser, and Y. Liu, "Osseointegration: The slow delivery of BMP-2 enhances osteoinductivity," *Bone*, vol. 51, no. 1, pp. 98–106, 2012.
- [115] M. A. Lauzon, É. Bergeron, B. Marcos, and N. Faucheux, "Bone repair: New developments in growth factor delivery systems and their mathematical modeling," *J. Control. Release*, vol. 162, no. 3, pp. 502–520, 2012.
- [116] F. Deschaseaux, L. Sensébé, and D. Heymann, "Mechanisms of bone repair and regeneration," *Trends Mol. Med.*, vol. 15, no. 9, pp. 417–429, 2009.
- [117] C. E. A. Dutra and M. M. Pereira, "In vivo evaluation of bioactive glass foams associated with platelet-rich plasma in bone defects," *J. Tissue Eng. Regen. Med.*, vol. 2, pp. 221–227, 2008.
- [118] N. Hasiwa, J. Bailey, P. Clausen, M. Daneshian, and S. Farkas, "Critical evaluation of the use of dogs in biomedical research and testing," *ALTEX*, vol. 28, pp. 326–340, 2011.

Chapter 4

Materials and Methods

4.1 Introduction to the Experimental Activity and Scope of the Work

The use of multifunctional biomaterials for the treatment of malignant tumours is maybe one of the most appealing application fields of mesoporous and ion-doped bioactive glasses in tissue engineering and regenerative medicine. As an example, biocompatible glass microspheres have been already successfully used in clinical practice for the treatment of hepatocellular carcinoma and metastatic liver cancer [1], [2].

The present experimental activity deals with the development of holmium-doped bioactive glass scaffolds for bone tumour treatment by brachytherapy.

To date brachytherapy was used for the treatment of different kinds of cancer and for palliative treatment of bone metastases.

Compelling data supporting the use of Holmium-166 (^{166}Ho) as a radiotherapist have been provided by various research groups [3], and bioactive glass seeds containing holmium for brachytherapy have been already produced by Campos et al. [4] and Nogueira et al. [5]. However, no examples of bioactive glass scaffolds containing holmium have been reported to date.

Holmium (Ho) is a rare earth element discovered in the 1870s. Ho has an atomic number of 67 and an atomic weight of 164.93 g/mol [3]. Ho has a 100% natural abundance of the stable isotope holmium-165, which can be neutron activated to produce the radionuclide holmium-166, as well as of holmium-166m, which is produced in such a small quantity that it is neglected. The product of the decay of both radioactive isomers is non-radioactive erbium-166, whose fate depends on the material with which it is incorporated [3].

^{166}Ho has a half-life of 26.8 h and emits both β -particles and γ photons. β -particles have a decay energy of 1.85 MeV and they are responsible for the therapeutic effect; indeed, they damage the DNA of the cancer cells, causing their death. γ photons have an energy of 81 keV and they can be used for nuclear imaging purposes [3].

Johnson et al. [6] have found that the maximum tissue range of the β -particles in soft tissue is 8.7 mm, the average range 2.2 mm and 90% of the total radiation dose is delivered in the first 2.1 mm. This results in an interesting relatively high dose-rate if the same cumulative dose is compared to other radioisotopes often used for cancer treatment, such as phosphor-32 (^{32}P), yttrium-90 (^{90}Y), iodine-131 (^{131}I), lutetium-177 (^{177}Lu) and rhenium-186 (^{186}Re), with half-lives between 2.7 and 14.3 days [7].

Thanks to its special physical properties, ^{166}Ho has gained the attention of many researchers for its application in the fight against cancer.

Using ^{166}Ho as a radiotherapeutic in the clinic is justified, especially because pharmaceutical formulations can be made while Ho is non-radioactive and becomes radioactive (^{166}Ho) just prior to use [3].

In order to be suitable vectors for ^{166}Ho radiation therapy, BG scaffolds need to have a high Ho content, be able to endure neutron-activation, be physically stable, which means releasing little or no ^{166}Ho , and have low toxicity [8].

This therapeutic approach is designed to be used in combination with surgical therapy. Indeed, after the tumour is surgically removed, the BG scaffold containing holmium, which was made radioactive (^{166}Ho) by neutron activation in the last step of the scaffold fabrication process, is implanted in the tumour area. β -particles kill the remaining cancer cells damaging their DNA. Meanwhile, the bioactive glass scaffold bonds to living bone and stimulates the adhesion of the osteogenic cells that induce the formation of new bone tissue in the area where the tumour was destroyed. While the new tissue forms, the scaffold is able to degrade.

In conclusion, Ho-doped bioactive glass scaffold has the potential to meet the grand challenge of creating a bioactive and biodegradable device that destroys cancer and promotes the regeneration of bone tissue at the same time.

This project started at the Federal University of ABC, in São Paulo, Brazil, where the bioactive glass containing holmium (Ho-BG) was produced by sol-gel synthesis. After thermal analysis on the dried-gel and compositional and physicochemical analyses the glass, Ho-BG powders were sent to Politecnico di Torino (Turin, Italy). Figure 1 shows the Ho-BG powders path.

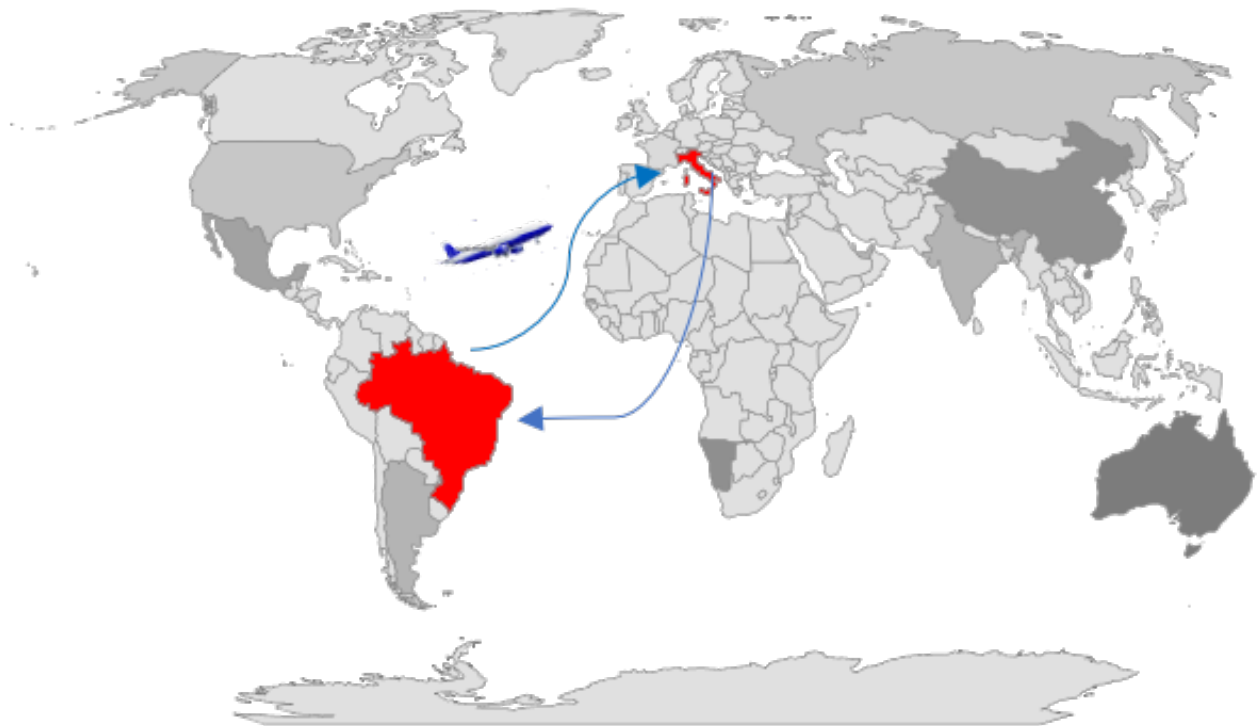


Figure 1: Schematization of the Ho-BG path.

The experimental activity carried out at the Department of Applied Science and Technology at Politecnico di Torino involved the investigation of Ho-BG powders coming from the Federal University of ABC, the scaffolds' development using this glass, and their subsequent characterization (Figure 2).



Figure 2: Schematic representation of the experimental activity concerning Ho-BG.

The purpose of this chapter is to describe the materials and methods used for sample preparation and characterization techniques employed to define physicochemical and biological properties.

4.2 Synthesis of Ho-doped Sol-Gel Glass

Ho-doped bioactive glass was produced by sol-gel process at the Federal University of ABC (São Paulo, Brazil).

58S ternary sol-gel glass was doped by introducing 5 wt % of Ho_2O_3 , as reported in Table 1.

Table 1: Nominal compositions (mol% and wt%) of 58S BG and Ho-doped BG.

Glass	mol%				wt%			
	SiO_2	CaO	P_2O_5	Ho_2O_3	SiO_2	CaO	P_2O_5	Ho_2O_3
58S	60	36	4	-	58	33	9	-
Ho-BG	59.35	36.13	3.87	0.65	55.10	31.3	8.6	5

The synthesis was based on the quick alkali-mediated sol-gel method proposed by Xia et al. [9] for the production of nano-bioactive 58S glass [9].

The oxide precursors used were:

- Tetraethyl orthosilicate (TEOS, $\text{Si}(\text{OC}_2\text{H}_5)_4$) for SiO_2
- Triethyl phosphate (TEP, $\text{OP}(\text{OC}_2\text{H}_5)_3$) for P_2O_5
- Calcium nitrate tetra-hydrate ($\text{Ca}(\text{NO}_3)_2 \cdot 4\text{H}_2\text{O}$) for CaO
- Holmium (III) nitrate pentahydrate ($\text{Ho}(\text{NO}_3)_3 \cdot 5\text{H}_2\text{O}$) for Ho_2O_3

Nitric acid (HNO_3) and ammonia (NH_3) were used respectively as hydrolysis and condensation catalysts.

The sol-gel synthesis was carried out according to the following steps:

1. TEOS, distilled water, and 2 M HNO_3 were dissolved in ethanol and stirred at room temperature for 30 min.
2. TEP was dissolved into the acid silica sol and stirred for 20 min.
3. $\text{Ca}(\text{NO}_3)_2 \cdot 4\text{H}_2\text{O}$ and $\text{Ho}(\text{NO}_3)_3 \cdot 5\text{H}_2\text{O}$ were added in the previous solution and stirred for more than 20 min.
4. 10 ml of 1 M NH_3 solution was added to induce the condensation of TEOS and TEP, which showed a gel consistency.
5. The gel was freeze-dried (Operon, South Korea) for 24 h.
6. The dried-gel powders were calcined at 550 °C for 1h (EGD 300, Brazil).

4.3 Glass Processing at Politecnico di Torino (Turin, Italy)

At Politecnico di Torino, Ho-BG powders were ground for 20 minutes by using a zirconia ball-milling machine (ANALYSETTE 3 SPARTAN-FRITSCH) in order to produce fine powders (Figure 3). In such system, grinding was mechanically performed by a zirconia ball, moving in the jar (Figure 3a) under the action of the vibrating plate (Figure 3b).

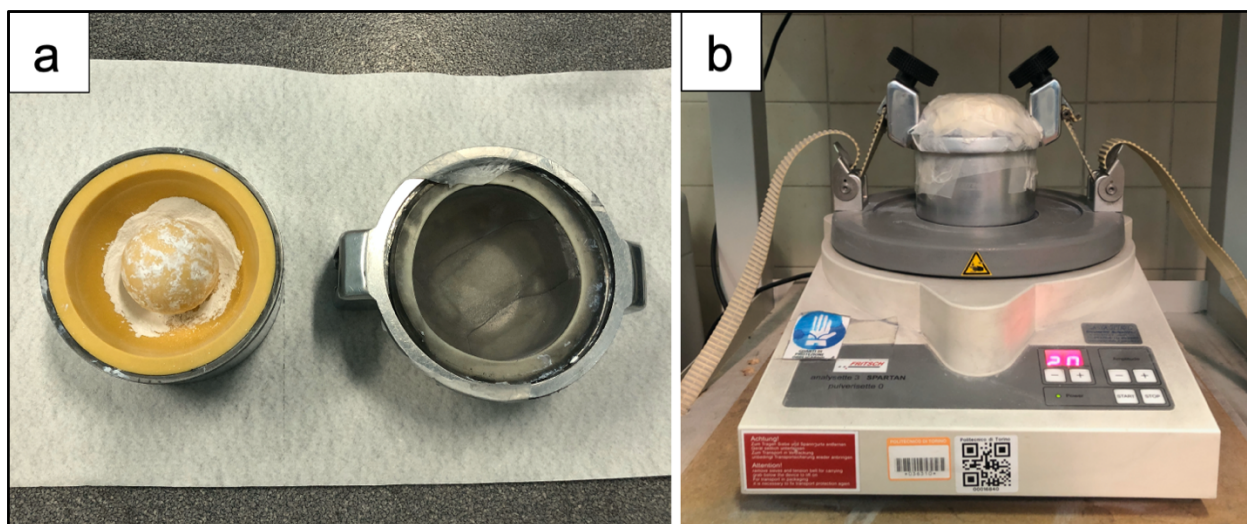


Figure 3: (a) Alumina jar containing Ho-BG after grinding. (b) Vibrating plate grinder (ANALYSETTE 3 SPARTAN).

After that, Ho-BG powders were sieved using a stainless-steel sieve with a mesh of 32 μm diameter (Figure 4) in order to obtain all particles of controlled size. Ground and sieved powders were identified as Ho-BG32.

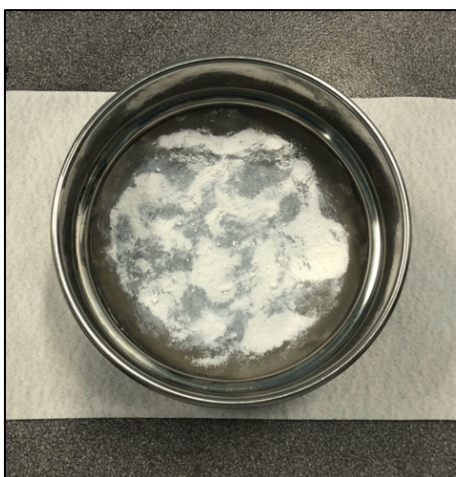


Figure 4: Sieve with mesh of 32 μm diameter containing Ho-BG powders.

Ho-BG and Ho-BG32 powders were then characterized in terms of compositional and physicochemical properties. Results were compared and discussed according to the preliminary characterization analyses performed at the Federal University of ABC on the raw powders.

4.3.1 Scaffold Manufacturing

For the scaffold production, the foam replica method was chosen, because it offers a number of advantages over other scaffold fabrication methods, including the ability to produce foams with a highly porous structure with adjustable pore dimensions [10]. In addition, this method allows producing scaffolds with a microstructure similar to that of human trabecular bone [11], and with irregular shapes to match the size and shape of the bone defect. It does not involve the use of toxic chemicals, and it is more rapid and cost-effective than other techniques [10].

Ho-doped BG-based scaffolds were produced by foam replica method, using polyurethane sponges as sacrificial template.

The main stages of the process are shown in Figure 5.

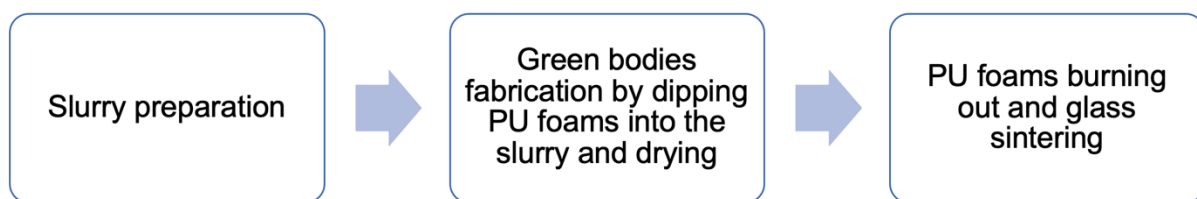


Figure 5: Schematic representation of foam replica method for scaffold's fabrication.

4.3.1.1 Materials

The starting material was Ho-BG32, while cube shaped polyurethane PU foams (45 ppi) of 1 cm in size were used as sacrificial templates.

4.3.1.2 Scaffold Fabrication Stages

1. Choice of the slurry composition

The first step for scaffold production was the definition of the slurry composition.

The original idea was to use the composition reported in Table 2 [12], previously used for the production of melt-derived BG-based scaffolds.

Table 2: Original slurry composition.

Component	wt%
Ho-BG32	30
Bi-distilled water	64
PVA	6

However, this composition was considered inadequate for the present study, since the suggested quantity of bioactive glass occupied an enormous volume compared to that of bi-distilled water and PVA, as a result of the low density of Ho-BG. According to this, a new slurry composition was

designed by modifying the percentage by weight of glass and bi-distilled water, while maintaining the same percentage by weight of PVA. The adapted slurry composition is shown in Table 3.

Table 3: Adapted slurry composition.

Component	wt%
Ho-BG32	15
Bi-distilled water	79
PVA	6

2. Preparation of the slurry

In order to produce 8 scaffolds, 10 g of slurry were needed.

0.6 g of PVA were dissolved into 7.9 g of bi-distilled water at 60 °C under continuous magnetic stirring at 200 rpm, until a clear and transparent solution was obtained. In order to limit water evaporation during this phase, the beaker was covered with a glass lid. After PVA dissolution, some additional water was added dropwise to restore the initial PVA:H₂O ratio and the solution was left to cool at room temperature for about 30 min.

1.5 g of Ho-BG32 powders were then added to the solution and stirred at room temperature (200 rpm) for at least 5 min in order to obtain a homogeneous milky suspension (Figure 6).



Figure 6: The beaker containing PVA, BG and bi-distilled water placed on the magnetic stirrer.

3. Green bodies production

PU foam sheets of 1 cm thickness and 45 ppi were cut into cubes and used as sacrificial template for the replica process.

The experimental set-up used for the preparation of the green bodies is shown in Figure 7.

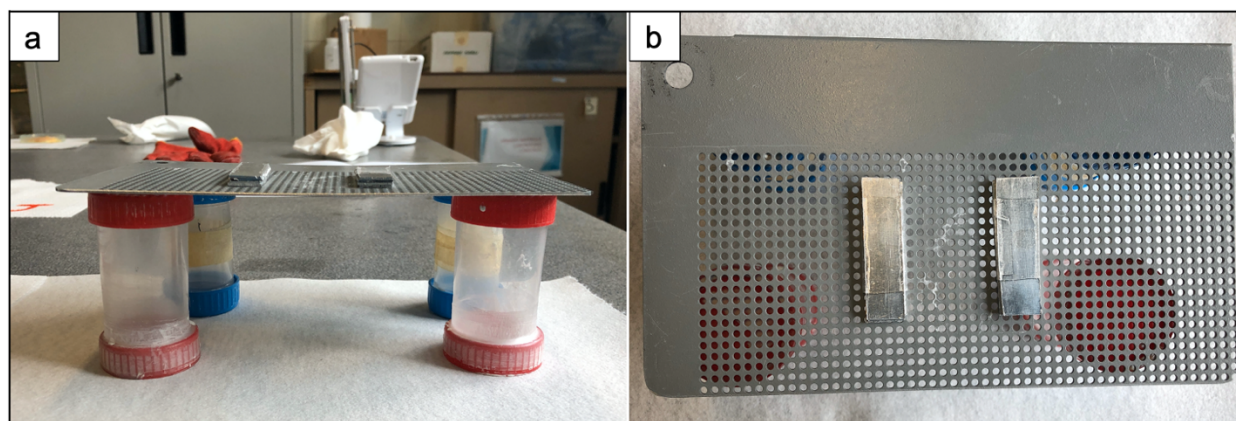


Figure 7: (a) Front, and (b) top view of the experimental set-up used for the preparation of the green bodies.

The polymer template was immersed in the slurry, which subsequently infiltrated the structure and glass particles adhered to the surface of the foam thanks to the action of PVA, used as binder. Then, the PU foam was compressed to 60% of its size, so as to remove the exceeding slurry.

Each sample underwent 3 complete immersion-compression cycles, in order to obtain a continuous and resistant coating. Once the 3th cycle was completed, the green bodies were turned 180° for at least 2h so that the slurry could be evenly distributed in the whole foam volume.

4. Drying process

Finally, the samples, called green bodies, were placed onto a plastic Petri dish and left to dry.

Half of the green bodies were air-dried at room temperature overnight, while the other half was dried inside an incubator at 37 °C for 4 h.

5. Heat treatment

A heat treatment program was properly set for PU template burning-out and glass sintering on the basis of thermal characterization analyses performed on the glass. In order to optimize the scaffolds mechanical resistance, eight different tests were carried out, varying, one at a time, the drying method and the sintering temperature, as shown in Table 4. Sintering conditions were set as follows: 800 for 3h, 850 °C for 3h, 950 °C for 3h, 1000 °C for 3h and 1050 °C for 3h. The heating rate was 5 °C/min for all the sintering treatments.

Table 4: Summary of the test performed for the optimization of Ho-BG32 scaffolds.

Test	Sample Name	Drying Method	Sintering Temperature (°C)	Heating Rate (°C/min)	Sintering Time (h)
1	Ho-I-800	Incubator/37 °C	800	5	3
2	Ho-AD-850	Air drying/room temperature	850	5	3
3	Ho-I-850	Incubator/37 °C	850	5	3
4	Ho-AD-950	Air drying/room temperature	950	5	3
5	Ho-I-950	Incubator/37 °C	950	5	3
6	Ho-AD-1000	Air drying/room temperature	1000	5	3
7	Ho-I-1000	Incubator/37 °C	1000	5	3
8	Ho-AD-1050	Air drying/room temperature	1050	5	3

The Ho-AD-1050 (Test 8) was measured in order to make some considerations on the density and porosity of the structure. Scaffold dimensions are summarized in Table 5.

Table 5: Physical properties of Ho-AD-1050 scaffold.

Test	Sample	Side 1 (mm)	Side 2 (mm)	Side 3 (mm)	Mass (g)	Volume (cm ³)	Density (g/cm ³)
8	Ho-AD-1050	6.34	6.52	6.83	0.1	0.28	0.36

The percentage of porosity related to the sample was evaluated using the Equation 1:

$$\% \text{ porosity} = \left(1 - \frac{\rho}{\rho_{ref}}\right) * 100 \quad (1)$$

Where:

ρ = density of the sample (g/cm³)

ρ_{ref} = 2.6 g/cm³ (glass skeletal density).

4.4 Glass Characterization - Federal University of ABC (São Paulo, Brazil)

The analysis techniques that were used to characterize samples at Federal University of ABC are presented in Table 6.

Table 6: Characterization technique adopted by Federal University of ABC.

Characterization technique	Aim of the analysis	Sample
Differential Scanning Calorimetry (DSC)	Determination of glass transition, crystallization onset and melting temperatures (T_g , T_x , T_m)	Ho-dried-gel powders
Thermogravimetric Analysis (TGA)	Evaluation of the thermal stability	Ho-dried-gel powders
Derivative Thermogravimetry (DTG)	Evaluation of the mass change rate	Ho-dried-gel powders
Neutron Activation Analysis (NAA)	Compositional analysis	Ho-BG powders
Fourier Transform-Infrared Spectroscopy (FTIR)	Compositional analysis	Ho-BG powders

4.4.1 Thermal Analysis

Thermal analysis includes a group of techniques in which a physical property of a substance is measured as a function of temperature, while the substance is subjected to a controlled temperature program [13].

The main methods adopted to determine the thermo-physical properties are: differential thermal analysis (DTA), differential scanning calorimetry (DSC), thermogravimetric analysis (TGA), derivative thermogravimetry (DTG), hot stage microscopy (HSM) and dilatometry (DIL) [14].

4.4.1.1 Differential Scanning Calorimetry

Differential Scanning Calorimetry (DSC) measures the change of the difference in the heat flow rate to the sample compared to a reference material which are both subjected to a controlled temperature program [14].

DSC allows determining the temperatures of the phase transitions including melting point, solidification onset, re-crystallization onset and evaporation temperature, as well as enthalpy and specific heat (c_p). [14].

The result of a DSC measurement is a heat flux versus time or temperature curve.

Typically, in a DSC curve, peaks in the positive verse of y-axis are related to exothermic reactions, and peaks in the negative verse of the same axis are related to endothermic reactions.

DSC can be classified into 2 main instrumentation types:

- Heat flux DSC [15].

- Power compensated DSC [15].

In heat flux DSC (Figure 8), a pan enclosing the material and an empty reference are put on a thermoelectric disk enveloped by a furnace. The furnace is heated following a linear heating rate, and the thermoelectric disk transfers heat to the sample and reference pan. Due to the differences in heat capacity (C_p), there is a temperature difference between the sample and reference pans, which is measured by area thermocouples [15].

Consequently, thermal equivalent of Ohm's law determines heat flow according to Equation 2 [15]:

$$\dot{Q} = \frac{\Delta T}{R} \quad (2)$$

Where:

\dot{Q} : heat flow rate (W) [15].

ΔT : temperature difference between the sample and reference (K) [15].

R: resistance of thermoelectric disk (Ω) [15].

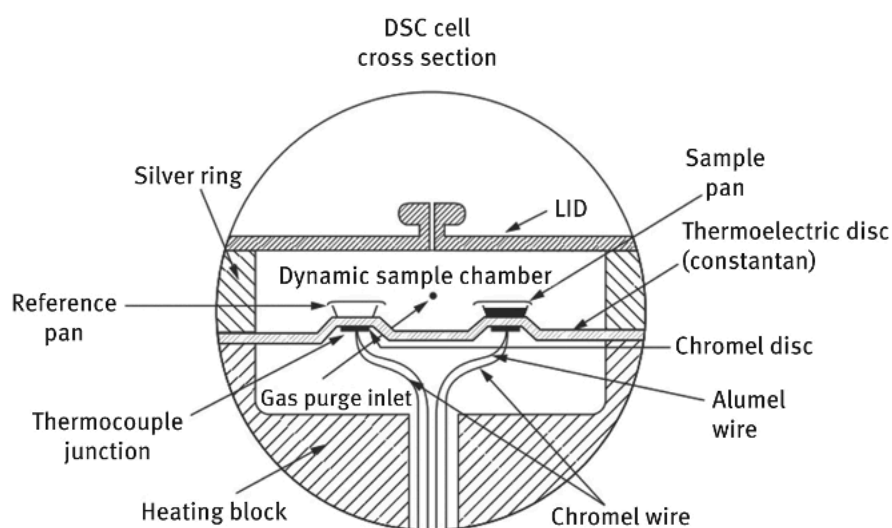


Figure 8: Schematic of a heat-flux DSC. (Courtesy of TA Instruments) [16].

In a power-compensated DSC (Figure 9), the sample and reference pans are located in distinct furnaces heated by distinct heaters. The sample and reference are kept at the same temperature, and the difference in thermal power necessary to keep them at the same temperature is measured [15].

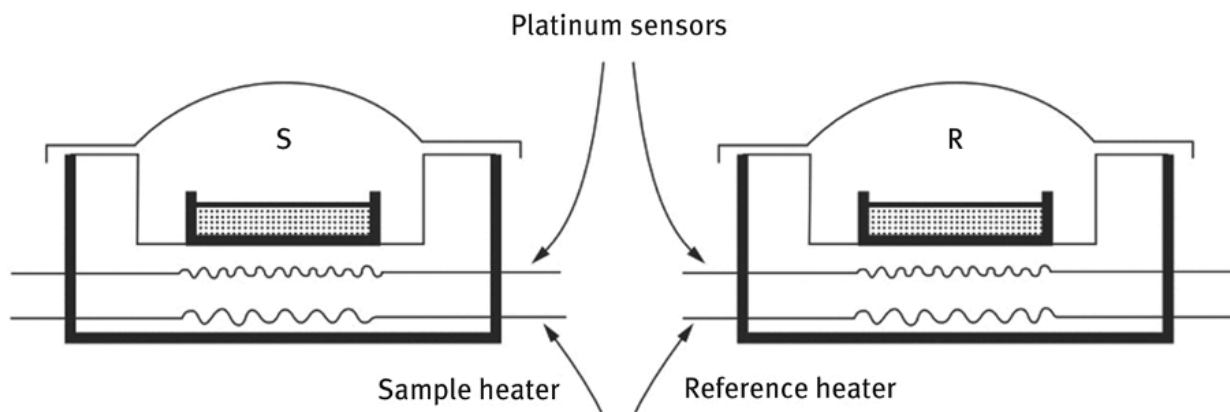


Figure 9: Schematic of a power-compensated DSC. (Courtesy of PerkinElmer) [16].

DSC was carried out on the Ho-dried-gel powders. The sample was subjected to a thermal cycle of up to 1000 °C in order to study the behaviour of the gel under heat treatment and to select the right temperature to calcinate the gel.

4.4.1.2 Thermogravimetric Analysis

Thermogravimetric Analysis (TGA) measures weight changes in a material as a function of temperature or time, under controlled atmosphere conditions [17].

The purpose of this analysis is to determine the material's thermal stability and composition [17].

A common thermogravimetric analyser is made up of a sample pan located inside a furnace, and a precision balance placed outside of the furnace [18], as shown in Figure 10.

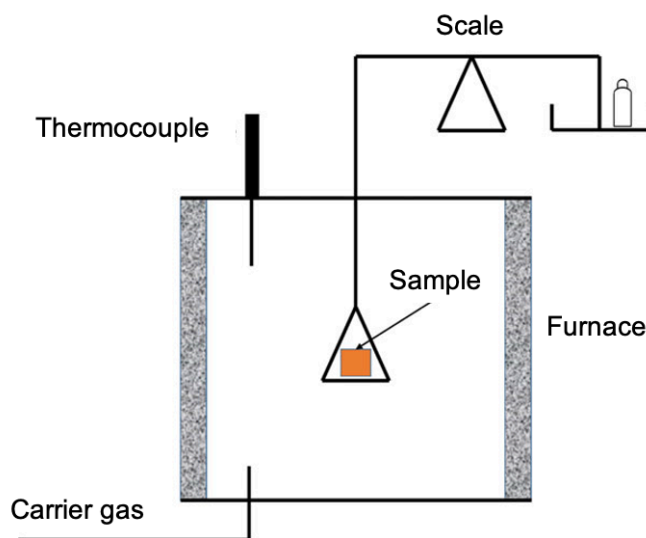


Figure 10: Representation of the thermogravimetric method. Figure adapted from De Blasio [19].

TGA is carried out by progressively increasing the temperature of the sample [17]. Due to the thermal treatment, some mass will be lost in terms of volatiles or thermal decomposition. The variation of weight of the sample as a consequence of the thermal treatment is measured by means of the microscale [19].

TGA results are plotted as mass versus temperature or time [19].

The sample is inserted into a sample pan which is expressly designed for this analysis. The sample pans can be produced using different shapes and materials. They should be able to safely store the sample, not to react with the sample, and be apt for the selected temperature. Generally, sample pans are made of alumina, platinum, and aluminium [19].

As regards the temperature conditions and its measurement, the temperature change is set according to a customized temperature program which may include isothermal and ramp stages with various heating rates, while the temperature is measured with thermocouples which are in contact with the sample pan [19].

TGA was performed on the Ho-dried-gel powders in order to evaluate the behaviour of the gel under heat treatment and to choose the appropriate temperature to calcinate the gel. The sample was subjected to a thermal cycle of up to 1000 °C.

4.4.1.3 Derivative Thermogravimetry

Derivative Thermogravimetry (DTG) is another kind of representation of the results coming out from the thermogravimetric analyser [19].

DTG is the first derivative of the TGA curve. Hence, it represents the mass change rate [19].

DTG plot supports the detection of transformations that either overlap or are associated with poor mass loss because they are able to detect more subtle effects. It is also used to investigate kinetic parameters. In addition, the peaks of DTG indicate a specific transformation, and the minimum values coincide with the maximum rate of mass loss of the related decomposition step [19].

DTG was performed on the Ho-dried-gel powders to in order to complete the study of the gel behaviour during the heat treatment.

4.4.2 Neutron Activation Analysis

Neutron Activation Analysis (NAA) is an isotope specific analytical technique for the qualitative and quantitative measurement of chemical elements [20].

The discovery of NAA dates back to 1936, when Hevesy and Levi discovered that samples incorporating some rare earth elements became highly radioactive after being exposed to a source of neutrons. From this discovery, they recognized the potential of applying nuclear reactions on samples followed by measurement of the induced radioactivity to simplify both qualitative and quantitative recognition of the elements present in the samples [21].

NAA has a higher sensitivity to detect rare earth elements compared to energy dispersive x-ray spectrometry. Moreover, NAA is commonly considered as the "referee method" of choice when new procedures are under development or when other methods give discordant results [21].

The needed elements to perform an analysis of the samples by NAA are a source of neutrons, useful apparatus for detecting gamma rays, and a deep knowledge of the reactions that take place when neutrons interact with target nuclei [21].

The most common type of nuclear reaction employed in NAA is called the neutron capture or (n,gamma) reaction. The sequence of events that take place during this reaction is shown in Figure 11 [22].

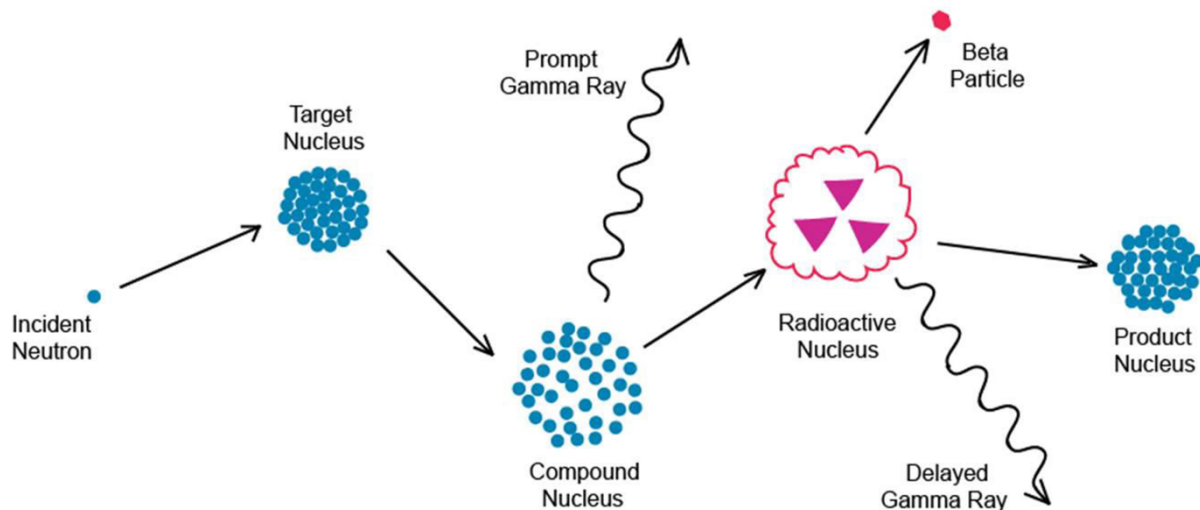


Figure 11: Schematic illustration of the process of neutron capture by a target nucleus followed by the emission of gamma rays [23].

First, the interaction of the neutron with the target nucleus occurs through a non-elastic collision, which forms a compound nucleus in an excited state [21].

The excitation energy of the compound nucleus is due to the binding energy of the neutron with the nucleus. The compound nucleus almost instantly de-excite into a more stable configuration through emission of one or more characteristic prompt gamma rays [22].

Generally, this new configuration generates a radioactive nucleus which also de-excites (or decays) by emission of one or more characteristic delayed gamma rays, but at a much lower rate according to the unique half-life of the radioactive nucleus [22].

Half-life times may vary from fraction of a second to several years depending on the radioactive species [22].

In principle, NAA can be classified into two categories according to the time of measurement:

- Prompt Gamma-Ray Neutron Activation Analysis (PGNAA), where measurements occur during irradiation [22].
- Delayed Gamma-Ray Neutron Activation Analysis (DGNA), where measurements follow radioactive decay. This is the most common category; thus, when referring to NAA it is usually assumed the measurement of the delayed gamma rays [22].

About 70% of the elements in the periodic table have properties suitable for measurement by NAA [22].

In NAA, almost exclusively the energy of the gamma-radiation is measured due to the penetrating power of this type of radiation, and the selectivity that can be achieved from the specific energies of the photons [20].

The gamma-spectrum is analysed to identify the radionuclides and their amounts of induced activity in order to trace the target elements from which they have been generated [20].

The masses of the elements are determined from the net peak areas by comparison with the induced activity of the same neutron activation produced radionuclides from known amounts of the element of interest [20].

NAA was carried out on Ho-BG powders to evaluate the composition of the glass.

4.4.3 Fourier-Transform Infrared Spectroscopy

Fourier Transform-Infrared Spectroscopy (FT-IR) is an analytical technique aimed at identifying organic and inorganic materials by the study of chemical bonds [24].

FT-IR measures the absorption of infrared radiation by the sample material as a function of wavelength. Molecular components are denoted by the infrared absorption bands [24].

When the infrared (IR) beam is directed towards the sample, part of the IR radiation is absorbed, while the other is transmitted [24].

Figure 12 provides a schematization of FTIR operation [24].

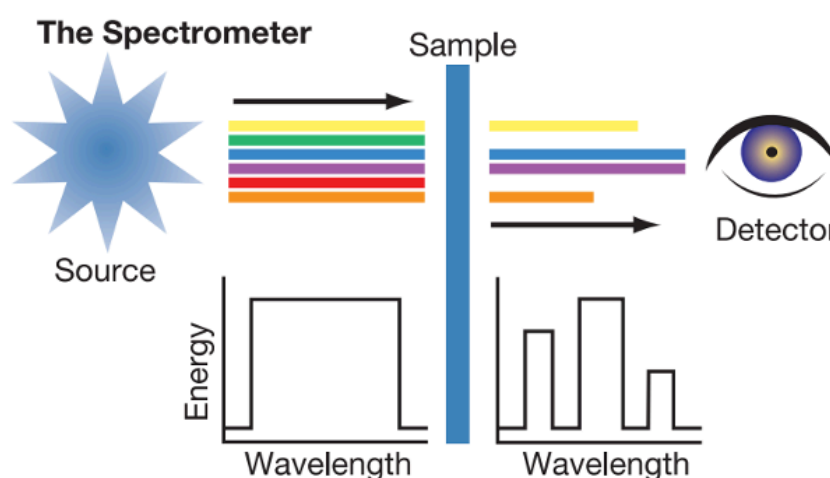


Figure 12: Schematization of FTIR operation [25].

When a material is irradiated with IR radiation, molecules are excited to a higher vibrational state by absorbed IR radiation. Each molecule absorbs light at a specific wavelength, which depends on the energy difference between the at-rest and excited vibrational states. The wavelengths that are absorbed by the sample are characteristic of its molecular structure [24].

The FTIR instrumentation includes an interferometer, a detector, and a computer [24].

The interferometer modulates the wavelength from a broadband IR source; the detector measures the intensity of transmitted or reflected light as a function of its wavelength; the computer analyses the signal obtained from the detector, which is an interferogram. The computer uses Fourier transforms to obtain a single-beam infrared spectrum [24].

The FTIR spectra are plots of intensity as function of wavenumber, defined as the reciprocal of the wavelength. The intensity can be plotted as the percentage of light transmittance or absorbance at each wavenumber [24].

FTIR was carried out on Ho-BG powders in order to identify the materials and the reactions involved.

4.5 Glass Characterization - Politecnico di Torino (Turin, Italy)

Table 7 provides an overview of the analysis techniques used to characterize Ho-BG powders and Ho-doped BG scaffolds at Politecnico di Torino.

Table 7: Characterization technique performed at Politecnico di Torino.

Characterization technique	Aim of the analysis	Sample
Particle Size Analysis	Determination of the material size range	Ho-BG Ho-BG32
Differential Thermal Analysis (DTA)	Determination of glass transition, crystallization onset and melting temperatures (T_g , T_x , T_m)	Ho-BG Ho-BG32
Hot Stage Microscopy (HSM)	Evaluation of the volumetric shrinkage upon heating	Ho-BG Ho-BG32
X-Ray Diffraction (XRD)	Individuation of crystalline phases	Ho-BG Ho-BG32
Scanning Electron Microscopy and Energy Dispersive X-ray Spectrometry (SEM and EDS)	Morphological and compositional analysis	Ho-BG Ho-doped BG scaffolds
Brunauer, Emmett and Teller Theory (BET)	Determination of the textural properties	Ho-BG Ho-BG32

4.5.1 Particle Size Analysis

Particle size analysis is an analytical technique which determines the size range, and/or the mean size of the particles in a powder or liquid sample [26].

Particle size analyser based on laser diffraction method is able to accurately measure a wide range of particles, ranging from $\sim 0.1 \mu\text{m}$ to several thousand μm [26].

Laser diffraction determines particle size distribution by measuring the angular variation in intensity of light scattered when a laser beam crosses a dispersed particulate sample [27]. Particles of a given size diffract light through a given angle that increases logarithmically with decreasing size [28]. The angular scattering intensity data is then assessed in order to calculate the size of the particles creating the scattering pattern [27].

Mie theory of light scattering is used to calculate the particle size distribution, adopting a volume equivalent to sphere model. This theory requires knowledge of the optical properties of the sample analysed [27].

If the optical properties of the sample are unknown, the Fraunhofer approximation can be used. It approximates the particles to circular, two-dimensional, opaque disks; it considered just the interaction of light around a particle; and it takes into account only scattering in the near-forward direction [29].

This approach provides accurate results for large particles, while it requires special attention to small or relatively transparent particles [27].

The main components of a particle size analyser based on laser diffraction method (Figure 13) are as follows:

- Irradiation optical system for irradiating laser beam to particles. It has a semiconductor laser in an output beam wavelength of 300 to 500 nm as a light source. This allows the measurement of particles having diameters of the order of sub-microns [26].
- Measurement optical system, which measures a space intensity distribution by receiving light diffracted/scattered by the particles of the laser beam from the irradiation optical system [26].
- Operation portion aimed at obtaining a particle size distribution of the particles from the results measured by the measurement optical system [26].

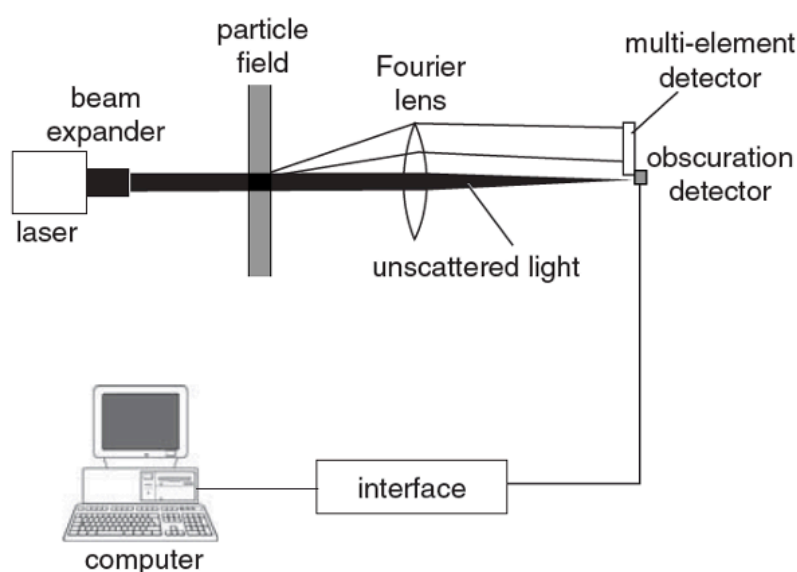


Figure 13: Typical set up of a laser diffraction analyser. Figure reproduced from Merkus [29].

Particle size analysis was performed both on Ho-BG powders and Ho-BG32 powders by Beckman Coulter LS Particle Size Analyzer.

The LS Particle Size Analyzer is the most versatile and sophisticated laser diffraction particle sizing analyser available today.

The software provides a plot of volume (%) as function of particle diameter (m) and a plot of number (%) as function of particle diameter (m).

4.5.2 Thermal Analysis

Ho-BG and Ho-BG32 powders were characterized by DTA and HSM in order to determine glass transition (T_g), crystallization onset (T_x) and melting temperatures (T_m), as well as volume shrinkage resulting from the heating treatment.

DTA and HSM data were analysed in parallel in order to facilitate the interpretation of the curves and the identification of characteristic thermal phenomena.

4.5.2.1 Differential Thermal Analysis

Differential Thermal Analysis (DTA) involves either heating or cooling a test sample and an inert reference under identical conditions, while recording any temperature difference between the sample and reference. This differential temperature (T) is then plotted against time t , or against temperature T [13].

The main components of a DTA apparatus are:

1. Sample holder including 2 thermocouples, the first one for the sample and the other for the reference, sample containers and a ceramic or metallic block which ensures an even heat distribution. The sample and the reference are both contained in small crucibles (Pt or Al_2O_3) that adheres perfectly to the thermocouple. Thermocouples should not be placed in direct contact with the sample so as to avoid contamination and degradation [13].
2. Furnace, which should produce a stable and adequately large hot-zone and should respond rapidly to commands from the temperature programmer [13].
3. Temperature programmer, fundamental to achieve constant heating rates as well as an adequate control on the measure parameters [13].
4. Recording system, which should have a low inertia to faithfully reproduce variations in the experimental set-up [13].

The complete device for DTA used to perform the analysis (DTA 404 PC-NETZSCH) is shown in Figure 14.

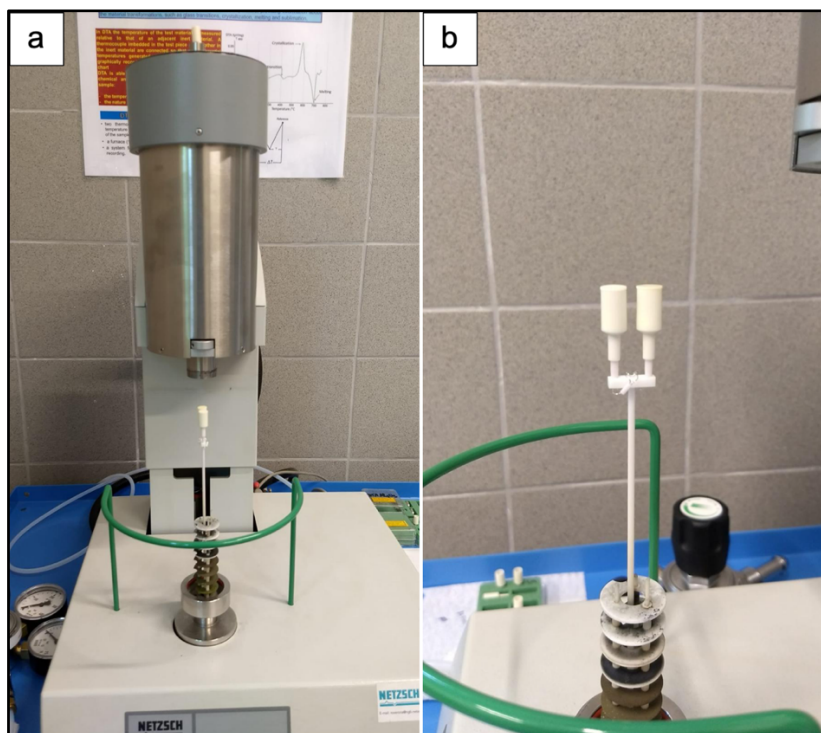


Figure 14: (a) DTA device and (b) sample holder.

The purpose of this analysis is to determine the characteristic temperatures of the sample by examining phase transitions associated to the emission or the absorption of heat [14].

DTA measures the temperature difference between the reference and the sample, which is converted to enthalpy change (ΔH) through conversion factors [14].

Conventionally, in DTA curve, peaks in the positive verse of y-axis are related to exothermic reactions, while negative peaks are associated to endothermic ones.

The shape of DTA peaks is affected by the weight of the sample and the heating rate. Generally, low heating rates, as well as higher sample weights lead to sharper peaks and better resolution [13].

Both solid samples and reference materials are usually used in powdered form. The particle-size and the packing conditions influence results [13].

For this reason, DTA was performed both on Ho-BG powders and Ho-BG32 powders. For both the analyses, Al_2O_3 powders were used as inert reference. Each measurement was performed by introducing 50 mg of Al_2O_3 in the reference crucible and 50 mg of glass powders in the sample crucible. Al_2O_3 crucibles were used.

The parameters used for the measurements are shown in Table 8.

Table 8: Parameters used for DTA analysis performed on Ho-BG powders and Ho-BG32 powders.

Sample	Heating Rate (°C/min)	Final Temperature (°C)	Treatment Conditions
Ho-BG powders	5	1400	air
Ho-BG32 powders	5	1400	air

DTA and DSC described above, are both techniques which aim at determining the characteristic temperatures of the sample [14].

The main difference between DSC and DTA apparatus is that the former is more sensitive, while DTA device is primarily used for the qualitative measurements. In addition, due to the materials used for sample holders and heat conduction path, DTA device can be used at very high temperatures and in aggressive environments where the DSC device may not function [14].

The sample holder of the DTA device is cheaper than that of the DSC apparatus, and it is commonly used for the study of materials for which the relationship of contamination between the crucible and the sample holders is unknown [14].

4.5.2.2 Hot Stage Microscopy

Hot Stage Microscopy (HSM) was invented by Welch in the 1950s [30].

This device allows monitoring and recording (photographic or digital recording) the changes of sample contours with temperature, making it possible to determine fusibility by observing shape and geometry. Other parameters that can be determined are viscosity, wettability and surface tension of the material close to their melting point [31], [32].

HSM is used to identify the characteristic temperatures, such as first shrinkage (T_{FS}), maximum shrinkage (T_{MS}), flowing and melting.

In a typical HSM curve, the volumetric variation or the height variation of a sample of known geometry is plotted as function of the temperature [30].

Modern hot-stage microscopes provide a continuous recording of such measurements and a computer-aided handling of laboratory data [30].

HSM analysis was performed by Hesse Instruments Heating Microscope (Figure 15) both on Ho-BG powders and Ho-BG32 powders.

To perform each measurement, first the glass powders and ethanol drops were mixed together to obtain a slurry. Then, the slurry was pressed with a dedicated piston into a cylindrical mold ($d = h = 3 \text{ mm}$). Finally, the sample was extruded on an alumina plate and placed inside the chamber.

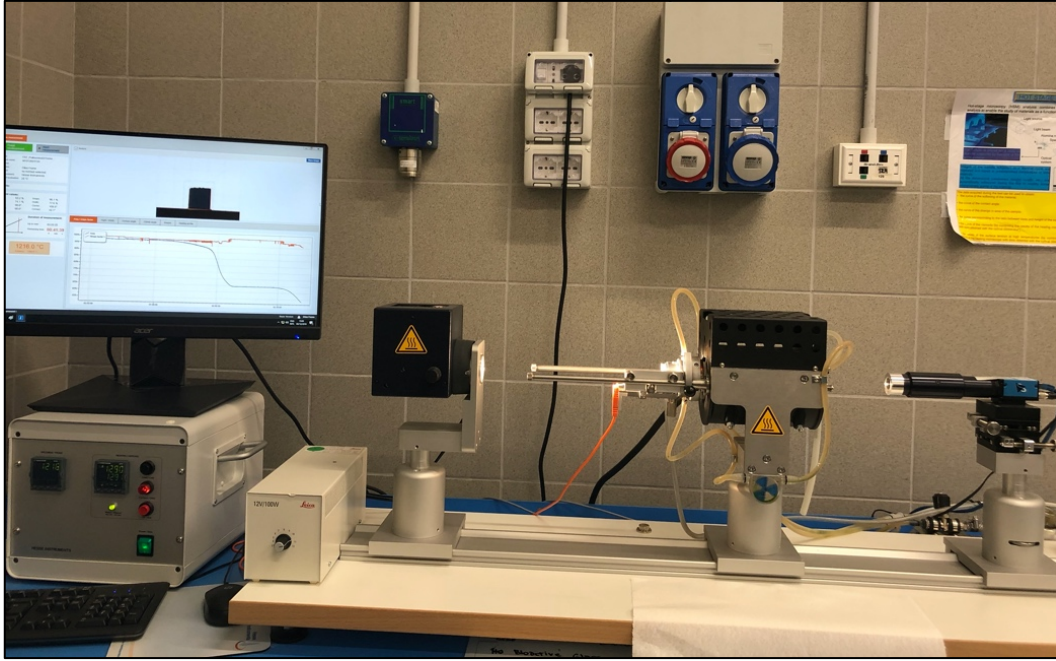


Figure 15: Hot stage microscope.

The parameters used for the measurements are shown in Table 9.

Table 9: Parameters used for HSM analysis performed on Ho-BG powders and Ho-BG32 powders.

Sample	Heating Rate (°C/min)	Final Temperature (°C)	Treatment Conditions
Ho-BG powders	5	1300	air
Ho-BG32 powders	5	1400	air

HSM analysis was first performed on the Ho-BG powders by setting the final temperature to 1300 °C. In fact, in order to protect the HSM device, it was decided to set a low temperature as the maximum temperature.

Since the sample at 1300 °C was not melted, HSM analysis of the Ho-BG32 powders was performed by setting the final temperature to 1400 °C. However, even at 1400 °C the sample did not melt.

4.5.3 X-Ray Diffraction

X-Ray Diffraction (XRD) was developed in 1912, when Max Von Laue discovered that crystalline substances behave as three-dimensional diffraction gratings for X-ray [33].

XRD is an analytical technique mainly used to identify crystalline phases within a material and to get information on unit cell dimensions [33].

X-ray diffractometers is composed of three basic elements:

- X-ray tube, which generates X-rays by heating a filament in order to produce electrons. The electrons are then accelerated to the target material by applying a voltage. When electrons have sufficient energy to dislodge inner shell electrons of the target material characteristic X-ray spectra are generated [33].
- Sample holder, in which a thin and homogeneous layer of powders is placed.
- X-ray detector, which processes the x-ray signal and converts it to a count rate, representing the output of the device [33].

In XRD analysis, X-rays, generated by the cathode ray tube, are filtered to obtain a monochromatic radiation which is collimated and deviated toward a powdered sample [33]. The interaction of the incident rays with the sample creates constructive interference when conditions satisfy Bragg's Law (Equation 3):

$$n\lambda = 2d \sin \theta \quad (3)$$

Where:

λ : wavelength of electromagnetic radiation (m) [33].

θ : diffraction angle (°) [33].

d : lattice spacing in a crystalline sample (m) [33].

The equation is used to determine d [33].

These diffracted X-rays are then detected, processed and counted. The sample is scanned through a range of 2θ angles, so that all possible diffraction directions of the lattice should be reached due to the random orientation of the powdered material. Conversion of the diffraction peaks to d -spacings allows identification of the mineral because each mineral has a set of unique d -spacings. Commonly, this is executed by comparing d -spacings with standard reference patterns [33].

XRD analysis was performed both on Ho-BG powders and Ho-BG32 powders by using PANalytical diffractometer (Figure 16) with a Bragg-Brentano chamber (operating conditions: 40 kV and 30 mA), schematically represented in Figure 17.

A Cu K_{α} incident radiation with wavelength $\lambda = 0.15405$ nm and 2θ range of 10° - 70° was used.

For XRD spectra analysis was used a data analysis software called X'Pert HighScore which compares the spectrum of the unknown material to highly pure standards collected in a database.



Figure 16: PANalytical diffractometer used for the characterization of Ho-BG powders and with Ho-BG32 powders.

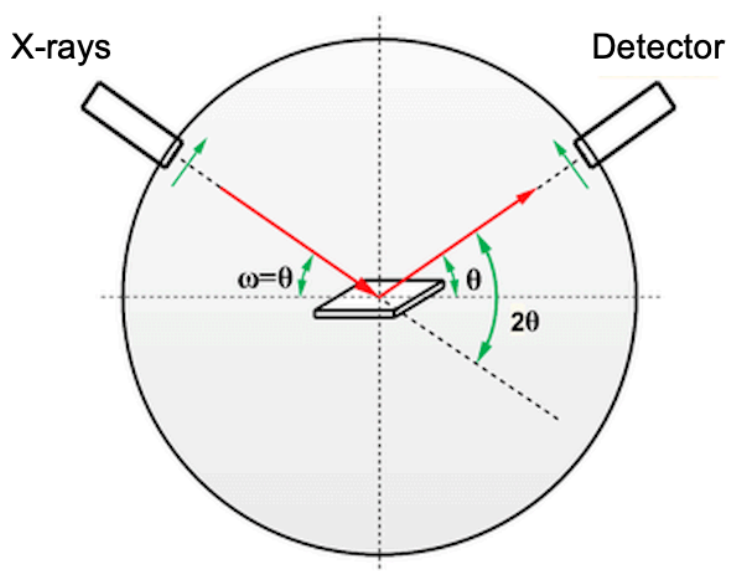


Figure 17: Basic set-up for a Bragg-Brentano diffractometer. The X-Ray tube and the detector move concurrently with the same angular displacement [34].

4.5.4 Scanning Electron Microscopy and Energy Dispersive Spectroscopy

Scanning Electron Microscopy (SEM) is an electron microscopy technique able to achieve an accurate visual image of a particle or bulk with high-quality and spatial resolution [35].

In SEM, the sample is exposed to a high-energy electron beam, thus providing accurate information about topography, morphology, composition, chemistry, orientation of grains, crystallography [35]. Morphology refers to the shape and the size of the sample, while topography refers to its surface features, i.e. textural properties, smoothness or roughness. Composition includes elements and compounds that form the material, while crystallography indicates the arrangement of atoms in the materials [35].

SEM device consists of the following components, as shown in Figure 18:

- Electron gun, which comprises electron source and accelerating anode [36].
- Electromagnetic lenses to focus the electrons [36].
- Vacuum chamber, able to house the specimen stage [36].
- Detectors, to collect the signals emitted from the specimen [36].
- Output device [36].

In addition, SEM device needs a stable power supply, vacuum and cooling system, vibration-free space and requires to be housed in an area that isolates the instrument from ambient magnetic and electric fields [37].

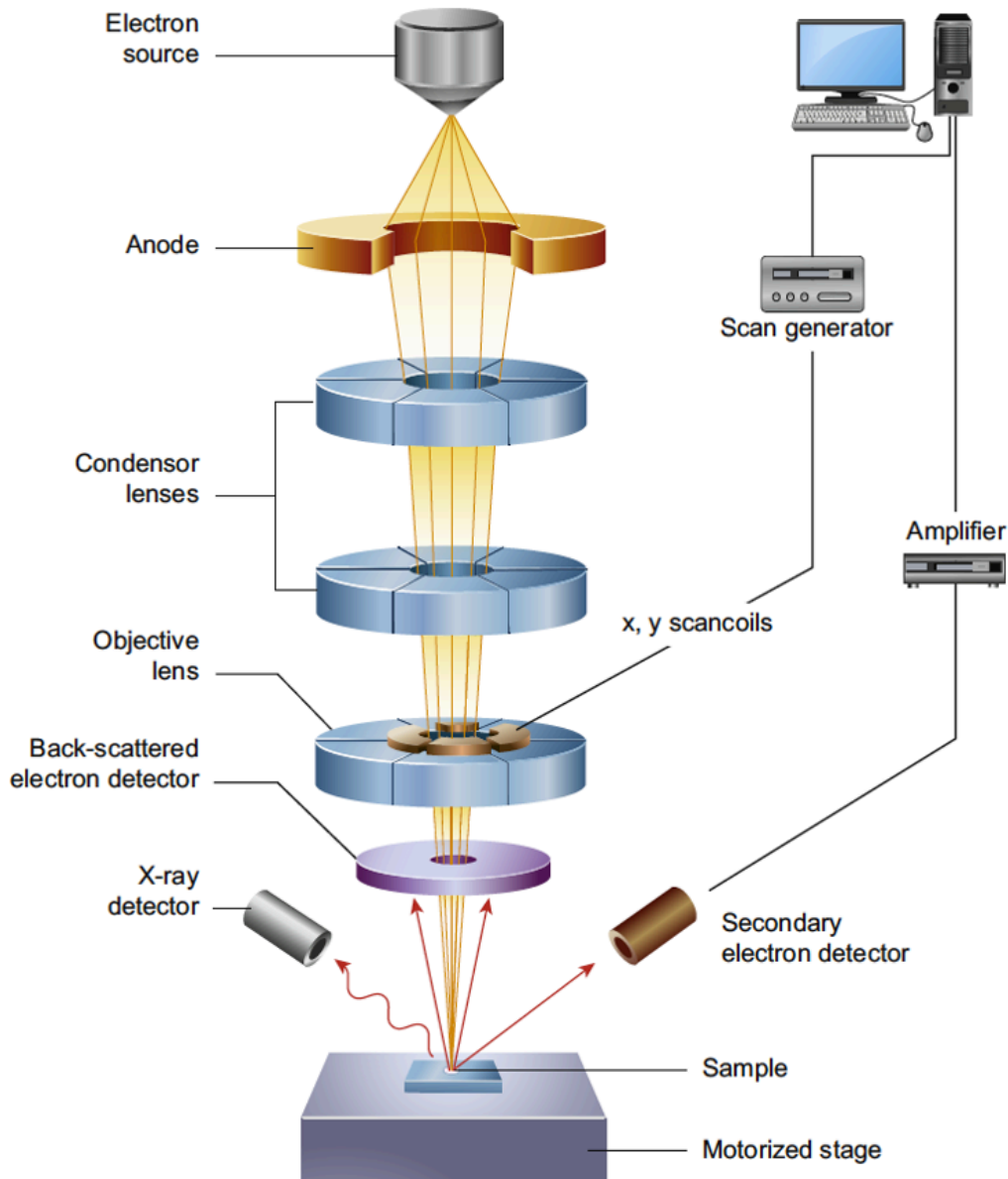


Figure 18: Representation of the core components of an SEM microscope. Figure reproduced from Inkson [36].

During the analysis, the electron gun generates a beam of energetic electrons towards a series of electromagnetic lenses. These lenses are tubes wound in a coil and called solenoids. The coils are regulated to focus the incident electron beam onto the sample; these regulations produce fluctuations in the voltage, thus increasing or decreasing the impact speed of the electrons on the sample surface [37].

By means of computer, it is possible to adjust the beam, in order to control magnification and determine the surface area to be scanned. The beam is focused onto the stage, where a solid sample is placed [37].

The interaction between the incident electrons and the surface of the specimen is affected by the acceleration rate of incident electrons, which transport considerable amounts of kinetic energy before focusing onto the sample [37].

When the incident electrons come in contact with the sample, the surface of the sample releases energetic electrons [37], as shown in Figure 19.

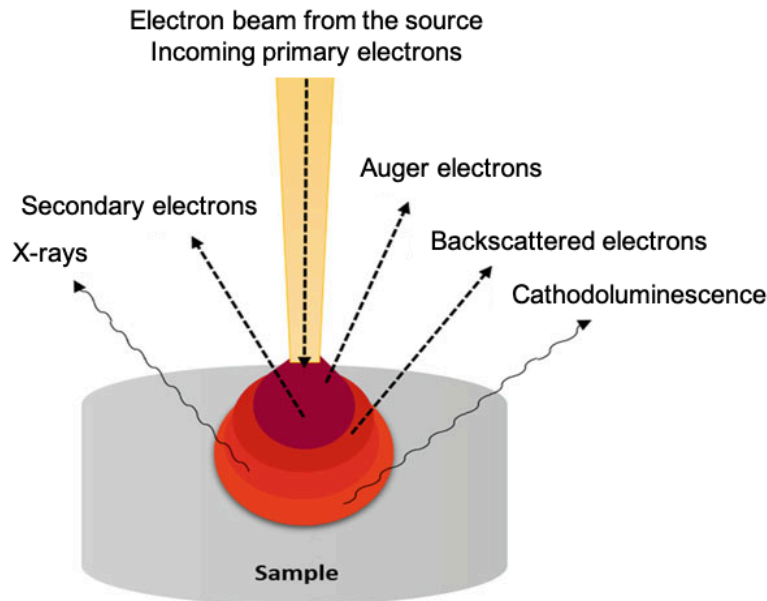


Figure 19: The interaction of electron beam with sample and the signal emitted from the specimen. Figure reproduced from Akhtar et al. [35].

The scatter patterns generated by the interaction give information on size, shape, texture and composition of the sample [37].

In order to detect different types of scattered electrons, such as X-rays, secondary and backscattered electrons, different detectors are employed [37].

Secondary electrons are captured by Secondary Electron Detector (SED), and produce images that give topographic information [37].

Backscatter electrons are incidental electrons reflected backwards; images provide composition data related to element and compound detection [37].

Diffraction backscatter electrons give information about crystalline structures and the orientation of minerals and micro-fabrics. The technique behind this process is called Electron Backscattered Diffraction (EBSD) [37].

X-rays are emitted from the bottom of the sample surface and provide element and mineral information. The technique behind this process is known as Energy Dispersive X-ray Spectrometry (EDS) [37].

EDS makes a localized chemical analysis by analysing the X-ray spectrum emitted by the sample. Qualitative analysis consists in identifying spectrum lines, while quantitative analysis permits to determine the concentrations of the elements by measuring lines intensity for each element and for the same elements in calibration Standards of known composition [38].

SEM analysis produces black and white, three-dimensional images [37]. Commonly, the analysed area in conventional SEM device ranges from 1 cm to 5 μm in width with a spatial resolution of 50 to 100 nm [39].

SEM analysis is considered as a conservative analysis, since the characteristics of the sample do not vary during the analysis [39], [37].

Samples must meet specific requirements in order to be analysed correctly. They must be solid and of appropriate size in order to enter the chamber and they need to handle the low pressure inside the vacuum chamber [39], [37].

Most samples require some preparation before being placed in the vacuum chamber. The two most used sample preparation processes are sputter coating with a conductive material such as chromium, gold or platinum for non-conductive samples and dehydration of most biological specimens [37].

Benchtop SEM is a device belonging to the SEM family. It is a small SEM that is set up on a bench or table. Its main advantages are the ease of use; indeed, no special training is required, and the low cost. Nevertheless, it presents less resolution than full size SEM, scaled down features to accommodate size, such as no motorization, tilt or rotate, etc. In the end, benchtop SEM is useful, but cannot replace the role of a full-size SEM [40].

Ho-BG powders and Ho-doped BG scaffolds were analysed by SEM and EDS in order to study surface topography, sample morphology and elementary compositions.

The devices used to analyse Ho-BG powders are SEM ZEISS MERLIN (Figure 20) and JCM-6000Plus Versatile Benchtop SEM (Figure 21). While Ho-doped BG scaffolds were only analysed with the device SEM ZEISS MERLIN.



Figure 20: SEM device (ZEISS MERLIN) used for morphological and compositional characterization of the Ho-BG powders and the Ho-doped BG scaffolds [41].



Figure 21: Benchtop SEM (JCM-6000Plus Versatile Benchtop SEM) used for morphological and compositional characterization of the Ho-BG powders [42].

Powders were stuck on dedicated stabs by using a carbon adhesive tape and were coated with a thin layer (≈ 7 nm) of chromium.

Scaffolds were fixed on the stabs by using a conductive glue containing Ag nanowhiskers. The preparation of the sample was performed under hood because of the toxic potential of the glue. Moreover, a conductive Cr layer (≈ 7 nm) was employed also for the scaffold in order to make the surface of the sample conductive.

4.5.5 Brunauer, Emmett and Teller Theory (BET)

The BET theory was developed by Stephen Brunauer, Paul Emmett, and Edward Teller in 1938. This theory takes its name from the first letter of each inventor's surname. The BET theory is considered as an improvement of the Langmuir theory, developed by Irving Langmuir in 1916 [43].

The Langmuir theory describes the relation between the monolayer adsorption of gas molecules (Figure 22a), also called adsorbates, onto a solid surface and the gas pressure of a medium above the solid surface at a fixed temperature [43].

The Langmuir theory is based on the following assumptions:

- Adsorption energy for the adsorbate is the same for all the surface sites. The adsorbate is generally argon, krypton or nitrogen gas. The surface site denotes the sample's area where one molecule can adsorb onto [43].
- The solvent is adsorbed at one site independently of how it is adsorbed at nearby sites [43].
- Activity of adsorbate is directly proportional to its concentration [43].
- Adsorbates create a monolayer [43].
- A single particle can occupy an active site [43].

The BET theory expands the Langmuir theory to multilayer adsorption (Figure 22b) adding three further assumptions:

- Gas molecules will physically adsorb on a solid in layers infinitely [43].
- The various adsorption layers do not affect each other [43].
- This theory can be employed to each layer [43].

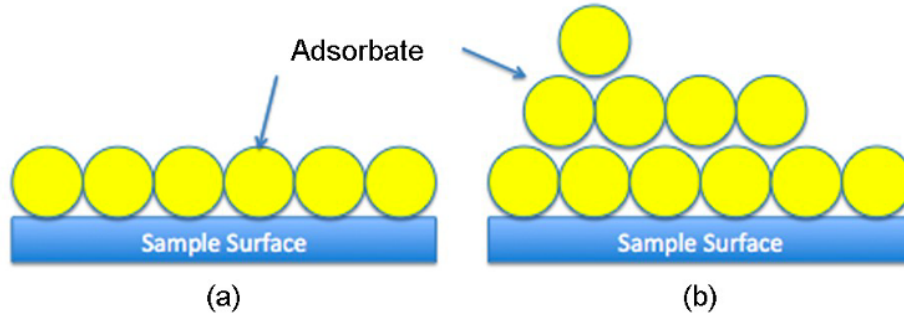


Figure 22: Representation of the adsorption of gas molecules onto the surface of a sample illustrating (a) the monolayer adsorption model adopted by the Langmuir theory and (b) the multilayer adsorption model adopted by the BET theory. Figure reproduced from Hwang et al. [43].

BET analysis allows the determination of the specific surface area by physical adsorption of a gas. Adsorption is defined as the adhesion of atoms or molecules of gas to a surface. Adsorption should not be confused with absorption, in which a fluid permeates a liquid or solid [43].

The quantity of gas adsorbed depends on the exposed surface, but also on the temperature, gas pressure and strength of interaction between gas and solid [43].

Nitrogen is commonly used as it is available in high purity and it strongly interacts with most solids. Due to the weak interaction between gaseous and solid phases, the surface is cooled using liquid N₂ in order to obtain appreciable adsorption levels. Then, known quantities of nitrogen gas are gradually released into the sample cell [43].

Relative pressures less than atmospheric pressure are obtained by generating conditions of partial vacuum. After the saturation pressure, no more adsorption happens independently from any further pressure increase. Pressure variations are monitored by highly precise and accurate pressure transducers due to the absorption process. After the formation of the adsorption layers, the sample is removed from the nitrogen atmosphere and heated so that the adsorbed nitrogen is released from the material and quantified [43].

The data accumulated is shown in the form of a BET isotherm, which plots the amount of gas adsorbed as a function of the relative pressure [43].

The information from the isotherm is used to determine the surface area of the sample by BET equation (Equation 4):

$$\frac{1}{W\left(\frac{p}{p_0}-1\right)} = \frac{1}{W_m C} + \frac{C-1}{W_m C} \left(\frac{p}{p_0}\right) \quad (4)$$

Where:

W: weight of gas adsorbed at a relative pressure (N) [43].

W_m: weight of adsorbate constituting the surface monolayer (N) [43].

C: BET constant which indicates the magnitude of the interactions between adsorbate (gas molecules) and adsorbent (solid particles surface) [43].

Before each surface area measurement, the sample must be degassed to remove water and other contaminants. Samples are degassed in a vacuum at high temperatures. Generally, the highest temperature possible that does not harm the sample is chosen in order to reduce the degassing time. IUPAC suggests that samples should be degassed for at least 16 hours. Usually, samples that are able to stand higher temperatures without structural adjustments need shorter degassing times [43].

Samples are placed in glass cells to be degassed and analysed by the BET machine (Figure 23). Sample cells can have sizes of 6, 9 and 12 mm and different shapes. The cell is positioned into heating mantle and joined with the outgas port of the machine. Once the sample is degassed, the cell is shifted to the analysis port [43].

The sample is cooled by immersion into dewars of liquid nitrogen and then is kept at a constant temperature [43].

It is recommended to keep a low temperature in order to achieve a strong interaction between the gas molecules and the surface of the sample. Indeed, the interaction should be strong enough for measurable quantities of adsorption to happen [43].

A calibrated piston is used to inject nitrogen into the sample cell [43].

The calibration of the dead volume in the sample cell must always be performed before and after each measurement. Since helium does not adsorb onto the sample, helium gas is used for a blank run [43].

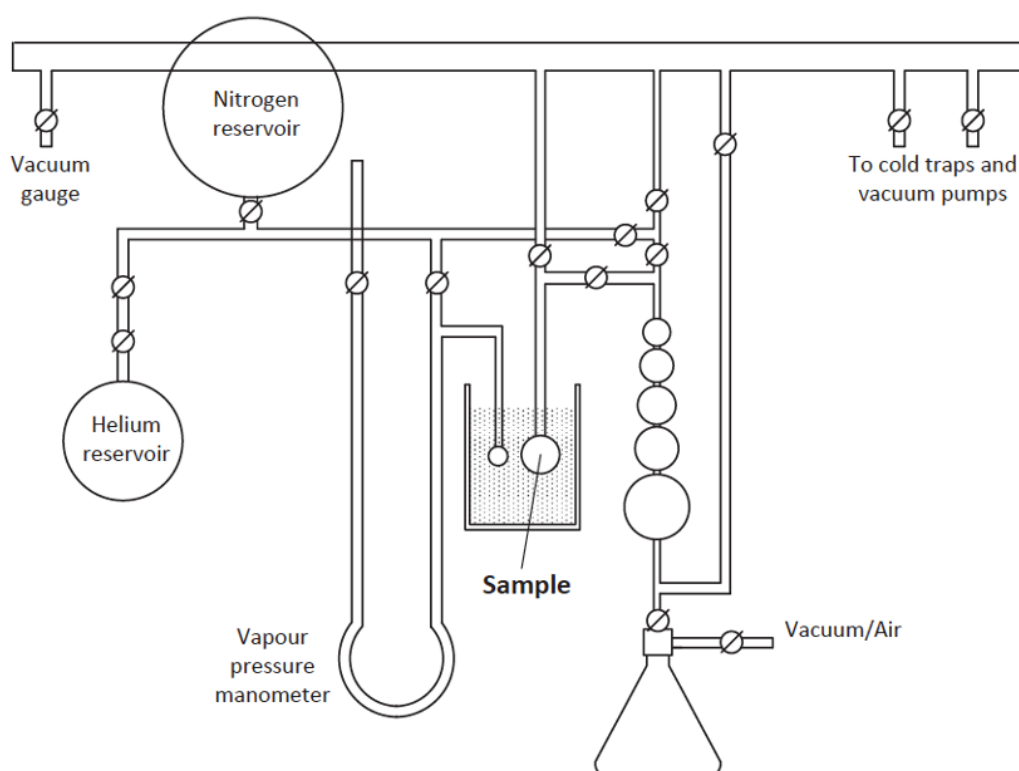


Figure 23: Schematic representation of BET machine for measuring the surface area by nitrogen gas adsorption. Figure reproduced from Naderi [44].

Ho-BG powders and Ho-BG32 powders were analysed by Micromeritics ASAP 2020 Plus BET (Figure 24) in order to determine the specific surface area of the sample as well as the pore size distribution.



Figure 24: Micromeritics ASAP 2020 Plus BET [45].

Preparation of the sample requires first the measurement of the mass of the powders by using a digital precision scale. Then, sample powders were introduced within glass burettes by using a section adaptor and subsequently purified by degassing under opportune temperature ($T=140-150\text{ }^{\circ}\text{C}$), time ($t > 180$ minutes) and vacuum conditions.

The weight of the sample was recorded both before and after degassing and a reduction of the mass was observed, as reported in Table 10.

Table 10: Mass of glass powders before and after degassing.

Sample	Mass before degassing (g)	Mass after degassing (g)
Ho-BG powders	0.1661	0.1639
Ho-BG32 powders	0.1707	0.1534

References

- [1] L. L. Hench, D. E. Day, W. Höland, and V. M. Rheinberger, "Glass and Medicine," *Int. J. Appl. Glas. Sci.*, vol. 1, no. 1, pp. 104–117, 2010.
- [2] J. E. White and D. E. Day, "Rare earth aluminosilicate glasses for in vivo radiation delivery," *Mech. Corros. Prop. Ser. A, Key Eng. Mater.*, vol. 94–95, pp. 181–208, 1994.
- [3] Y. Shi, A. M. Johnsen, and A. J. Di Pasqua, "Holmium for Use in Cancer Therapy," *Comments Inorg. Chem.*, vol. 37, no. 6, pp. 281–300, 2017.
- [4] L. B. Nogueira and T. P. R. Campos, "Nuclear Characterization of Radioactive Bioglass Seed for Brachytherapy Studies," *Int. Conf. Math. Comput. Methods Appl. to Nucl. Sci. Eng.*, pp. 1–9, 2011.
- [5] L. B. Nogueira and T. P. R. Campos, "Synthesis, chemical characterization and radiological response of Ho and HoZr bioglass seeds," *J. Sol-Gel Sci. Technol.*, vol. 77, no. 3, pp. 688–698, 2016.
- [6] S. L. Johnson and J. C. Yanch, "Absorbed dose profiles for radionuclides of frequent use in radiation synovectomy," *Arthritis Rheum.*, vol. 34, no. 12, pp. 1521–1530, 1991.
- [7] N. J. M. Klaassen, M. J. Arntz, A. Gil Arranja, J. Roosen, and J. F. W. Nijssen, "The various therapeutic applications of the medical isotope holmium-166: a narrative review," *EJNMMI Radiopharm. Chem.*, vol. 4, no. 1, pp. 1–26, 2019.
- [8] W. Bult *et al.*, "Intratumoral Administration of Holmium-166 Acetylacetonate Microspheres: Antitumor Efficacy and Feasibility of Multimodality Imaging in Renal Cancer," *PLoS One*, vol. 8, no. 1, 2013.
- [9] W. Xia and J. Chang, "Preparation and characterization of nano-bioactive-glasses (NBG) by a quick alkali-mediated sol-gel method," *Mater. Lett.*, vol. 61, no. 14–15, pp. 3251–3253, 2007.
- [10] Q. Z. Chen and A. R. Boccaccini, "Chapter 6: Tissue Engineering Scaffolds from Bioactive Glass and Composite Materials," in *Topics in Tissue Engineering, Vol. 4.*, 2008.
- [11] Q. Fu, E. Saiz, M. N. Rahaman, and A. P. Tomsia, "Bioactive glass scaffolds for bone tissue engineering: state of the art and future perspectives," *Mater. Sci. Eng. C*, vol. 31, no. 7, pp. 1245–1256, 2011.
- [12] C. Vitale-Brovarone, F. Baino, O. Bretcanu, and E. Verné, "Foam-like scaffolds for bone tissue engineering based on a novel couple of silicate-phosphate specular glasses: synthesis and properties," *J. Mater. Sci. Mater. Med.*, vol. 20, no. 11, pp. 2197–2205, 2009.
- [13] Bhadeshia, "Thermal analysis techniques. Differential thermal analysis (DTA)," *Mater. Sci. Metall.*
- [14] G. Klancnik, J. Medved, and P. Mrvar, "Differential thermal analysis (DTA) and differential scanning calorimetry (DSC) as a method of material investigation," *Mater. Geoenvironment*, vol. 57, no. 1, pp. 127–142, 2010.
- [15] P. Gill, T. T. Moghadam, and B. Ranjbar, "Differential Scanning Calorimetry Techniques: Applications in Biology and Nanoscience," *J. Biomol. Tech.*, vol. 21, no. 1, pp. 167–193, 2010.

- [16] M. Abd-Elghany and T. M. Klapötke, “A review on differential scanning calorimetry technique and its importance in the field of energetic materials,” *Phys. Sci. Rev.*, pp. 1–14, 2018.
- [17] “Thermogravimetric Analysis (TGA) – PhotoMetrics.” [Online]. Available: <https://photometrics.net/thermogravimetric-analysis-tga/>. [Accessed: 03-Apr-2020].
- [18] “Membrane Characterisation Equipment | Thermal Analysis: Thermogravimetric analysis | European Membrane Institute (EMI) - University of Twente.” [Online]. Available: https://www.utwente.nl/en/tnw/emi/characterisation/thermo_grav/. [Accessed: 03-Apr-2020].
- [19] C. De Blasio, “Thermogravimetric Analysis (TGA),” in *Fundamentals of Biofuels Engineering and Technology*, 2019, pp. 91–102.
- [20] P. Bode, “Neutron Activation Analysis (NAA),” in *Neutron Scattering Applications and Techniques*, 2017, pp. 209–219.
- [21] M. D. Glascock, “An overview of neutron activation analysis,” 2004.
- [22] L. Hamidatou, H. Slamene, T. Akhal, and B. Zouranen, “Concepts, Instrumentation and Techniques of Neutron Activation Analysis Chapter,” in *Imaging and Radioanalytical Techniques in Interdisciplinary Research - Fundamentals and Cutting Edge Applications*, 2013, pp. 141–178.
- [23] “Neutron Activation Analysis - Analytical Chemistry Group.” [Online]. Available: <https://acg.missouri.edu/NAA.html>. [Accessed: 20-May-2020].
- [24] “Fourier Transform Infrared Spectroscopy | FTIR Failure Analysis | FTIR Material Analysis.” [Online]. Available: <https://www.mee-inc.com/hamm/fourier-transform-infrared-spectroscopy-ftir/>. [Accessed: 04-Apr-2020].
- [25] “Introduction to Fourier Transform Infrared Spectroscopy.”
- [26] N. (JP) Haruo Shimaoka, “PARTICLE SIZE ANALYZER BASED ON LASER DIFFRACTION METHOD,” 2002.
- [27] “Laser Diffraction Particle Size Analysis | Malvern Panalytical.” [Online]. Available: <https://www.malvernpanalytical.com/en/products/technology/light-scattering/laser-diffraction>. [Accessed: 01-Apr-2020].
- [28] F. Storti and F. Balsamo, “Particle size distributions by laser diffraction: sensitivity of granular matter strength to analytical operating procedures,” *Solid Earth*, vol. 1, no. 1, 2010.
- [29] H. G. Merkus, “Laser Diffraction,” in *Particle Size Measurements*, 2009, pp. 259–285.
- [30] W. Panna, P. Wyszomirski, and P. Kohut, “Application of hot-stage microscopy to evaluating sample morphology changes on heating,” *J. Therm. Anal. Calorim.*, vol. 125, no. 3, pp. 1053–1059, 2016.
- [31] M. Garcia-Valles *et al.*, “Calculation of viscosity-temperature curves for glass obtained from four wastewater treatment plants in Egypt,” *J. Therm. Anal. Calorim.*, vol. 111, no. 1, pp. 107–114, 2013.
- [32] F. M. Stábile, M. Piccico, M. F. Serra, M. Rafti, G. Suárez, and N. M. Rendtorff, “Viscosity and Thermal Evolution of Density and Wetting Angle of a Commercial Glaze by Means of Hot Stage Microscopy,” *Procedia Mater. Sci.*, vol. 9, pp. 563–570, 2015.

- [33] “X-ray Powder Diffraction (XRD).” [Online]. Available: https://serc.carleton.edu/research_education/geochemsheets/techniques/XRD.html. [Accessed: 30-Mar-2020].
- [34] “4: Schematic of (a) Bragg-Brentano (θ - 2θ) and (b) GIXRD geometry. | Download Scientific Diagram.” [Online]. Available: https://www.researchgate.net/figure/4-Schematic-of-a-Bragg-Brentano-th-2th-and-b-GIXRD-geometry_fig30_315142103. [Accessed: 31-Mar-2020].
- [35] K. Akhtar, S. A. Khan, S. B. Khan, and A. M. Asiri, “Scanning electron microscopy: Principle and applications in nanomaterials characterization,” in *Handbook of Materials Characterization*, Springer International Publishing, 2018, pp. 113–145.
- [36] B. J. Inkson, “Scanning electron microscopy (SEM) and transmission electron microscopy (TEM) for materials characterization,” in *Materials Characterization Using Nondestructive Evaluation (NDE) Methods*, Elsevier Ltd, 2016, pp. 17–43.
- [37] “Scanning Electron Microscope - Advantages and Disadvantages in Imaging.” [Online]. Available: <https://www.microscopemaster.com/scanning-electron-microscope.html>. [Accessed: 31-Mar-2020].
- [38] “Introduction to Energy Dispersive X-ray Spectrometry (EDS) - PDF Free Download.” [Online]. Available: <https://docplayer.net/14887332-Introduction-to-energy-dispersive-x-ray-spectrometry-eds.html>. [Accessed: 01-Apr-2020].
- [39] “Scanning Electron Microscopy (SEM).” [Online]. Available: https://serc.carleton.edu/research_education/geochemsheets/techniques/SEM.html. [Accessed: 31-Mar-2020].
- [40] “Scanning Electron Microscopes (SEM). Comparison between benchtop SEM, tabletop SEM, desktop SEM, Compact SEM and Full size SEM.” [Online]. Available: <http://www.nanounity.com/SEM.php>. [Accessed: 01-Apr-2020].
- [41] “ZEISS MERLIN FE-SEM | Acquire images within seconds. Achieve... | Flickr.” [Online]. Available: <https://www.flickr.com/photos/zeissmicro/13445097885>. [Accessed: 26-Jun-2020].
- [42] “JCM-6000Plus Versatile Benchtop SEM (Tabletop SEM) | Products | JEOL Ltd.” [Online]. Available: <https://www.jeol.co.jp/en/products/detail/JCM-6000Plus.html>. [Accessed: 19-May-2020].
- [43] N. Hwang and A. R. Barron, “BET Surface Area Analysis of Nanoparticles,” *OpenStax-CNX*, 2011.
- [44] M. Naderi, “Surface Area: Brunauer-Emmett-Teller (BET),” in *Progress in Filtration and Separation*, 2015, pp. 585–608.
- [45] “ASAP 2020 Plus | ALFATEST Materials science.” [Online]. Available: <https://www.alfatest.it/prodotti/asap-2020-plus>. [Accessed: 19-May-2020].

Chapter 5

Results and Discussion

The present experimental work aimed at the production of holmium-doped bioactive glass scaffolds for bone cancer treatment by brachytherapy.

The strength of this device lies in the possibility to be therapeutically effective on multiple fronts, by reducing tumour dimension while gradually regenerating bone in the target area.

In the present chapter, the achievements of the experimental work performed at Politecnico di Torino, in cooperation with the Federal University of ABC, will be discussed in detail and compared with the most relevant results obtained by other research groups. In addition, an operative protocol aimed at further improving structural and morphological properties of Ho-doped BG scaffolds will be presented.

5.1 Characterization of Ho-doped Dried Gel and Ho-doped Bioactive Glass at Federal University of ABC (São Paulo, Brazil)

At Federal University of ABC, both Ho-dried-gel powders and Ho-BG powders were analysed according to the characterization methods reported in Table 6, Chapter 4.

5.1.1 Thermal Analysis

Thermal analysis such as DSC, TGA and DTG were performed on the dried-gel powders in order to study the behaviour of the gel during heat treatment and choose a suitable calcination treatment.

Figure 1 provides DSC and TGA curves. The DSC curve was coloured blue to distinguish it from the TGA curve, which is black.

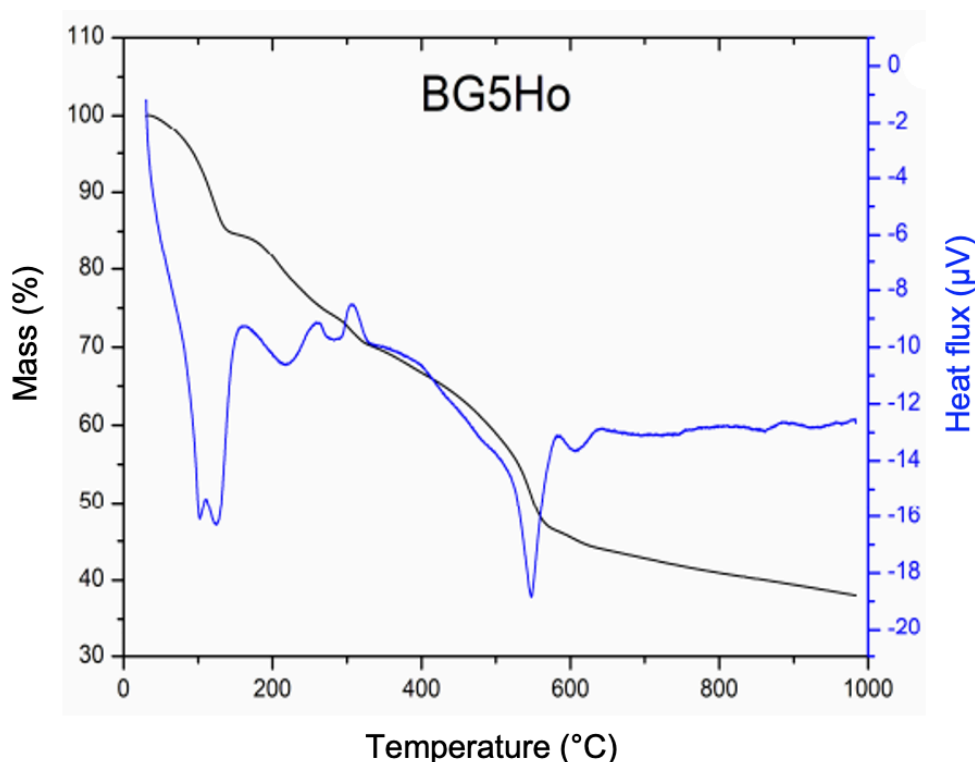


Figure 1: DSC / TGA curves of Ho-dried-gel powders.

DSC curve shows two peaks in the negative y-axis, as 100 °C and 550 °C respectively.

The first endothermic peak at 100 °C is attributable to water evaporation.

At 550 °C, powders still contained organic phase represented by nitrates used as oxide precursors during the synthesis process. In particular, calcium nitrate tetra-hydrate and holmium (III) nitrate pentahydrate were present. Accordingly, it is reasonable to attribute the endothermic peak at 550 °C to the thermal decomposition of organic phase, which was eliminated as gas product as a result of chemical reactions with oxygen present in the heating chamber of the DSC device.

TGA curve exhibits a negative slope throughout the temperature range. This means that the mass of the sample decreased as the temperature of the sample increased during the thermal cycle. In particular, the curve shows a mass loss of up to 60% between room temperature and 1000 °C, which indicates that the gel was not thermally stable.

In the curve, three zones can be distinguished:

- 1) The first zone is between room temperature and 150 °C. It is characterized by a high slope because in a short temperature range a significant decrease in mass occurred (15%). This zone corresponds to the first endothermic peak of DSC curve and the weight change is attributable to the loss of water.
- 2) The second zone is between 150 °C and 600 °C. It is characterized by an intermediate slope corresponding to a change in mass of 40%.

The weight variation is attributable to the organic phase represented by nitrates, which began to feel the effect of the temperature at 150 °C, reaching a considerable rate of mass loss at around 200 °C and maintaining that rate up to 550 °C.

Around 550 °C, in correspondence to the second endothermic peak of the DSC curve, the TGA curve is characterized by a higher slope. This indicates an increase in the rate of mass loss due to the complete decomposition of the organic phase.

Above this temperature, a subsequent loss occurred, which was most likely due to the evaporation of the decomposition products of the organic phase.

- 3) The third zone is between 600 °C and 1000 °C. The curve is characterized by a low slope corresponding to a 10% change in the weight of the sample.

DTG of the Ho-dried-gel powders is shown in Figure 2.

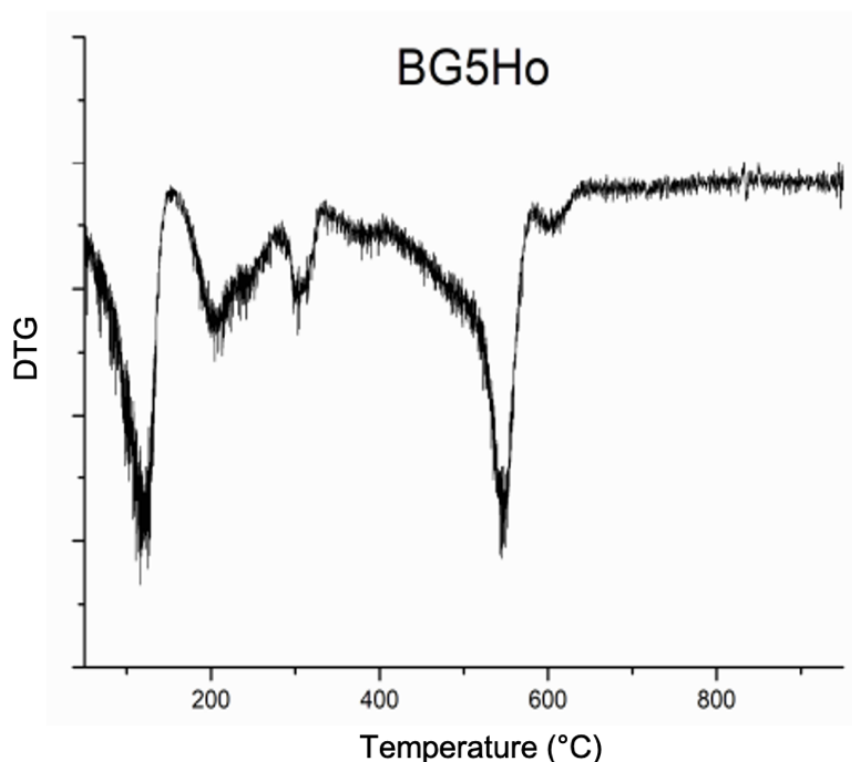


Figure 2: DTG curve of the Ho-dried-gel powders.

As in the DSC curve, two main peaks can be observed in the DTG curve, respectively at 100 °C and 550 °C.

It is reasonable to attribute the peak at 100 °C to water evaporation, since this phenomenon is characteristic of that temperature.

The peak at 550 °C can be associated with the thermal decomposition of the organic phase for the reason explained above.

Thus, the peaks at 100 °C and 550 °C indicate that the maximum rate of mass loss was due to water evaporation and the decomposition of the organic phase respectively.

Since both DSC, TGA and DTG agree that 550 °C is the temperature at which decomposition of the organic phase occurs, this temperature was chosen for the calcination of Ho-dried-gel powders.

5.1.2 Neutron Activation Analysis

NAA was performed on Ho-BG powders in order to study the composition of the system. The composition of Ho-BG measured by NAA is given in Table 1.

Table 1: Experimental composition (wt%) of Ho-BG powders obtained by NAA.

Oxide	Experimental (wt%)
SiO ₂	52.3 ± 1.6
CaO	31.2 ± 1.3
Ho ₂ O ₃	4.3 ± 0.1

In Table 1, there is not P₂O₅ because the NAA does not detect P₂O₅. Therefore, the percentage of P₂O₅ was calculated as complement to 100%, thus obtaining the correct composition of Ho-BG. The correct experimental composition of Ho-BG was compared with the designed one (Table 2).

Table 2: Designed composition (wt%) and correct experimental composition (wt%) of Ho-BG powders.

Oxide	Design (wt%)	Experimental (wt%)
SiO ₂	55.10	52.3 ± 1.6
CaO	31.3	31.2 ± 1.3
Ho ₂ O ₃	5.0	4.3 ± 0.1
P ₂ O ₅	8.6	12.2

By comparing the oxide compositions, it turned out that the correct experimental composition is comparable with the designed one.

5.1.3 Fourier Transform-Infrared Spectroscopy

FTIR was performed on Ho-BG powders in order to identify the materials and the reactions involved. Figure 3 shows FTIR spectra related to different compositions of 58S bioactive glass doped with different amounts of holmium.

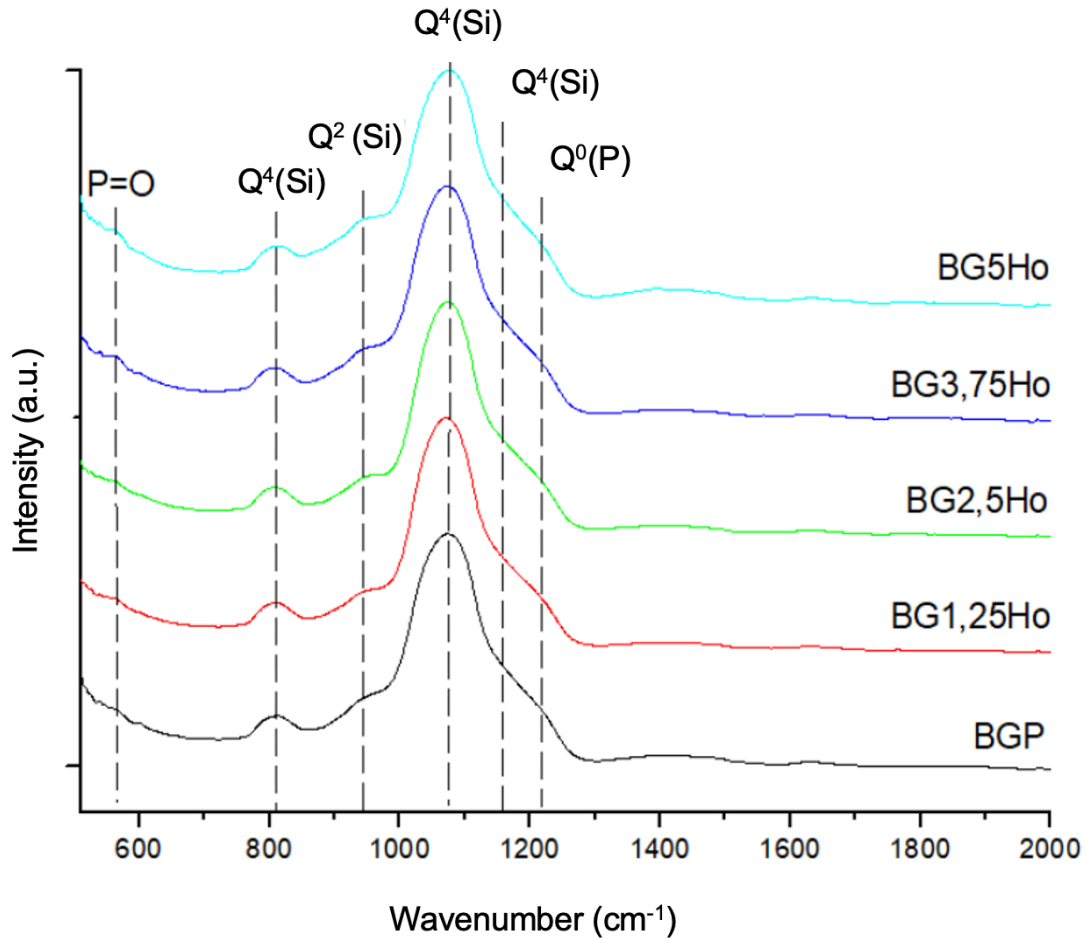


Figure 3: FTIR spectra of the 58S bioactive glass doped with different amounts of holmium.

As already mentioned, the designed composition of Ho-BG includes 5 wt% of Ho_2O_3 . Thus, the spectrum of interest is coloured light blue.

The synthetic 58S bioactive glass doped with different amounts of holmium shows the characteristic bands of silica network.

The bands at ~ 800 , ~ 1100 cm^{-1} and ~ 1150 cm^{-1} are characteristics of the deformation vibration of Si–O–Si bridging bonds in the SiO_4 tetrahedrons which have four oxygen atoms linked to four Si neighbours; these tetrahedrons are called $\text{Q}^4(\text{Si})$ [1]. The band at 950 cm^{-1} is attributed to the stretching vibration of Si–O–Si bonds in the $\text{Q}^2(\text{Si})$ tetrahedrons, which involves 2 bridging oxygen atoms [2]. The band at 1230 cm^{-1} corresponds to the symmetric and antisymmetric modes of Si–O–Ca bonds in the $\text{Q}^0(\text{Si})$ units which have non-bridging oxygen atoms [3]. Moreover, the band at 570 cm^{-1} is characteristic of bending vibration of P–O bonds in the PO_4^{3-} groups which correspond to the tetrahedron $\text{Q}^0(\text{P})$ or $\text{Q}^1(\text{P})$ [4]. Their intensity is weak because of the small amount of phosphate connected to the glassy matrix [5].

5.2 Ho-doped Bioactive Glass Characterization at Politecnico di Torino (Turin, Italy)

Ho-BG and Ho-BG32 powders were analysed according to the characterization methods reported in Table 7, Chapter 4.

5.2.1 Particle Size Analysis

Particle size analysis allowed to determine the particles size both of Ho-BG powders and of Ho-BG32 powders.

Figure 4 shows the particle size distribution (PSD) of Ho-BG powders and Ho-BG32 powders.

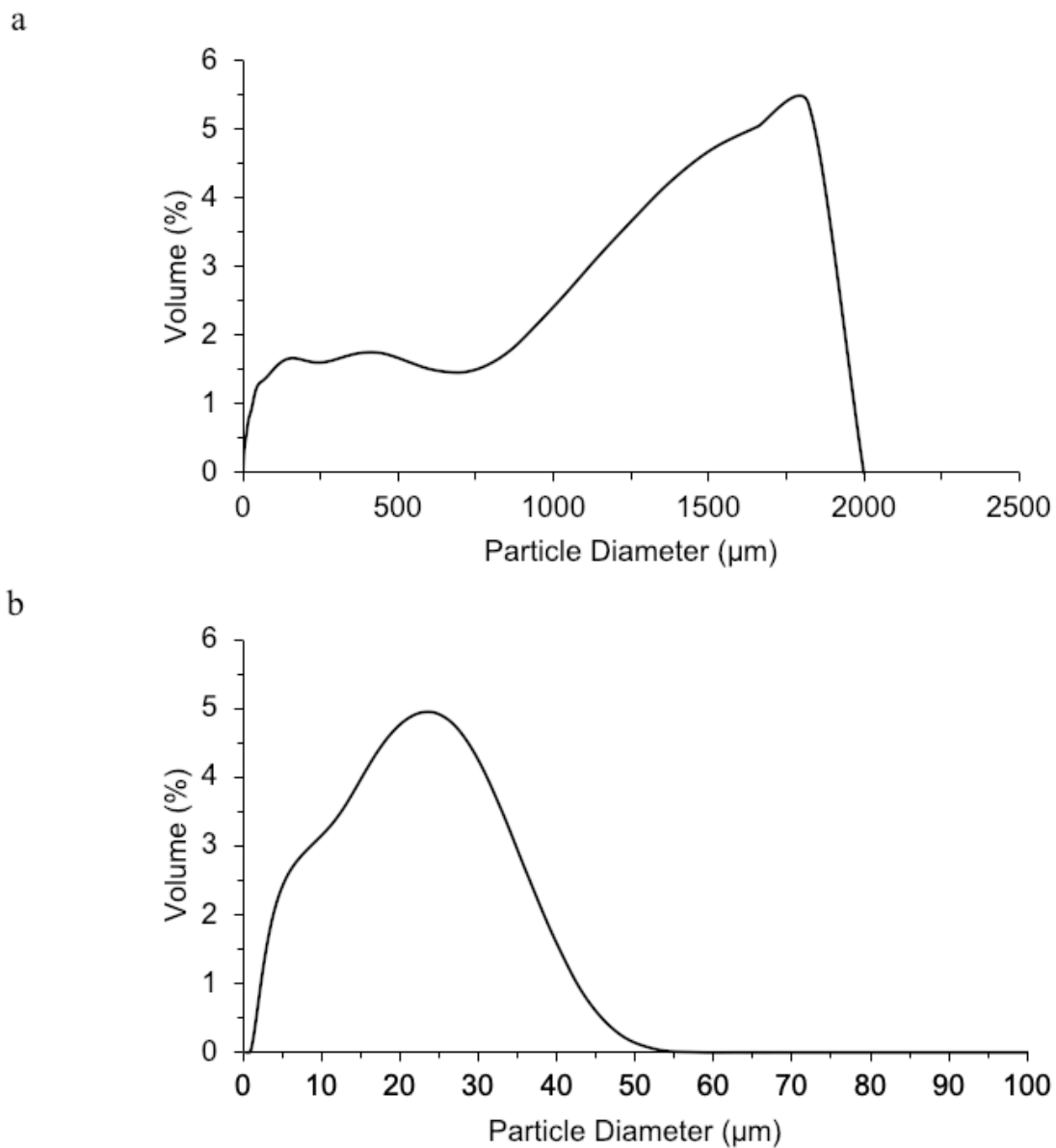


Figure 4: PSD of (a) Ho-BG powders and (b) Ho-BG32 powders.

As can be seen in Figure 4a, Ho-BG powders have different dimensions, with particles size ranging from 0.37 μm to 2000 μm .

Even before the powders were ground and sieved, particles with a diameter $< 32 \mu\text{m}$ were already present, albeit in very small quantities.

Two zones can be distinguished in the PSD curve: the first between 1 and 750 μm and the second between 750 and 2000 μm .

By comparing the area under the curve between 1 μm and 750 μm with the area under the curve between 750 μm and 2000 μm , it can be observed that the area under the curve between 750 μm and 2000 μm is larger than that between 1 μm and 750 μm . This means that the set of particles with a diameter between 750 μm and 2000 μm occupy a larger volume than the set of particles with a diameter between 1 μm and 750 μm . This may be due both to the fact that each particle with a larger diameter occupies a larger volume, and to the fact that there is a larger quantity of particles with a diameter between 750 μm and 2000 μm than the quantity of particles with a diameter between 1 μm and 750 μm .

With regard to the trend of the curve, after an initial slope, the first part of the curve is characterized by a plateau. This plateau denotes that, between 1 μm and 750 μm , the total volume occupied by the particles is constant. Since as the diameter increases, the volume of the particle increases, the only reason why the total volume between 1 μm and 750 μm is constant is that as the diameter of the particles increases, the number of particles with that diameter decreases.

The second part of the curve is characterized by an increase in the slope of the curve, until it reaches a maximum peak. Also this phenomenon can be due both to the fact that each particle with a larger diameter occupies a larger volume, and to the fact that there is a larger quantity of particles with a diameter between 750 μm and 2000 μm , compared to the quantity of particles with a diameter between 1 μm and 750 μm .

The Ho-BG32 PSD (Figure 4b) is much narrower than the Ho-BG PSD. This indicates that Ho-BG32 powders have controlled size due to grinding and sieving.

Since the powders were ground and sieved using a sieve with mesh of 32 μm in diameter, all particles were expected to be less than 32 μm in diameter. However, it can be seen from the graph that the instrument detected particles with a diameter between 1 and 52 μm .

It is reasonable to attribute the diameters larger than 32 μm to particles aggregates. In fact, although the sample was subjected to ultrasound before being subjected to particle size analysis, it is possible that particle aggregates were still present.

Indeed, particles tend to agglomerate to form either lumps or secondary particles due to the attractive Van der Waals interaction between particles and the thermodynamics of minimizing the total surface energy of the system [6].

In addition, it should be considered that Van der Waals interactions are a surface phenomenon and are amplified as the surface area increases. Since sol-gel materials, due to the intrinsic nanoporosity, have a larger surface area than melt-derived materials, Van der Waals interactions are amplified in sol-gel materials. Therefore sol-gel materials, such as Ho-doped bioactive glass, tend to agglomerate more than melt-derived materials.

Moreover, the area under the curve between 1 and 32 is larger than the area under the curve between 32 and 52. This means that particles with a diameter between 1 and 32 occupy a larger total volume than aggregates of particles with a diameter between 32 and 52 because they are present in greater quantities.

5.2.2 Thermal Analysis

Thermal analysis allowed the determination of the characteristic temperatures. Glass transition temperature (T_g), crystallization onset (T_x), maximum rate of crystallization temperature (T_c) were assessed by analysing DTA curves, while the volume shrinkage of each sample was assessed by determining temperatures related to first shrinkage (T_1), end of first shrinkage (T_2), second shrinkage (T_3), end of second shrinkage (T_4), softening (T^*) through HSM curve.

Moreover, HSM analysis allowed the variation of sample silhouettes to be monitored upon thermal treatment.

As already mentioned in Chapter 4, DTA and HSM analyses were performed both on Ho-BG and Ho-BG32 powders in order to assess the effect of the particle size on the thermal behaviour of the material.

DTA analyses of Ho-BG and Ho-BG32 powders were performed by subjecting the samples to a thermal cycle up to 1400 °C.

HSM analysis of Ho-BG was performed by setting 1300 °C as the final temperature in order to protect the HSM device.

Therefore, the DTA and HSM curves of the Ho-BG powders were both studied up to 1300 °C.

Since it was observed that Ho-BG sample had not melted during the HSM analysis, the HSM analysis of the Ho-BG32 powders was carried out by setting 1400 °C as the final temperature. Consequently, the DTA and HSM curves of the Ho-BG32 powders were studied up to 1400 °C.

Figure 5 represents the (a) DTA curve and (b) HSM curve related to Ho-BG powders.

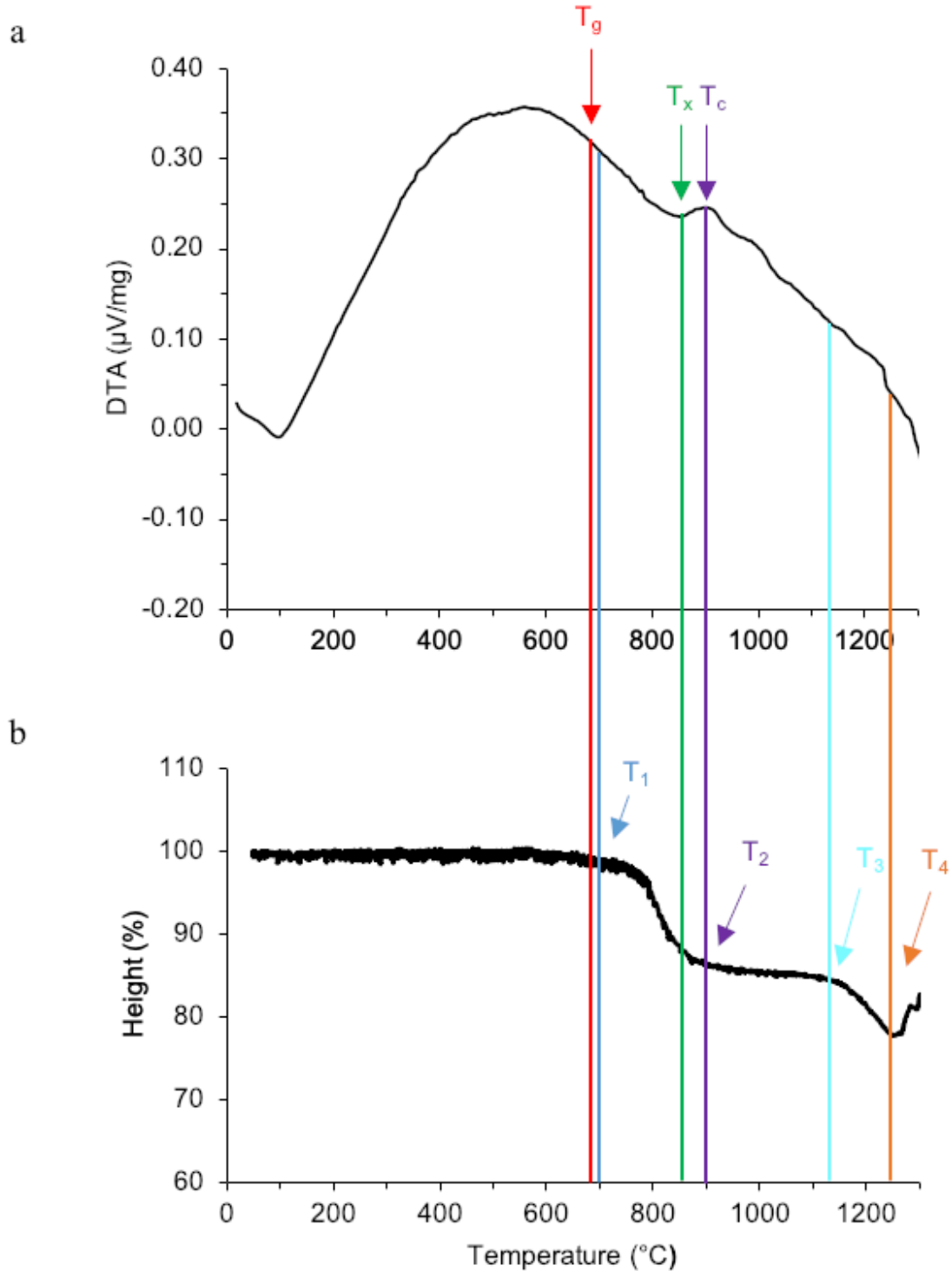


Figure 5: (a) DTA curve and (b) HSM curve related to Ho-BG powders.

The first endothermic peak observed in the DTA curve (Figure 5a) at 100°C is attributable to water evaporation.

Then, the curve develops on a hump, which consists of a positive trend until 550°C , followed by a negative one in the middle of which $T_g = 690^\circ\text{C}$ was identified.

After that, the curve is characterized by an exothermic peak, followed by a negative slope until the end of the graph.

The insertion point of the exothermic peak identifies the crystallization onset, while the central point of the peak identifies the maximum rate of crystallization.

For Ho-BG, crystallization onset and maximum crystallization rate were identified at $T_x=860\text{ }^{\circ}\text{C}$ and $T_c=900\text{ }^{\circ}\text{C}$, respectively.

The exothermic peak at $T_c=900\text{ }^{\circ}\text{C}$ was associated to the nucleation of wollastonite crystals (CaSiO_3) for two reasons:

- 1) Ho-BG mainly consists of SiO_2 and CaO , as well as smaller amounts of P_2O_5 and Ho_2O_3 . Therefore, according to the composition of the analysed system, the nucleation of a calcium silicate upon heating is highly probable.
- 2) Pérez et al. [7] observed that the crystallization process of wollastonite develops following a two-stage mechanism, with a devitrification experimental range defined between $850\text{ }^{\circ}\text{C}$ and $950\text{ }^{\circ}\text{C}$ [7]. Therefore, $T_c=900\text{ }^{\circ}\text{C}$ is within the wollastonite devitrification range.

In addition, several literature studies reported the formation of wollastonite in the “parent” 58S bioactive glass. For example, both Goudouri et al. [8] and Balamurugan et al. [9] observed the wollastonite nucleation in 58S BG between 850 and $950\text{ }^{\circ}\text{C}$.

Commonly, a crystalline phase is thermodynamically more stable than an amorphous one. Thus, the presence of a crystalline phase in a material should result in lower dissolution behaviour and bioactivity compared to totally amorphous materials [10].

However, Xin et al. [11] found that wollastonite formation does not deteriorate the bioactivity of sintered glass ceramic. This phenomenon can be explained through two considerations: (1) glass ceramic materials have good biocompatibility and bioactivity [12]; and (2) wollastonite ceramic itself has good bioactivity [13].

Moreover, it was found that the presence of wollastonite enhances the mechanical properties of the material. Indeed, wollastonite, due it is fibrous morphology, may increase the fracture toughness by different mechanisms such as crack deflection and crack bridging [14].

In the DTA curve, there are no obvious endothermic peaks that can give information about the melting temperature.

As clearly evident in the HSM curve (Figure 5b) the Ho-BG powders exhibits a double-stage shrinkage.

The first part of the curve is characterized by a plateau: as the temperature increases, the height and silhouette of the sample do not vary.

The first densification stage occurs between T_1 and T_2 . During this phase the height of the sample significantly reduces, in fact the curve has a negative slope.

After that, the curve is characterized by another plateau, since the sample height remains constant despite the temperature increases.

Subsequently, a second densification stage begins at T_3 and ends with the achievement of the maximum sample withdrawal at T_4 . During this phase the sample height reduces again, indeed the curve shows a negative slope.

Finally, the curve is characterized by an irregular trend.

T_1 was identified at $700\text{ }^{\circ}\text{C}$, shortly after T_g . T_2 was detected at $900\text{ }^{\circ}\text{C}$ and coincides with T_c . Therefore, T_x is between T_1 and T_2 . This means that the sample begins to crystallize during the first densification stage and the maximum rate of crystallization is achieved at the end of the first

shrinkage. Thus, the material is already partially crystalline before the start of the second densification phase.

T_3 and T_4 were detected at 1150 °C and 1250 °C, respectively.

Analysing not only the HSM curve but also the silhouettes of the sample subjected to the thermal cycle (Figure 6), it can be seen that the sample at 1300 °C does not start to soften, nor melt. Therefore, in order to identify the softening and melting temperature it is necessary to perform the HSM analysis by setting the final temperature above 1300 °C.

This two-phase densification behaviour was also observed in the studies of Baino et al. [15] and Bretcanu et al. [16] for 45S5 Bioglass®. For Bioglass®, as well as for Ho-BG, densification begins shortly after T_g and crystallization begins before T_2 . Therefore, both the materials are highly crystalline before the second stage of densification.

In accordance with the theory, the plateau between T_2 and T_3 corresponds to the crystallization process, during which the viscosity increases, and viscous flow sintering is inhibited. As the temperature increases further, the viscosity decreases and the second shrinkage stage occurs [15].

Figure 6 represents the HSM curve and the silhouettes of the sample subjected to HSM analysis related to Ho-BG powders.

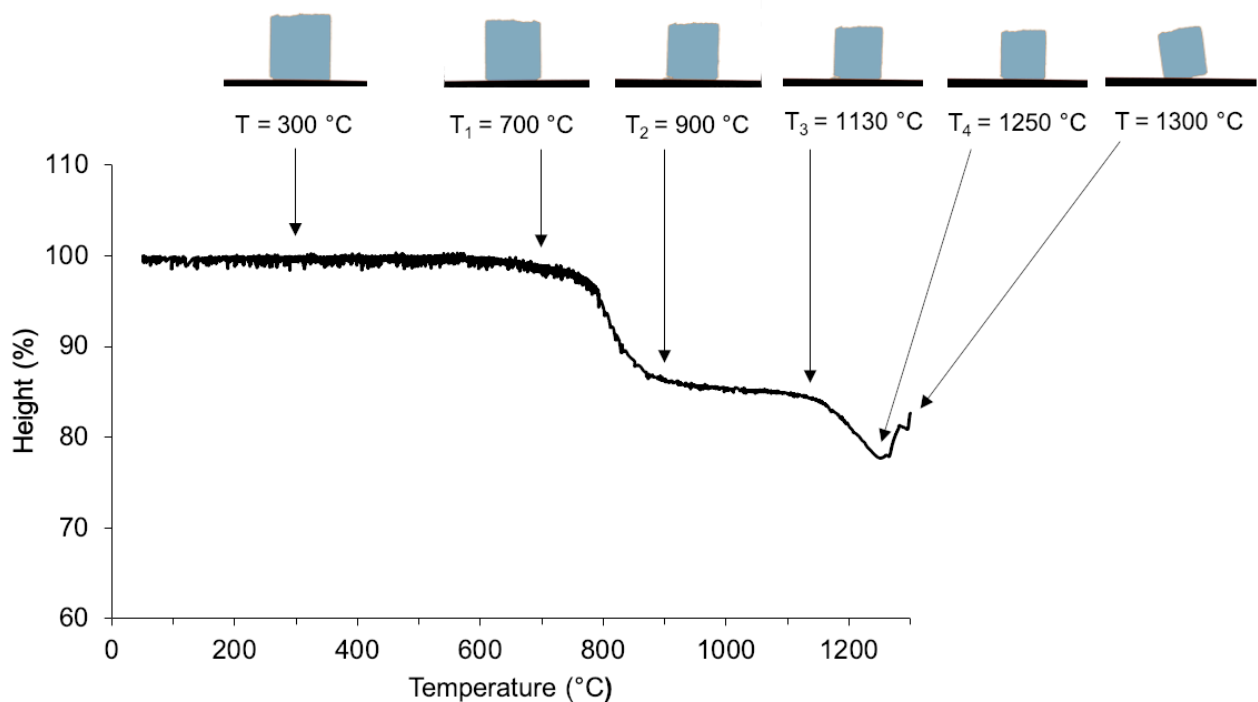


Figure 6: HSM curve related to Ho-BG powders.

Both from the HSM curve and from the silhouettes of the sample, the reduction in size (densification) of the sample subject to thermal cycle can be observed. During the first shrinkage, the height of the sample reduced by ~ 15%, and during the second one, the height of the sample reduced by ~ 8%.

Although the sample size decreased, the sample geometry remained the same throughout the thermal cycle, without any distortion.

The images of the samples show that at 1300 °C the sample began to tilt.

Figure 7 represents the (a) DTA curve and (b) HSM curve related to Ho-BG32 powders.

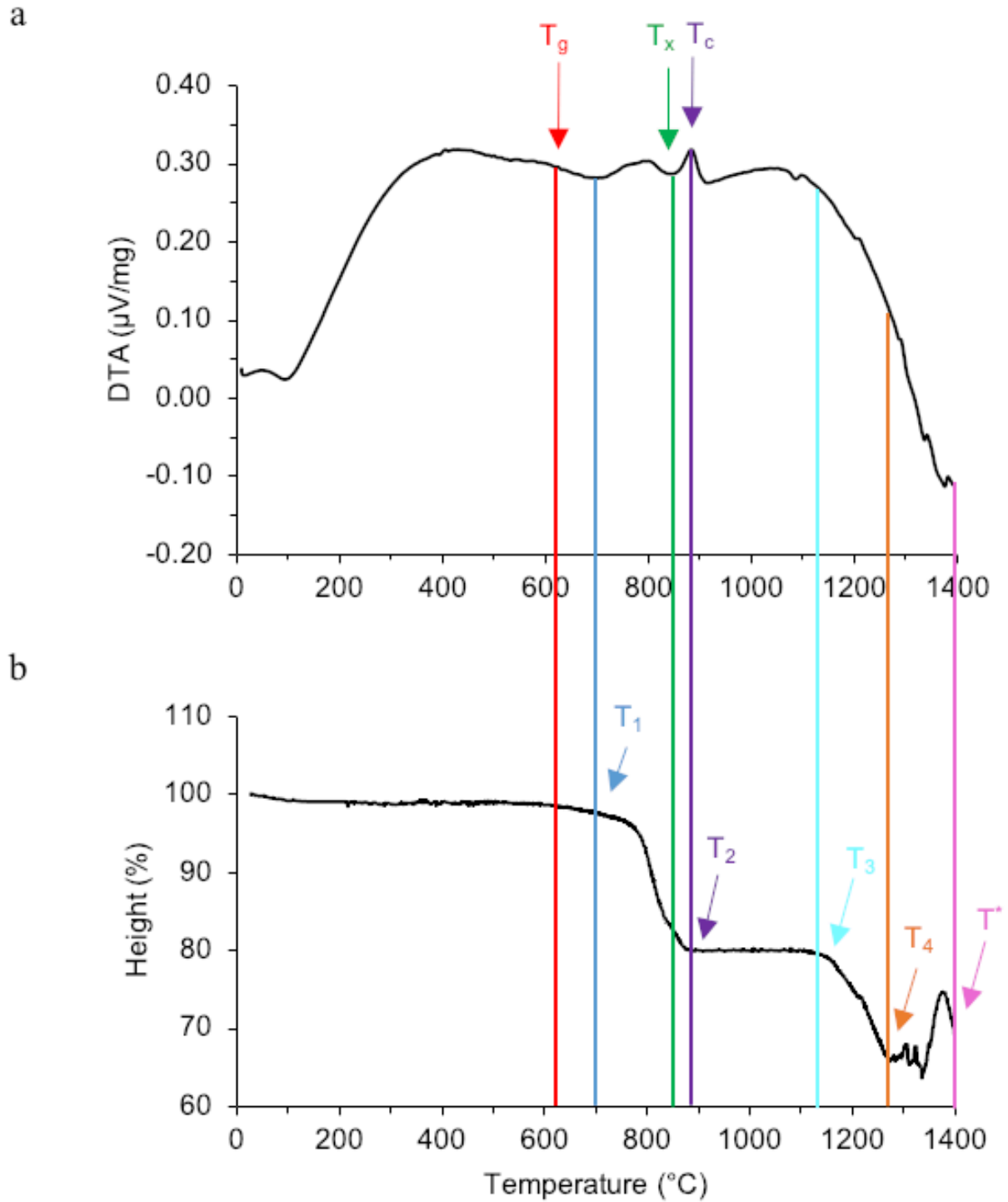


Figure 7: (a) DTA curve and (b) HSM curve related to Ho-BG32 powders.

As in the previous case, in the DTA curve, an endothermic peak related to water evaporation is detected at 100 °C.

Then, the curve is characterized by a steep positive trend, followed by a slight negative slope, about halfway of which T_g was identified. Therefore, T_g was identified at 625 °C.

Between 730 °C and 830 °C the curve shows a hump, and shortly afterwards a pronounced exothermic peak.

T_x and T_c were identified at the insertion point and at the central point of the exothermic peak respectively. Therefore, T_x and T_c were respectively assessed at 850 °C and 890 °C.

Considering the Ho-BG32 oxide composition and the wollastonite devitrification range (850-950 °C), the exothermic peak at $T_c=890$ °C was associated to the nucleation of wollastonite crystals, like for Ho-BG. As a result, the hump between 730 °C and 830 °C could correspond to the formation of metastatic phases that evolve in wollastonite.

As the temperature rises above T_c , the curve develops in a sort of second hump until the softening condition.

The melting of the sample was not even achieved by setting 1400 °C as the final temperature. In fact, there are no endothermic peaks in the DTA curve that can be associated with sample melting.

Since the HSM curve of Ho-BG32 powders is superimposable to the HSM curve of Ho-BG powders, similar considerations can be made to those made for the Ho-BG sample.

First of all, a double-stage shrinkage is observed also in this case.

From the beginning of the thermal cycle up to T_1 the curve is characterized by a plateau. In fact, as the temperature increases, the size and silhouette of the sample remain constant.

Then between T_1 and T_2 the curve shows a negative slope. In fact, in this temperature range the sample shrinks as the first phase of densification occurs.

After that, the curve is characterized by a second plateau: as the temperature increases, the height of the sample does not change.

At T_3 the sample begins the second stage of densification which ends with the maximum sample shrinkage at T_4 . Between T_3 and T_4 the height of the sample decreases, and therefore the curve shows a negative slope.

The last part of the curve has an irregular trend, which was attributed to the beginning of the softening of the sample.

With regard to temperatures, T_1 was identified at 700 °C, just above T_g . T_2 was found at 890 °C and it corresponds to T_c . As in the previous case, T_x is between T_1 and T_2 . Therefore, during the first phase of densification, the nucleation of crystalline phases begins, and it reaches the maximum rate at the end of this phase. As a result, at the end of the first shrinkage, the sample is a glass-ceramic.

T_3 and T_4 were identified at 1130 °C and 1280 °C, respectively.

Observing both the HSM curve and the silhouette of the sample (Figure 9), the softening temperature was identified at $T^* = 1400$ °C.

In addition, the sample silhouette shows that the sample at 1400 °C was not yet melted. This means that the sample melts at a temperature above 1400 °C.

This is confirmed by the appearance of the sample after the HSM analysis (Figure 8). The sample shows round edges and shiny appearance; only a small portion of the glass melted forming a halo on the alumina plate.

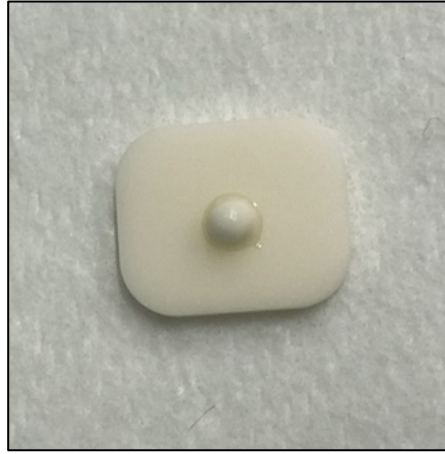


Figure 8: Ho-BG32 cylinder after HSM analysis.

Figure 9 represents the HSM curve and the silhouettes of the sample subjected to HSM analysis related to Ho-BG32 powders.

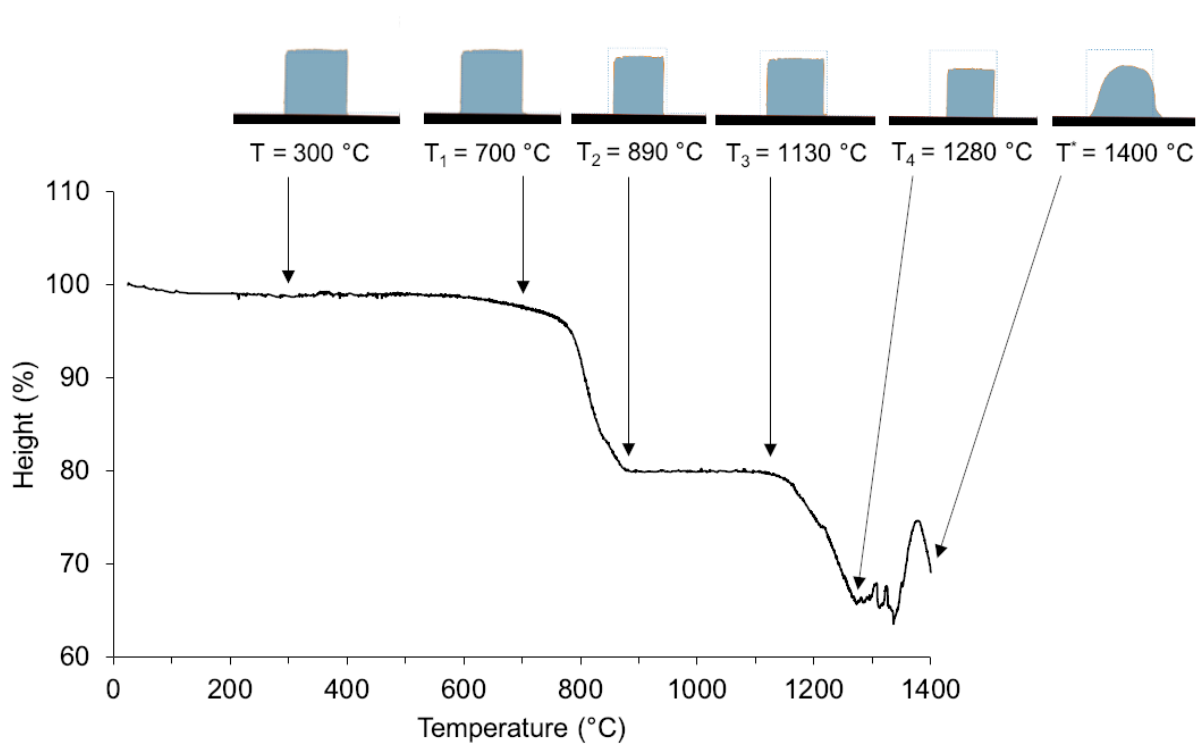


Figure 9: HSM curve related to Ho-BG32 powders.

The sample silhouette confirms the two-stage densification behaviour.

The height of the sample decreased by 20% between T_1 and T_2 still retaining the original geometry. Then, the height of the sample remained stable till the T_3 . From the T_3 to T_4 , the sample height decreased by 15% maintaining its form without distortion.

At T^* , edges began to appear smoothed and the original geometry of the sample was lost (distortion of the sample).

Table 3 summarizes the characteristic temperatures identified by DTA and HSM analyses.

Table 3: Characteristic temperatures derived by DTA and HSM curves.

Sample	T _g (°C)	T _x (°C)	T _c (°C)	T ₁ (°C)	T ₂ (°C)	T ₃ (°C)	T ₄ (°C)	T* (°C)
Ho-BG	690	860	900	700	900	1130	1250	-
Ho-BG32	625	850	890	700	890	1130	1280	1400

By comparing DTA curves of the two samples, it is noted that the glass transition temperature related to Ho-BG32 has a lower value than one of Ho-BG, while the other characteristic temperatures of the Ho-BG32 do not differ significantly from those of the Ho-BG (Table 3).

In addition, it was noticed that DTA curve related to Ho-BG32 has most pronounced peak temperatures than Ho-BG.

By comparing HSM curves of the two samples, it was observed that the temperature at which the first shrinkage starts (T₁) is the same for both Ho-BG and Ho-BG32.

Moreover, the temperature corresponding to the beginning of the second shrinkage (T₃) is also the same for both samples.

Whereas, the temperature at which the first shrinkage ends (T₂) for Ho-BG32 is lower than for Ho-BG, and the maximum shrinkage temperature (T₄) for Ho-BG32 is higher than for Ho-BG.

Particle size affects also the sample shrinkage. Indeed Ho-BG sample shrunk overall by 23%, while Ho-BG32 sample withdrew by a total of 35%. Therefore, Ho-BG32 sample shrunk overall 12% more than the Ho-BG sample.

Ho-BG32 sample shrunk more than Ho-BG sample because it consists of smaller particles. Indeed, the smaller the size of the particles, the greater the contact points between the particles, and in turn sintering is more efficient. While, between the particles that have larger size and irregular geometry, more gaps are created, and consequently a lower level of sintering is achieved.

Considerations Concerning the Glass Sintering and Crystallization

The stability of the glass against crystallization upon heating was assessed by considering the difference T_x – T_g identified from DTA curves.

The greater the difference between the two temperatures, the smaller the tendency towards crystallization of the glass composition. As a result, the greater the stability of the materials in the glassy state when heated [15].

In addition, the ability of sintering versus crystallization during heating was evaluated by sinterability (S_c), which is defined according the following equation [17]:

$$S_c = T_x - T_4 \quad (1)$$

Where T_x and T₄ were identified by DTA and HSM curves.

Lara et al. [17] proposed a general rule to interpret S_c: if S_c < 0, the sample only partially densifies before crystallization begins, while if S_c ≥ 0 the sample fully densifies before crystallization. Therefore, a higher S_c value suggests a better sintering behaviour, which results in a higher densification of the final sample.

The parameters obtained for Ho-BG and Ho-BG32 are shown in Table 4.

Table 4: T_x - T_g and S_c related of Ho-BG and Ho-BG32.

Sample	T_x - T_g	S_c
Ho-BG	170	<0 (- 390)
Ho-BG32	225	<0 (- 430)

Since the difference between T_x and T_g is higher for Ho-BG32 than for Ho-BG, the stability of Ho-BG32 in the glassy state when heated is greater than that of Ho-BG.

In addition, a negative S_c value was obtained for both samples. Therefore, in accordance with the rule proposed by Lara et al. [17], only partial densification is achieved before crystallization begins. This result indicates that there is no sintering temperature for Ho-BG and Ho-BG32 that allows complete densification and avoids crystallization phenomena at the same time.

A similar situation ($S_c < 0$) was observed by Bairo et al. [15] for 45S5 Bioglass®.

5.2.3 X-Ray Diffraction

Ho-BG and Ho-BG32 powders were studied by XRD analysis in order to identify the possible presence of crystalline phases within the material at room temperature

Figure 10 shows the diffraction patterns obtained for (a) Ho-BG and (b) Ho-BG32 samples.

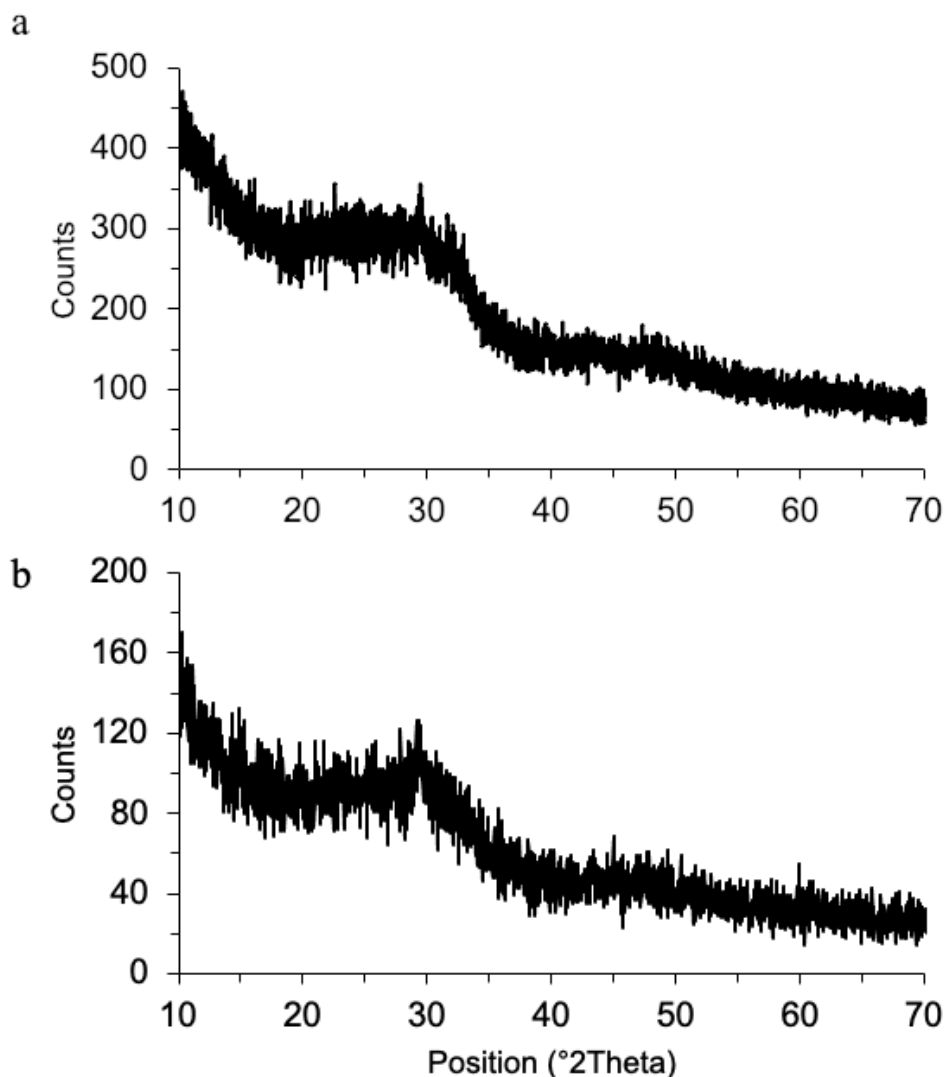


Figure 10: X-ray spectra related to (a) Ho-BG powders, and (b) Ho-BG32 powders.

Figure 10 shows that the diffraction patterns obtained for (a) Ho-BG powders and (b) Ho-BG32 powders have not diffraction peaks. This fact demonstrates that the BG particles have an amorphous structure, which agreed with glass definition.

The halo between 25-35° is typical of amorphous silica-based materials [18]. It is due to the absence of long-range order. In fact, glass is characterized by a high degree of disorder, similar to the liquid from which it originated.

Since x-ray spectra related to Ho-BG powders and Ho-BG32 powders show no significant difference, it can be inferred that the particle size did not affect the XRD spectrum.

However, usually, XRD spectrum is particle size dependent. For example, Bhaskar et al. [19] found that XRD analysis yielded a lower peak for the smaller sized particle sample and vice versa. The cause of this phenomenon was not clear [19].

X-ray patterns of Ho-BG and Ho-BG32 powders are qualitatively comparable with the X-ray pattern of nano-bioactive “parent” 58S glass, obtained for example by Xia et al. [20] (Figure 11).

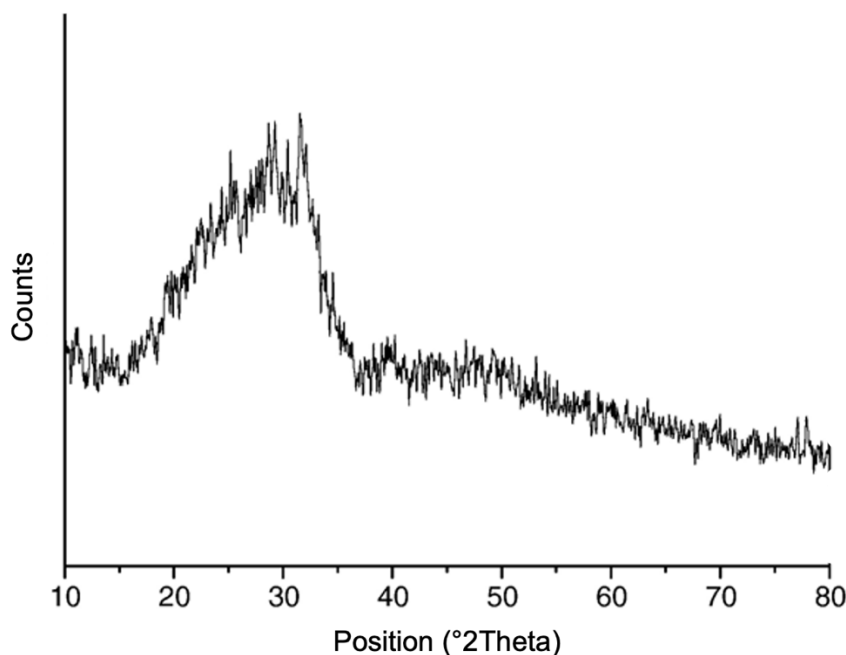


Figure 11: X-ray spectrum of nano-bioactive 58S glass. Figure adapted from Xia et al. [20].

The XRD peaks of 58S BG particles are dispersive and there is no sharp diffraction peak, which demonstrates that the BG particles are typically with amorphous structure [21]. There is just a broad halo between 20 and 35° that is typical of amorphous structures [18].

5.2.4 Scanning Electron Microscopy and Energy Dispersive Spectroscopy

Powders were analysed by SEM to investigate particles morphology and qualitatively evaluate the nature of the sample (amorphous, crystalline or semi-crystalline).

EDS was carried out in order to evaluate the composition of the system, compare it with the theoretical composition and with the composition measured by NAA, and detect the presence of contaminants.

The molar percentage and the mass percentage related to each element and each oxide were calculated and mediated on three different areas.

The Si : Ca and Si : Ho molar ratios, and the molar ratio between the oxides of the glass were calculated.

Both JCM-6000Plus Versatile Benchtop SEM and SEM ZEISS MERLIN were used to analyse the powders.

Since neither the particle morphology nor elemental composition is affected by particle size, SEM and EDS analyses were performed only on Ho-BG powders.

Figure 12 shows SEM images of Ho-BG powders acquired by JCM-6000Plus Versatile Benchtop SEM.

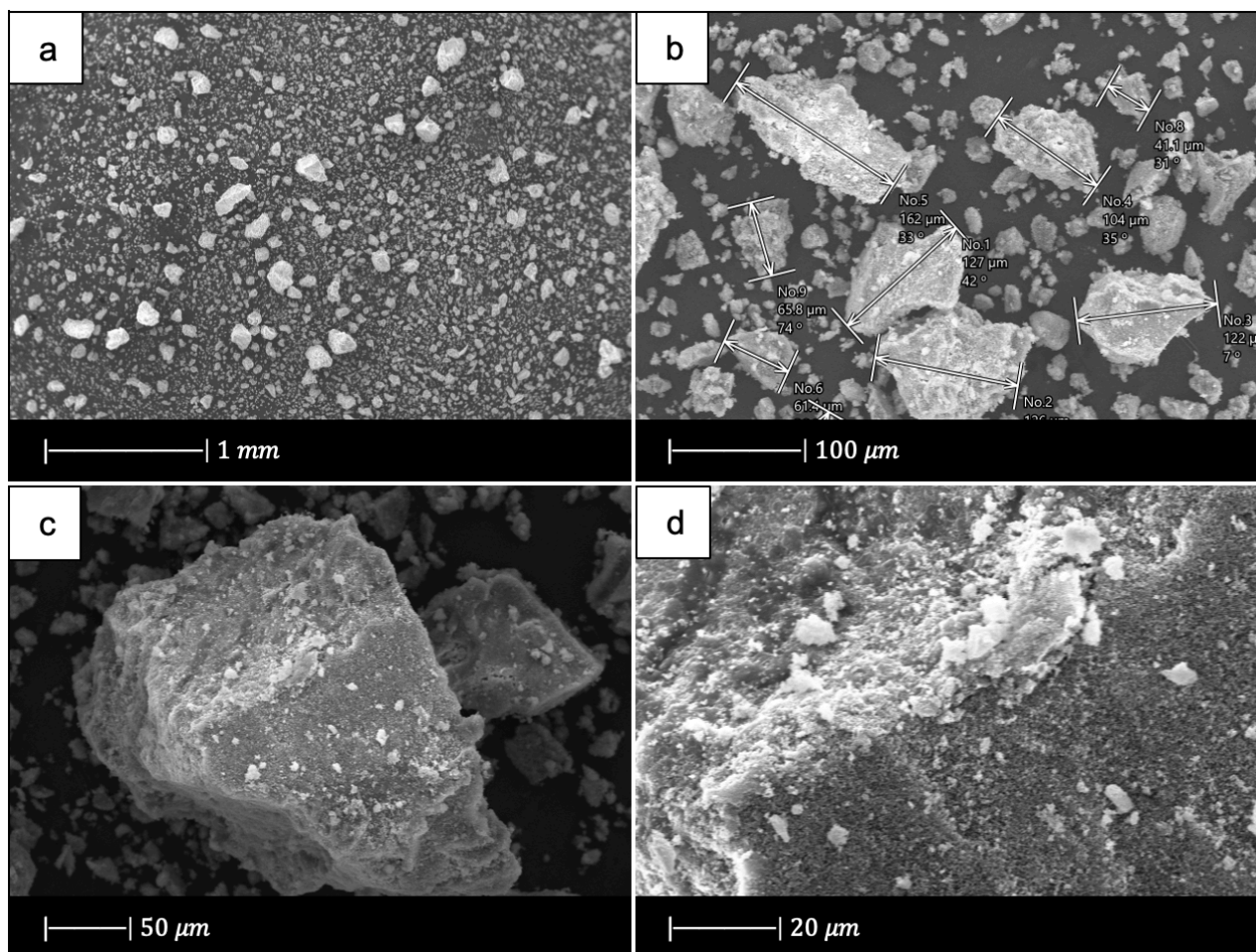


Figure 12: SEM micrographs of Ho-BG powders obtained by JCM-6000Plus Versatile Benchtop SEM.

Figures 12a-d provide pictures at different magnifications of the particles deposited on the surface of the conductive tape.

First of all, it is possible to observe a remarkable heterogeneity in the distribution of particles size. This is due to the fact that the powders which were analysed at SEM were not ground and sieved.

Figure 12-b shows that bigger particles have a diameter of about 160 μm , while the smaller ones have a diameter of about 10 μm . This result is in agreement with the result of the particle size analysis, which found that the particles have diameters between 0 and 2000 μm . It should also be considered that the particle size depends on the fraction of the sample being analysed, and large particles could be the result of smaller particle size aggregates.

The particles had an angular, irregular, nonspherical shapes.

In Figure 12-c, it is possible to observe how smaller particles deposit on the surface of the bigger ones, by creating a sort of coating.

Figure 12-d shows a very porous and rough texture, typical of sol-gel glass powders.

Since generally benchtop SEM presents less resolution than full size SEM, SEM Merlin was used to capture images at higher magnifications.

Figure 13 shows SEM images of Ho-BG powders acquired by SEM ZEISS MERLIN.

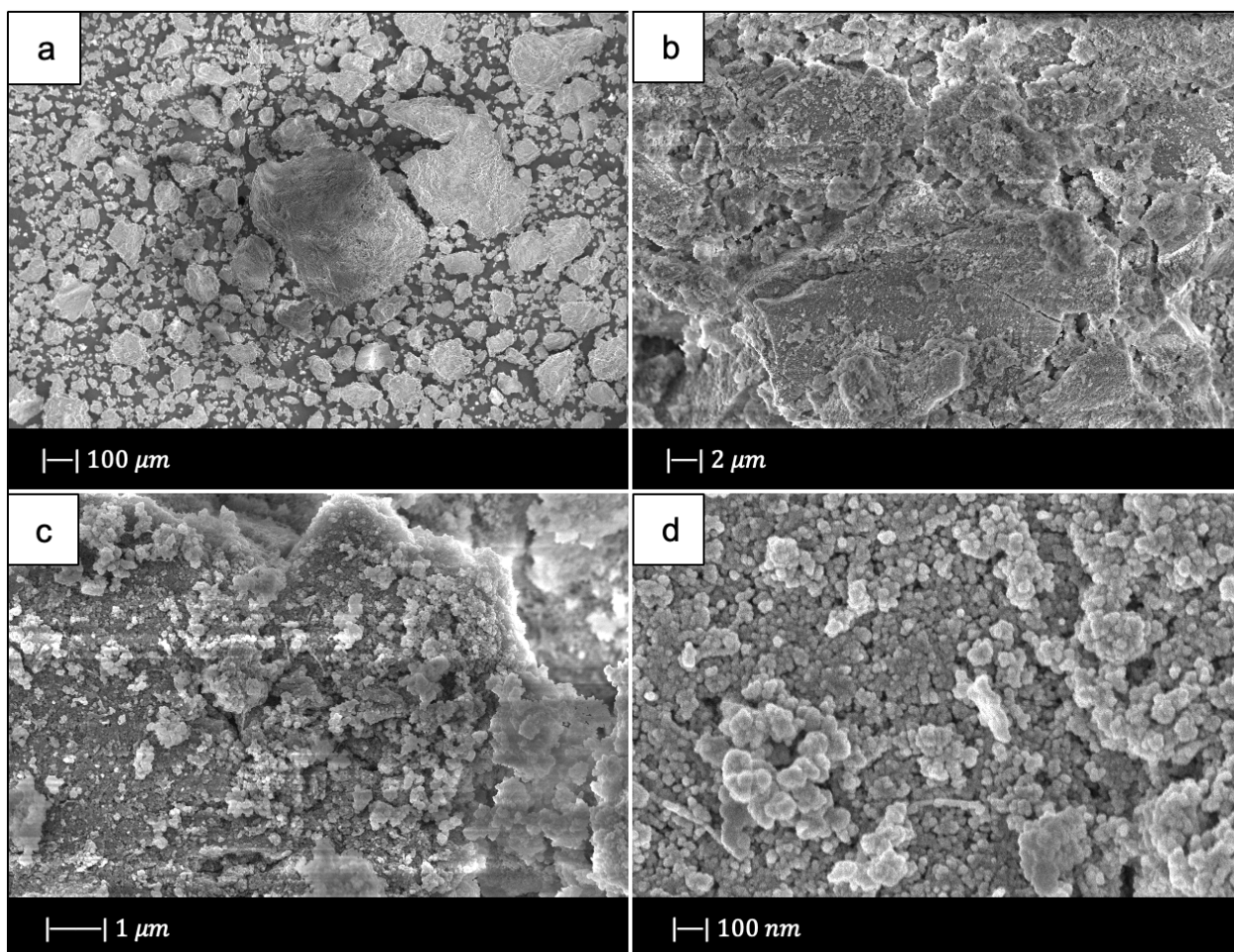


Figure 13: SEM micrographs of Ho-BG powders obtained by SEM ZEISS MERLIN.

The images of the samples acquired by SEM ZEISS MERLIN show similar features compared to the images acquired by benchtop SEM concerning particles size distribution and the geometry of the powders. In fact, also these images show a remarkable heterogeneity in the particle size and exhibits powders with irregular shapes. Most of the powder has a shape that resembles a parallelepiped with rounded corners.

In addition, the powders seem to form agglomerates as a result of weak-attraction van der Waals forces (Figure 13a).

From the images obtained at higher magnifications, it appears that the surface is characterized by a rough and nanoporous texture, which derives from the sol-gel synthesis of the glass.

No crystalline formations were observed, neither in the images obtained using benchtop SEM nor in those obtained by means of SEM ZEISS MERLIN. This result is consistent with that of the x-ray analysis, which demonstrated the predominantly amorphous nature of the material.

Figures 14 and 15 show representative EDS spectra Ho-BG powders obtained by JCM-6000Plus Versatile Benchtop SEM and SEM ZEISS MERLIN respectively.

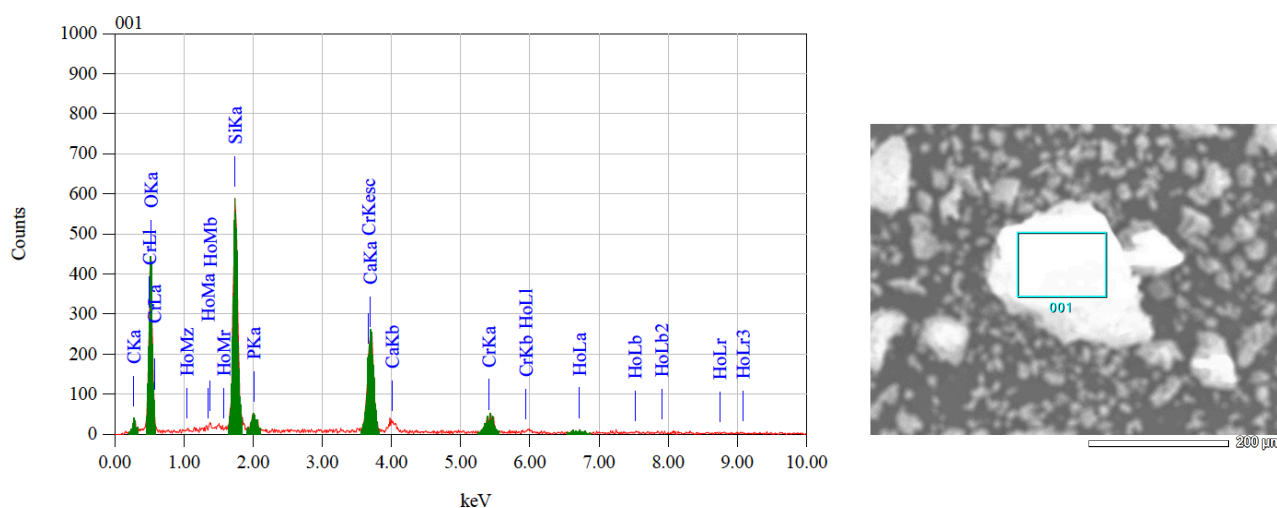


Figure 14: EDS analysis performed on Ho-BG powders using JCM-6000Plus Versatile Benchtop SEM.

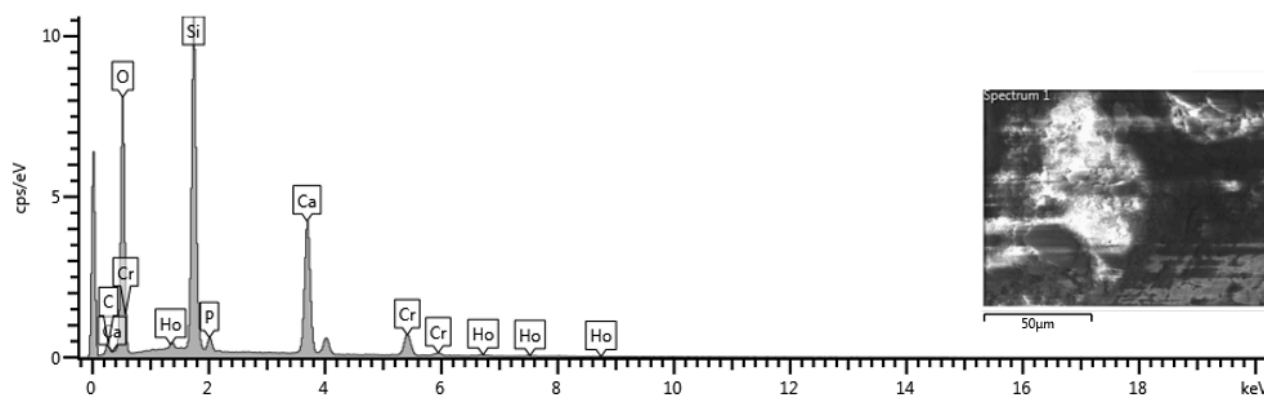


Figure 15: EDS analysis performed on Ho-BG powders using SEM ZEISS MERLIN.

EDS spectrum exhibits which elements were detected in the samples by EDS analysis, and the amount of each of them.

Each peak in the spectrum corresponds to an element, and different peaks may correspond to the same element. The peak height indicates the amount of the element relative to the peak that was detected. The EDS analysis was performed by each SEM device on three different areas of the sample and depending on the area considered, a slightly different spectrum was obtained.

However, the EDS spectra obtained by JCM-6000Plus Versatile Benchtop SEM and SEM ZEISS MERLIN are very similar. This means that the two instruments detected the presence of approximately the same elements in the sample.

The elements in the spectra, except chromium, are the same as the theoretical composition of glass. Therefore, there are no contaminations in the glass powders. Indeed, the presence of Cr is justified since the sample was coated with a conductive Cr layer in order to achieve a higher resolution during SEM analysis.

Tables 5-8 were obtained by processing the EDS data collected with JCM-6000Plus Versatile Benchtop SEM and SEM ZEISS MERLIN.

Table 5: Element composition (wt% and mol%) of Ho-BG obtained by processing EDS data derived by JCM-6000Plus Versatile Benchtop SEM.

Element	wt%	mol%
Si	48.34 ± 3.47	58.39 ± 3.29
Ca	43.69 ± 1.82	37.02 ± 2.07
P	3.31 ± 0.94	3.63 ± 1.07
Ho	4.66 ± 0.74	0.96 ± 0.16

Table 6: Element composition (wt% and mol%) of Ho-BG obtained by processing EDS data derived by SEM ZEISS MERLIN.

Element	wt%	mol%
Si	50.14 ± 1.11	60.01 ± 1.17
Ca	42.03 ± 2.71	35.26 ± 2.35
P	3.56 ± 1.39	3.87 ± 1.5
Ho	4.26 ± 0.62	0.87 ± 0.12

Table 7: Oxide composition (wt% and mol%) of Ho-BG obtained by processing EDS data derived by JCM-6000Plus Versatile Benchtop SEM.

Oxide	wt%	mol%
SiO ₂	58.25 ± 3.53	59.75 ± 2.99
CaO	34.47 ± 1.8	37.9 ± 2.35
P ₂ O ₅	4.94 ± 2.18	1.86 ± 0.56
Ho ₂ O ₃	3.44 ± 1.13	0.49 ± 0.09

Table 8: Oxide composition (wt% and mol%) of Ho-BG obtained by processing EDS data derived by SEM ZEISS MERLIN.

Oxide	wt%	mol%
SiO ₂	59.88 ± 0.98	61.47 ± 1.48
CaO	32.85 ± 2.4	36.10 ± 2.16
P ₂ O ₅	4.55 ± 1.73	1.98 ± 0.79
Ho ₂ O ₃	2.72 ± 0.37	0.44 ± 0.07

Table 9 shows the molar ratios between the elements and the oxides of Ho-BG, obtained by processing the data obtained from JCM-6000Plus Versatile Benchtop SEM and SEM ZEISS MERLIN.

Table 9: Molar ratios of Ho-BG.

Device	Si : Ca Molar Ratio	Si : Ho Molar Ratio	SiO ₂ : CaO : P ₂ O ₅ : Ho ₂ O ₃ Molar Ratio
JCM-6000Plus Versatile Benchtop SEM	1.58	60.82	121.94 : 77.35 : 3.8 : 1
SEM ZEISS MERLIN	1.70	68.98	139.7 : 82 : 4.5 : 1

As can be seen by observing Tables 5 and 6, the element composition (wt% and mol%) of Ho-BG obtained by processing EDS data derived by benchtop SEM is about the same as the one obtained by processing EDS data derived by SEM ZEISS MERLIN.

Oxygen is not present in the tables although it is an element present in the glass. In fact, it was decided not to consider it in the element composition of the glass, because the amount of measured oxygen is highly dependent on the instrument used.

The fact that the element compositions obtained by processing the data acquired from the two different instruments are about the same confirms that the one obtained is actually the element composition of the glass.

From Tables 7 and 8, it can be seen that also the oxide composition (wt% and mol%) of Ho-BG obtained by processing EDS data derived by benchtop SEM is about the same as the one obtained by processing EDS data derived by SEM ZEISS MERLIN.

Also in this case, the fact that the oxide compositions obtained by processing the data acquired by the two different instruments are the same, further confirms that the one obtained is the real oxide composition of the glass.

Since the element and oxide compositions identified by the two different instruments are the same, the molar ratios Si : Ca, Si : Ho and SiO₂ : CaO : P₂O₅ : Ho₂O₃ obtained by using the values deriving from benchtop SEM are very similar to ones obtained by using the values resulting from SEM ZEISS MERLIN (Table 9).

In addition, the oxide composition of the Ho-BG detected by EDS analysis is comparable to both the composition detected by the NAA, and the theoretical composition of the glass.

In detail, the composition of Ho-BG detected by EDS analysis shows a higher amount of SiO_2 and a lower amount of P_2O_5 and Ho_2O_3 than oxide composition detected by the NAA and the theoretical composition of the glass. While the percentage of CaO is approximately the same in all three compositions.

Moreover, the molar ratio $\text{SiO}_2 : \text{CaO} : \text{P}_2\text{O}_5 : \text{Ho}_2\text{O}_3$ obtained from the EDS analyses is in agreement with the molar ratio $\text{SiO}_2 : \text{CaO} : \text{P}_2\text{O}_5 : \text{Ho}_2\text{O}_3$ of the designed composition, which is 91.31 : 55.58 : 5.95 : 1.

5.2.5 Textural Analysis

BET analysis was performed both on Ho-BG and Ho-BG32 powders.

The aim of the analysis was to evaluate the mesoporosity of the powders resulting from the sol-gel process.

The control of pore structure and size is central for the development of substitutes of living tissues, since porosity features are fundamental in determining the entity of the interactions between cells and the surrounding environment [22].

In order to evaluate the porosity, it is necessary to analyse interconnectivity, shape of the pores and size distribution [22].

Isotherm curves, deriving from adsorption and desorption of nitrogen on the surface of the sample and evaluated at different relative pressures, were analysed.

In addition, pore diameter distribution was calculated by considering the desorption branch of isotherms, that is more reliable to approximate the thermodynamic equilibrium.

The textural porosity was evaluated by referencing to the physisorption isotherm classification and the IUPAC classification of hysteresis loops, both represented in Figure 16.

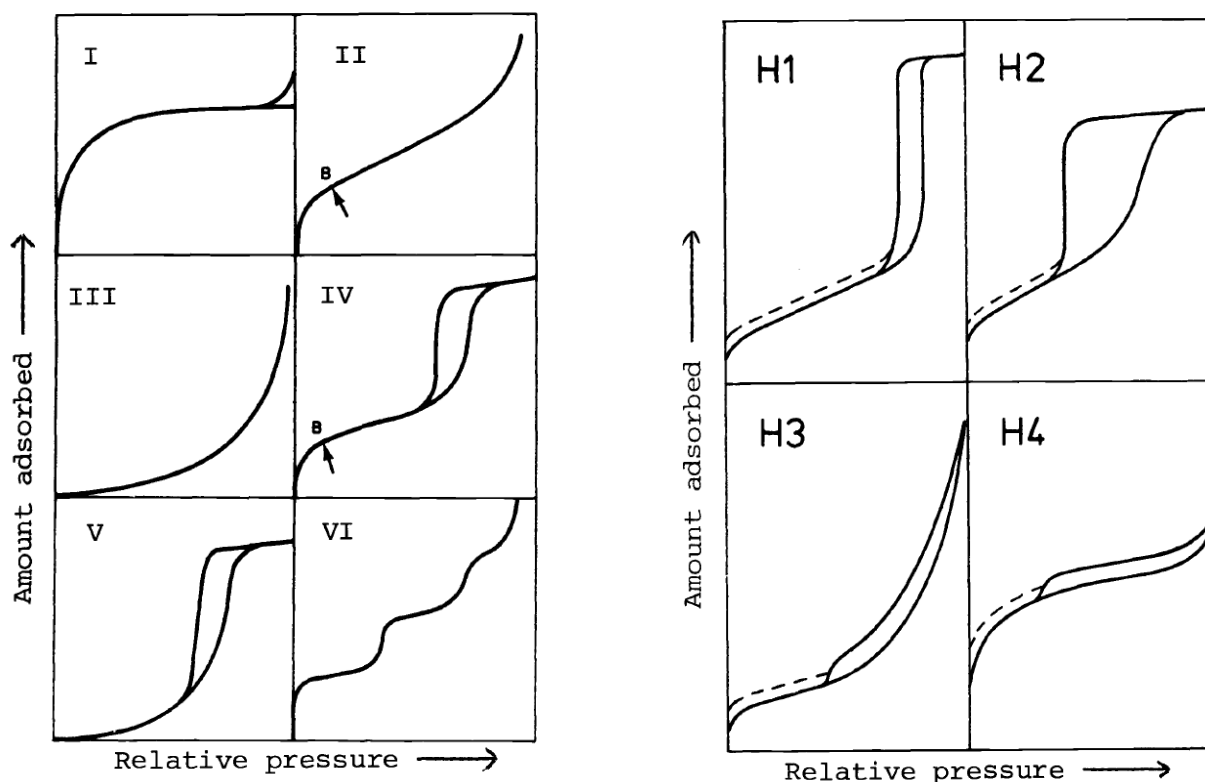


Figure 16: IUPAC classification of adsorption isotherms on the left and IUPAC classification of hysteresis loops on the right. Figure reproduced from Sing et al. [23].

According to the classification provided by Thommes et al. [24], physisorption isotherms could be classified into 6 types:

- Type I: given by microporous solids characterized by relatively small external surfaces. This curve is concave to the p/p^0 axis and the adsorbed amount of gas gets close to a limit value. This limiting absorption is adjusted by the accessible micropore volume rather than by the internal surface area [24].
- Type II: given by nonporous or macroporous materials. The shape is the result of unrestricted monolayer-multilayer adsorption up to high p/p^0 . Point B, shown in Figure 16, corresponds to the completion of the first adsorbed monolayer, and so the beginning of the multilayer adsorption [24].
- Type III: characterized by convexity to the p/p_0 axis over its entire range, and since there is no point B, no monolayer formation is detectable. The adsorbent-adsorbate interactions are now approximately weak, and the adsorbed molecules are grouped around the most favourable sites on the surface of a nonporous or macroporous solid [24].
- Type IV: given by mesoporous adsorbents. It presents a hysteresis loop caused by capillary condensation occurring within the mesoporous structure. The beginning of the curve is related to monolayer-multilayer adsorption and has analogies with type II isotherms. Furthermore, it is characterized by a final saturation plateau, of variable length [24].
- Type V: generally associated to porous adsorbents where the adsorbent-adsorbate interaction is weak [24].
- Type VI: characterized by a stepwise trend. It is representative of layer-by-layer adsorption on a highly uniform nonporous surface. The step-height indicates the capacity for each adsorbed layer,

while the sharpness of the step depends on the temperature and features of the system. Such isotherms are frequently obtained by argon or krypton at low temperature on graphitized carbon blacks [24].

Original IUPAC classification in 1985 identified four types of hysteresis loop [25]:

- Type H1: given by porous materials which exhibit a narrow distribution of relatively uniform (cylindrical-like) pores. H1 hysteresis loop mostly determined by the effect of delayed condensation and not by network effects [25].
- Type H2: generally associated to materials containing a more complex pore structure in which network effects are relevant [25].
- Type H3: given by non-rigid aggregates of plat-like particles or assemblages of slit-shaped pores. Generally, it does not provide a reliable evaluation of the pore size distribution and the total pore volume. Isotherms with type H3 hysteresis do not show any limiting adsorption at high p/p_0 [25].
- Type H4: typical of complex materials containing both micropores and mesopores [25].

Figure 17 shows the nitrogen sorption isotherm of Ho-BG powders. In particular, it exhibits the relationship at constant temperature ($T=77K$) between the amount of gas adsorbed (mmol/g) and the relative pressure p/p^0 (p^0 =saturation pressure of pure nitrogen).

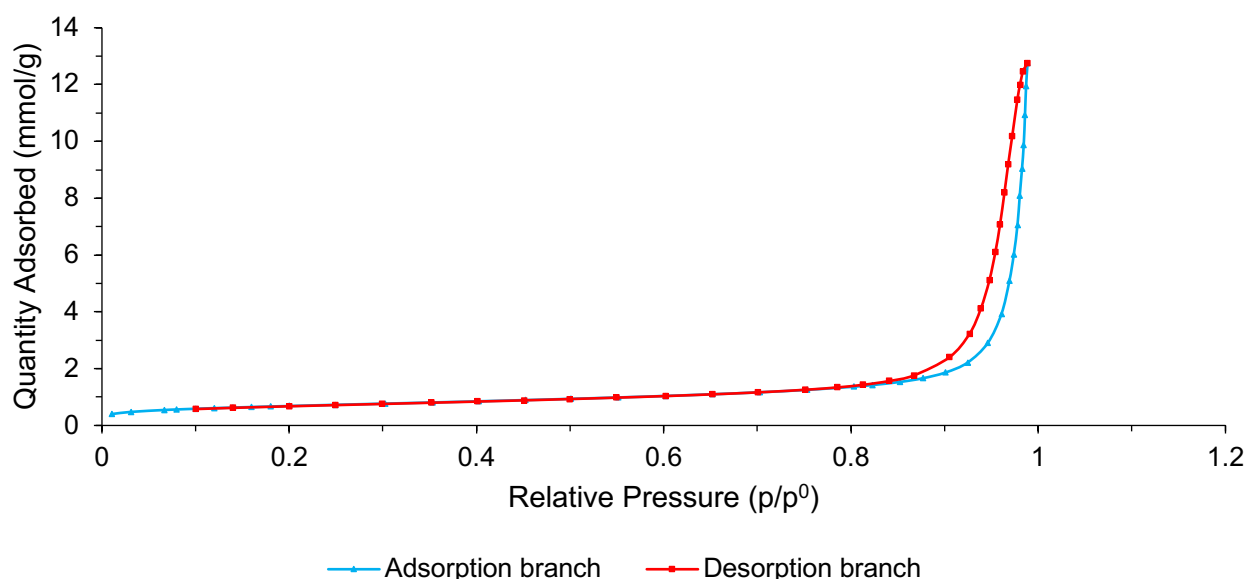


Figure 17: Nitrogen sorption isotherm of Ho-BG powders.

According to isotherms classification provided above, the curve could be classified as isotherm of type IV. The isotherm exhibits a hysteresis loop originated by capillary condensation taking place in mesopores. The initial part of the curve is associated with monolayer-multilayer adsorption, while the final part shows a saturation plateau.

According to the IUPAC classification of hysteresis loops represented in Figure 16, the isotherm exhibits a type H3 hysteresis. Hysteresis H3 suggests the presence of non-rigid aggregates of plat-like with slit-shaped porosity.

The analysis of the isotherm suggests the mesoporous nature of the material, which is a feature partly confirmed by the analysis of the textural pore size distribution, shown in Figure 18.

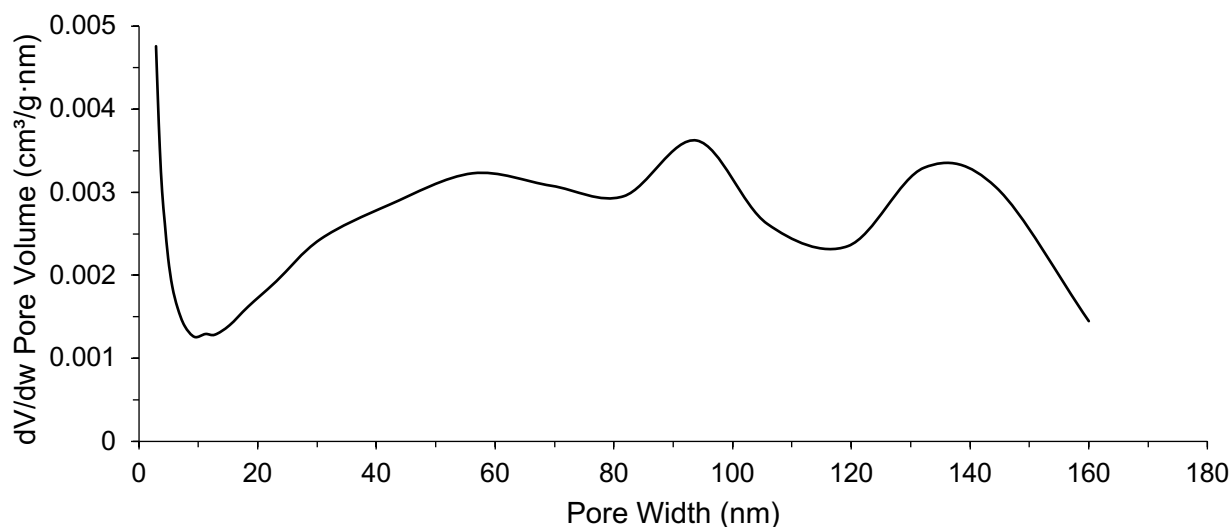


Figure 18: Pore size distribution of Ho-BG powders.

Since the analysed powders have pores with diameters between 2.86 and 160 nm, Ho-BG has the characteristics of both mesoporous (2-50 nm) and macroporous (>50 nm) material. This result differs from the 58S BG pore size, which varies from 6 to 9 nm.

The value of the surface area obtained is 53.52 m²/g. Thus Ho-BG surface area is higher than melt-derived BG surface area one, which is usually < 0.25 m²/g [26]. This high surface area is beneficial to the interactions between the material and the biological environment.

However, Ho-BG surface area is inferior to the surface area values commonly assessed for silicate sol-gel BGs, which are > 100 m²/g [22], and in particular to 58S BG surface area, which usually ranges from 126.5 to 164.7 m²/g [26].

Ho-BG powders pore volume is 0.442 cm³/g. This value is comparable with the pore volume of 58S BG powders, which is 0.213-0.498 cm³/g.

Consequently, it is reasonable to attribute the larger pore size and the smaller surface area of Ho-BG powders compared to 58S BG powders to the presence of holmium oxide in the glass composition. In fact, the presence of modifying oxides such as holmium oxide can influence the gelation phase, leading to the formation of a more disorganised nanoporous network, which in turn leads to a decrease in textural properties.

Similar phenomena were observed by Fiume et al. [27] and Wu et al. [28], [29]. In particular, they found that the incorporation of iron, strontium and copper into the scaffolds causes a decrease in specific surface area [27], [28], [29].

However, unlike holmium oxide, the presence of iron and copper involved a decrease in mesopore size and in pore volume [27], [29].

Figure 19 shows the nitrogen sorption isotherm of Ho-BG32 powders. As in the previous case, it exhibits the relationship at constant temperature (T=77K) between the amount of gas adsorbed (mmol/g) and the relative pressure p/p^0 (p^0 = saturation pressure of pure nitrogen).

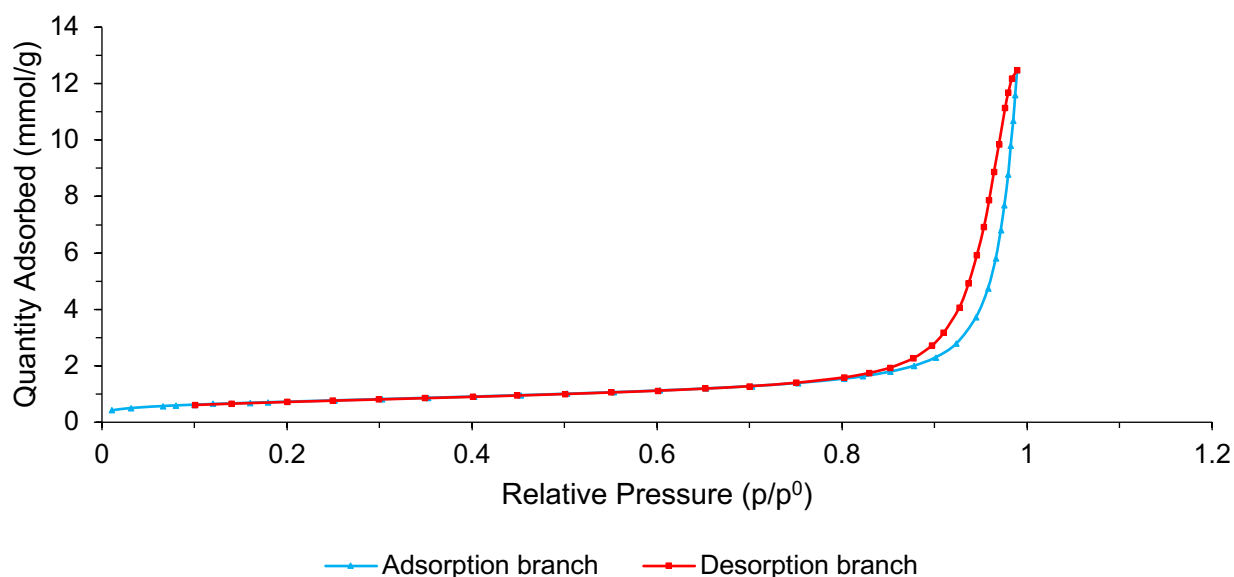


Figure 19: Nitrogen sorption isotherm of Ho-BG32 powders.

The isotherm shows a type IV behaviour, so analogous considerations to those relating to the Ho-BG isotherm could be made concerning mesoporous texture.

According to the IUPAC classification of hysteresis loops represented in Figure 16, like Ho-BG, the isotherm exhibits a type H3 hysteresis loop, typical of slit-shaped porosity.

Also in this case, the mesoporous nature of the powders were partially confirmed by the analysis of the textural pore size distribution, shown in Figure 20.

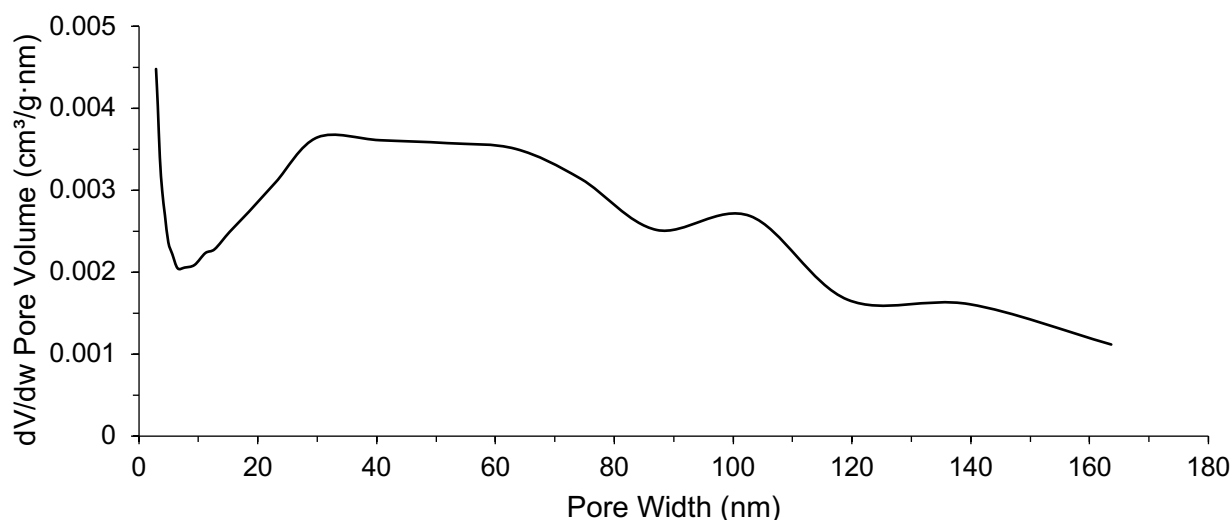


Figure 20: Pore size distribution of Ho-BG32 powders.

The concerned powders have pores with diameters ranging from 2.86 to 163.64 nm, so the sample has the characteristics of both mesoporous (2-50 nm) and macroporous (>50 nm) materials. As expected, the size of Ho-BG32 powders pores is the same as Ho-BG powders.

Ho-BG32 powders surface area is 57.19 m²/g. It is slightly larger than the surface area of Ho-BG powders and smaller than the surface area of 58S bioactive glass. Therefore, as the particle size decreased, the surface area increased.

An opposite behaviour was found by Hench et al. [26] concerning 58S BG; as the particles size increased, the surface area increased [26].

Ho-BG32 powders pore volume is 0.427 cm³/g, which is slightly less than Ho-BG powders pore volume and comparable with 58S BG one.

A summary of the textural parameters of the analysed samples and the 58S bioactive glass is provided in Table 10.

Table 10: Summary of BET data for the powders analysed and 58S bioactive glass

Sample	Specific Surface Area (m ² /g)	Pore Diameter Range (nm)	Pore Volume (cm ³ /g)	Ref.
Ho-BG	53.52	2.86 - 160	0.442	-
Ho-BG32	57.19	2.86 - 163.64	0.427	-
58S BG	126.5 - 164.7	6-9	0.213-0.498	[26]

5.3 Ho-doped Scaffold Preparation and Characterization - Politecnico di Torino (Turin, Italy)

Scaffolds were produced by foam replica method, dipping polyurethane foams into the slurry in order to obtain the green bodies. After the drying process, the green bodies were thermally treated to burn out the PU foam and sinter the glass.

In order to optimize the process, eight different tests were carried out. Drying method and sintering temperature were varied one by one in order to identify critical aspects of the procedure. The parameters used for each test are summarized in Table 4, Chapter 4.

Some of the samples were dried in incubator because during the preliminary tests, in which the samples were air-dried, an uneven distribution of the slurry inside the PU foam was observed. In fact, because the green bodies took too long to dry in air, the slurry settled on the bottom of the sponge. The uneven distribution of slurry led to extremely fragile scaffolds, which crumbled in places where there was a shortage of material.

Therefore, it was assumed that by speeding up the drying process of the green bodies through the use of the incubator, samples with homogeneous slurry distribution would be obtained. As a result, more resistant scaffolds would have been obtained.

However, since the Ho-doped scaffolds which were air dried and those dried inside the incubator did not show any significant differences, it may be assumed that the drying method did not play a crucial role.

Data from DTA and HSM analyses were very useful to select the right sintering temperature for fabricating scaffolds.

However, it should be considered that the sintering process of the scaffolds is different from the sintering of compacts of glass powders, like those used for HSM. Indeed, the green bodies have large macropores due to the structure of the PU template, while between the compacts of glass powders there are small intraparticulate voids. Moreover, during thermal treatment of the glass powders only the densification/crystallization of glass particles occurs, while during thermal treatment of the green bodies, also to the burning-out of the PU template occurs. Nevertheless, HSM analysis on glass powder compacts is useful to understand glass behaviour upon thermal cycle and thus to select the appropriate temperature for sintering the scaffolds [15].

Generally, if a completely densified and purely glassy scaffold is desired, sintering temperature should be chosen in the range between the maximum densification and the onset of crystallization [15].

Indeed, in order to obtain a fully densified scaffold, the sintering temperature should be above the maximum shrinkage temperature, and in order to preserve the amorphous structure, the glass should be thermally treated at a temperature within the sintering window [30].

The scaffolds were produced by using Ho-BG32 powders, which were characterized by $T_x=850\text{ }^{\circ}\text{C}$ and $T_4=1280\text{ }^{\circ}\text{C}$, as mentioned above. Since $T_4 > T_x$, it was not possible to thermally treat the glass at a temperature that allowed to obtain a purely glassy and fully densified structure at the same time.

This result was in agreement with that of the sinterability calculated for Ho-BG32, which indicated that it was not possible to obtain complete densification of the glass before crystallization began.

Therefore, in order to find the optimal sintering temperature, eight tests were carried out, which result in eight scaffolds (Figure 21).

The first test (Test 1, Table 4, Chapter 4) was aimed at obtaining a purely glassy scaffold, so a temperature within the sintering window, which is bounded by $T_g=625\text{ }^{\circ}\text{C}$ and $T_x=850\text{ }^{\circ}\text{C}$, was set as sintering temperature. Their choice fell on $T=800\text{ }^{\circ}\text{C}$.

The scaffold resulting (Ho-I-800) was so fragile that it crumbled. For this reason, the image related to the scaffold produced by this test is not present in Figure 21.

It is reasonable to attribute the failure of Test 1 to the use of a too low sintering temperature, which did not allow to obtain a sufficient densification of the glass particles and to fill the voids deriving from the burnout of the PU foam. Indeed, at $T=800\text{ }^{\circ}\text{C}$ compacts of glass powders used for HSM analysis had not yet completed the first stage of densification, which occurred at $T_2=890\text{ }^{\circ}\text{C}$, and only shrunk by 8%.

The second and third tests (Test 2 and Test 3, Table 4, Chapter 4) were aimed at obtaining glassy scaffolds which were more resistant than that obtained from Test 1. Thus, the upper limit of the sintering window (T_x) was used as sintering temperature.

Ho-AD-850 scaffold (Test 2) lost the cubic shape of the starting template and assumed an irregular shape. Moreover, it was so fragile that it could not be handled (Figure 21a). Ho-I-850 scaffold (Test 3) crumbled (Figure 21b).

Also in this case, it is reasonable to think that the green bodies during the heat treatment achieved a low densification, which did not allow to fill the voids resulting from the burnout of the sponge. Indeed, at T_x compacts of glass powders used for HSM analysis had not yet completed the first stage of densification, because $T_x < T_2$, and they shrunk by only 18%.

Since it was not possible to obtain well densified scaffolds while preserving the amorphous nature of glass, the subsequent tests were carried out by setting a sintering temperature above T_x . In particular, the chosen sintering temperatures were $950\text{ }^{\circ}\text{C}$, $1000\text{ }^{\circ}\text{C}$ and $1050\text{ }^{\circ}\text{C}$, which are values between T_2 and T_3 . At these temperatures, compacts of glass powders used for HSM analysis completed the first

stage of densification and shrunk by 20%. Therefore, the greater resistance showed by the scaffolds is attributable to the greater densification achieved due to the higher used sintering temperature. However, the scaffolds were still too fragile for bone tissue engineering applications. As a result, the scaffold fabrication process needs to be optimized.

In addition, the obtained scaffolds by Tests 4-8 maintained the cubic shape of the starting template without distortion despite the considerable volume shrinkage of the structure (Figure 21c-g). This result is very important for future clinical use of the scaffold in case complex bone substitutes are needed.

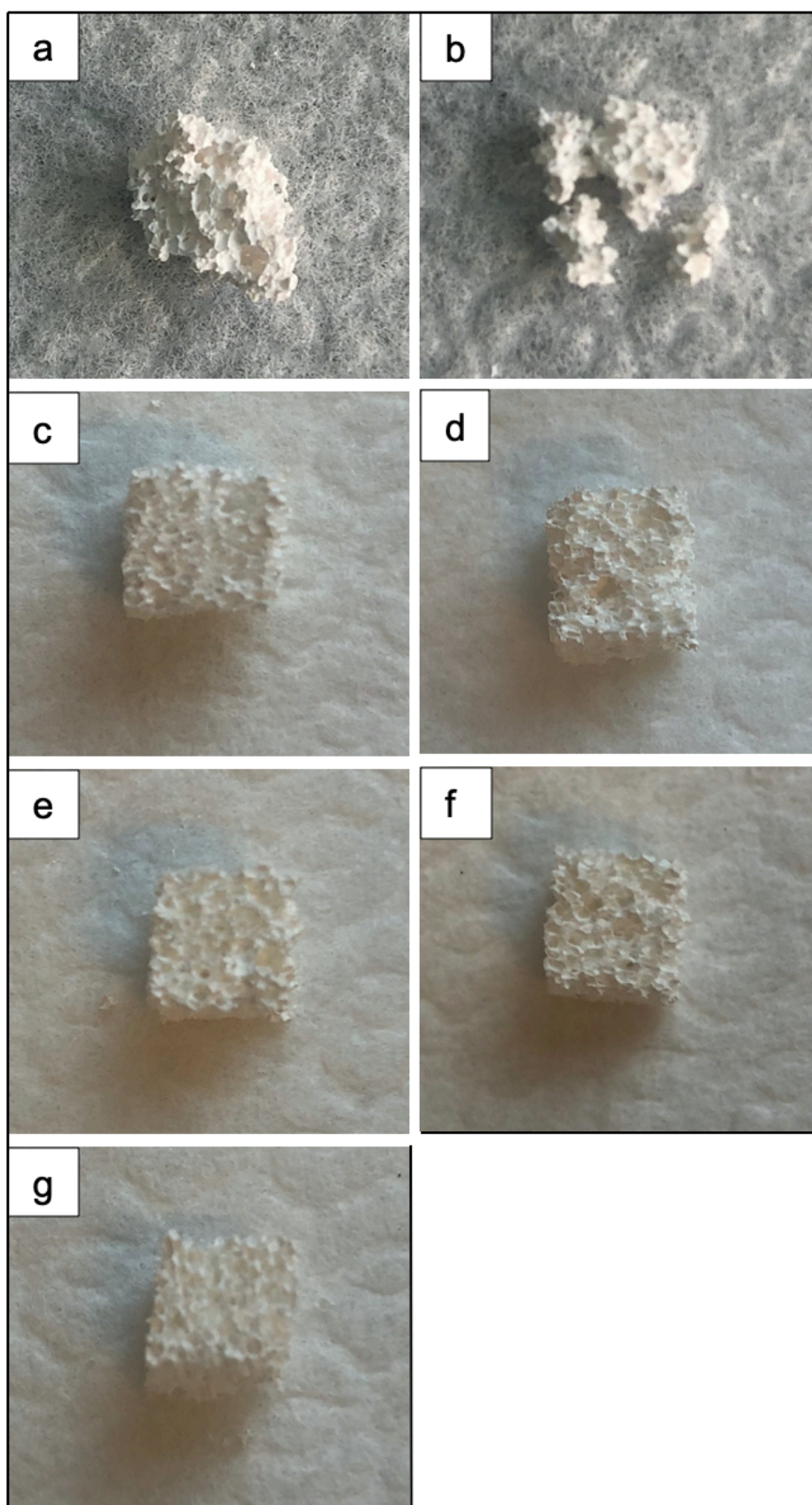


Figure 21: Scaffolds referring to the test number (a) 2, (b) 3, (c) 4, (d) 5, (e) 6, (f) 7, (g) 8.

5.3.1 Morphological and Compositional Analysis of the 3D Structures

A first evaluation of the scaffolds was carried out by the morphological analysis at SEM, which made it possible to examine the pores size and their interconnectivity, as well as the level of sintering between the particles.

EDS was performed in order to evaluate the composition of the scaffold, compare it both with the theoretical composition and with the results of previous compositional analysis, and detect the presence of contaminants.

The molar percentage and the mass percentage related to each element and each oxide were calculated and mediated on three different areas.

The Si : Ca and Si : Ho molar ratios, and the molar ratio between the oxides of the glass were calculated.

Only SEM ZEISS MERLIN was used to analyse the scaffolds.

SEM analysis was performed on Ho-AD-950, Ho-I-1000, and Ho-AD-1050 scaffolds.

EDS analysis was carried out only on Ho-AD-1050 scaffold because all the scaffolds have the same composition.

Figure 22 shows morphological characteristics of Ho-AD-950 scaffold (Test 4).

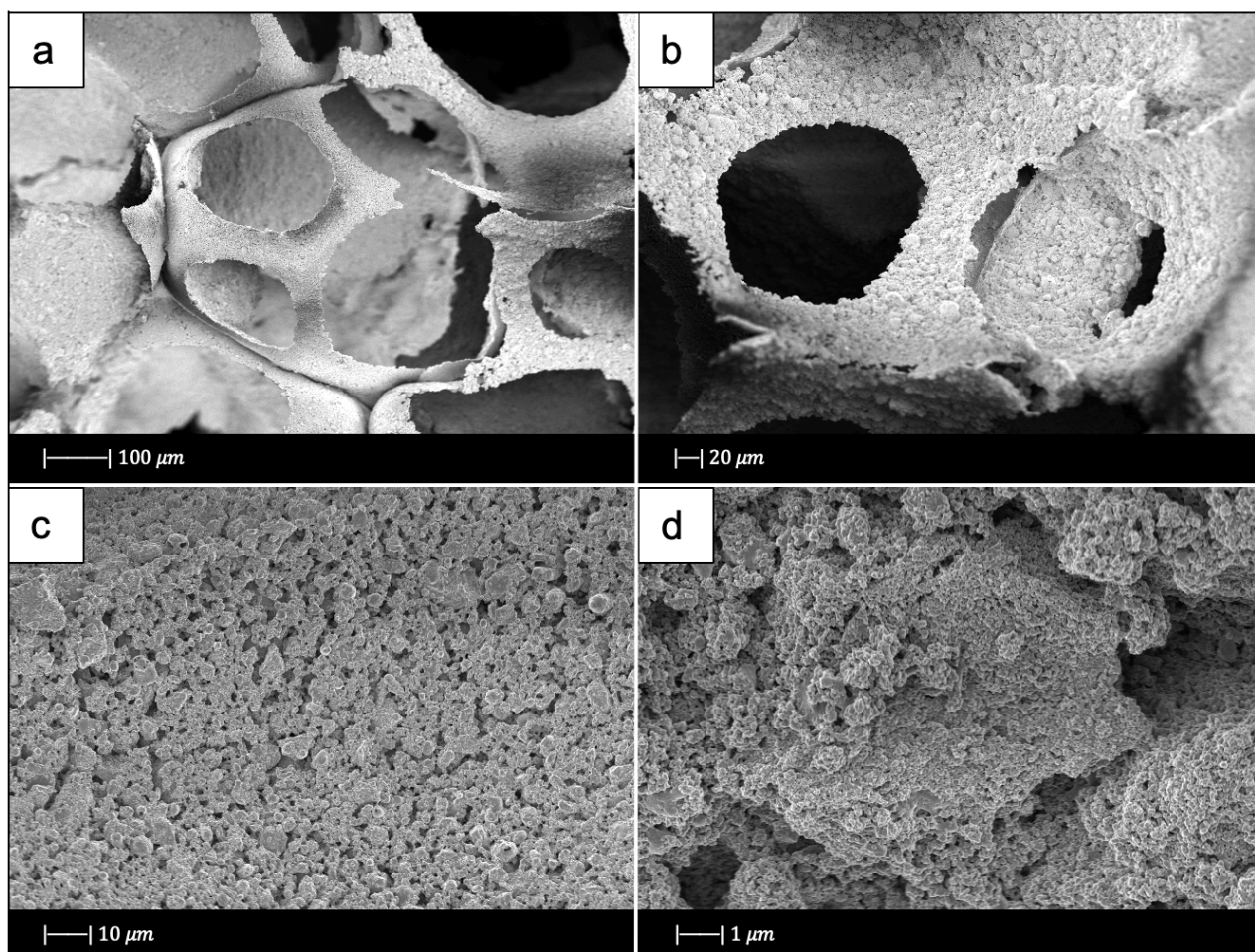


Figure 22: SEM micrographs of Ho-AD-950 scaffold (Test 4).

The SEM images at lower magnification (from 300X to 650X) (Figure 22a, b) shows that the scaffold replicated the porous structure of the PU template.

Highly interconnected macropores can be observed. Therefore, SEM micrographs revealed adequate characteristics of the 3D structure in terms of macro-porosity and pore interconnectivity, according to was deeply discussed in Chapter 2.

Interconnection between pores is a fundamental characteristic for cell seeding, tissue ingrowth and vascularization, as well as for nutrient delivery and waste removal [31], [32], [33], [34].

Furthermore, the images show approximately spherical pores with diameters of about 200 μm .

Pore diameter is an important parameter in TE applications, and the minimum value suitable to allow new bone formation, bone ingrowth, and capillaries formation is 100 μm [35].

In addition, it can be observed that the thickness of pores walls varies between 40 μm and 80 μm , and pore distribution is more or less uniform everywhere.

The pore structure is hierarchical because the mesoporosity inherent to the sol–gel process is maintained, as shown in images at higher magnification (from 2000X to 20000X) (Figure 22c, d). Textural properties are beneficial to cells as they mimic the hierarchical structure of natural tissues, and so simulate a physiological environment that promotes cell behaviour more than a surface without nanopores [36].

In Figure 22d, it is still possible to observe the presence of glass particles. This meant that a low sintering level of glass struts was achieved because of the too low sintering temperature.

Figure 23 shows morphological characteristics of Ho-I-1000 scaffold (Test 7).

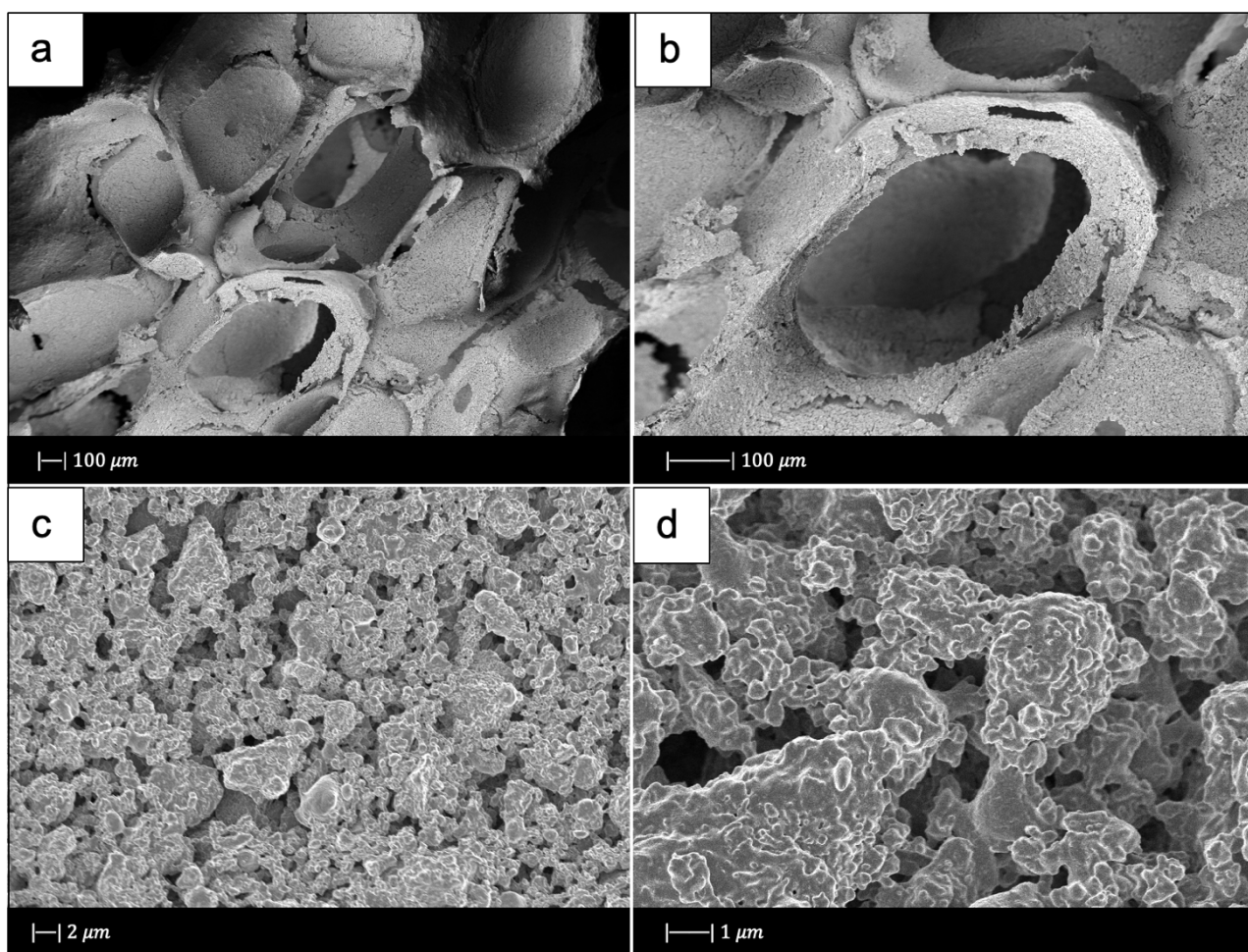


Figure 23: SEM micrographs of Ho-I-1000 scaffold (Test 7).

In this case too, the scaffold replicated the structure of the PU template, and it is characterized by a highly interconnected porosity, as shown in images at lower magnification (Figure 23a, b).

The pores are approximately spherical in shape and have the major axis in excess of 400 μm .

The thickness of pores walls ranges from 50 μm to 100 μm , and the distribution of pores is quite uniform.

SEM micrographs at higher magnification (Figure 23c, d) also revealed the presence of spherical pores with diameters less than 2 μm .

This bimodal pore size distribution is advantageous because it mimics the morphologic characteristics of trabecular bone. Pores below 50 μm facilitate the interaction between cells and materials, and osteointegration, while, on the other hand, pores of 100–500 μm enhance direct osteogenesis [35].

Figure 23d exhibits that the glass achieved a high sintering. Indeed, glass particles are not distinguishable, and the scaffold is characterized by a round and smooth surface.

Figure 24 shows SEM micrographs of Ho-AD-1050 scaffold (Test 8).

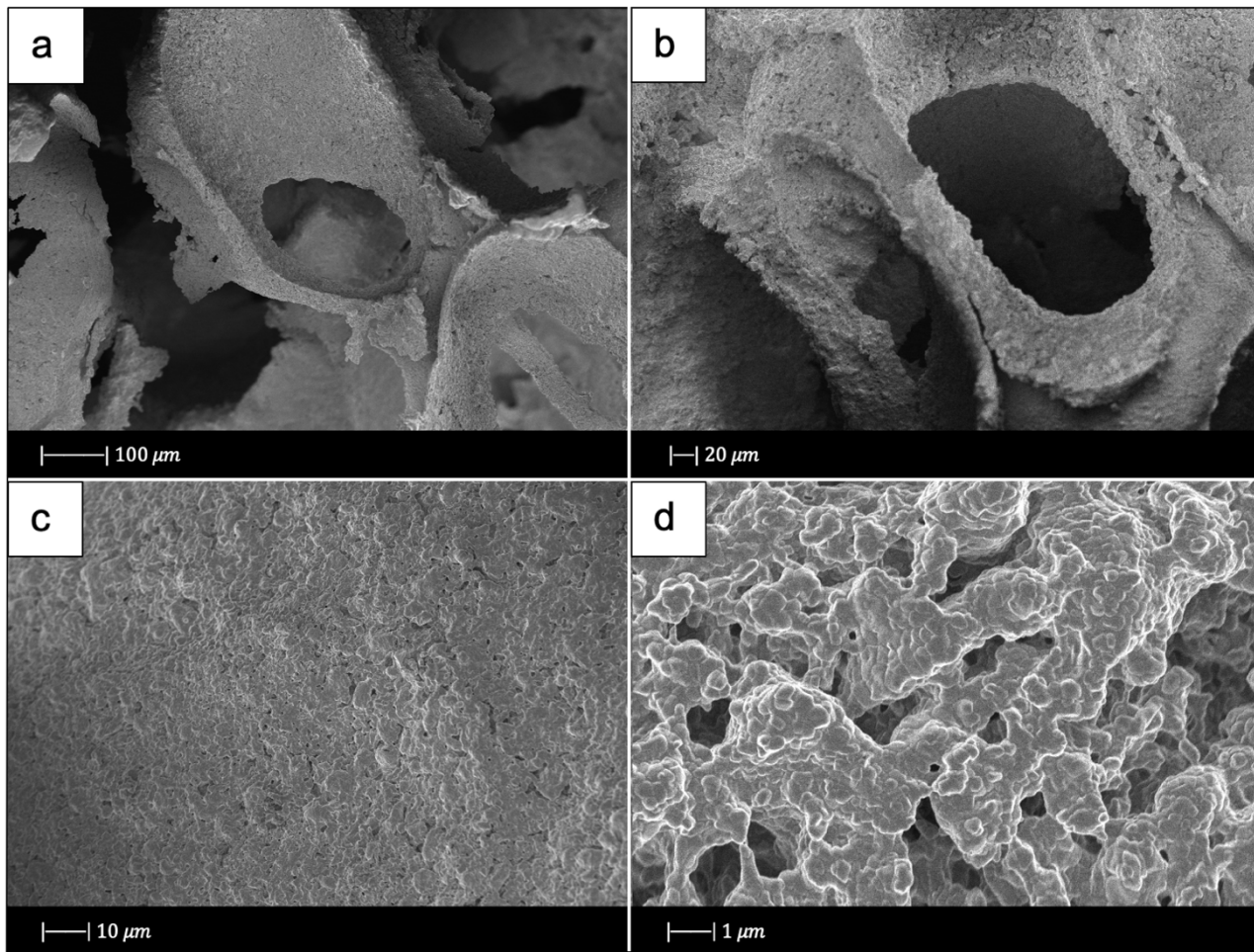


Figure 24: SEM micrographs of Ho-AD-1050 scaffold (Test 8).

As in the previous cases, the images at lower magnification (Figure 24a, b) show that the scaffold replicated the structure of the PU template and the macropores are well interconnected.

There are both ellipsoidal and spherical shaped pores, which have respectively the major axis and the diameter of about 300 μm . The distribution of the pores does not seem to be very uniform and the thickness of pores walls was found to be between 50 μm and 150 μm .

Images at higher magnification (Figure 24c, d) confirmed the presence of nanopores due to the sol-gel process. The diameter of these pores varies from 100 nm to 1 μm .

As in the previous test, the scaffold shows a dense microstructure, which is due to the high sintering achieved (Figure 24d).

The morphology of all the Ho-doped scaffolds shown in the SEM micrographs above resembles the trabecular structure of spongy bone, thus suggesting possible applications in biomimetic approaches for the regeneration of the tissue.

All the scaffolds replicated the structure of the starting templates and are characterized by a bimodal pore size distribution; they exhibit pores with diameters between 200 and 400 μm , and pores with diameter $< 2 \mu\text{m}$.

The size of the pores falls in the pore size range of bioactive glass scaffolds produced by foam replication method, which is 0-900 μm , as shown in Table 2, Chapter 3. Therefore, it is reasonable to believe that the presence of holmium did not significantly affect the pore size of the scaffold.

This consideration is in agreement with the result of the study by Wang et al. [37]–[39], who by loading the same glass with three different element obtained scaffolds with the same pore size, thus suggesting the non-influence of the doping element on the scaffold morphology [37]–[39].

The sintered samples at higher temperatures show a thicker pores walls because the high temperatures led to greater glass densification.

The sample thermally treated at 950 $^{\circ}\text{C}$ (Figure 22d) shows an unsatisfactory sintering. Indeed, the scaffold trabeculae are not sufficiently densified, and the glass particles can still be observed.

While the samples thermally treated respectively at 1000 $^{\circ}\text{C}$ and 1050 $^{\circ}\text{C}$ (Figures 23d and 24d) are mostly sintered. In fact, as the temperature increased, the viscosity decreased and the viscous flow sintering increased. The trabeculae of the scaffolds progressively densified, thus leading to the typical round and relatively smooth structure of the strut, on whose surface glass particles can no longer be distinguished.

Figure 25 shows a representative EDS spectrum of Ho-AD-1050 scaffold obtained by SEM ZEISS MERLIN.

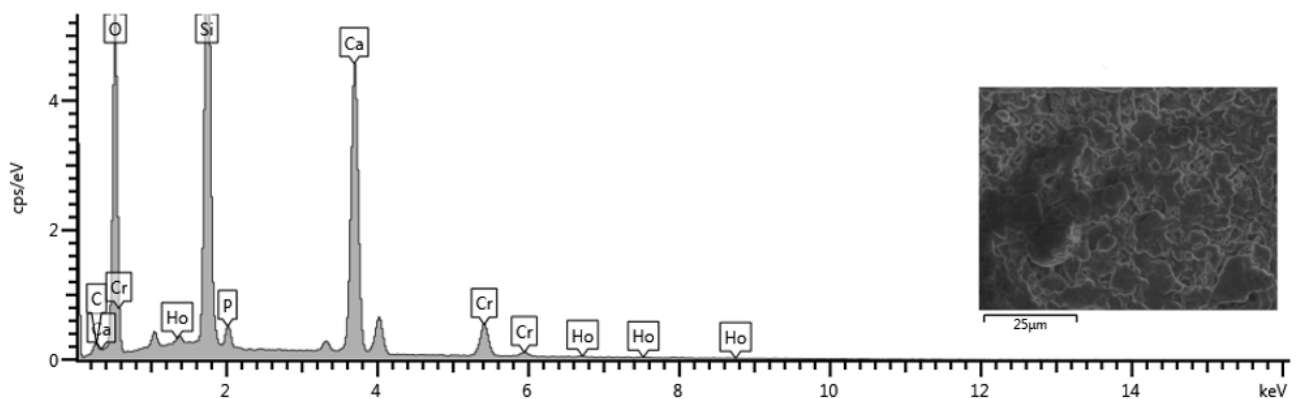


Figure 25: EDS analysis performed on Ho-AD-1050 scaffold using SEM ZEISS MERLIN.

Figure 25 shows which elements were identified in the scaffolds by EDS analysis, and the amount of each of them.

Each element corresponds to one or more peaks in the spectrum, and the higher the peak, the greater the amount of element detected.

The EDS analysis was carried out on different areas of the scaffold and depending on the area considered, a slightly different spectrum is obtained.

All the elements that were detected by the EDS analysis apart from chromium, correspond to the elements of the theoretical composition of the glass. Also in this case, the presence of chromium is due to the conductive Cr layer with which the sample was coated in order to achieve a higher resolution during SEM analysis.

In addition, it can be observed that no contaminants were detected.

Tables 11 and 12 have been obtained by processing the EDS data collected by SEM ZEISS MERLIN.

Table 11: Element composition (wt% and mol%) of Ho-AD-1050 scaffold obtained by processing EDS data derived from SEM ZEISS MERLIN.

Element	wt%	mol%
Si	36.48 ± 5.86	44.36 ± 6.73
Ca	52.1 ± 3.78	44.49 ± 4.11
P	9.82 ± 6.33	10.82 ± 6.93
Ho	1.6 ± 0.98	0.33 ± 0.20

Table 12: Oxide composition (wt% and mol%) of Ho-AD-1050 scaffold obtained by processing EDS data derived from SEM ZEISS MERLIN.

Oxide	wt%	mol%
SiO ₂	44.54 ± 7.22	46.88 ± 5.81
CaO	41.65 ± 3.4	47.12 ± 4.22
P ₂ O ₅	12.75 ± 8.11	5.82 ± 3.8
Ho ₂ O ₃	1.06 ± 0.66	0.18 ± 0.11

Table 13: Molar ratios of Ho-AD-1050 scaffold.

Device	Si : Ca Molar Ratio	Si : Ho Molar Ratio	SiO ₂ : CaO : P ₂ O ₅ : Ho ₂ O ₃ Molar Ratio
SEM ZEISS MERLIN	~ 1	134.42	65.93 : 65.87 : 31.13 : 1

The element composition (wt% and mol%) of Ho-AD-1050 scaffold obtained by processing EDS data derived from SEM ZEISS MERLIN (Table 11) differs from the ones of Ho-BG powders obtained by processing EDS data arising out of benchtop SEM and SEM ZEISS MERLIN (Table 5 and 6).

In particular, less Si and Ho and more Ca and P were found in the scaffolds than in the powders. This is due to the fact that the EDS analysis was carried out on different areas of the material, which had different morphology.

Although oxygen is present in the scaffold, it wasn't taken into account in the calculation of the element composition of the scaffold in order to compare the element composition of the Ho-AD-1050 scaffold with that of the Ho-BG powders. In fact, the element composition of the powders was

calculated not considering the oxygen because both the data derived from benchtop SEM and SEM ZEISS MERLIN were used and because the amount of oxygen measured depends strongly on the instrument used.

Even the oxide composition (wt% and mol%) of Ho-AD-1050 scaffold obtained by processing EDS data derived from SEM ZEISS MERLIN (Table 12) differs from the ones of Ho-BG powders obtained by processing EDS data derived from benchtop SEM and SEM ZEISS MERLIN (Table 7 and 8).

The main differences concern the amounts of P_2O_5 and of Ho_2O_3 . The amount of P_2O_5 detected by EDS analysis in the scaffold is more than doubles the one detected by EDS analysis in the powders. Whereas, the amount of Ho_2O_3 in the scaffold turns out to be less than half of that in the powders. In addition, in the scaffold there is a smaller amount of SiO_2 and a greater quantity of CaO compared to the powders.

The oxide composition of Ho-AD-1050 scaffold detected by EDS analysis differs from the NAA results and the theoretical composition of the glass.

In fact, apart from the quantity of P_2O_5 , which is approximately the same for all three compositions, a lower quantity of SiO_2 and Ho_2O_3 and a higher quantity of CaO was detected in the scaffold compared to the composition detected by the NAA and the theoretical composition of the glass.

The differences between the oxide composition of the scaffold, the oxide composition of the powders and the theoretical composition of the glass can be attributed to the different area that was considered in the analysis; furthermore, the geometry of samples also played a role (the higher the surface irregularity, the higher the error on compositional assessment).

The molar ratios Si : Ca, Si : Ho and SiO_2 : CaO : P_2O_5 : Ho_2O_3 of Ho-AD-1050 scaffold differ from the ones of Ho-BG powders.

Furthermore, the molar ratio SiO_2 : CaO : P_2O_5 : Ho_2O_3 of Ho-AD-1050 scaffold is different from that of the designed composition.

It was expected that the molar ratios of the scaffold would differ from both the molar ratios of the powders and the design composition, because both the element and oxide compositions obtained for the scaffold were different from those obtained for powders and from the design composition.

The density and porosity of Ho-AD-1050 scaffold were calculated according to data reported in Table 5, Chapter 4, and are respectively:

- $\rho = 0.36 \text{ g/cm}^3$
- % porosity = 86.15 vol%

The % porosity of the Ho-AD-1050 scaffold is comparable with the porosity of most bioactive glass scaffolds produced by foam replication method, as shown in Table 2, Chapter 3. In particular, approximately the same porosity value was obtained by Fu et al. [40] for 13-93 scaffold (85 vol%) and Bretcanu et al. [41] for 45S5 Bioglass[®] scaffold (85 vol%); both used a PU sponge as sacrificial template. A similar porosity value (89.3 vol%) was obtained by Xia et al. [42] for 58S scaffold using DBM as sacrificial template.

Therefore, it can be inferred that the presence of holmium oxide within the glass composition did not greatly affect the porosity of the scaffold produced by foam replica method.

The non-influence of the doping element on scaffold porosity was also proved by Bi et al. [43] who obtained 13-93 scaffolds and Cu-doped 13-93 scaffolds with the same porosity.

In addition, since the minimum porosity value necessary to allow tissue ingrowth is 50 vol% [44], [45] the porosity value of Ho-AD-1050 is very promising.

5.4 Ho-doped Bioactive Glass Scaffold Limitations

All Ho-doped bioactive glass scaffolds obtained by the eight different tests were characterized by high brittleness that made them unhandled.

First of all, it must be considered that a sol-gel glass was used for scaffolds fabrication, which conferred the scaffolds an intrinsic porosity, in addition to the typical porosity of the scaffolds produced by foam replica method, due to the template structure. This double porosity was certainly responsible for the high scaffolds' fragility.

In addition, a not suitable choice of process parameters may also have contributed to the brittleness of the scaffolds. In particular, two hypotheses were made:

1) The amount of material used for the production of the scaffold might be too little.

Each polyurethane template was dipped into the slurry three times; it is likely that this number of cycles was not sufficient to deposit an adequate layer of material on the surface of the PU sponge and, thus more impregnation cycles might be necessary.

However, too many impregnation cycles could result in the deposit of too much slurry in the sponge which in turn could cause pores closure, thus negatively affecting scaffolds properties in biological environment, especially those connected to mass transport phenomena and the capability to induce proper tissue ingrowth and vascularization after implantation.

In addition, the slurry composition included 15 wt% Ho-BG32 powders - 79 wt% double distilled water - 6 wt% PVA.

As already explained in Chapter 4, the idea of using the composition 30 wt% Ho-BG32 powders - 64 wt% double distilled water - 6 wt% PVA, commonly used for the production of BG-based scaffolds, was abandoned due to the low density typical of sol-gel glasses, as the glass occupied a very large volume compared to that occupied by water and PVA particles.

2) The heat treatment needs to be further optimised.

Most Ho-doped BG scaffolds were sintered at a temperature higher than T_2 , which allowed the scaffolds to complete the first stage of densification. Nevertheless, the scaffolds were very brittle, thus suggesting the need to use a higher sintering temperature. Indeed, an increase of sintering temperature causes a decrease of viscosity and an increase of the viscous flow sintering. Accordingly, the material densification increases, the porosity reduces and in turn the mechanical properties improve.

However, the sintering temperature could not be indiscriminately raised for several reason:

- The majority of the scaffolds obtained were sintered at temperatures above the crystallization onset, and as a result they were glass-ceramics. Thus, using a higher sintering temperature will also increase the formation of crystalline phases.

Generally, crystals nucleation, in addition to making the scaffolds stronger, reduces the bioactivity of the material because the crystalline phase is more stable than the amorphous one [46].

- The choice of a too high sintering temperature causes the viscosity of the glass to decrease considerably and the porous structure of the scaffold to deform easily under its own weight [15].

The fragility of the Ho-doped BG scaffolds might be also due to the use of a too high heating rate. According to what previously reported by Legeros et al. [47], samples which are undergone a

higher heating rate are usually very weak or locally collapsed. This phenomenon is attributed to the removal of the sponge before the formation of necking particles and to the insufficient binding strength of the particles. While the samples which are undergone a lower heating rate are usually much more resistant and the struts of the porous skeleton are characterized by dense and homogeneous grains [47].

Therefore, it might be necessary to lower the heating rate in order to obtain more resistant scaffolds.

5.5 Conclusions

This experimental activity aimed at the production of holmium-doped bioactive glass scaffolds by foam replica method. At Federal University of ABC, the Ho-BG was produced by sol-gel synthesis, and then analysed. At Politecnico di Torino Ho-BG and Ho-BG32 were characterized and the scaffolds were produced and subsequently analysed.

Thermal analysis performed on the dried-gel powders allowed to select $T=550\text{ }^{\circ}\text{C}$ as the optimal temperature for the calcination treatment.

NAA revealed that the oxide composition of Ho-BG was comparable with the theoretical one, and the FTIR found that the glass showed the typical functional groups of a silica-based glass.

Particle size analysis showed that Ho-BG particle diameters varied in a wide range, while, after being ground and sieved, the powders (Ho-BG32) had controlled dimensions.

DTA and HSM analyses allowed the determination of the characteristic temperatures for Ho-BG and Ho-BG32.

XRD spectra confirmed that both Ho-BG and Ho-BG32 were amorphous.

SEM analysis exhibited that Ho-BG powders had very different sizes and geometries because they had neither been ground nor sieved. The oxide composition and the molar ratios of Ho-BG obtained by processing EDS data were similar to NAA results and to the theoretical composition of the glass.

BET analysis identified both mesoporous and macroporous in the range 2.86-164 nm.

Ho-doped BG powders had larger pore size and smaller surface area compared to 58S BG. These differences were attributed to the presence of holmium oxide.

As regards the scaffolds fabrication, eight different tests were performed varying drying method and sintering temperature. The drying method did not visibly affect the scaffolds properties, while sintering temperature did it. Scaffolds that were sintered at a temperature $\leq T_x$ crumbled or were very fragile, while scaffolds that were heat-treated at temperatures $> T_2$ had a cubic shape and were more resistant than the previous ones. The use of a higher sintering temperature has resulted in greater densification and consequently better mechanical properties.

SEM analysis showed that the scaffolds were characterized by a hierarchical porosity with mesopores, deriving from the sol-gel synthesis, and well interconnected macropores, resulting from the replica of the template. Macropore diameters were in the pore diameter range of the scaffolds produced by foam replica method, thus suggesting that the presence of holmium oxide did not affect the pore size. Sintered samples at higher temperatures (Ho-I-1000, and Ho-AD-1050) had thicker pore walls and a smoother and rounder surface compared to Ho-AD-950 due to the high sintering temperatures which led to greater glass densification.

The oxide composition and molar ratios of Ho-AD-1050 obtained by processing EDS data differed from the Ho-BG composition due to the different area on which EDS analysis was performed.

Ho-AD-1050 scaffold had a porosity of 86.15 vol%, which was comparable with the characteristic-porosity values of scaffolds produced with foam replica method and fell within the range of spongy bone porosity, thus suggesting possible application in TE approaches.

References

- [1] P. Innocenzi, "Infrared spectroscopy of sol-gel derived silica-based films: a spectro-microstructure overview," *J. Non. Cryst. Solids*, vol. 316, pp. 309–319, 2003.
- [2] C. I. Merzbacher, "Structure of Na in aluminosilicate glasses - a far-infrared reflectance spectroscopic study," *Am. Mineral.*, vol. 73, pp. 1089–1094, 1988.
- [3] A. G. Kalampounias, "IR and Raman spectroscopic studies of sol-gel derived alkaline-earth silicate glasses," *Bull. Mater. Sci.*, vol. 34, no. 2, pp. 299–303, 2011.
- [4] J. Ding, "Effect of P2O5 addition on the structural and spectroscopic properties of sodium aluminosilicate glass," *Chinese Opt. Lett.*, vol. 10, no. 7, 2012.
- [5] M. Handke, M. Sitarz, M. Rokita, and E. Galuskin, "Vibrational spectra of phosphate-silicate biomaterials," *J. Mol. Struct.*, vol. 651–653, pp. 39–54, 2003.
- [6] S. Taherkhani and F. Moztaezadeh, "Influence of strontium on the structure and biological properties of sol-gel-derived mesoporous bioactive glass (MBG) powder," *J. Sol-Gel Sci. Technol.*, vol. 78, no. 3, pp. 539–549, 2016.
- [7] J. M. Pérez, S. R. Teixeira, J. M. Rincón, and M. Romero, "Understanding the crystallization mechanism of a wollastonite base glass using isoconversional, IKP methods and master plots," *J. Am. Ceram. Soc.*, 2012.
- [8] O. M. Goudouri *et al.*, "Study of the bioactive behavior of thermally treated modified 58S bioactive glass," *Key Eng. Mater.*, vol. 396–398, pp. 131–134, 2009.
- [9] A. Balamurugan *et al.*, "Synthesis and characterisation of sol gel derived bioactive glass for biomedical applications," *Mater. Lett.*, vol. 60, no. 29–30, pp. 3752–3757, 2006.
- [10] M. M. Erol *et al.*, "Copper-releasing, boron-containing bioactive glass-based scaffolds coated with alginate for bone tissue engineering," *Acta Biomater.*, vol. 8, no. 2, pp. 792–801, 2012.
- [11] R. Xin, Q. Zhang, and J. Gao, "Identification of the wollastonite phase in sintered 45S5 bioglass and its effect on in vitro bioactivity," *J. Non. Cryst. Solids*, vol. 356, no. 23–24, pp. 1180–1184, 2010.
- [12] V. Cannillo, F. Pierli, S. Sampath, and C. Siligardi, "Thermal and physical characterisation of apatite/wollastonite bioactive glass-ceramics," *J. Eur. Ceram. Soc.*, vol. 29, no. 4, pp. 611–619, 2009.
- [13] X. Liu, M. Morra, A. Carpi, and B. Li, "Bioactive calcium silicate ceramics and coatings," *Biomed. Pharmacother.*, vol. 62, no. 8, pp. 526–529, 2008.
- [14] V. K. Marghussian and A. Sheikh-Mehdi Mesgar, "Effects of composition on crystallization behaviour and mechanical properties of bioactive glass-ceramics in the MgO-CaO-SiO₂-P₂O₅ system," *Ceram. Int.*, vol. 26, no. 4, pp. 415–420, 2000.
- [15] F. Baino, M. Ferraris, O. Bretcanu, E. Verné, and C. Vitale-Brovarone, "Optimization of composition, structure and mechanical strength of bioactive 3-D glass-ceramic scaffolds for bone substitution," *J. Biomater. Appl.*, vol. 27, no. 7, pp. 872–890, 2011.
- [16] O. Bretcanu, X. Chatzistavrou, K. Paraskevopoulos, R. Conradt, I. Thompson, and A. R. Boccaccini, "Sintering and crystallisation of 45S5 Bioglass® powder," *J. Eur. Ceram. Soc.*, vol. 29, no. 16, pp. 3299–3306, 2009.
- [17] C. Lara, M. J. Pascual, and A. Durán, "Glass-forming ability, sinterability and thermal properties in the systems RO-BaO-SiO₂ (R = Mg, Zn)," *J. Non. Cryst. Solids*, vol. 348, pp. 149–155, 2004.

- [18] L. L. Hench, *Bioactive Ceramics: Theory and Clinical Applications*, vol. 7, no. July. Butterworth-Heinemann Ltd, 1994.
- [19] R. Bhaskar, J. Li, and L. Xu, "A comparative study of particle size dependency of IR and XRD methods for quartz analysis," *Am. Ind. Hyg. Assoc. J.*, vol. 55, no. 7, pp. 605–609, 1994.
- [20] W. Xia and J. Chang, "Preparation and characterization of nano-bioactive-glasses (NBG) by a quick alkali-mediated sol-gel method," *Mater. Lett.*, vol. 61, no. 14–15, pp. 3251–3253, 2007.
- [21] J. Chen, L. Zeng, X. Chen, T. Liao, and J. Zheng, "Preparation and characterization of bioactive glass tablets and evaluation of bioactivity and cytotoxicity in vitro," *Bioact. Mater.*, vol. 3, no. 3, pp. 315–321, 2018.
- [22] F. Baino, E. Fiume, M. Miola, and E. Vern, "Bioactive sol-gel glasses: Processing, properties, and applications," no. December 2017, pp. 841–860, 2018.
- [23] K. S. W. Sing, "Reporting Physisorption Data for Gas/Solid Systems with Special Reference to the Determination of Surface Area and Porosity," *Pure Appl. Chem.*, vol. 54, no. 11, pp. 2201–2218, 1982.
- [24] M. Thommes *et al.*, "Physisorption of gases, with special reference to the evaluation of surface area and pore size distribution (IUPAC Technical Report)," *Pure Appl. Chem.*, 2015.
- [25] G. Cao and Q. Zhang, *Annual review of nano research, Volume 3*. 2006.
- [26] P. Sepuvela, J. R. Jones, and L. L. Hench, "In vitro dissolution of melt-derived 45S5 and sol-gel derived 58S bioactive glasses," *Key Eng. Mater.*, 2011.
- [27] F. Baino, E. Fiume, M. Miola, F. Leone, B. Onida, and E. Verné, "Fe-doped bioactive glass-derived scaffolds produced by sol-gel foaming," *Mater. Lett.*, vol. 235, pp. 207–211, 2019.
- [28] C. Wu, Y. Zhou, C. Lin, J. Chang, and Y. Xiao, "Strontium-containing mesoporous bioactive glass scaffolds with improved osteogenic/cementogenic differentiation of periodontal ligament cells for periodontal tissue engineering," *Acta Biomater.*, vol. 8, no. 10, pp. 3805–3815, 2012.
- [29] C. Wu *et al.*, "Copper-containing mesoporous bioactive glass scaffolds with multifunctional properties of angiogenesis capacity, osteostimulation and antibacterial activity," *Biomaterials*, vol. 34, no. 2, pp. 422–433, 2013.
- [30] J. R. Jones, "Review of bioactive glass : From Hench to hybrids," *Acta Biomater.*, vol. 9, no. 1, pp. 4457–4486, 2013.
- [31] K. Rezwan, Q. Z. Chen, J. J. Blaker, and A. R. Boccaccini, "Biodegradable and bioactive porous polymer/inorganic composite scaffolds for bone tissue engineering," *Biomaterials*, vol. 27, no. 18, pp. 3413–3431, 2006.
- [32] S. Yang, K. F. Leong, Z. Du, and C. K. Chua, "The design of scaffolds for use in tissue engineering. Part I. Traditional factors," *Tissue Eng.*, vol. 7, no. 6, pp. 679–689, 2001.
- [33] V. Karageorgiou and D. Kaplan, "Porosity of 3D biomaterial scaffolds and osteogenesis," *Biomaterials*, vol. 26, no. 27, pp. 5474–5491, 2005.
- [34] Y. Tabata, "Biomaterial technology for tissue engineering applications," *J. R. Soc. Interface*, vol. 6, no. SUPPL. 3, 2009.
- [35] L. C. Gerhardt and A. R. Boccaccini, "Bioactive glass and glass-ceramic scaffolds for bone tissue engineering," *Materials (Basel)*, vol. 3, no. 7, pp. 3867–3910, 2010.
- [36] J. R. Jones, E. Gentleman, and J. Polak, "Bioactive Glass Scaffolds for Bone Regeneration," 2007.
- [37] H. Wang *et al.*, "Evaluation of borate bioactive glass scaffolds as a controlled delivery system for copper ions in stimulating osteogenesis and angiogenesis in bone healing," *J. Mater. Chem. B*, vol. 2, no. 48, pp. 8547–8557, 2014.

- [38] H. Wang *et al.*, “Biocompatibility and osteogenic capacity of borosilicate bioactive glass scaffolds loaded with Fe₃O₄ magnetic nanoparticles,” *J. Mater. Chem. B*, vol. 3, no. 21, pp. 4377–4387, 2015.
- [39] H. Wang *et al.*, “Three-dimensional zinc incorporated borosilicate bioactive glass scaffolds for rodent critical-sized calvarial defects repair and regeneration,” *Colloids Surfaces B Biointerfaces*, vol. 130, pp. 149–156, 2015.
- [40] Q. Fu, M. N. Rahaman, B. Sonny Bal, R. F. Brown, and D. E. Day, “Mechanical and in vitro performance of 13-93 bioactive glass scaffolds prepared by a polymer foam replication technique,” *Acta Biomater.*, vol. 4, no. 6, pp. 1854–1864, 2008.
- [41] O. Bretcanu, S. Misra, I. Roy, R. Chiara, F. Fiori, and A. R. Boccaccini, “In vitro biocompatibility of 45S5 Bioglass®-derived glass–ceramic scaffolds coated with poly(3-hydroxybutyrate),” *J. Tissue Eng. Regen. Med.*, vol. 3, pp. 139–148, 2009.
- [42] W. Xia and J. Chang, “Bioactive glass scaffold with similar structure and mechanical properties of cancellous bone,” *J. Biomed. Mater. Res. - Part B Appl. Biomater.*, vol. 95 B, no. 2, pp. 449–455, 2010.
- [43] L. Bi *et al.*, “Effect of bioactive borate glass microstructure on bone regeneration, angiogenesis, and hydroxyapatite conversion in a rat calvarial defect model,” *Acta Biomater.*, vol. 9, no. 8, pp. 8015–8026, 2013.
- [44] S. F. Hulbert, F. A. Young, R. S. Mathews, J. J. Klawitter, C. D. Talbert, and F. H. Stelling, “Potential of ceramic materials as permanently implantable skeletal prostheses,” *J. Biomed. Mater. Res.*, vol. 4, no. 3, pp. 433–456, 1970.
- [45] J. O. Hollinger, J. Brekke, E. Gruskin, and D. Lee, “Role of bone substitutes,” *Clin. Orthop. Relat. Res.*, no. 324, pp. 55–65, 1996.
- [46] F. Baino, G. Novajra, and C. Vitale-Brovarone, “Bioceramics and scaffolds: A winning combination for tissue engineering,” *Front. Bioeng. Biotechnol.*, vol. 3, no. December, pp. 1–17, 2015.
- [47] Y. S. Park *et al.*, “Feasibility of three-dimensional macroporous scaffold using calcium phosphate glass and polyurethane sponge,” *J. Mater. Sci.*, vol. 41, no. 13, pp. 4357–4364, 2006.

Chapter 6

Conclusions and Future Developments

6.1 Contextualization of the Research Activity

In Italy, the annual incidence of new primary malignant bone tumours is estimated to be around 500 cases. In almost all cases, treatment for these tumours involves a combination of surgery, chemotherapy and external beam radiation therapy.

In external radiotherapy, the radioactive source is placed outside the body. Therefore, high dose of β – and/or γ – rays cross the healthy tissue in order to hit the tumour. As a result, besides the cancer cells, also the healthy ones are damaged.

This problem could be overcome by brachytherapy, an innovative therapeutic approach based on the implantation of the radioactive source directly in the cancerous tissue. Due to the *in-situ* irradiation, brachytherapy uses a weaker, shorter range radiation that minimizes the damage to adjacent, healthy tissue. In turns, it allows to use a larger dose of radiation, increasing the probability of destroying the tumour.

To date brachytherapy was used for treatment of several types of cancer and for palliative treatment of bone metastases, but there are no cases where it was used for curative treatment of bone cancer.

Most commercialized radioactive seeds are composed of a titanium capsule containing iodine-125. The main limit of this device is that titanium is undegradable and a second surgery is necessary to remove it.

An alternative is represented by yttria-alumina-silica (YAS) glass microspheres which are clinically used for the treatment of hepatocellular carcinoma and metastatic liver cancer. However, YAS glasses have high chemical durability and remain in the body for years.

Biodegradable glasses offer a solution to this problem, since they are able to degrade once the radioisotope completed the therapeutic action. Several biodegradable glasses containing radioisotopes were developed by different research groups.

Among the various radioisotopes suitable for brachytherapy, holmium-166 (^{166}Ho) stands out for its properties.

In literature there are several examples of biodegradable glass containing holmium, while there are no cases of scaffolds produced with this biomaterial.

Therefore, the present experimental work introduces two innovations:

1. The application of brachytherapy for curative treatment of bone cancer.
2. Fabrication of holmium-doped bioactive glass scaffolds.

In fact, bioactive glass scaffold containing holmium developed in the present work represents a novel strategy for future treatment of bone tumours by brachytherapy.

Ho-doped bioactive glass scaffolds were produced by foam replica method, because it is a versatile, relatively easy and cost-effectiveness technique.

According to previous studies, this method produces highly porous and interconnected 3D bone-like scaffolds. Besides morphological properties, also mechanical properties and mass transport properties of scaffolds fabricated by foam replica are very similar to those of spongy bone, thus suggesting the suitability of these scaffolds in tissue engineering applications.

Ho-doped BG scaffold is designed to be used in combination with surgical therapy.

After surgical removal of the tumour, the bioactive glass scaffold containing holmium, which was made radioactive (^{166}Ho) by neutron activation in the last step of the scaffold fabrication process, is implanted in the tumour area.

^{166}Ho β -particles damage the DNA of the remaining tumour cells, causing their death.

Bioactive glass scaffold bonds to living bone and through the release of biologically active ions spur the adhesion of the osteogenic cells that induce the formation of new bone tissue.

Therefore, while the scaffold degrades, the new tissue forms.

The potential of this device consists in the double action of destroying the tumour and regenerating the bone tissue in the target area.

6.2 Main Experimental Results

This activity was carried out in collaboration with the Federal University of ABC (São Paulo, Brazil), where the Ho-doped bioactive glass with composition 55.19 SiO_2 - 31.3 CaO - 8.6 P_2O_5 - 5 Ho_2O_3 (wt%) was produced by sol-gel route starting from the undoped 58S composition (58 SiO_2 - 33 CaO - 9 P_2O_5 , wt%).

In Brazil, thermal characterization was performed on the Ho-dried-gel powders in order to study the behaviour of the gel under heat treatment and to select a suitable calcination treatment. Moreover, preliminary compositional and chemical assessments on the glass were performed by Neutron Activation Analysis (NAA) and Fourier Transform Infrared Spectroscopy (FT-IR), respectively. Differential Scanning Calorimetry (DSC) identified at 550 °C the decomposition of organic phase represented by nitrates used as oxide precursors during the synthesis process. This result was confirmed by DTG, which identified the maximum rate of mass loss in the dried gel at the same temperature. TGA showed that the dried gel lost 60% of its mass between room temperature and 1000 °C with an increase in the rate of mass loss around 550 °C. On the basis of these results, it was decided to calcine the dried-gel powders at 550 °C.

FT-IR found that the glass exhibited the typical functional groups of a silica-based glass, and NAA revealed a good correspondence between the theoretical and the experimental composition.

Ho-BG powders were then sent to Politecnico di Torino (Turin, Italy) where the powders characterization was completed, and the scaffolds were fabricated.

First of all, particle size analysis was performed, which revealed the heterogeneity of the glass particles size. Indeed, their diameters ranged from 0.37 μm to 2000 μm .

In order to obtain particles of homogeneous size, needed for the optimization of scaffold manufacturing process, the glass powders were grinded and sieved using a sieve with mesh of 32 μm in diameter (Ho-BG32).

A subsequent particle size analysis revealed that the sifted particles had diameter between 1 and 52 μm . Diameters larger than 32 μm were attributed to particles aggregates. Indeed, Van der Waals interaction between particles, which is amplified in sol-gel materials, and the thermodynamics of minimizing the total surface energy of the system led the particles to agglomerate.

Thermal analyses were performed both on Ho-BG and Ho-BG32 powders.

Differential Thermal Analysis (DTA) allowed the determination of the characteristic temperatures of the two systems analysed: $T_g=690$ °C, $T_x=860$ °C, $T_c=900$ °C and $T_g=625$ °C, $T_x=850$ °C, $T_c=890$ °C for Ho-BG and Ho-BG32 powders, respectively.

The crystallization peaks detected at 900 °C and 890 °C for the Ho-BG and the Ho-BG32 systems, respectively, were attributed to the nucleation of wollastonite crystals. This agrees with the oxide

composition of the glass and the previous literature studies, according to which the crystallization process of wollastonite is characterized by a devitrification experimental range defined between 850 °C and 950 °C.

It was found that wollastonite has good bioactivity, and therefore it does not deteriorate the bioactivity of the glass-ceramic [1]. In addition, it is characterized by a fibrous morphology which enhances the mechanical properties of the material [2].

HSM curves were characterized by double-stage shrinkage, which means that the height of the sample did not vary until T_1 was reached, then densification occurred until T_2 , followed by a plateau. Afterwards, a second densification stage began at T_3 and ended with the achievement of the maximum sample shrinkage at T_4 . Finally, the sample started to soften.

$T_1=700$ °C, $T_2=900$ °C, $T_3=1130$ °C, $T_4=1250$ °C were identified for the Ho-BG powders, and $T_1=700$ °C, $T_2=890$ °C, $T_3=1130$ °C, $T_4=1280$ °C and $T^*=1400$ °C were recognised for Ho-BG32 powders.

For both samples, T_1 was selected shortly after T_g , and T_2 coincided with T_c . Thus, T_x was detected between T_1 and T_2 . This means that the sample began to crystallize during the first densification phase and the maximum rate of crystallization was achieved at the end of the first shrinkage. As a result, the material was already a glass ceramic before the beginning of the second densification phase.

This result was confirmed by the sinterability (S_c) value calculated, which indicated that both the sample only partially densified before crystallization began.

The height of the Ho-BG sample decreased by 15% between T_1 and T_2 , and 8% between T_3 and T_4 , while the height of Ho-BG32 sample reduced by 20% between T_1 and T_2 , and 15% between T_3 and T_4 ; in both cases, the samples retained the original geometry.

The height of the Ho-BG sample decreased overall by 23% and the height of Ho-BG32 by 35%. Ho-BG32 sample shrunk more than Ho-BG sample due to the smaller size of its particles. Indeed, the smaller the particle size, the greater the contact points between the particles, and as a result, sintering is more efficient.

XRD analysis, which was performed both on Ho-BG powders and Ho-BG32 powders, revealed no significant differences between the samples analysed, confirming the amorphous nature of both.

Morphological and compositional analyses were performed only on Ho-BG powders because neither the particle morphology nor elemental composition is affected by particle size.

Both SEM ZEISS MERLIN and JCM-6000Plus Versatile Benchtop SEM were used.

SEM images revealed a remarkable heterogeneity in the distribution of particles size and in the geometry of the powders; this result was expected since the analyses powders had neither been grounded nor sieved.

Smaller particles deposited on the surface of the bigger ones, by creating a sort of coating.

The particle surface was characterized by a nanoporous texture, which derived from the sol-gel synthesis of the glass.

Moreover, no crystalline formations were observed, in agreement with XRD results.

The element and oxide compositions (wt% and mol%) of Ho-BG obtained by processing EDS data derived by JCM-6000Plus Versatile Benchtop SEM were about the same as those obtained by processing EDS data derived by SEM ZEISS MERLIN. As a results, the molar ratios Si : Ca, Si : Ho and SiO₂ : CaO : P₂O₅ : Ho₂O₃ obtained by using the values deriving from two SEM devices were very similar to each other. The fact that the element and oxide compositions obtained by processing the data acquired by the two different instruments were the same, further confirmed that the ones obtained were the real compositions of the glass.

In addition, the oxide composition of the Ho-BG resulting from the processing of EDS data was comparable to NAA results and to the theoretical composition of the glass. Accordingly, the molar ratio $\text{SiO}_2 : \text{CaO} : \text{P}_2\text{O}_5 : \text{Ho}_2\text{O}_3$ obtained from the EDS analyses was in agreement with the molar ratio $\text{SiO}_2 : \text{CaO} : \text{P}_2\text{O}_5 : \text{Ho}_2\text{O}_3$ of the designed composition.

The intrinsic nanoporosity of the powders deriving from the sol-gel process was investigated by BET analysis.

The nitrogen sorption isotherms of Ho-BG and Ho-BG32 were both classified as isotherm of type IV with a H3 hysteresis; they suggested the mesoporous nature of the material.

Ho-BG and Ho-BG32 powders showed both mesoporous (2-50 nm) and macroporous (>50 nm) features as pores size ranged between 2.86 and 160 nm and 2.86 and 164 nm, respectively. The pore size of the holmium-doped BG was not affected by the particle size but differed from that of the 58S glass which varied between 6 and 9 nm.

The surface area of Ho-BG powders and Ho-BG32 powders were found to be respectively 53.52 m²/g and 57.19 m²/g. Indeed, it is known that as the particle size decreases, the surface area increases. Both the materials exhibited higher surface area than melt-derived glasses (< 0.25 m²/g [3]), which is beneficial to the interactions between the material and the biological environment. However, Ho-BG and Ho-BG32 surface areas were inferior to the surface area values commonly assessed for silicate sol-gel BGs (> 100 m²/g [4]), and in particular to 58S BG surface area (126.5 - 164.7 m²/g [3]).

Ho-BG and Ho-BG32 powders pore volume were 0.442 cm³/g and 0.427 cm³/g, respectively. These values were comparable with the one of 58S BG powders, which was 0.213-0.498 cm³/g.

The larger pore size and smaller surface area of Ho-doped BG powders compared to 58S BG powders were attributed to the presence of holmium oxide in the glass composition.

As regards the production of Ho-doped BG-based scaffolds by foam replication method, cubic polyurethane sponges were used as sacrificial templates. The slurry composition by weight included 15% Ho-BG32 - 79% H₂O - 6% PVA.

In order to optimize scaffold manufacturing, eight different tests were carried out, varying, one at a time, the drying method and the sintering temperature.

Since the air-dried samples and the samples dried inside the incubator did not show significant differences, it was reasonable to assume that drying conditions did not play a crucial role in the definition of scaffolds properties.

In order to produce a completely densified and purely glassy scaffold, sintering temperature should be chosen in the range between the maximum densification (T_4) and the onset of crystallization (T_x). For Ho-BG32, $T_4 > T_x$. Therefore, it was not possible to select a sintering temperature that allowed to obtain complete densification of the glass before crystallization began. This finding agreed with the sinterability result.

The first test (Test 1, Table 4, Chapter 4) was aimed at producing a purely glassy scaffold. So, it was decided to sinter the glass at $T=800$ °C for 3h. The resulting scaffold (Ho-I-800) was so brittle that it crumbled. The failure of this test was attributed to the use of a too low sintering temperature which did not allow to achieve a sufficient densification of the glass particles.

The second and the third tests (Test 2 and Test 3, Table 4, Chapter 4) were aimed at producing more resistant scaffolds while preserving the amorphous nature of glass. Therefore $T_x=850$ °C for 3h was used as sintering condition. Ho-AD-850 scaffold (Test 2) lost the cubic shape of the PU template and assumed an irregular shape. Furthermore, it was very brittle. Ho-I-850 scaffold (Test 3) crumbled. As in the previous case, the fragility of the scaffolds was attributed to the low densification of the glass

due to the too low sintering temperature. Indeed, according to HSM curve of Ho-BG32 powders, at $T=800\text{ }^{\circ}\text{C}$ and at $T=850\text{ }^{\circ}\text{C}$, the first stage of densification was not completed.

Since it proved impossible to produce purely glassy and well densified scaffolds at the same time, for the subsequent tests a sintering temperature above T_x was chosen. In particular, the following sintering conditions were used: $T=950\text{ }^{\circ}\text{C}$ for 3h, $T=1000\text{ }^{\circ}\text{C}$ for 3h and $T=1050\text{ }^{\circ}\text{C}$ for 3h.

The resulting scaffolds (Ho-AD-950, Ho-I-950, Ho-AD-1000, Ho-I-1000, Ho-AD-1050) exhibited the cubic shape of the PU template without distortion despite the considerable volume shrinkage of the structure. This is a very important achievement in case complex bone substitutes are needed. These scaffolds were more resistant than those obtained in previous tests. The higher strength was attributed to the more extensive densification, which was due to the higher sintering temperature. Indeed, according to HSM curve of Ho-BG32 powders, at these temperatures, the second stage of densification was completed.

Anyway, these scaffolds were not yet strong enough to be used in bone tissue engineering applications. Therefore, the manufacturing process must be optimized.

The scaffolds were analysed only from a morphological and composition point of view by SEM and EDS analysis through SEM ZEISS MERLIN.

SEM analysis was performed on Ho-AD-950, Ho-I-1000, and Ho-AD-1050 scaffolds.

It showed that the scaffolds replicated the porous structure of the PU template. Their morphology being similar to the trabecular one of spongy bone made them suitable for BTE applications.

All the scaffolds exhibited hierarchical porosity, with mesopores, resulting from the sol-gel synthesis, and macropores, deriving from the polyurethane template.

The scaffolds had macropores both with diameter $< 2\text{ }\mu\text{m}$ and with diameters between 200 and 400 μm . Larger pore size was within the pore size range of the scaffolds fabricated by foam replica method (100-800 μm) as shown in Table 2, Chapter 3. Therefore, it is reasonable to think that the presence of holmium oxide did not affect the pore size of the scaffold.

This bimodal pore size distribution is beneficial since pores below 50 μm facilitate the interaction between cells and materials and osteointegration, while pores of 100–500 μm enhance direct osteogenesis.

Ho-doped BG scaffolds were characterized by a highly interconnected porous architecture. Interconnection between pores is a fundamental characteristic for cell seeding, tissue ingrowth and vascularization, as well as for nutrient delivery and waste removal.

The thickness of pores walls ranged from 40 μm to 150 μm , and the sintered samples at higher temperatures exhibited a thicker pores walls because the high temperatures led to greater glass densification.

In the Ho-AD-950 scaffold, glass particles could still be noticed because $T=950\text{ }^{\circ}\text{C}$ did not allow the trabeculae of the scaffold to densify sufficiently. While in the Ho-I-1000 and Ho-AD-1050 scaffolds, glass particles were no longer visible because the higher temperature caused the densification of the scaffold trabeculae forming to a round and smooth surface.

EDS analysis was carried out only on Ho-AD-1050 scaffold.

Both the element and oxide compositions of the scaffold detected by EDS analysis differed from the results of EDS analysis performed on the Ho-BG powders.

In addition, the oxide composition of Ho-AD-1050 obtained by EDS analysis differed from the NAA outcome as well as from the theoretical composition of the glass.

As a result, the molar ratios Si : Ca, Si : Ho and SiO₂ : CaO : P₂O₅ : Ho₂O₃ of Ho-AD-1050 scaffold differed from the ones of Ho-BG powders, and the molar ratio SiO₂ : CaO : P₂O₅ : Ho₂O₃ of Ho-AD-1050 scaffold was different from that of the designed composition.

The element and oxide compositions of Ho-AD-1050 resulting from the EDS analysis differed from the results of previous compositional analyses and from the theoretical composition of the glass because the EDS analyses were carried out on always different areas of the sample, which had different morphology.

The density and porosity of Ho-AD-1050 scaffold were calculated and were respectively 0.36 g/cm³ and 86.15 vol%.

The porosity of the Ho-AD-1050 scaffold was in the range of porosity of most bioactive glass scaffolds produced by foam replication method, as shown in Table 2, Chapter 3. This suggested that the presence of holmium oxide within the glass composition did not affect the porosity of the scaffold. Moreover, considering that 50 vol% is the minimum porosity value necessary to allow tissue ingrowth [5], [6] the porosity value of Ho-AD-1050 was very promising.

6.3 Improvements and Future Developments

Holmium doped bioactive glass scaffolds were evaluated only from a morphological and compositional point of view. However, in order to evaluate their actual suitability for bone tissue engineering and tumour therapy, further analyses are recommended:

- 1) Mechanical testing to evaluate the suitability of the scaffolds for bone tissue engineering applications. In particular, compressive tests are mandatory [7].

Ho-doped BG scaffolds are expected to have poor mechanical properties because they cannot be handled because of their high brittleness. This could be due to either the intrinsic porosity of the glass and/or the choice of manufacturing process parameters, such as an insufficient amount of glass in the slurry composition, the number of impregnations performed and/or the use of a not suitable sintering conditions.

Therefore, in order to produce mechanically more performing scaffolds, it might be possible to increase the amount of glass in the slurry, increase the number of impregnation cycles of sponge in the slurry, and/or use different sintering conditions, as explained in Chapter 5.

- 2) *In vitro* bioactivity test to predict the *in vivo* bioactivity of Ho-doped BG scaffold [7].

Simulated Body Fluid (SBF) is a solution which has almost equal ion concentrations to those of human blood plasma [8].

The assessment of bioactivity in SBF is commonly performed using the standard procedure described by Kokubo et al. [9], which aims at investigating HA formation on the scaffold surface as a result of the ionic exchange between the materials and the surrounding environment. Indeed, it is known that HA formation on sample surfaces upon immersion in SBF is an indication of the *in vivo* bone bonding ability of a material [10], [11].

One limitation of this technique to evaluate the bioactivity lies in the fact that there are some materials that directly bond to living bone without the formation of HA layer. While one of the main advantages of this method is that it allows to predict the bioactivity of a material before testing on animals. This makes it possible to reduce the number of animals used and the duration of animal experiments [12].

In order to assess bioactivity of Ho-doped BG scaffolds, first of all the SBF is prepared. SBF can be prepared according to the protocol proposed by Kokubo and Takadama [12].

Subsequently, the samples are soaked for different times frames in SBF maintained at 37 °C. Ion-exchange phenomena induce pH variations, which are daily monitored (SBF reference value: pH = 7.40) [12].

The protocol provides that the samples are extracted from the SBF every 48 h, washed with distilled water and soaked in preheated fresh SBF, in order to simulate fluid circulation in physiological conditions [12].

Once the experiment is done, the sample is washed with distilled water, dried at room temperature and evaluated by SEM and EDS analyses [12].

If SEM and EDS analyses find that a layer of HA formed on the surface of the scaffold, it can be stated that the Ho-doped BG scaffold is a bioactive material.

On the contrary, if a layer of HA did not form on the surface of the scaffold, it can be inferred that the material is not bioactive.

The causes of the absence of bioactivity may be different:

- Since in previous studies, 58S undoped glass scaffolds showed rapid formation of HA upon immersion in SBF, it is reasonable to attribute the absence of bioactivity to the presence or too high content of holmium oxide.

In this case, the reactivity of the scaffold can be increased by decreasing holmium oxide content. However, Ho₂O₃ content cannot be reduced indiscriminately because by reducing it also the number of ¹⁶⁶Ho radionuclides and thus the therapeutic effect reduces.

Another way to overcome this problem consists in decreasing the silica content. In fact, decreasing the silica content, the rate of dissolution of glass ions from the surface increases causing an increase in bioactivity.

- Heat treatment may have caused the nucleation of several crystalline phases that have deteriorated the bioactivity of the material. It is necessary to decrease the sintering temperature and/or increase the heating rate to obtain a bioactive scaffold.

However, the sintering temperature cannot be decreased because the Ho-doped BG scaffolds produced are very fragile due to the low densification of the glass. By further decreasing the sintering temperature, the viscosity would increase, and the viscous flow would decrease. As a result, the densification would decrease further and thus the mechanical properties.

An increase in the heating rate would result in an increase in T_c [13]. This means that the glass would start to devitrify at higher temperatures. Therefore, fewer crystalline phases would form in the material and consequently the material would be more reactive.

- 3) Ion release test to determine concentrations of the ions released by Ho-doped BG scaffold after the immersion in SBF. In particular, this test is important to assess the holmium release from the scaffold.

This assay can be performed by using inductively coupled plasma-mass spectrometry (ICP-MS). Ideally, holmium should remain inside the glassy matrix for all the time necessary to carry out the therapeutic action i.e. until all the ¹⁶⁶Ho radionuclides decay. Therefore, the amount of Ho ions released in SBF during this time should be zero.

If Ho ions are released in SBF during this time two problems arise: the first is that the amount of ¹⁶⁶Ho radionuclides inside the scaffold decreases, as well as the number of β-particles emitted by

^{166}Ho , which damage the DNA of tumour cells causing their death. As a result, the therapeutic efficacy in the tumour area is lowered.

The second problem is that the β -particles emitted by ^{166}Ho radionuclides that were released from the scaffold could damage healthy cells elsewhere.

Therefore, in these cases, it is necessary to increase the chemical resistance of the glass matrix to body fluids. In particular, the dissolution rate of glass ions can be reduced by increasing the amount of silica in the glass composition.

- 4) Cytotoxicity test to evaluate the living cells' reaction to the Ho-doped BG scaffold in a cell culture assay. In particular, the effect of holmium on cell viability and on the ability for cellular growth are investigated [14].

For example, L-929 mouse fibroblast cells can be used. These cells may easily be tested utilizing the Ho-doped BG scaffold's extracts from semiphysiological media [14].

More in detail, the test involves exposing the extract fluid to L-929 mouse fibroblast cells. The cells are allowed to grow in the extract fluid for a certain period of time before they are evaluated by qualitative or quantitative methods [15].

Qualitative evaluation consists in microscopically examined the cells and assigning a cytotoxic grade (0-4). The cytotoxicity grade is assigned based on morphology of the cells and on the lysis estimated percentage (death). If the cytotoxic level is ≤ 2 ($\leq 50\%$ lysis), Ho-doped BG scaffolds pass the test [15].

Quantitative evaluation involves using a tetrazolium dye in order to assess the metabolic activity of cells. The results are reported as percent viability (% living cells). If the percent viability is $\geq 70\%$, ho-doped bioactive glass scaffolds pass the test [15].

If the Ho-doped BG scaffolds will not pass the test, and therefore are not cytocompatible, it is necessary to identify the reason and assess the toxicological risks.

The possible cytotoxicity of the scaffolds could be attributed to the presence of holmium oxide. In that case, by reducing the amount of holmium oxide in the glass composition, the material can be made cytocompatible.

However, the percentage of Ho_2O_3 in the glass composition can only be reduced within a certain limit because by reducing the holmium oxide content in the glass, the number of ^{166}Ho radionuclides and thus the therapeutic effect is also reduced.

- 5) Test to evaluate the effectiveness of the anti-cancer action of the Ho-doped BG scaffolds.

The selectivity of Ho-doped BG scaffolds in killing cancer cells rather than healthy cells can be assessed by using two different kinds of cells: healthy osteoblasts and murine osteosarcoma cells. The test consists of using two Ho-doped BG scaffolds and of making holmium radioactive (^{166}Ho) by neutron activation. Then, one scaffold is seeded with healthy osteoblasts and the other is seeded with murine osteosarcoma and the scaffolds are incubated to allow the cells to attach.

Once ^{166}Ho β -particles terminate the therapeutic action, the vitality of the cells is tested.

A qualitative evaluation can be carried out by labelling the cells with a live-dead cell staining kit and by inspecting under a fluorescence microscope [16].

A quantitative evaluation consists in using a tetrazolium dye in order to assess the metabolic activity of cells [17].

Ideally, the test should reveal the presence of dead murine osteosarcoma cells and live osteoblasts. Indeed, the β -particles emitted by the ^{166}Ho should cause only murine osteosarcoma cells to die,

because healthy osteoblasts should be able to repair the damage that the β -particles have done to their DNA. This would demonstrate the selectivity of the Ho-doped BG scaffolds in killing cancer cells.

If the test shows the presence of dead osteoblasts, it is likely that the radiation dose is too high. An excessive amount of ^{166}Ho may have caused irreparable damage to the DNA of the osteoblasts, resulting in death. In such a case, the holmium content should be reduced. However, as already mentioned above, the amount of holmium can only be reduced within a certain limit.

While, if the test exhibits that cancer cells are still alive it is probably that the amount of holmium is not sufficient to ensure an anticancer effect. In this case, it is necessary to increase the amount of Ho_2O_3 in the glass. However, this content cannot be increased indiscriminately, as too high concentration could cause toxicity.

6) Cell proliferation test to evaluate the bone regeneration ability of the Ho-doped BG scaffold after the cancer treatment.

For example, the ability of the Ho-doped BG scaffold to support the attachment and growth of osteoblastic cells may be evaluated. To make this experiment, the mouse MC3T3-E1 cell line may be chosen, since they were widely utilized in *in vitro* studies of biomaterials for bone repair and tissue engineering [18], [19], [20].

This test involves seeding the Ho-doped scaffold with the MC3T3-E1 cell and incubating the scaffold for a few hours to allow the cells to attach.

After established cell culture time intervals, the Ho-doped cell scaffolds should be observed at SEM.

If after 6 days of culture almost the entire scaffold surface is covered with cells and the cells begin to aggregate, the scaffold has an excellent ability to support the attachment and subsequent proliferation of MC3T3-E1 preosteoblastic cells. Therefore, it means that the Ho-doped BG scaffold is able to regenerate bone in the area where the tumor was destroyed.

On the other hand, if there are no cells on the surface of the scaffold, it means that the scaffold has no regenerative properties. The cause could be the presence of Ho_2O_3 . In which case it is necessary to reduce its quantity in the composition of the glass.

7) *In vivo* studies for the evaluation of Ho-doped BG scaffold performance in the complex physiological environment [7].

It is reasonable to choose a rabbit femoral head as the implant site of the Ho-doped BG scaffold because the femur is one of the anatomical districts most affected by bone tumours [21]. Moreover, the rabbit model is usually used to make an initial assessment of the implant materials before to test them in a larger animal model [22], [23].

In order to study the anticancer effect of Ho-doped BG scaffold, an osteosarcoma model by hypodermic inoculation of MG63 cells is created in the rabbit femoral head.

After removing a tumour fragment of scaffold equivalent volume, holmium within the scaffold is made radioactive by neutron activation and, Ho-doped BG scaffold is implanted into the tumour. After an established time, the rabbit is sacrificed, and the tissue samples are collected.

According to what previously reported by Rong et al. [16] the TUNEL staining and HE staining can be to evaluate under optical microscopy the anticancer activity of the scaffold.

In particular, TUNEL staining detects the DNA fragments which form in the last phase of apoptosis [24]. Therefore, it allows for visualization and quantification of apoptotic cells [25].

While, HE staining is a dichromic colouring based on the different pH value of the various tissues [26]. It allows observing tumour cells and necrosis.

If TUNEL staining results reveal a high number of apoptotic cells in the tumour area and HE staining results show tumour tissue necrosis, it can be inferred that Ho-doped BG is an effective material for tumour treatment.

If, on the other hand, TUNEL staining results show a low number of apoptotic cells and HE staining result do not detect the presence of necrosis, it means that Ho-doped BG has not an effective anti-tumour effect.

The reason may be that the holmium concentration is too low to guarantee the therapeutic effect. In this case, it is necessary to increase the concentration of Ho_2O_3 in the glass.

In accordance with the study of Rong et al. [16], the bone repair ability of the scaffold may be assessed by implanting the scaffold in a femoral condyle defect model of a rabbit.

The rabbit is sacrificed after an established time, and the femur is retrieved and scanned by x-rays and μ -CT.

If X-rays show that the femoral condyles have healed and the fracture lines have disappeared, and μ -CT reconstructions show that the region with bone defects is filled with new bone, Ho-doped BG scaffold can be considered a good bone defect filling material.

On the other hand, if it can be observed from the x-rays that the fracture line is still clearly visible and from the μ -CT that the bone defects remained significant, it means that the Ho-doped BG scaffolds have no bone repair skills.

References

- [1] X. Liu, M. Morra, A. Carpi, and B. Li, "Bioactive calcium silicate ceramics and coatings," *Biomed. Pharmacother.*, vol. 62, no. 8, pp. 526–529, 2008.
- [2] V. K. Marghussian and A. Sheikh-Mehdi Mesgar, "Effects of composition on crystallization behaviour and mechanical properties of bioactive glass-ceramics in the MgO-CaO-SiO₂-P₂O₅ system," *Ceram. Int.*, vol. 26, no. 4, pp. 415–420, 2000.
- [3] P. Sepuvela, J. R. Jones, and L. L. Hench, "In vitro dissolution of melt-derived 45S5 and sol-gel derived 58S bioactive glasses," *Key Eng. Mater.*, 2011.
- [4] F. Baino, E. Fiume, M. Miola, and E. Vern, "Bioactive sol-gel glasses: Processing, properties, and applications," no. December 2017, pp. 841–860, 2018.
- [5] S. F. Hulbert, F. A. Young, R. S. Mathews, J. J. Klawitter, C. D. Talbert, and F. H. Stelling, "Potential of ceramic materials as permanently implantable skeletal prostheses," *J. Biomed. Mater. Res.*, vol. 4, no. 3, pp. 433–456, 1970.
- [6] J. O. Hollinger, J. Brekke, E. Gruskin, and D. Lee, "Role of bone substitutes," *Clin. Orthop. Relat. Res.*, no. 324, pp. 55–65, 1996.
- [7] F. Baino and C. Vitale-Brovarone, "Three-dimensional glass-derived scaffolds for bone tissue engineering: Current trends and forecasts for the future," *J. Biomed. Mater. Res. - Part A*, vol. 97 A, pp. 514–535, 2011.
- [8] C. Ohtsuki, T. Kokubo, and T. Yamamuro, "Mechanism of apatite formation on CaO-SiO₂-P₂O₅ glasses in a simulated body fluid," *J. Non. Cryst. Solids*, vol. 143, pp. 84–92, 1992.
- [9] T. Kokubo, K. Hata, T. Nakamura, and T. Yamamuro, "Apatite Formation on Ceramics, Metals and Polymers Induced by a CaO SiO₂ Based Glass in a Simulated Body Fluid," *Bioceramics*, vol. 4, pp. 113–120, 1991.
- [10] L. L. Hench, O. Andersson, and A. Akademi, *An Introduction to Bioceramics*. 1969.
- [11] T. Kokubo, H. M. Kim, and M. Kawashita, "Novel bioactive materials with different mechanical properties," *Biomaterials*, vol. 24, no. 13, pp. 2161–2175, 2003.
- [12] T. Kokubo and H. Takadama, "How useful is SBF in predicting in vivo bone bioactivity?," *Biomaterials*, vol. 27, no. 15, pp. 2907–2915, 2006.
- [13] O. Bretcanu, X. Chatzistavrou, K. Paraskevopoulos, R. Conradt, I. Thompson, and A. R. Boccaccini, "Sintering and crystallisation of 45S5 Bioglass® powder," *J. Eur. Ceram. Soc.*, vol. 29, no. 16, pp. 3299–3306, 2009.
- [14] M. Assad and N. Jackson, "Biocompatibility Evaluation of Orthopedic Biomaterials and Medical Devices: A Review of Safety and Efficacy Models," in *Encyclopedia of Biomedical Engineering*, vol. 2, Elsevier, 2018, pp. 281–309.
- [15] "Cytotoxicity | Nelson Labs." [Online]. Available: <https://www.nelsonlabs.com/testing/cytotoxicity/>. [Accessed: 28-Jul-2020].
- [16] Z. J. Rong *et al.*, "Porous nano-hydroxyapatite/collagen scaffold containing drug-loaded ADM-PLGA microspheres for bone cancer treatment," *J. Mater. Sci. Mater. Med.*, vol. 27, no. 5, pp. 1–12, 2016.
- [17] T. L. Riss *et al.*, *Cell Viability Assays*. Eli Lilly & Company and the National Center for Advancing Translational Sciences, 2004.
- [18] Q. Fu, M. N. Rahaman, B. Sonny Bal, R. F. Brown, and D. E. Day, "Mechanical and in vitro performance of 13-93 bioactive glass scaffolds prepared by a polymer foam replication

technique,” *Acta Biomater.*, vol. 4, no. 6, pp. 1854–1864, 2008.

- [19] S. Foppiano, S. J. Marshall, G. W. Marshall, E. Saiz, and A. P. Tomsia, “The influence of novel bioactive glasses on in vitro osteoblast behavior,” *J. Biomed. Mater. Res. - Part A*, vol. 71, no. 2, pp. 242–249, 2004.
- [20] M. Inoue *et al.*, “In vitro response of osteoblast-like and odontoblast-like cells to unsubstituted and substituted apatites,” *J. Biomed. Mater. Res. - Part A*, vol. 70, no. 4, pp. 585–593, 2004.
- [21] “Tumore alle Ossa.” [Online]. Available: <https://www.my-personaltrainer.it/salute/tumore-alle-ossa.html>. [Accessed: 14-Aug-2020].
- [22] C. G. Trejo *et al.*, “The osteoinductive properties of mesoporous silicate coated with osteostatin in a rabbit femur cavity defect model,” *Biomaterials*, vol. 31, no. 33, pp. 8564–8573, 2010.
- [23] P. Niemeyer, K. Szalay, R. Luginbühl, N. P. Südkamp, and P. Kasten, “Transplantation of human mesenchymal stem cells in a non-autogenous setting for bone regeneration in a rabbit critical-size defect model,” *Acta Biomater.*, vol. 6, no. 3, pp. 900–908, 2010.
- [24] “TUNEL staining methods and kits | Abcam.” [Online]. Available: <https://www.abcam.com/kits/tunel-staining>. [Accessed: 14-Aug-2020].
- [25] “The TUNEL Assay | Protocol.” [Online]. Available: <https://www.jove.com/v/5651/the-tunel-assay>. [Accessed: 14-Aug-2020].
- [26] “Colorazioni istologiche.” [Online]. Available: <http://www.istologia.unige.it/page1/page29/page29.html>. [Accessed: 14-Aug-2020].

Ringraziamenti

Vorrei ringraziare il Professore Francesco Bainsi e la Professoressa Enrica Vernè per avermi dato l'opportunità di svolgere questo lavoro di tesi. Vi ringrazio per avermi guidato e supportato permettendomi di arrivare dove sono adesso. Vi ringrazio per avermi trasmesso la conoscenza, la passione e l'entusiasmo necessari affinché la tesi prendesse forma giorno dopo giorno.

Un grazie di cuore alla Dott.ssa Elisa Fiume. Grazie per i tuoi preziosissimi insegnamenti. Grazie per l'immensa disponibilità e pazienza. Grazie per il supporto costante e la complicità nella realizzazione del mio progetto di tesi. Grazie per aver reso questo periodo tanto formativo quanto piacevole.

Grazie alla Dott.ssa Juliana Marchi e al Dr. Roger Borges per aver fornito il materiale per la mia attività sperimentale.

Un sincero grazie a tutto il gruppo di ricerca del DISAT. Grazie per avermi calorosamente accolta e per aver contribuito a rendere così bella questa esperienza.

Un grazie particolare a Giulia e Carla per essere state compagne eccezionali in questa avventura.

Un immenso grazie alle mie amiche e coinquiline Marta M., Marica, e Marta B. Grazie per essere state le mie spalle nei momenti di sconforto, e in prima linea nel supportare le mie folli idee. Grazie per le giornate, ore e minuti che mi avete dedicato pur avendo altro da fare. Grazie per avermi dato la certezza che aldilà della porta di via L.L. Colli 14 avrei sempre trovato qualcuno ad aspettarmi. Vi voglio bene.

Un grazie speciale a Nunzia per la profonda amicizia e intesa. Grazie per esserci sempre stata nei momenti di difficoltà. Grazie per aver reso divertente ogni momento. Grazie per le risate, quelle che vengono dal cuore e che ti lasciano senza fiato.

Un ringraziamento particolare va a tutti i miei amici di Torino per avermi accompagnato in questo percorso. Senza la vostra complicità non sarebbe stato così bello.

Un grazie alle mie amiche di sempre. Grazie per avermi saputo ascoltare, rincuorare e incoraggiare in ogni momento. Grazie per avermi dato la certezza che non sarebbe cambiato nulla tra noi nonostante la distanza. Grazie per il vostro amore infinito e la vostra allegria fuori dal comune.

Un grandissimo grazie ad Alessandro per essermi stato sempre vicino nonostante i 500 Km che ci hanno separato in questi anni. Grazie per aver appoggiato ogni mia decisione e per avermi trasmesso l'entusiasmo necessario per raggiungere questo traguardo.

Il ringraziamento più grande va ai miei genitori che sono il mio punto di riferimento e che mi hanno dato la possibilità di vivere questo periodo universitario con serenità, appoggiando sempre le mie scelte e consigliandomi ogni volta la strada giusta da prendere.